1-1-2015

Minimum Hot Surface Ignition Temperature Diagnostics Including Infrared Imagery

Jesse Filmore Adams
Purdue University

PURDUE UNIVERSITY
GRADUATE SCHOOL
Thesis/Dissertation Acceptance

This is to certify that the thesis/dissertation prepared

By Jesse F. Adams

Entitled
MINIMUM HOT SURFACE IGNITION TEMPERTURE DIAGNOSTICS INCLUDING INFRARED IMAGERY

For the degree of Master of Science in Aeronautics and Astronautics

Is approved by the final examining committee:

Jay P. Gore
Chair

Stephen D. Heister

Timothée Pourpoint

To the best of my knowledge and as understood by the student in the Thesis/Dissertation Agreement, Publication Delay, and Certification Disclaimer (Graduate School Form 32), this thesis/dissertation adheres to the provisions of Purdue University's "Policy of Integrity in Research" and the use of copyright material.

Approved by Major Professor(s): Jay P. Gore

Approved by: Wayne Chen 12/18/2015
Head of the Departmental Graduate Program Date

MINIMUM HOT SURFACE IGNITION TEMPERATURE DIAGNOSTICS INCLUDING INFRARED IMAGERY

A Thesis

Submitted to the Faculty

of

Purdue University

by

Jesse F. Adams

In Partial Fulfillment of the

Requirements for the Degree

of

Master of Science in Aeronautics and Astronautics

December 2015

Purdue University

West Lafayette, Indiana

To my Mother and Father,

ACKNOWLEDGEMENTS

In many ways, this document is the culmination of my time and experiences at Purdue. It is the byproduct of not only my own effort, but of the help and guidance many others have given me on the way. I must begin by thanking my advisor, Professor Jay Gore for both providing me this tremendous opportunity and for his patience. I am also duly grateful to Professor Stephen Heister and Professor Timothée Poupoint for serving on my thesis committee.

I must also express my gratitude to several fellow students at working at Maurice J. Zucrow Laboratories. Acknowledgements go to Steven Hunt, Heather Wiest, Rohan Gejii, Vikrant Goyal, Andrei Anghelus, and Luke Mishler for all of their assistance in helping me realize this project. More than just outstanding engineers, they are all also outstanding people.

Sincere thanks go to Chris Potter and Charles Sese for their support and friendship throughout this process, and for always having a pep talk ready when I was unsure if I would make it.

Lastly, a very special thank you to Scott Meyer. I would never have accomplished this level of work without his advice and guidance. I am truly a better engineer from having known him.

This project was supported by Rolls-Royce Corporation through their UTC collaboration with Purdue University.

TABLE OF CONTENTS

Page

Page

LIST OF FIGURES

Figure Page

Figure Page

Figure Page

Figure Page

LIST OF TABLES

Table Page

NOMENCLATURE

Symbols	Description
W	Molar rate per unit volume
Z	Pre-exponential factor
c	Reactant concentration
E_a	Activation Energy
R	Universal Gas Constant
T	Temperature
Q	Heat rate
V	Volume
ΔH_r°	Heat of reaction per mole
h	Generalized heat transfer coefficient
A	Area
ρ	Density
c_p	Specific Heat
t	Time
k	Generalized thermal conductivity
λ	Latent heat of vaporization
a	Side length of a geometric object
θ	Angle
U, u	Velocity
$\dot{E}$	Generalized energy rate
$\bar{h}$	Average convective heat transfer coefficient
v	Kinematic viscosity

Re	Reynolds number
L, l, x	Length scale
$\overline{Nu}$	Nusselt Number
Pr	Prandtl number
ε	Emissivity
σ	Stefan-Boltzmann's constant
α	Absorptivity
G	Total incident radiation
Bi	Biot number
S	Arc length
r	Radius
α_{exp}	Linear coefficient of thermal expansion
$q^{"}$	Heat flux
δ_p	Thermal penetration depth
$\dot{m}$	Mass flow rate
C_d	Fluid discharge coefficient
γ	Ratio of specific heats
p	Pressure
M	Total mass
P	Probability
b_o, b_1	Coefficients for logistic curve fit
Da	Damköhler number
Δ	Delta, signifying a change in state

Subscripts	Description
$chem$	Relating to chemical process
$surr$	Relating to system surroundings
$cond$	Relating to conduction
Rad	Relating to radiation heat transfer
st	Relating to energy storage
in	Relating to energy inflow
out	Relating to energy outflow
gen	Relating to energy generation
s, w	Relating to a surface or wall
∞	Freestream condition
f	Relating to a fluid as opposed to a solid
L	Relating to a length scale or displacement
c	Indicates characteristic dimension
i	Relating to an initial condition
t	Relating to a throat restriction
1	Relating to an upstream condition
g	Relating to a gas
l	Relating to a liquid
x	Specifically relating to x displacement
y	Specifically relating to y displacement
cm	Indicating center of mass

Abbreviations	Description
AENFTS	Aircraft Engine Nacelle Fire Test Simulator
AFRL	Air Force Research Laboratory
MHSIT	Minimum Hot Surface Ignition Temperature
HSIC	Hot Surface Ignition in Crossflow

ABSTRACT

Adams, Jesse, F. M.S., Purdue University, December 2015. Minimum Hot Surface Ignition Temperature Diagnostics Including Infrared Imagery. Major Professor: Jay P. Gore, School of Aeronautical and Astronautical Engineering

Hot surface ignition caused by a leak from ruptured fuel or hydraulic lines impinging on high temperature engine surfaces poses dangers to both the automotive and aviation industries. Many previous studies have investigated the aircraft engine nacelle environments most conducive to hot surface ignition, but alterations and improvements in turbofan engine design have left many of these studies obsolete or in need of expansion.

A literature review is presented to survey these previous studies. Particular emphasis is made on a study conducted under the Air Force Wright Aeronautical Laboratory at Wright-Patterson Air Force Base. Additionally, a distinction is made between hot surface ignition and auto-ignition.

Finally, the design and verification of a new experimental apparatus to investigate hot surface ignition for modern turbofan engines is presented. Supplementary experiments including infrared imaging on a quiescent hot surface are also described.

CHAPTER 1. MOTIVATION AND OBJECTIVES

1.1 Motivation

The threat of hot surface ignition and its underlying causes are a source of ongoing concern for the aircraft and automotive industries. Property losses attributable to motor vehicle fires total in excess of 1 billion dollars annually in the U.S. alone [1]. Moreover, at least two-thirds of these fires can be traced back to vehicle engine compartments [1], where hot manifold surfaces and numerous fuel lines often exist in close proximity to one another. Dramatic reminders of the dangers of hot surface ignition in aircraft are found in both recent and not so recent headlines. The explosion of Trans World Airlines Flight 800 in July of 1996 was a fatal and costly disaster that resulted in the loss of 230 lives [2]. It was concluded during the subsequent investigation that the explosion was the result of a flammable mixture of fuel and air inside the aircraft's center wing fuel tank being subject to tremendous heat transfer rates due to the tanks contact with the surface of the hot, air conditioning packs located directly below [2]. In November 2010, Qantas Flight 32 was forced to make an emergency landing when a ruptured lubricant line led to an oil fire in one of the aircraft's Rolls-Royce Trent 900 engines [3].

Figure 1.1 Damaged engine No. 2 of Qantas Flight 32 [4]

Rolls-Royce's sponsorship of the present research is motivated by a desire to verify and extend the database it currently uses to certify the safety of its engines against the danger of hot surface ignition. The database was originally established from experimental trials conducted by Johnson et al. [5] at Wright-Patterson Air Force Research Lab. When evaluating the minimum hot surface ignition temperature of an aircraft fluid, Rolls-Royce applies a heat rejection model to predict engine skin temperature [6]. The heat rejection model subdivides the engine into cylindrical zones of interests, and calculates a single expected skin temperature for each zone. The average zone length is between 4 and 5 inches. The model incorporates one dimensional conduction through the core engine casing as well as the inner and outer bleed air ducts [6]. The effects of conduction propagate across zones, but radiation and convection are specifically treated for the cylindrical control volume of a single zone.

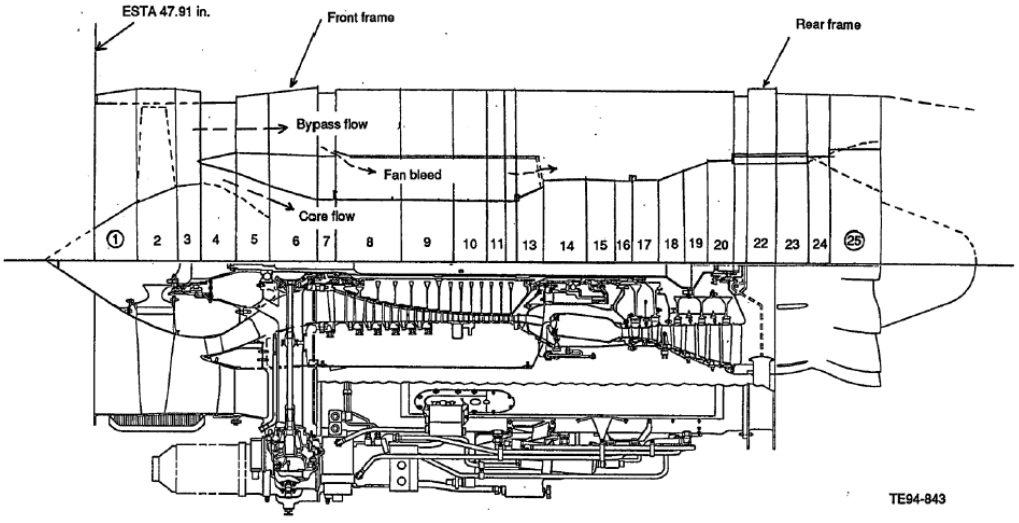

Figure 1.2. AE 3007 divided into 25 zones for the heat rejection model [6]

The skin temperature predicted for a zone is compared against the hot surface ignition database to produce what is referred to as a minimum hot surface ignition temperature or MHSIT margin [6]. The margin is the predicted skin temperature subtracted from the database temperature. Positive margins are associated with engine safety. The ignition temperature referenced from the database considers multiple factors including: leak fluid, local air temperature, local air velocity, pressure, and leak type (spray or stream).

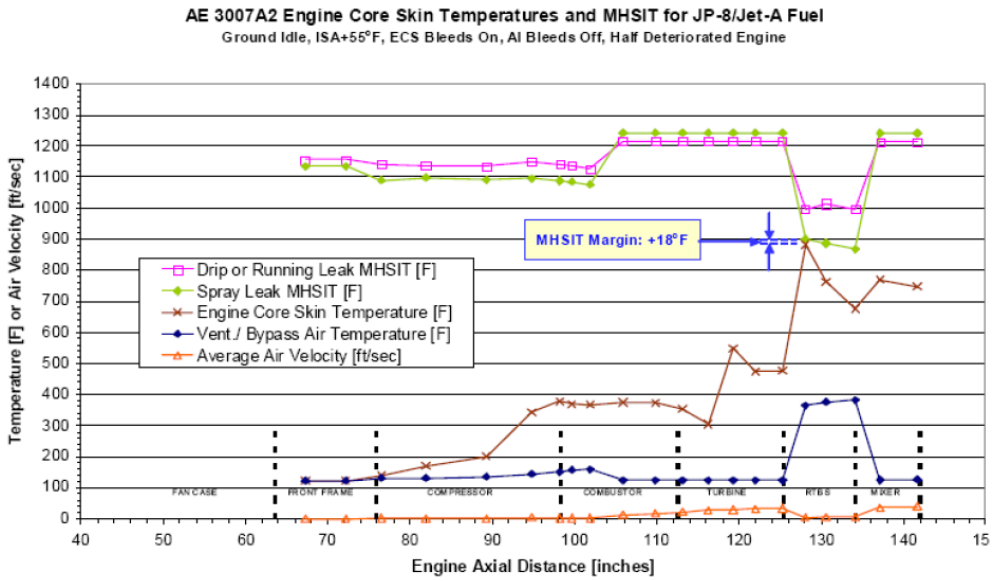

Figure 1.3. Skin temperatures compared against database MHSIT for JP-8/Jet-A [6]

Despite its usefulness, the current database presents a number of frustrations for Rolls-Royce. In the database, air velocities never exceed 11 ft/s. This is almost a full order of magnitude lower than velocities observed inside the engine nacelle. The database contains data that was taken over 2 decades ago. Some fluids that appear in the database, such as JP-4, have been phased out of general use while modern aircraft fluids such as the MIL-PRF-23699, a new lubricating oil, do not appear at all. The hot surface ignition project at Purdue is intended to redress these issues.

1.2 Objectives

At the outset of the hot surface ignition project, the following objectives were enumerated:

1. Conduct a literature review
    a. To cleanly identify the distinction between auto-ignition and hot surface ignition phenomena.

   b. To survey the range of hot surface ignition studies previously conducted
   c. To identify and to describe in detail the old experimental apparatus used to create the existing hot surface ignition database

2. Design and construct an experimental rig that is scaled, modular, and expands the scope of achievable experimental conditions from those already in the minimum hot surface ignition temperature database.
3. Begin the process of verifying the experimental rig's operation by repeating selected test conditions from the established database.

CHAPTER 2. LITERATURE REVIEW

2.1 Fundamentals of Hot Surface Ignition

Throughout the course of the literature review, multiple sources stressed the inherent differences between auto-ignition and hot surface ignition [7-9]. Thermal ignition is broadly understood to be the result of a combustible mixture (either with or without an external heating source) undergoing an exothermic reaction such that the heat release from reaction overcomes the heat losses to the surrounding environment [10]. This is modeled in theories by both Semenov [10] and Frank-Kamenetskii [10]. Semenov applied his approach to a gas mixture and assumed the rate of chemical reaction adheres to the Arrhenius law, with *W* representing a molar rate per unit volume.

$$W = Zc^n e^{-E_a/RT} \quad \text{[Eq. 2-1]}$$

In equation 2-1, *Z* is the pre-exponential factor, *c* is the initial reactant concentration, E_a is the activation energy, *R* is the universal gas constant, and *T* is the temperature of the system. The heating rate from chemical reaction was thus:

$$Q_{chem} = V\Delta H_r^\circ Z c^n e^{-E_a/RT} \quad \text{[Eq. 2-2]}$$

The heat of reaction per mole is ΔH_r° and V is the total system volume. Semenov modeled the heat loss to the surroundings [10] in the general formal of Newton's law of cooling.

$$Q_{surr} = h(T - T_w)A \quad \text{[Eq. 2-3]}$$

The temperature of the system is given as T, the temperature of the system walls is T_w, A is the surface area of the system wall, and h is a generalized heat transfer coefficient. The critical condition that sits on the boundary between ignition and extinction is the point when equations 2-2 and 2-3 are set equal to one another. Semenov effectively models the system as a well-stirred reactor at a uniform temperature [10]. Incidentally, these conditions align with those for auto-ignition. Frank-Kamenetskii presents a more rigorous formulation that takes into account temperature non-uniformity within the reacting system [10].

$$\rho c_p \frac{\partial T}{\partial t} = \rho \Delta H_r^{\circ} Z e^{-E_a/RT} + k\nabla^2 T \qquad \text{[Eq.2-4]}$$

The left-hand expression is the heating rate for the system. The first term on the right is the heating rate from chemical release, and the final expression is of the conduction heat loss at the system boundaries [10]. To an extent, the differences in Semenov's and Frank-Kamenetskii's approaches to ignition theory parallels the differences between auto-ignition and hot surface ignition. The auto-ignition temperature of a flammable fluid is determined under a well-documented standard, ASTM E659 [11]. To find auto-ignition temperature, a carefully metered sample of flammable liquid is inserted into a uniformly heated, 500 mL glass flask at ambient pressure. The temperature is steadily raised until the ignition is observed. There is no such standardization for hot surface ignition, which is most frequently considered within highly non-uniform environments and is subject to a host of variables including [8]: irregular surface geometry, airflow near the surface, ambient air temperature [5], whether fluid is introduced as a spray or stream, etc. Kuchta phrases the difference particularly clearly in terms of the quality of the ignition source [10]. Strong ignition sources have incredibly high heating rates and also tend to be highly localized

spatially or temporally (or both). Examples of this are spark ignition, lasers, and pilot flames. A weaker form of forced ignition is seen in diesel engines which exhibit a more uniformly distributed system energy, but must rely on compression to achieve ignition. Weaker still is auto-ignition which has a uniform distribution of system energy, but lacks any active compression. The weakest of all these ignition sources is the hot surface. It lacks both the high energy density of a spark, and the well-distributed properties seen in auto-ignition since the flammable mixture only contacts the hot surface at specific locations within the ignition system. Accordingly, experimentally observed hot surface ignition temperatures for flammable fluids are frequently at least 300°C higher than corresponding auto-ignition temperatures. Colwell [8] provides an elucidating figure on the differences across these ignition sources.

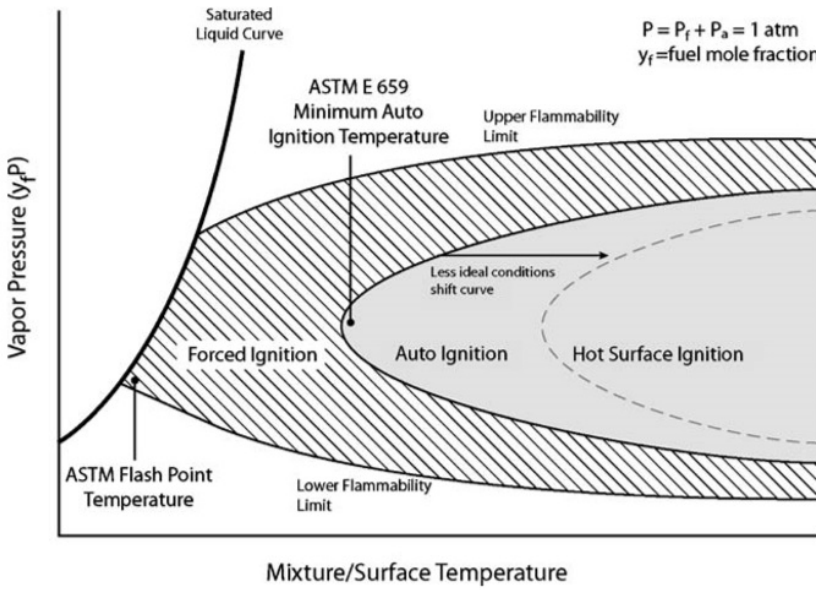

Figure 2.1. Flammability/ignition regimes as function of temperature and fuel vapor pressure [8]

2.2 Quiescent Hot Surface Experiments

The experimental work surveyed for this research is divided into two categories: those that did droplet ignition in quiescent environments and those that attempted to simulate the harsher environments of aircraft engine bays complete with crossflows, recirculation zones, and irregular surface geometries. Although the hot surface ignition project at Purdue is firmly in the latter category, the quiescent experiments offered considerable insight into the fundamentals of hot surface ignition.

The Leidenfrost phenomenon is intimately linked to droplet ignition on hot surfaces. When small quantities of liquid are spilled onto a surface that well exceeds their saturation temperature, a thin vapor film forms between the surface and the liquid. Because the liquid drop is only in contact with the vapor, it glides smoothly across the surface without wetting it. This vapor film has the added effect of acting as an insulator, slowing the evaporation rate of the drop. Gottfried et al. [12] describe the heat transfer processes attendant to the Leidenfrost effect on a spherical drop.

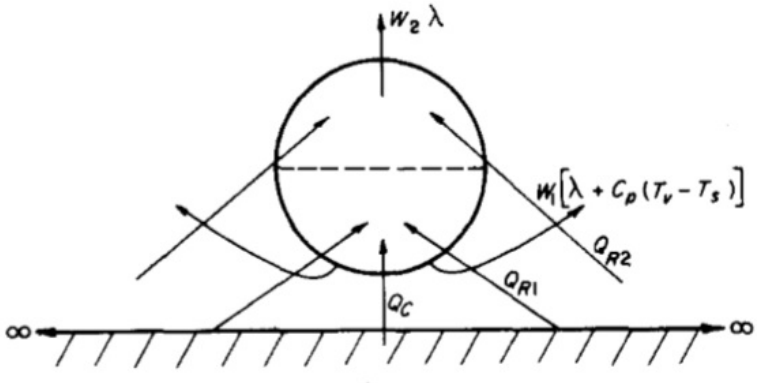

Figure 2.2. Heat transfer and mass transfer paths for the spherical droplet model [12]

$$Q_{cond} + Q_{Rad1} + Q_{Rad2} = W_1\left[\lambda + c_p(T_v - T_s)\right] + W_2\lambda \qquad \text{[Eq. 2-5]}$$

Heat is conducted to the lower surface of the droplet through the vapor film. The overheated plate also radiates heat to the upper (Q_{rad2}) and lower (Q_{rad1}) surfaces. These rates differ, however since radiation on the lower half occurs through the vapor film. Heat is lost from the droplet through the advection that accompanies evaporation; once again, W gives the rate. The latent heat of evaporation is represented by the symbol, λ. The vapor transported from the lower surface is trapped inside the vapor film and raised to its temperature. A sensible heat term is added to complete the energy balance. Numerical methods can be applied to this balance to approximate a droplet lifetime [12]. Experiments that vary drop volume on a heated plate could then be used to identify the effects, if any, that drop lifetime has on either hot surface ignition temperature or the ignition delay.

A number of researchers performed experiments wherein a metered droplet of flammable liquid was deposited on the surface of an isothermal plate [7-9, 13]. In these researches, the flammable fluids were tested exhaustively. It was typical to conduct over 200 ignition tests per fluid [8]. These experiments were valuable for their relative simplicity and repeatability. The apparatus used by Colwell [8] is presented as an example in the figure below.

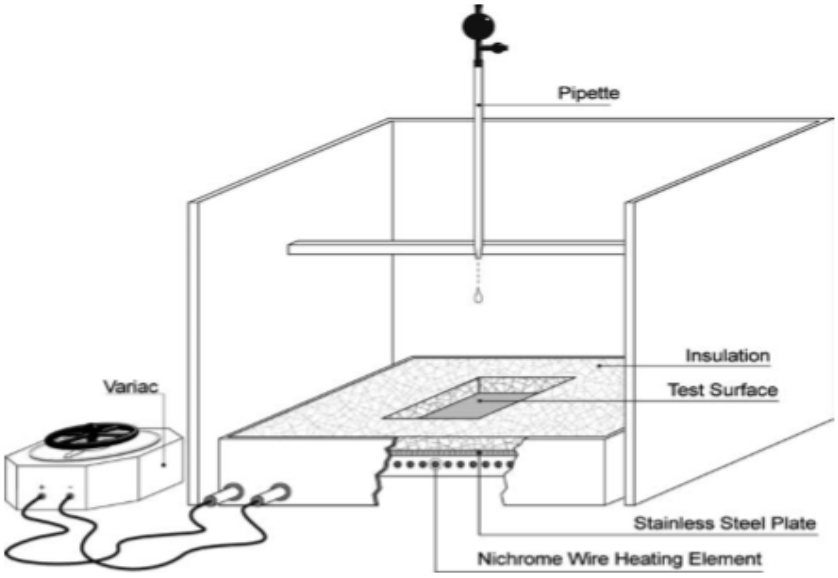

Figure 2.3. Test stand for an isothermal plate [8]

The test surface is a 48 cm by 38 cm by 4.8 cm thick stainless steel 304 plate. The 3-sided enclosure is a draft shield to minimize any cross-flow effects. The plate is electrically heated with a nichrome wire heating element, and the purpose of the insulation is to keep the plate temperature relatively isothermal. Tests were conducted with a wide variety of both automotive and aviation fluids. Rather than observing a specific plate temperature at which the fuel suddenly ignited (as with the auto-ignition temperature), ignition was found to be probabilistic in nature. At an established plate temperature, ignition was best characterized through a probability curve with the onset occurring at some minimum plate temperature. Ignition probability subsequently rose with increasing temperature across a range of plate settings before reaching the point when the probability of ignition became 100%. Colwell's [8] findings for several aviation fluids are shared in the plot below. Data was plotted using a logistic regression curve. The focus on the results for the aviation fluids came from the large overlap with the fluids

that were eventually selected for experimentation on the Purdue hot surface ignition project.

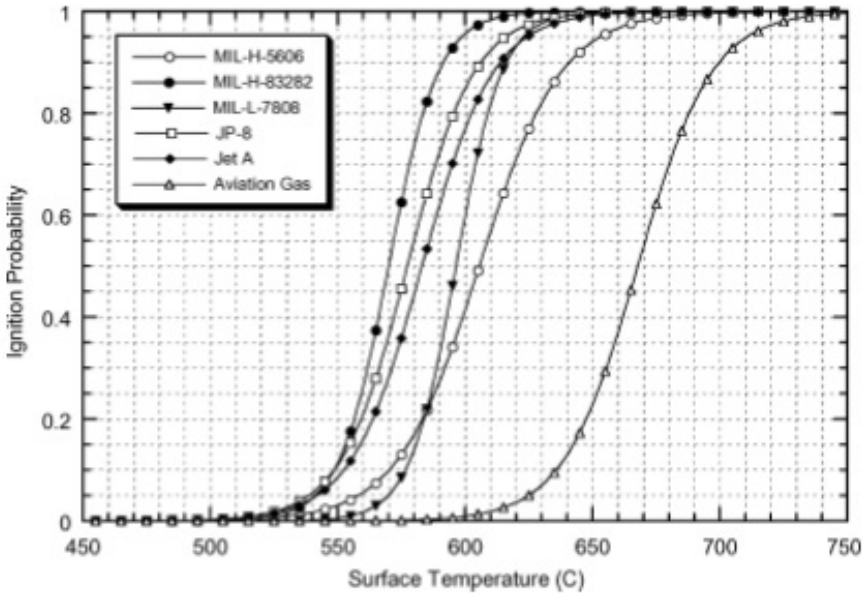

Figure 2.4. Ignition probability as a function of plate temperature for aviation fluids [8]

Probabilistic ignition behaviors were reported for practically all the quiescent plate experiments reviewed. This behavior was not reported for any of the higher velocity, higher realism test articles described in the upcoming section. This omission is either due to no attempt being made to quantify an ignition probability or because probabilistic ignition no longer applies. On these complex test articles, fuel is not administered as a drop, but as a stream or spray or steady drip. Odd surface geometries and bypass air streams add greater barriers to ignition. If this probabilistic behavior no longer applies, it could be a byproduct of these barriers rendering ignition much less likely to occur. Future work might focus on applying these probabilistic curves to more complex test environments.

2.3 Previous Hot Surface Ignition Experiments in a Crossflow

This section summarizes the experimental work on hot surface ignition done by Myronuk [14], Graves [15], and Ingerson [16]. The scale of the experimental rigs involved as well as the operational issues encountered were studied for supplementary insight during the design phase of the test apparatus at Purdue. The test rig at Wright-Patterson [5] is the basis of the current Rolls-Royce database and proved to be so influential on the design process that a separate section is devoted to its summary.

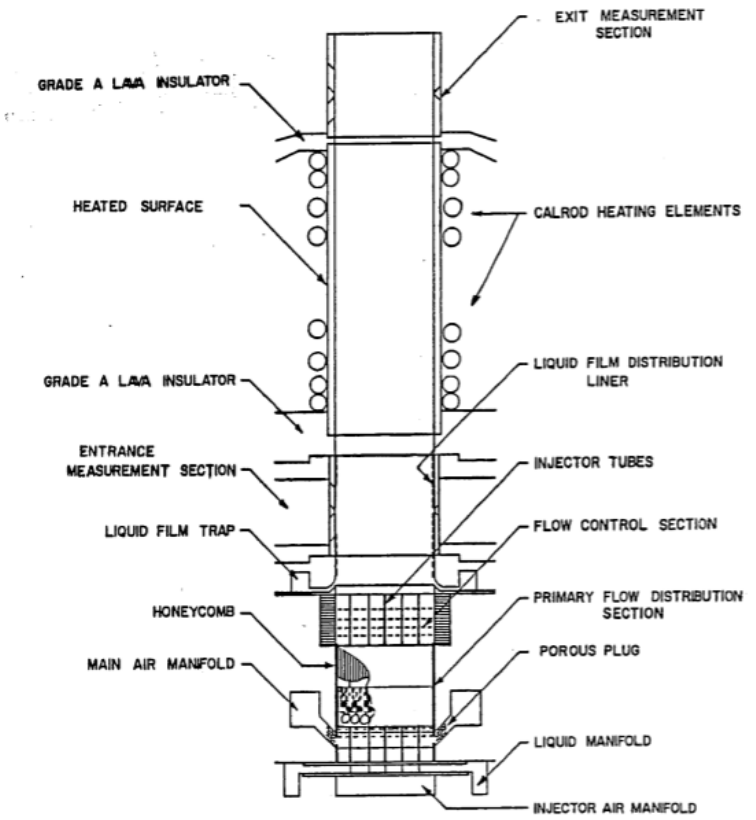

Figure 2.5. Experimental rig used by Graves [15]

Graves investigated hot surface ignition phenomena inside of a vertical duct that conditioned the airflow and introduced a liquid fuel spray at its base prior to sending the mixture up into the test section of the rig. The fuels used were propane and kerosene.

Attempts were made to tightly control the stoichiometry of the fuel-air mixture. The apparatus was left at atmospheric pressure. The test section ran 6 inches long and was insulated at it its inlet and exit by a ceramic lava insulator. Nickel or stainless steel were alternately used as the material for the test section walls with CALROD® elements coiled around the exterior to supply heat. The temperature of the target surface was varied from 1445°F to 1726°F, and the velocity of air flowing through the test section varied from 3.5 to 13 ft/s. At the 13 ft/s velocity condition, the wall temperature of ignition was 1726°F for propane [15]. Issues encountered with the apparatus involved the splash-back of liquid fuel falling under the influence of gravity. Liquid film traps were added to somewhat mitigate this effect. This splash-back also interfered with the collection of kerosene data since controlling the momentum of the liquid fuel became a serious restriction on the experiments conducted. Propane's inclusion in the experimental test matrix was viewed as a correction of sorts. The low-flash point meant a fuel that easily vaporized and mixed with the airflow to more readily create the targeted stoichiometries and even mixture distributions desired by the researchersx. Also being a hydrocarbon, propane was considered to compliment the other fuel, effectively approximating a well-behaved kerosene spray. Graves did observe that for very diffuse sprays, it was possible to visually determine the location of ignition. This is recommended for those future experiments on the Purdue test article where there are a large number of flow disturbances.

Myronuk and Ingerson performed experiments on test articles that more closely resembled the environment inside an engine Nacelle [14, 16]. Of the two, Ingerson's experiment was more limited in scope, only using JP-8 as test fluid and focusing

primarily on the introduction of Halon 1301 as a fire suppressant. Myronuk used a host of aircraft fluids including JP-4, JP-5, Jet-A, MIL-H-5606, MIL-H-83282, Freon, among others [14]. Myronuk heated his test section using the hot product gases of a propane-air flame.

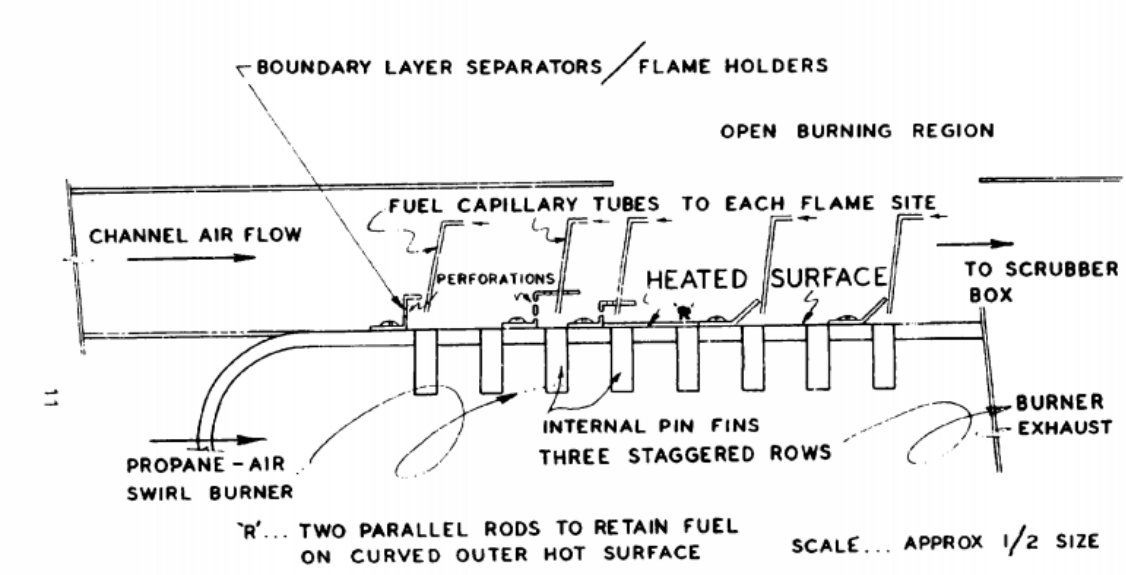

Figure 2.6. Cut side view of Myronuk test apparatus [14]

Pin fins extended into the hot gas stream and transferred heat to the test surface. Capillary tubes transported and deposited fuel onto the test site. Boundary layer separators were staggered throughout the test site to create flame holders and recirculation zones. Myronuk demonstrated the largest air flows and surface temperatures, having a maximum achievable velocity of 164 ft/s and a maximum achievable surface temperature of 1922°F [14]. Myronuk first observed the trend that would later be observed at Wright-Patterson [5]: the more volatile the fuel under consideration, the more difficult it was to ignite. It was posited that although the more volatile fuel readily evaporates and mixes with the oncoming airstream, the process occurs so quickly that the vapor-air mixture is easily

transported away from the ignition source by bulk fluid velocity. It was therefore observed that the less volatile fuels ignited at lower surface temperatures since the flammable vapor mixture formed more slowly and remained closer to the ignition source [14]. The specific fuel noted to most consistently exhibit this behavior was JP-4, a pattern that would be repeated on the Wright-Patterson apparatus [5].

2.4 The Wright-Patterson Test Rig

The work done with the Wright-Patterson test rig, alternatively known as the Aircraft Engine Nacelle Fire Test Simulator (AENFTS), was the most impactful previous research. This stemmed largely from its direct relationship with Rolls-Royce's established approach to managing hot surface ignition. The test article:

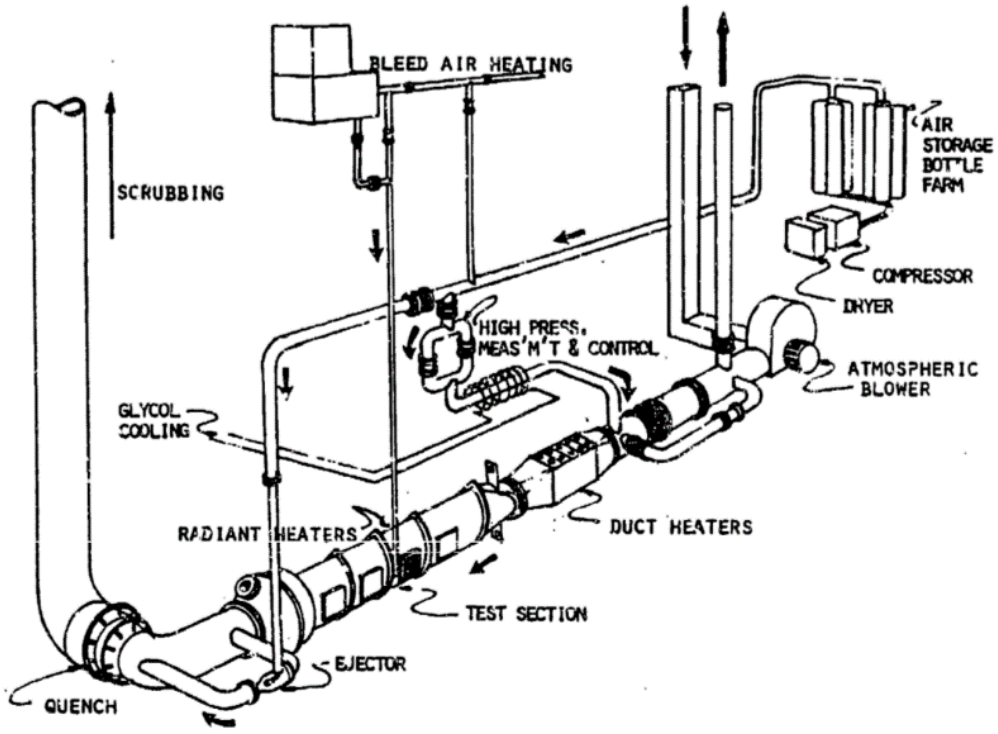

Figure 2.7. The Wright-Patterson test article, the AENFTS [5]

The test rig was designed to study nacelle fires under simulated flight conditions. The data included in the report by Johnson et al. was taken in the period from May 1987 to May 1988 [5].

The test rig simulated ventilation air velocity, air pressure, air temperature, bleed air ducting, nacelle geometry, and the introduction of fuel leaks. Five common aircraft fluids were tested under the Wright-Patterson experimental campaign. These included: JP-4 (jet fuel), MIL-H-5606 (hydraulic fluid), MIL-H-83283 (hydraulic fluid), MIL-L-7808 (lubricant oil), and JP-8 (jet fuel). All of these fluids were introduced to the test section of the apparatus in the form of either a spray or stream via the nitrogen-pressurized fluid delivery system. The test section of the Wright-Patterson rig is the 114 degree segment of the annulus between a 15 inch radius inner duct, and a 24 inch radius outer duct. A close-up of the test section is featured below.

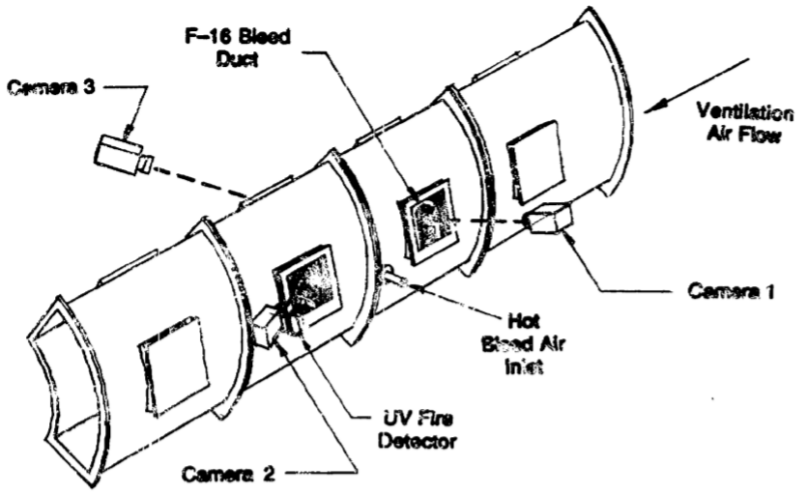

Figure 2.8. Close-up of test section with connection to bleed air source and flow direction shown

Figure 2.8 [5] also shows the placement of the 3 cameras and UV detector respectively intended to gather visual data and to detect ignition during experiments. Although the UV detector was successful at indicating ignition, the cameras were generally unable to pinpoint the initial flame location visually due to the clutter of features installed inside the test section. The Wright-Patterson rig had two distinct test articles that could be inserted into the test section for experiments. The *Simple Duct* test article was a 6.5 inch long Inconel tube and the *High Realism* test article was the complete forward, right section of an F-16 nacelle [5]. The *High Realism* test article included a 13 stage bleed air duct, an air-oil heat exchanger tank, a fuel pump, and various tubes and clamps. When sprayed into the test section, fluid was either injected from upstream or downstream of the test article. When a stream or drip was used, fluid was typically injected at or near the location of installed thermocouple sensors. Fluid injection rate could run as low as 1 mL/s or as high as 12 mL/s, but 8 mL/s was the most common injection rate.

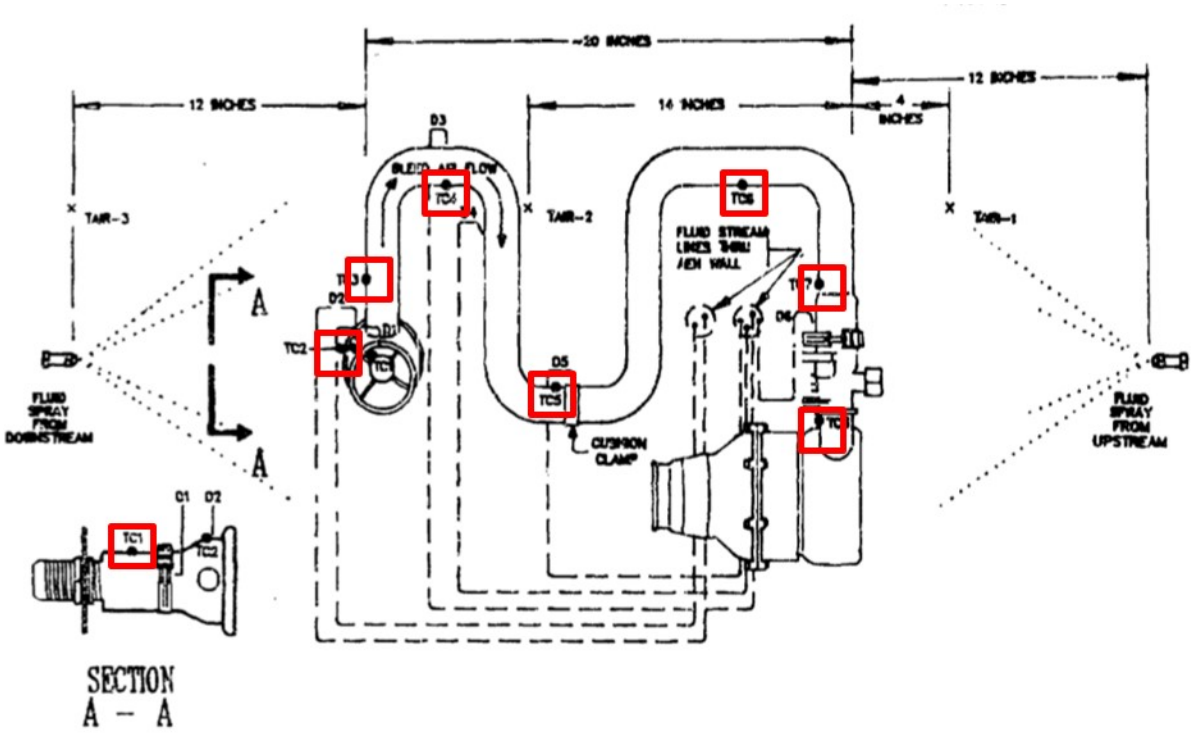

Figure 2.9. Bleed air ducting that comprised much of the High Realism article, thermocouple locations are boxed in red [5]

The Wright-Patterson rig relied on two methods of heating depending on its target test article. The *Simple Duct* test article was alternately heated using electrical resistance heating or with bleed air piped into the test section from the bleed air system. The *High Realism* test article was exclusively heated with bleed air that ran through the length of bleed air ducting included on the *High Realism* test article. The hottest temperature recorded during testing was in the vicinity of 1500°F. Over the course of many tests, the Johnson et al. were able to identify general relationships between the minimum hot surface ignition temperature, and conditions within the test section [5].

Table 2.1. Effect of Duct Conditions on Minimum Hot Surface Ignition Temperature (MHSIT)

Experimental Parameter	Effect on MHSIT	Degree of Influence
Flow Obstruction	Decrease	Weaker with volatile fluids
Fluid Exists as a Stream	Decrease	-
Fluid Exists as a Spray	Increase	-
Fluid Flowrate	-	Extremely weak (no real effect)
Fluid Flow Duration	-	Extremely weak (no real effect)
Rising Ventilation Pressure	Decrease	Stronger on sprays
Rising Ventilation Temperature	Decrease	Strongest on volatile sprays
Rising Ventilation Velocity	Increase	Weaker on streams

Just as Myronuk noticed the added difficulty of igniting the highly volatile JP-4 [14], Johnson et al. [5] similarly noticed the difficulty of igniting more volatile test fluid. As an addendum to Myronuk's observation, Johnson et al., who raised the air temperature of their test section above ambient, noticed that the more volatile fuels became easier to ignite with rising temperature [5]. Because the overall air temperature throughout the test section was higher, the transport of the ignitable mixture away from the target thermal

source was less detrimental to its ability to absorb heat from the surroundings. These experimental findings, as well as the arrangement of the test apparatus, informed a sound working knowledge of the fluid behaviors to expect and how to manage them as work proceeded on to the design process.

CHAPTER 3. THE DESIGN PROCESS

3.1 Design Rational

Design objectives of a test article that is scaled and modular while extending the range of flow conditions previously achieved by the Wright-Patterson rig [5], necessitated a departure from that experimental arrangement. The new experiment maintains selected features of the Wright-Patterson rig for the purpose of data continuity but takes a modified approach to surface heating, test article symmetry (configuration), pressurization, and duct geometry.

The Wright-Patterson rig included the method of heating the target surface as a variable in its text matrix. The test article was heated using either electrical resistance or air from a bleed air heating system. Despite having multiple means of heating, only bleed air was applied to the high realism test article. For the simple Inconel tube test article, electrical resistance heating was managed by the insertion of three 1 KW Watlow Firerod® heaters into a 6.5 inch long steel cylinder which was itself inserted into the inner diameter of the tube. For bleed air heating, this steel cylinder was removed to allow air to be piped through the Inconel tube. Ultimately, since only one heating method was common to both test articles, it was decided that a single approach to surface heating would be appropriate for the Purdue experiment. The Wright-Patterson rig used bleed air as its common heating method, but the added complexity of supplying and maintaining separate streams of air at different temperatures (one stream to simulate bypass air and

the other to heat the target surface) made this a less viable design. Purdue's test article uses electrical resistance heating, but eliminates the steel cylinder previously used to hold the 1 KW heating elements in place. Instead, the new target surface is dimensioned such that the heater elements can be directly inserted. By providing immediate contact between the heating elements and the hot surface, the Purdue rig improves upon the thermal management possible when air and steel were used as intermediaries. Greater detail on the design of the target surface is provided in the section on Hot Centerbody design.

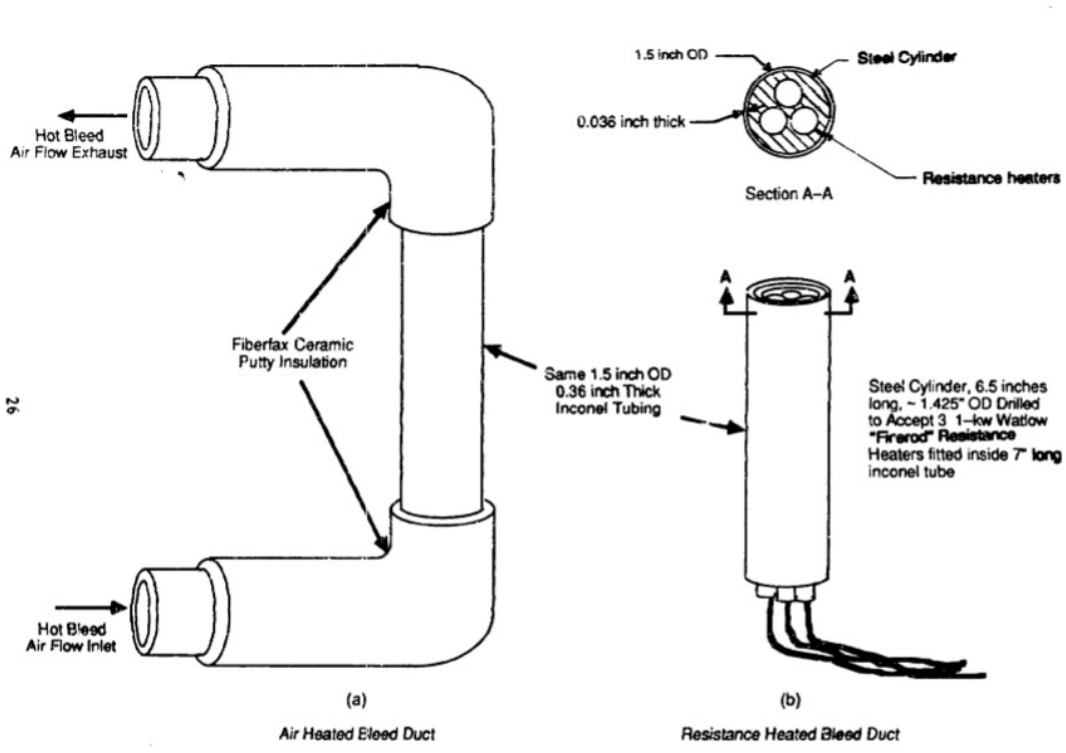

Figure 3.1. Wright-Patterson heating methods for the Simple Duct test article [5]

It was mentioned in the literature review chapter that the test section of the Wright-Patterson rig was a 114 degree section taken from the annular gap between a 15

inch radius inner duct that simulated the engine casing, and a 24 inch radius outer duct that simulated the engine compartment outer wall. This annular section could be rotated to either a vertical or horizontal position so that the test article is oriented either perpendicular or parallel to the floor respectively.

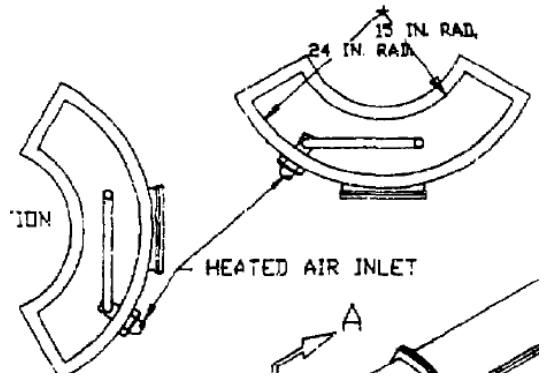

Figure 3.2. Wright-Patterson test article in vertical (right) and horizontal (left) orientations [5]

However, as with the heating method, only one orientation, the vertical position, was used for both the simple and high realism test articles. Rather than assume axisymmetric flow conditions are being approximated and rely on a section of the annulus to simulate the engine nacelle environment, the scaled nature of the Purdue test article allows the full circumference to be recovered without the concerns of size and weight. This permits both the “vertical” and “horizontal” orientations of the Wright-Patterson rig to be replicated simultaneously, and brings the Purdue experiment closer to simulating actual engine conditions.

The Wright-Patterson rig made provisions for test section pressures that were off-atmospheric. An air ejector was used to lower pressure to either 5 or 10 psia and represent high altitude flight [5]. A compressor was used to simulate ram conditions, and

raise test section pressure to 20 psia. These functions existed in addition to a blower that supplied air at atmospheric conditions. Upon consulting with Rolls-Royce on how the current MHSIT database is used, the pressure requirements were relaxed to only atmospheric conditions. This is achieved by permitting the Purdue test article to exhaust to ambient.

The geometry of the outer duct shaping and directing the flow through the annulus of the new test article has been changed substantially from the Wright-Patterson rig. A new design constraint introduced by using an infrared camera to take planar images of ignition phenomena near the hot target surface is that of flat visualization windows. Instead of attempting to adapt a flat window to a circular duct, an octagonal design was chosen to provide both the flat surface required by the optical windows and a rough approximation of a circular cross-section. Adapting flat rectangular windows to a circular duct was avoided since this would have created recessed zones around the windows which could trap the injected fuel, and disrupt the air flow field near the surface. Consequently, the octagonal duct is a compromise between geometric simplicity, projected planar surfaces, and a quasi-circular flow area.

These aspects of the test article, the choices of heating and pressurization and geometry, do not cover the breadth of the decisions made in its design, but they proved to be foundational. As it will be described throughout the remainder of this chapter, these core concepts informed nearly every feature of the test article’s design.

3.2 Dimensioning the Experimental Rig

The first task of designing the Purdue test article, hereafter referred to as the Hot Surface Ignition in Crossflow, or HSIC test rig, was the determination of the scaled annular test section. As mentioned earlier, the test section of the Wright-Patterson rig was the annular gap between a 15-inch radius inner wall simulating an engine casing, and a 24-inch radius outer wall. The weight and cost of reproducing such cross-sectional dimensions for the HSIC test article made direct imitation an undesirable option. The additional requirement of increased test section flow velocities (as much as 80 ft/s) also meant air mass flowrates that would be taxing for the High Pressure test facility (over 11 lb/s for the full annular cross-section). The scalability of fluid physics [17] permitted the dimensions of the HSIC test rig's cross-section to be reduced from the Wright-Patterson rig so long as the geometric proportions were conserved.

The central area of the HSIC rig had to be chosen such that the corresponding annular gap was large enough to provide visual resolution for ignition occurring within the test section as well as space to secure mechanical features to modify the air flow field. If the central area chosen was too small, there would be very little space to install either injectors or the tubing, flanges, etc. that would allow the test rig to more closely resemble an operating engine casing. Taking the proportion of the outer wall radius to the inner wall radius in the Wright-Patterson rig, table 3.1 provides associated dimensions for a series of scaled test sections. The 3 inch radius was selected because the corresponding annular gap accommodated features ranging from 1-1/4 to 1/8 of an inch while avoiding the concerns of cost and weight.

Table 3.1. Dimensions of Scaled Test Sections

Assumed Inner Radius, in	Outer Radius, in	Annular Gap, in
1”	1.6”	.6”
2”	3.2”	1.2”
3”	4.8”	1.8”
4”	6.4”	2.4”

Once an appropriate flow cross-section was selected, it needed to be adapted to the octagonal duct. It was determined that the relevant length was the 4.8 inches from the centerline of the test section to the midpoint of any of the outer duct’s eight walls. This had the effect of completely capturing the flow volume of the corresponding circular duct within the octagon and making the center point of the optics windows coincident with that circular duct’s walls. A camera or flow visualization device pointed at the center of a window will effectively see the same flow field as it would for a circular duct. The dimensions of the regular octagon that would permit this were then derived from a simple geometric analysis using interior triangles and the constraint of a 4.8 inch distance from the center of a side to the center of the octagon.

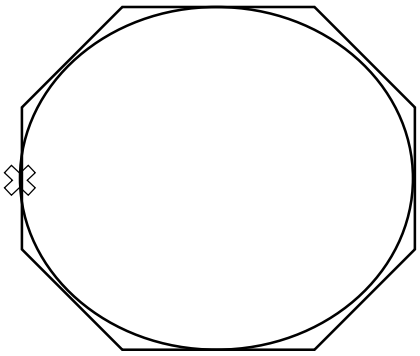

Figure 3.3. Circle Inscribed inside Octagon

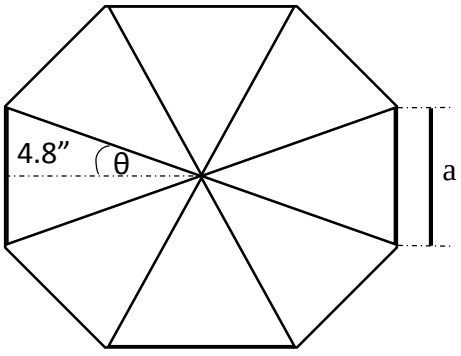

Figure 3.4. 8 congruent interior triangles

From figure 3.2, it can be shown that the side of the octagon, *a*, is given by the following relationship:

$$a = 2(4.8)\tan\theta \qquad \text{[Eq. 3-1]}$$

The area, A, of the regular octagon is then taken as a function of *a*:

$$A = 2\left(1+\sqrt{2}\right)a^2 \qquad \text{[Eq. 3-2]}$$

The central circular area is subtracted from this quantity to determine the cross-sectional area the air flow encounters. Mass continuity [17] provides the flow rates necessary to satisfy the range of targeted air velocities.

$$\dot{m} = \rho u A \qquad \text{[Eq. 3-3]}$$

The value of θ in figure 3.4 is found by first dividing 360 degrees by 8 and then by 2. This results in an octagonal side length of 3.98 inches and an annular flow area of 48.1 square inches (.334 square feet). The total flow area has been reduced from the Wright-Patterson rig by a factor of 7.26. Representative air mass flowrates for the test section are given in table 3.2. Except for temperature, ambient conditions are assumed.

Table 3.2. Representative Air Mass Flowrates

Air Temperature	Air Density	Flow Area	Air Velocity	Air Mass Flow
120°F	.069 lb/ft^3	.334 ft^2	8 ft/s	.184 lb/s
120°F	.069 lb/ft^3	.334 ft^2	40 ft/s	.922 lb/s
120°F	.069 lb/ft^3	.334 ft^2	80 ft/s	1.844 lb/s

Table 3.2 cont.

300°F	.052 lb/ft^3	.334 ft^2	8 ft/s	.139 lb/s
300°F	.052 lb/ft^3	.334 ft^2	40 ft/s	.695 lb/s
300°F	.052 lb/ft^3	.334 ft^2	80 ft/s	1.389 lb/s
600°F	.038 lb/ft^3	.334 ft^2	8 ft/s	.102 lb/s
600°F	.038 lb/ft^3	.334 ft^2	40 ft/s	.508 lb/s
600°F	.038 lb/ft^3	.334 ft^2	80 ft/s	1.015 lb/s

Stainless steel 304 was selected as the material for the test rig cross-section due to its structural strength and ability to resist oxidation at elevated air temperatures. The two test rig components essential to forming the flow cross-section are the Center Cylinder and Octagonal Duct. The Center Cylinder is a roughly 21 inch long section of 6 inch stainless steel tubing with a 5.5 inch inner diameter. The hollow interior of the tubing was necessary to route the various electrical leads running from the target surface instrumentation and heater elements to the facility power supply without exposing them to the hot, turbulent environment inside the test section flow area. The Octagonal Duct is a 32.25 inch long section of stainless steel ducting formed from gauge 12 (.1046 inch thick) sheet metal with an attachment flange to connect to the test rig air plenum (Section 3.6) and rectangular holes to permit windows. Images of the Octagonal Duct and Center Cylinder are shown below and detailed engineering drawings can be found in Appendix A.4.

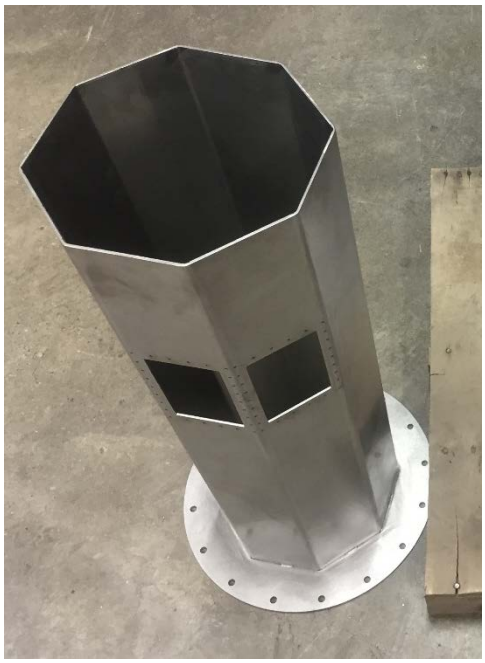

Figure 3.5. Octagonal Duct with Rectangular Window Holes and Attachment Flange at the base

Figure 3.6. Center Cylinder

3.3 Hot Centerbody Design

The critical element for this research is the Hot Centerbody component used as the hot target surface. Great care had to be taken to ensure that this piece of hardware was capable of reaching and sustaining the temperatures necessary to achieve ignition under the range of designed experimental conditions. As such, consideration was given to the following: surface material and dimensions, power input requirement to balance heating losses, surface temperature uniformity, physical deformation from thermal loading, and temperature sensing methods.

The surface material chosen for the Hot Centerbody evolved from discussions with Rolls-Royce to establish a representative metal. Although aircraft engine bays contain a variety of materials, a representative metal could be based on either a common material used throughout the engine bay or the material used for an especially vulnerable engine component. Inconel 718 was ultimately recommended. The length of the Inconel Hot Centerbody was also determined through conversations with Rolls-Royce. In the zone-based heat transfer model used by Younes Khamliche [6], the average zone length was between 4 and 5 inches. Consequently, the Inconel Centerbody is 6 inches long. The middle 5 inches are centered in the viewing plane of the test section windows with the additional ½ inch of Inconel on both ends acting as buffer zones for any temperature discontinuities that might result from contact with the target surface's ceramic insulation. The diameter of the Hot Centerbody was already constrained by the choice of flow cross-section to match the outer diameter of the Center Cylinder component. This meant that the ingot from which the Hot Centerbody would be formed had to be a 6 inch diameter by 6 inch long section of Inconel 718.

The final appearance of the Hot Centerbody was the result of a heat transfer analysis to calculate the power input required to sustain the hottest design surface temperature at the most taxing test section air velocity. As stated in the literature review section, the Wright-Patterson rig reported ignition up to the point of 1550°F and achieved its maximum air velocity at 11 ft/s [5]. The HSIC test rig is designed to accommodate air velocities as high as 80 ft/s. Since the potential for hot surface ignition decreases with increasing airflow [5], the HSIC rig would need to have a maximum design temperature over 1550°F in order to have a chance of ignition at the higher air velocities. 1850°F was selected as the maximum design temperature because it exceeded the old temperature range by roughly 20% while remaining comfortably below the melting range of Inconel (2200-2400°F). To further guarantee conservatism in the estimated power requirements, the heat transfer balance assumed a maximum air velocity of 100 ft/s. Bergman et al. [18] give a broad formulation for the instantaneous thermal-mechanical energy equation:

$$\dot{E}_{st} \equiv \frac{dE_{st}}{dt} \equiv \dot{E}_{in} - \dot{E}_{out} + \dot{E}_{gen} \qquad \text{[Eq. 3-4]}$$

The left-hand side term in equation 3-4 refers to the volumetric rate at which energy is stored within a system, and the subscripts *in*, *out*, and *gen* indicate the rates of energy flowing in to the system, flowing out of the system, and being generated inside the system respectively. The energy generation term is neglected in this instance since no appreciable chemical or electromagnetic conversion of energy occurs within the Hot Centerbody. Emphasis was placed on the terms for energy storage and heat outflow under the conditions of the 100 ft/s bypass air velocity with the 1850°F surface temperature. The following is the simplified energy equation:

$$\dot{E}_{in} \equiv \dot{E}_{st} + \dot{E}_{out} \quad \text{[Eq. 3-5]}$$

It is clear from this formulation that the power that must be delivered to the surface can be quantified by understanding the thermal mass (energy storage) and modes of heat loss from the Hot Centerbody. The possible avenues of heat loss from the surface correspond to the three modes of heat transfer: conduction, convection, and radiation. Although conduction typically represents a significant share of the heat loss from the thermal system of a solid, it was neglected due to the Hot Centerbody being placed against a high temperature ceramic insulator at all contact points. This left convection and radiation as the primary modes of heat loss.

$$\dot{E}_{out} = Q_{conv} + Q_{rad} \quad \text{[Eq. 3-6]}$$

Average convective heat transfer [18] takes the form:

$$Q_{conv} = \bar{h}(T_s - T_\infty)A \quad \text{[Eq. 3-7]}$$

T_s is the temperature of the surface, T_∞ is the temperature of the surroundings, and A is the surface area in contact with the convective fluid. The average convective heat transfer coefficient, $\bar{h}$, was found using the methods for laminar boundary layers detailed in chapter 7 of the text by Bergman et al. [18]. The general approach to finding $\bar{h}$ begins with the approximation of an intermediate film temperature between the temperatures of the surface and freestream.

$$T_f \equiv \frac{T_s + T_\infty}{2} \quad \text{[Eq. 3-8]}$$

It should be noted that all work done to identify the appropriate input power was performed using SI units; this meant that T_s went from 1850°F to 1283K and T_∞ became 294 K. The subsequent value for T_f was then used to interpolate various properties of the air such as the kinematic viscosity, ν, the thermal conductivity, *k*, and the Prandtl number, *Pr*. From the table of air properties given by Bergman et al., it was found that ν was 8.299 x 10^{-5} m^2/s, *k* was 56.76 x 10^{-3} W/m-K, and the dimensionless Prandtl number was .707. The decision to apply the laminar boundary layer method to find $\bar{h}$ was reached after calculating the Reynolds number at the edge of the Hot Centerbody where the axial displacement, L, was equal to 6 inches (.1524m).

$$Re = \frac{uL}{\nu} \qquad \text{[Eq. 3-9]}$$

Setting the flow velocity, *u*, to 100 ft/s (30.48 m/s) gives an approximate Reynolds number of 5.6 x 10^4. Conventionally, the critical Reynolds number, $Re_{x,c}$, which indicates the point where the flow transitions from laminar to turbulent behavior is considered to be 5 x 10^5 [18]. Thus, the flow over the entire length of the Hot Centerbody is in the laminar regime. The average convective heat transfer coefficient was then found by using the established laminar empirical relations [18]:

$$\overline{Nu}_L \equiv \frac{\bar{h}_L L}{k} \qquad \text{[Eq. 3-10]}$$

$$\overline{Nu}_L \equiv 0.664 Re_L^{1/2} Pr^{1/3} \quad Pr \geq 0.6 \qquad \text{[Eq. 3-11]}$$

The calculated average coefficient, $\bar{h}$, is 52.12 W/m^2-K, and the surface area for a .1524 m diameter by .1524 m long cylinder is .0730 m^2. With equation 3-7, this gives the maximum convective heat loss experienced by the system:

$$Q_{conv} = 3.76\ KW \qquad \text{[Eq. 3-12]}$$

Radiative heat loss [18] from a system is given by:

$$Q_{rad} \equiv (\varepsilon\sigma T_s^4 - \alpha G)A \qquad \text{[Eq. 3-13]}$$

The first term on the right-hand side of the equation details the radiation emitted from the surface, and the second term details the radiation absorbed. The function σT_s^4 corresponds to the idealized emission from a blackbody with the total hemispherical emissivity, ε, correcting for the fraction of radiation emitted by a real surface. Being simultaneously temperature and material dependent, the total hemispherical emissivity for Inconel is roughly .32 for temperatures around 1500°F (1090 K) [19]. Although Inconel's emissivity was shown to increase after oxidation in air at temperatures over 1830°F (1273 K) for extended periods of time [19], this was disregarded since the 1850°F temperature corridor was reserved for only the highest air flowrates to prolong the work life of the Hot Centerbody. The quantity *G* from equation 3-13 is the total radiation incident on the surface, and the total hemispherical absorptivity gives the fraction of the incident radiation absorbed by the surface. Because Inconel 718 is such a highly polished metal, it was assumed that incident radiation is reflected to the point that absorption becomes negligible [18]. Neglecting absorption by the surface had the effect of maximizing the calculated heat flux out of the surface, and applying conservatism to the estimated radiative heat loss. The revised equation for the radiative heat transfer became:

$$Q_{rad} = \epsilon \sigma T_s^4 A \qquad \text{[Eq. 3-14]}$$

The symbol σ represents the Stefan-Boltzmann constant which has a value of 5.67 x 10^{-8} W/m^2-K^4. Evaluating equation 3-14 provides:

$$Q_{rad} = 3.59\ KW \qquad \text{[Eq. 3-15]}$$

Thus, by combining the radiative and convective quantities, the maximum total heat loss is estimated to be 7.35 KW.

In order to fully characterize the power input needed to achieve the 1850°F maximum surface temperature, it was necessary to determine the rate of energy storage within the Hot Centerbody. The internal thermal energy of a system can be divided into two components: the sensible energy associated with changes in system temperature, and the latent energy associated with the system phase. Because any shift of phase in the solid Inconel is explicitly avoided (temperatures are kept well away from the alloy's melting point), the latent energy is excluded from this analysis. The rate of change of the sensible energy of a system is described by the relation [18]:

$$\dot{E}_{st} \equiv \rho c_p V \frac{\partial T}{\partial t} \qquad \text{[Eq. 3-16]}$$

The density, ρ, of Inconel 718 is .293 lb/in^3 (8192 kg/m^3), and the constant pressure-specific heat, c_p, at 1850°F is .147 Btu/lb-°F (617 J/kg-K). The constant pressure-specific heat is temperature dependent and rises with increasing temperatures; the assumption of the high temperature value for the specific heat slightly overestimates the expected energy storage rate, and continues the practice of conservatism for the input power. The eventual volume, *V*, of the Hot Centerbody component was designed with the intention of

minimizing the mass of Inconel that needed to be heated. The initial mass reduction came from the removal of a 6 inch long, 4 inch diameter cylindrical section from the centerline of the Hot Centerbody. Further mass reductions came from the removal of material to provide space for the cartridge heater elements used to raise the temperature of the target surface. The heater elements chosen each had a .5 inch diameter and extended throughout the full length of the Hot Centerbody. Through an iterative process that considered both the final thermal mass and the temperature uniformity of the Inconel, 15 heater elements where ultimately selected. Accounting for all of the excavated material left the Hot Centerbody with a mass of 22.67 lb. The rate of change of temperature with time was approximated to a simple linear slope according to:

$$\frac{\partial T}{\partial t} \approx \frac{\Delta T}{\Delta t} = \left(T_{final} - T_{initial}\right)/(desired\ heating\ time) \quad \text{[Eq. 3-17]}$$

By setting T_{final} equal to 1850°F, $T_{initial}$ equal to 70°F, and requiring that the heaters should take no longer than 30 minutes to accomplish this temperature change, a value was found for the energy storage rate of the Hot Centerbody.

$$\dot{E}_{st} = 3.48\ KW \quad \text{[Eq. 3-18]}$$

Combining this rate with the total rate of heat loss per equation 3-5 identifies the full input power requirement for the Hot Centerbody.

$$\dot{E}_{in} = 10.83\ KW \quad \text{[Eq. 3-19]}$$

Consistent with the conservative assumptions made throughout the process of evaluating this power requirement, the selected heaters were each rated for 1 KW or an overall power budget of 15KW. The capacity to comfortably exceed the expected requirement makes the provision for future research to investigate test conditions beyond even the most aggressive of the current experimental envelope.

Figure 3.7. The Inconel Hot Centerbody with excavated center diameter and heater holes

Ensuring a uniform temperature profile throughout the Hot Centerbody component was essential to both the repeatability of experiments on the HSIC test rig and to simulating an axisymmetric environment. To understand which Hot Centerbody configuration was suitable for sustaining such a temperature distribution, a Biot number [18] calculation was performed.

$$Bi = \frac{hL_c}{k} \qquad \text{[Eq. 3-20]}$$

The Biot number is a measure of the competing effects of conduction and convection on the temperature of a solid. For cases where the Biot number is small (Bi<0.1), conduction within the solid is large enough to counterbalance any convective transport of heat at the

interface with the fluid. From equation 3-20, h is unchanged from the average convective heat transfer coefficient, $\bar{h}$, used to find the convective heat loss, and k is the thermal conductivity of Inconel 718. It should be noted that despite appearing to be identical to the definition for the Nusselt number, the Biot number differs by its thermal conductivity, which is specified for a solid instead of a fluid. Thermal conductivity, like emissivity and the specific heat, increases as a function of temperature. Confidence in the ability of the Hot Centerbody to maintain a uniform temperature distribution was gained from calculating the Biot number for two crucial experimental cases. These two cases were for the HSIC rig at the upper extreme of its operational envelope (1850°F with a 100 ft/s air velocity), and for the case of a low-temperature surface being subjected to the most extreme air velocity (once again, 100 ft/s). 400°F was chosen for the low-temperature case since this was the lowest temperature from the Wright-Patterson test article to ever achieve ignition [5]. The thermal conductivity of Inconel at 400°F and 1850°F, is 87 Btu-in/ft^2-hr-°F (12.4 W/m-K) and 195 Btu-in/ft^2-hr-°F (28.4 W/m-K) respectively. By coincidence the average heat transfer coefficient for the high temperature-high velocity case is approximately the same as for the low temperature-high velocity case, 54.23 W/m^2-K. L_c is a characteristic length indicating the largest expected length scale for conduction [18]. Two characteristic lengths were calculated for the cases mentioned by assuming that the Biot number equal to .1 condition was satisfied. Both dimensions were then examined relative to the actual characteristic length of the Hot Centerbody. For the high temperature-high velocity arrangement the characteristic length was 2 inches. For the low temperature-high velocity arrangement the characteristic length was .9 inches. As long as the value of the characteristic length is kept below these bounds, temperature

uniformity can be presumed. For the present design, the characteristic length is the arc separating two heater elements.

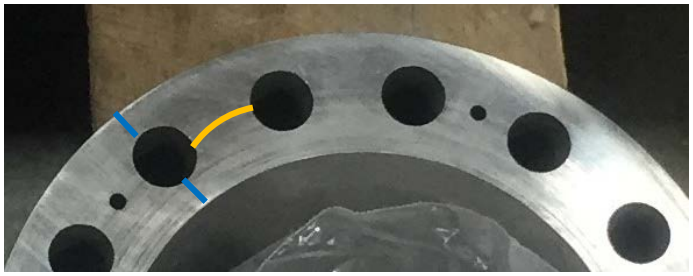

Figure 3.8. The arc length between heaters is shown in yellow with radial distances in blue

As seen in figure 3.8, this arc length was compared against the radial distances taken from the edge of the heater hole to either the edge of the inner or outer diameter. With the heater openings centrally spaced within the Hot Centerbody, the radial distances are both .25 inches. The arc length was found by:

$$S = r\theta \qquad \text{[Eq. 3-21]}$$

An initial arc length, *S*, was taken from the product of the angle θ (in radians) between the center of two heaters and the radius *r* from the centerline of the Hot Centerbody to the center of a heater. The angle between heaters was known simply by dividing 2π by the number of heating elements. As stated previously, iterating to find the number of heating elements that yielded a low Inconel mass while meeting favorable Biot number specifications gave a final heater count of 15. The initial arc length was thus:

$$S = 1.047\ inches \qquad \text{[Eq. 3-22]}$$

This satisfied the bound given by the upper extreme but failed the bound from the low-temperature configuration. However, this initial calculation overestimated the magnitude of the arc because a portion of its length included the actual heater elements.

Approximating the segment of the arc passing through the heating elements to be linear allowed .5 inches to be subtracted from the initial estimate. The true length of the arc became:

$$S = .547\ inches \quad \text{[Eq. 3-23]}$$

Both of the bounds on the conduction path were met and temperature uniformity could now be comfortably inferred.

Beyond supplying heat to the Hot Centerbody, it was necessary to plan for any deformation that might result from thermal loading. Specifically, attention was paid to the effects of thermal expansion on the length and circumference of the Inconel component. Elongation of the Inconel body would affect the method used to axially constrain the surface. Changes in the circumference of the Inconel would affect its radius, *r*, and reduce the cross-sectional area designated for the air flow. Shigley [20] provides an expression for the linear thermal expansion of a body:

$$\frac{\Delta l}{l_{initial}} = \alpha_{exp}\Delta T \quad \text{[Eq. 3-24]}$$

The body dimension under consideration is denoted by l with α_{exp} representing the mean coefficient of thermal expansion for the temperature rise ΔT. The coefficient of thermal expansion for Inconel 718 is roughly 8.9 x 10^{-6} in/in-°F in the range from 70°F to 1850°F [21]. After rearranging to find the final linear dimension, equation 3-24 becomes:

$$l_{final} = \left(\alpha_{exp}\Delta T\right)l_{inital} + l_{initial} \quad \text{[Eq. 3-25]}$$

Applying this to both the circumference and the length of the Hot Centerbody component gave the following final measurements:

$$r_{final} = 3.048\ inches \quad \text{[Eq. 3-26]}$$

$$length_{final} = 6.095\ inches \qquad \text{[Eq. 3-27]}$$

The lengthening of the Inconel is accommodated by adjusting the nut and threaded rod used to fasten the HSIC rig assembly (section 3.5) so that the Hot Centerbody has space to grow. The change in radius is only on the order of 5 one hundredths and reduces the cross-sectional flow area by less than 2%. The relatively small magnitude of the deformations experienced by the Hot Centerbody meant that no serious modifications had to be made to counteract the effects of thermal expansion.

The design of the target surface was finally settled with the provisions made for sensory instrumentation. The primary diagnostic under investigation in this research is the Inconel surface temperature necessary to ignite a leak of some flammable engine fluid. Accordingly, the instrumentation used for the Hot Centerbody would need to provide a thorough representation of its temperature profile. Five .125 inch diameter thermocouple profile probes were inserted into the Hot Centerbody at different azimuthal locations to accomplish this. One of the .125 inch clearance holes drilled into the Inconel 718 is visible in figure 3.9.

Figure 3.9. A .125 inch thermocouple probe clearance hole between 2 heater holes

Each thermocouple is made of stainless steel 316 (to lessen galling effects with the Inconel) and outfitted with 3 ungrounded type K sensing points for a total of 15 thermocouple readings. The sensing points are distributed axially along the probe such

that temperature is reported at the 1, 3, and 5 inch points of the Hot Centerbody. The sensing points at the 3 inch location are used as feedback control for the heater elements, and the sensing points at the 1 and 5 inch locations are read into the LabVIEW program operating and monitoring the HSIC test rig instrumentation.

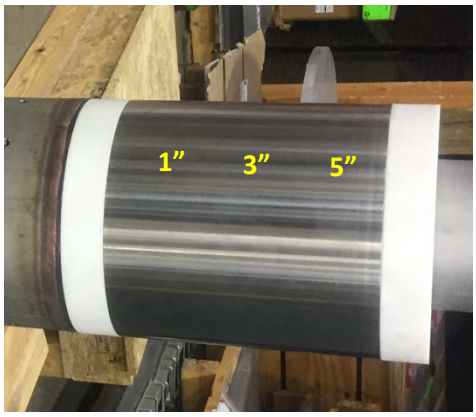

Figure 3.10. Axial location of thermocouple sensing points

A quirk of the thermocouple probe design by Omega® prevented any sensing points from being placed within an inch of the probe tip; this meant the absolute location of the sensing points did not have a 1 to 1 correspondence between the probe and the Hot Centerbody. The probe lead wires depicted in Figure 3.11 are insulated with both a glass braid and a stainless steel over-braid. All sensing points have a miniature male connector at their termination.

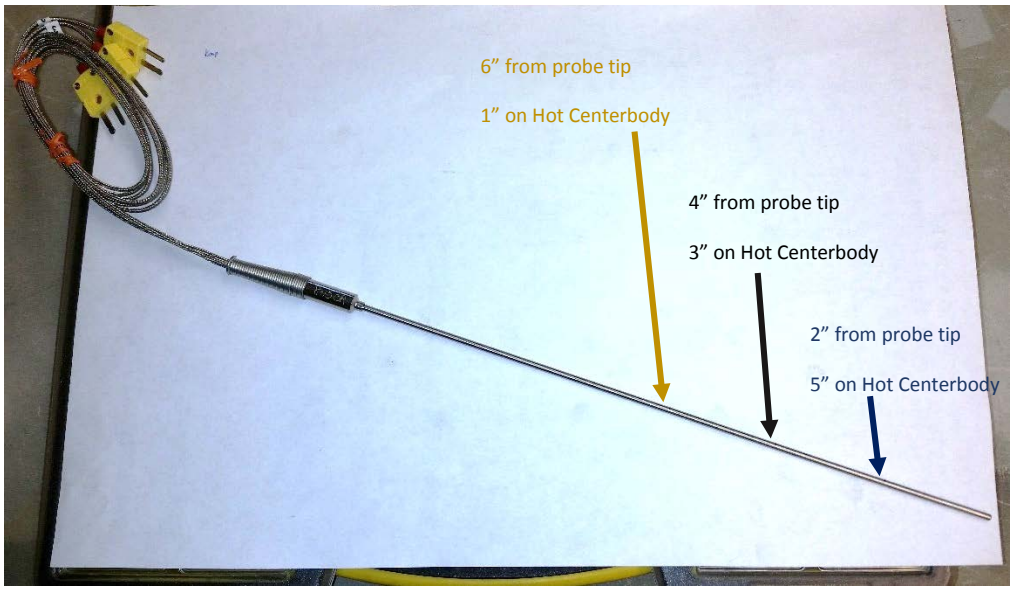

Figure 3.11. Thermocouple profile probe with sensing points identified

Control of the Hot Centerbody temperature was managed across 5 zones, with each zone containing 1 thermocouple probe and 3 cartridge heater elements. Zone layout can be seen in figure 3.12 below.

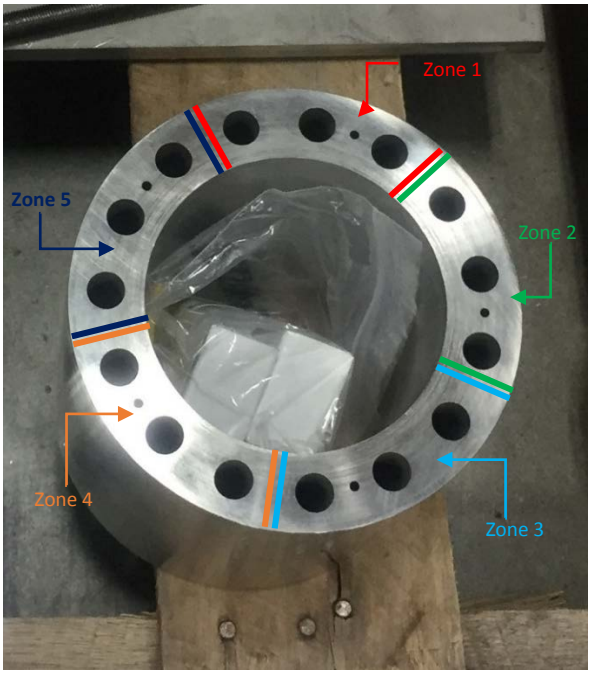

Figure 3.12. Zone configuration in the Hot Centerbody

The 15 cartridge heaters used were all 240V with 1 KW maximum power output and a .5 diameter Incoloy sheath. Precaution was taken to protect the leads of these heating elements since they were identified as the point of highest vulnerability in the heating arrangement. The lead wire was distanced from the hot section of the cartridge heater by a 2 inch, unheated buffer section that brought the total heater length to 8 inches. The leads were further protected with ceramic fiber beads rated up 1200°F.

Figure 3.13. Cartridge Heater with insulating beads shown

Having a modular, adaptable design means that the rig will likely encounter arrangements and conditions that the original designer never anticipated. In keeping with this open philosophy, effort was made a several points in the design of the Hot Centerbody to not only satisfy, but to exceed the anticipated needs of the HSIC test rig. It must be noted, however, that the present arrangement is not without its drawbacks. As the Hot Centerbody and its embedded instrumentation are taken to higher and higher temperatures, the issue of galling between the multiple metal surfaces becomes unavoidable. The intent in documenting this design process is not to merely inform future research on how to replicate the experiment, but to provide a platform for its improvement.

3.4 Ceramic Materials

Once the Hot Centerbody component had been designed, the immediate concern became finding insulation to retain its heat. The materials ultimately chosen were

Corning Macor®, a white machinable glass ceramic produced by Corning Inc. [22], and grade ‘A’ lava, a machinable alumina silicate ceramic. The two types of ceramic components were the Ceramic Ends used to axially insulate the Hot Centerbody, and the Ceramic Sleeve used as radial insulation. These ceramics were chosen for their favorable material properties and high temperature integrity. A brief transient conduction calculation was also made to confirm the suitability of the Macor® and grade ‘A’ lava.

Porosity, thermal conductivity, and high temperature integrity were the primary material qualities evaluated in the candidate insulators. Porosity was critical since liquid fuel is sprayed or dripped into the test section multiple times over the course of an experiment. Notably, the 15 cartridge heater elements and the 5 thermocouple probes inside the target surface pass through the ceramic in order to connect their lead wires to facility power. If the ceramic was porous or absorbed water, fuel would be permitted to build up in undesirable regions such as this and interfere with hardware. A comparative data sheet obtained from Professional Plastics® [22] identified Macor® as the ideal insulator due to it demonstrating no water absorption. Macor® was further shown to possess superior thermal conductivity relative to similar ceramics, having a k equal to 1.46 W/m-K. In fact, Macor® would have been preferable for both types of ceramic parts used on the HSIC test rig, but the available dimensions of the raw material restricted its usage to the Ceramic End component.

Figure 3.14. Macor® Ceramic End after machining

Figure 3.15. Grade ‘A’ lava Ceramic Sleeve after machining

In figure 3.14, it can be seen that the Ceramic End was designed to match the layout of the Hot Centerbody. The dimensional specifications are unchanged except for the thickness, which was reduced to 1 inch. As stated previously, this was done to allow the instrumentation to pass from the Inconel component to the facility power and data channels without risking exposure to the test environment. Two Ceramic End pieces were created to be placed at both ends of the Hot Centerbody. The pieces were left identical to allow interchangeability, to ease the insertion of the cartridge heaters into the Inconel,

and to act as an anchor for the unusable first inch of the thermocouple probes. The installed Ceramic Ends can be viewed back in figure 3.10. The Ceramic Sleeve shown in figure 3.15 is an 8 inch long, .5 inch thick cylinder with a 4 inch outer diameter and was designed to slide underneath the Hot Centerbody and two Ceramic Ends. The Ceramic Sleeve component required a small compromise since no raw Macor® stock could be acquired to create it. On the Professional Plastics reference [22], the grade 'A' lava (alumina silicate) is listed as having the second best thermal conductivity with k equal to 1.98 W/m-K. Grade 'A' lava was also readily available in the desired raw dimensions. However, lava does experience some small water absorption at room temperature, having an absorptivity of .025. It was reasoned that this absorptivity was permissible since the Ceramic Sleeve is underneath the Inconel and Macor® components and has no opportunity to directly encounter the injected fuel. Both the Macor® and grade 'A' lava ceramics have maximum use temperatures in the range between 1850 to 2100°F, in line with the operational envelope of the HSIC test rig.

The brief transient conduction analysis for the ceramic components looked at the instance with the greatest heat flux from the Hot Centerbody. The ceramic and Inconel 718 were treated as semi-infinite solids to establish a contact surface temperature at their interface. This contact surface temperature was then used to find the conductive heat loss through the ceramic. The semi-infinite solid approach is justified by looking at the thermal penetration depth defined in the text by Bergman et al. [18]. The thermal penetration depth is the depth within a material at which the effects of the temperature gradient caused by its interface can be felt. The semi-infinite solid analysis is deemed valid for a particular time step when this penetration depth is less than the total thickness

of the medium. Figure 3.16 is a general pictorial representation of contact between two semi-infinite solids [18].

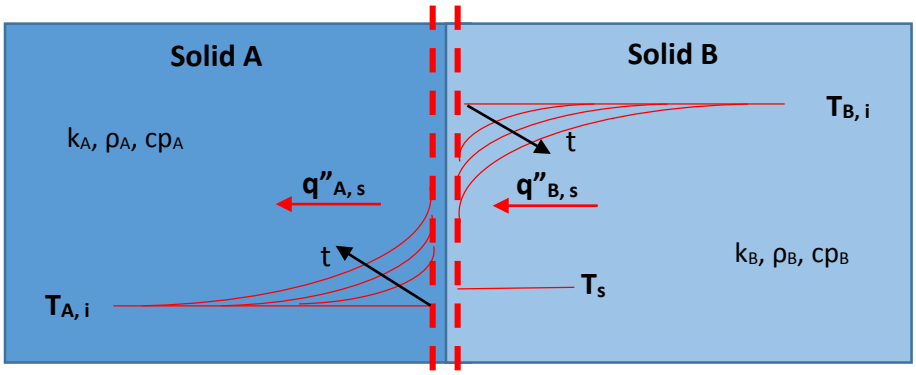

Figure 3.16.Ssemi-infinite solid model for the interface between solid A and solid B

In figure 3.16, $T_{B,i}$ and $T_{A,i}$ are the global temperatures of solids A and B; they give the temperatures of their respective solids sufficiently removed from the disruptive influence of the material interface (the dotted red lines). The interface temperature T_s is an intermediate value between the high temperature of solid B and the relatively low temperature solid A. The curved red lines detail the temperature profile at different time steps, *t*. As *t* increases (the arrow points in the direction of increasing *t*), the region affected grows larger and the temperature profile shifts from a step-like to a more linear appearance. The penetration depth corresponds roughly to the point where the temperature profile flattens into a horizontal line. Bergman et al. [18] offer an expression for the penetration depth, δ_p that ends at the point where the quantity $T-T_s$ is 90% of T_i-T_s with T being the temperature at some distance x into the medium.

$$\delta_p = 2.3\sqrt{\frac{kt}{\rho c_p}} \qquad \text{[Eq. 3-28]}$$

Knowing the density, ρ, the specific heat c_p, and the conductivity *k* of the Macor®, lava, and Inconel 718 determines the penetration depth at a specified time step. The values for

some of these properties have been given previously, but they are presented in their entirety in Table 3.3.

Table 3.3. Material properties of Inconel 718 and ceramic components

Material	Density, ρ	Specific Heat, c_p	Conductivity, *k*
Inconel 718	8192 kg/m^3	617 J/kg-K	28.4 W/m-K
Macor®	2520 kg/m^3	795 J/kg-K	1.46 W/m-K
Grade 'A' Lava	2300 kg/m^3	837 J/kg-K	1.98 W/m-K

One second was chosen as the time step of interest since the overall heat flux for the ceramics will be greatest early in the conduction process when the ceramics are treated as though they are still at room temperature and when thermal gradients are steepest. In fact, the predicted conductive heat transfer from the Inconel to the ceramics will exceed any actual rates experienced on the test rig since the analysis assumes the Inconel to be at 1850°F and the ceramics to be at 70°F, a scenario that would be highly unlikely to occur since the thermal mass of the Inconel cannot reach such a temperature instantaneously. This conservative methodology is carried over from the approach used to design the Hot Centerbody. For the 1 second time step, the penetration depth of the Inconel, Macor®, and lava are 5.5 mm, 1.96 mm, and 2.33 mm respectively. In each case the penetration depth is smaller than the thickness of the medium, so the semi-infinite solid analysis is accepted. Neglecting contact resistance between the Inconel and the ceramics (the finished parts are relatively smooth) the surface energy balance required by Figure 3.16 becomes:

$$q''_{A.s} = q''_{B,s} \qquad \text{[Eq. 3-29]}$$

Through substitution and solving for the interfacial temperature T_s, Bergman et al. [18] found:

$$T_s = \frac{(k\rho c_p)_A^{1/2} T_{A,i} + (k\rho c_p)_B^{1/2} T_{B,i}}{(k\rho c_p)_A^{1/2} + (k\rho c_p)_B^{1/2}} \quad \text{[Eq. 3-30]}$$

The interfacial temperature between the Inconel 718 and the Macor® was 1628°F. The interfacial temperature between the Inconel 718 and the lava was 1600°F. These temperatures are preliminary signs of the good quality of the ceramics. Had the ceramics acted as poorer insulators, the temperature of the interface would have been lowered from the additional heat being pulled out of the Inconel. The one-dimensional form of Fourier's law was then used to find a conductive heat transfer rate through the ceramic:

$$q_{cond} = -kA\frac{dT}{dx} \quad \text{[Eq. 3-31]}$$

Assuming the temperature distribution within the ceramic component to be linear:

$$\frac{dT}{dx} = \frac{T_{A,i} - T_s}{L} \quad \text{[Eq. 3-32]}$$

Conductive heat transfer finally becomes:

$$q_{cond} = kA\frac{\Delta T}{L} \quad \text{[Eq. 3-33]}$$

The letter L indicates the overall thickness of the medium. Using the contact temperature obtained from equation 3-30 and the assumption that the far temperature is at 70°F:

$$q_{cond-Macor®} = .820\ KW \quad \text{[Eq. 3-34]}$$

For the grade 'A' lava, the far temperature was averaged between room temperature and 1850°F because the relative thinness of the Ceramic Sleeve component and the higher amount of surface contact made the assumption of a 70°F temperature untenable.

$$q_{cond-lava} = 2.7KW \quad \text{[Eq. 3-35]}$$

Thus, the conservative estimate for the transient conduction through the ceramic components becomes 3.52 KW (still covered within the original power budget). Steady state analysis would render these losses even smaller as the ceramic temperature rises and the thermal gradients driving the heat flow weaken. Taken in conjunction with their high temperature integrity and hydrophobic qualities, these findings confirmed the choice of Macor® and lava for the HSIC rig's ceramic insulation.

3.5 Supporting the Hot Centerbody

Direct support and fastening for the assembly of Inconel and ceramic parts is handled across 3 components: the Cantilever Base Plate, the Cantilevered Support, and the End Piece. All are made from stainless steel 304. The Cantilever Base Plate and Cantilevered Support are joined to the overall rig via welds. The End Piece is secured with the use of a .5 inch diameter threaded rod that runs through the centerline of the HSIC test rig and along the full length of the Inconel-ceramic assembly. Because the test section is held at ambient pressure, each component detailed in this section was kept as light as structural rigidity would allow; the Cantilevered Support and End Piece are both hollow, and the Cantilever Base Plate is effectively a disc. These mass reductions, as well as those afforded by removing material from the Hot Centerbody, made the HSIC rig easier to support while providing interior spaces for future modification.

Like the Ceramic End that rests against it, the Cantilever Base Plate was machined to match the hole configuration of the Hot Centerbody and permit the leads of its instrumentation to pass through before connecting with facility power. A .5 inch clearance hole was added at its center so the treaded rod running the length from the End Piece could be fastened in place with a nut. The .25 inch thick, 6 inch diameter Cantilever

Base Plate was welded to one of the open ends of the Center Cylinder to join it with the HSIC rig assembly. The Cantilever Base Plate is presented prior to welding in figure 3.17.

Figure 3.17. Cantilever Base Plate prior to welding

In addition to its function as a restraining surface for the End Piece, the Cantilever Base Plate acts as the attachment point for the Cantilevered Support. The Cantilever Supported is permanently joined to the Cantilever Base Plate by a weld. In figure 3.17, a threaded hole for a 3/8” NPT fitting offset from the center hole by .875 inches can be seen. In the baseline configuration of the HSIC test rig, this opening is unused. The threaded hole was placed as a contingency in the event that the radial temperature profile within the Hot Centerbody and Cantilevered Support proved to be too high. The threaded NPT connection would then be used to send nitrogen through the rig centerline as a relieving stream. This arrangement would also modify the End Piece to include a thru-hole and give the nitrogen stream an exit path.

The Cantilevered Support welded to the Cantilever Base Plate is a 10 inch long section of 3.5 inch diameter, schedule 40 pipe. The pipe is centered and welded on the

Cantilever Base Plate such that the holes for the threaded rod and 3/8” NPT connection were within its inner diameter. The 3.5 inch outer diameter mates with the inner diameter of the Ceramic Sleeve. The welded Cantilevered Support and Cantilever Base Plate can be seen with the Ceramic Sleeve back in figure 3.15. The bare Cantilevered Support is presented in figure 3.18.

Figure 3.18. The bare Cantilevered Support and Cantilever Base Plate post welding

The End Piece was created by welding 3 constituents together. The largest constituent was a 4.88 inch section of the same 6 inch diameter tubing used for the Center Cylinder. The remaining constituents were both formed from gauge 11 (.1196 inch thickness) stainless steel sheet metal and welded to either end of the tube section. The first was a 6 inch diameter ring with a 3.5 inch interior diameter. This interior diameter is intended to mate with the Cantilevered Support so the completed End Piece slides smoothly onto the end of the HSIC test rig. The final constituent was a 6 inch diameter disc with a centered, .5 inch clearance hole for the threaded rod. Just as the back of the Cantilever Base Plate was used as a clamping surface for the threaded rod, the forward face of this last

constituent served as the second clamping surface holding the Hot Centerbody and ceramics in place. The thinness of these 2 final constituents was the result of the minimal structural loading they experience in the assembled rig. The finished End Piece is depicted in figure 3.19.

Figure 3.19. End Piece with 3.5 inch diameter lip, and .5 inch rod clearance hole on the far face

Accounting for the high temperature testing environment was done by adding Belleville washers at both ends of the central rod and treating its threads with anti-seize. When tightening the End Piece in place, a small gap should be left to accommodate the thermal expansion of the Inconel. A progression for the assembly of the Inconel 718 Hot Centerbody, the ceramics, and their supports is given in the subsequent images.

Figure 3.20. The bare Cantilevered Support at the proper (horizontal) orientation

Figure 3.21. Cantilevered Support with the Ceramic Sleeve

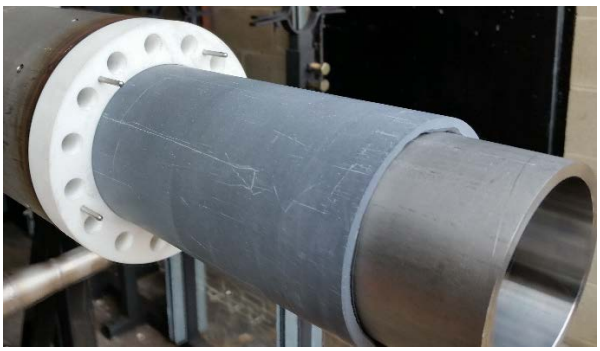

Figure 3.22. After adding first Ceramic End

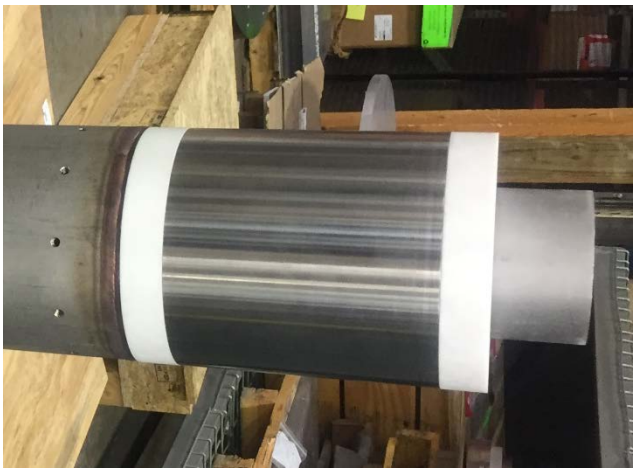

Figure 3.23. With Hot Centerbody and 2nd Ceramic End in place

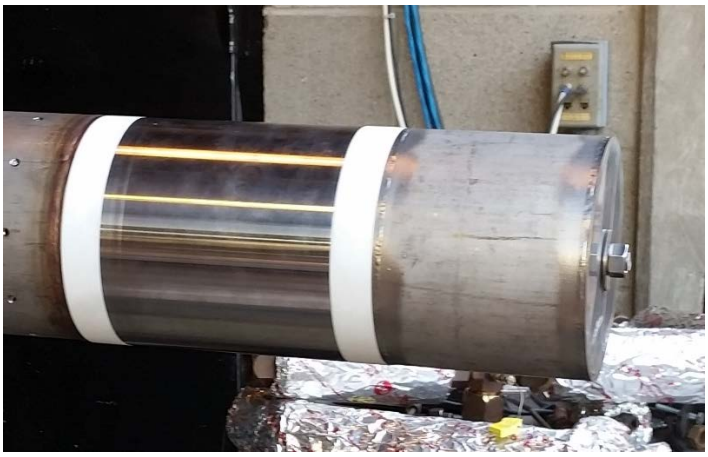

Figure 3.24. With the End Piece secured (the Belleville washer and nut are visible)

3.6 Flow Conditioning

Delivering well-conditioned air flow to the test section of the HSIC rig was of paramount importance. In devising a system to support the varied air flow requirements of the experiment, attention was focused on: air heating, mass flow metering, plenum sizing, orifice plate design, and air plumbing.

The experiments conducted on the Wright-Patterson test rig had air temperatures that generally ranged from 70 to 600°F. An internal flow heat transfer balance was performed

to determine the associated power input to the fluid. Once again, Bergman et al. [18] supply the relevant relation:

$$q_{conv} \equiv \dot{m} c_p (T_{out} - T_{in}) \qquad \text{[Eq. 3-36]}$$

The heat convected from the walls of a passage to the fluid flowing through it is expressed in the sensible energy difference between the fluid at the passage inlet and the fluid at the passage outlet. The general range of mass flowrates was originally presented in table 3.2 and T_{out} indicates the desired air temperature within the test section. The inlet temperature T_{in}, can be assumed to be at or near ambient (~70°F) and the specific heat is readily available in look up tables. A new table detailing the heating rates for the air is presented below.

Table 3.4. Representative Air Heating Rates

Mass Flow Rate	Final Air Temperature	Specific Heat	Power Required
.184 lb/s	120°F	1.007 KJ/kg-K	2.3 KW
.922 lb/s	120°F	1.007 KJ/kg-K	11.7 KW
1.844 lb/s	120°F	1.007 KJ/kg-K	23.4 KW
.139 lb/s	300°F	1.015 KJ/kg-K	8.2 KW
.695 lb/s	300°F	1.015 KJ/kg-K	40.9 KW
1.389 lb/s	300°F	1.015 KJ/kg-K	81.7 KW
.102 lb/s	600°F	1.050 KJ/kg-K	14.2 KW
.508 lb/s	600°F	1.050 KJ/kg-K	71.2 KW
1.015 lb/s	600°F	1.050 KJ/kg-K	142.3 KW

Because the High Pressure Lab is supported by a 20 MW air heater, the range of heating rates listed here fall easily within the scope of the site's capability. Indeed, the facility exceeds the design requirements so thoroughly that future test campaigns will easily be able to test bypass air temperatures above 600°F should the interest arise.

With the range of air flow rates known, establishing a controlled method of metering mass to the test section was the next system progression. The sonic venturi, which operates under the principles of choked flow, was the device used to accomplish this. Under choked conditions, the cross-section of a flow passage cannot permit more than a limited amount of fluid to continue downstream. For conditions where the size of this passage cross-section do not change, the only way to move more fluid through the restriction is to change the pressure or temperature upstream. Thus, the sonic venturi works to meter gas flow by introducing an area restriction to the flow path; in using a regulator to set the pressure upstream of the sonic venturi, fluid mass flow can be carefully controlled. The following compressible flow equation specifically describes choked mass flow phenomena in gases, and is taken from Sutton and Biblarz [23]

$$\dot{m} = C_d A_t p_1 \gamma \frac{\sqrt{[2/(\gamma+1)]^{(\gamma+1)/(\gamma-1)}}}{\sqrt{\gamma R T_1}} \qquad \text{[Eq. 3-37]}$$

The universal gas constant, R, is equal to 287.058 J/kg-K (53.35 ft-lbf/lb-°R) for dry air. The discharge coefficient through the restriction, C_d, is traditionally assumed to be .993. Gamma, γ, is the ratio of the specific heats for the gas under consideration, and does not vary significantly for air in the temperature corridor under investigation. The value of γ is equal to 1.4 for air. This effectively leaves the numerator of the fraction in equation 3-37 as a constant. The size of the area restriction, A_t, is generally constrained at the smallest

desired flow rate. Accordingly, the lowest intended feed pressure (~100 psia) and the highest intended test temperature (~600°F) were used to find it. The upper bound on the mass flow achieved through a given sonic venturi was then set by limits on the system pressure upstream. 500 psia was chosen as this upper pressure bound because it remained comfortably within the safety limits of the HSIC rig (~1500 psia for the plumbing supporting the rig) and because the pressure regulator used to obtain the lower range of flowrates had a relief valve rated for 600 psia. The span of air flowrates needed for the HSIC test rig was ultimately so broad that 3 separate sonic venturi devices were required to accomplish the full extent of the mass metering. As a consequence, testing can be divided into 3 regimes based on the expected range of air velocities. These regimes were: the low-flow regime (~2-8 ft/s), the mid-flow regime (~8-35 ft/s), and the high-flow regime (~35-80 ft/s). The diameters of the area restriction for the low, mid, and high flow regimes were .124, .300, and .706 inches respectively. The tables describing the fluid states and area restrictions associated with several of the experimental cases were too large to be included in the body of this Chapter, so they are shared in appendix A.2. It is noted that the specifications for the venturi throat diameters and upstream pressures given in these tables are representative rather than fixed. Alternative venturi devices and feed pressures can be used so long as they are conducive to the HSIC test rig's safety and operational lifetime.

Having well-distributed air is essential to ensuring uniform air flow inside the HSIC rig test section. The purpose of the plenum is to slow and distribute the air upstream of the orifice plate feeding the test section. The effectiveness of the plenum was evaluated using the continuity equation to check its internal fluid velocity. The plenum internal

velocity for the experimental condition with the highest mass flow rate was the sizing parameter. A cylindrical volume was chosen to avoid the recirculation effects that occur with sharp corners. The plenum is formed from the annular gap between two components: the Center Cylinder and the Plenum Vessel. The Center Cylinder used to create the inner diameter of the test section flow area fulfills the same function for the plenum. The Plenum Vessel is a pipe section that acts as the plenum outer wall. Both the Center Cylinder and the Plenum Vessel are welded to the Base component of the HSIC test rig. The Base component of the HSIC test rig is .5 inch thick, 18 by 18 inch square with a 5.5 inch diameter central hole that mates with the Center Cylinder. The Base also serves as the back wall of the plenum; the forward wall is the orifice plate leading to the test section.

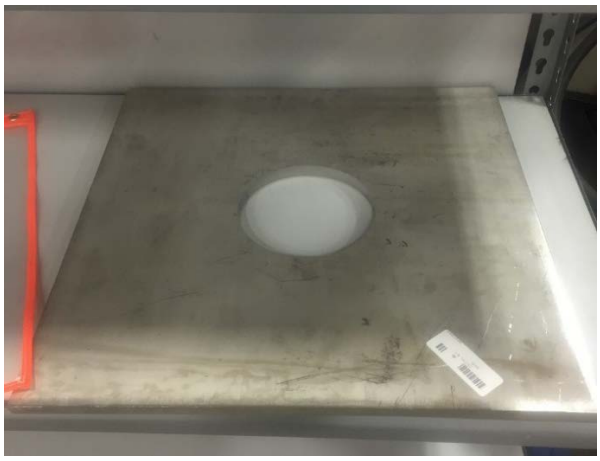

Figure 3.25. The stainless steel 304 Base component

Since the inner wall of the plenum is the outer wall of the Center Cylinder, the plenum surrounds a 5.5 inch diameter voided space. This is the exit point where the lead wires running from the Hot Centerbody instrumentation connect to facility power. Air is delivered via 2 openings on either side of the plenum. A pictorial representation detailing

how the air flow is introduced and then spreads through the plenum is given below in figure 3.26.

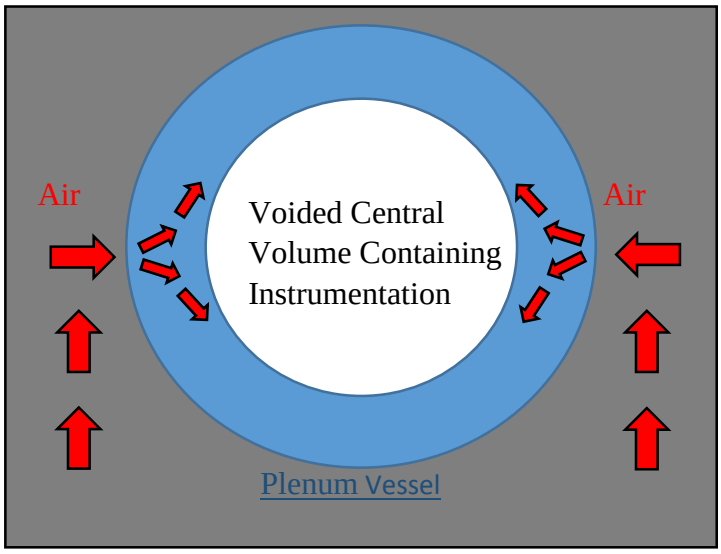

Figure 3.26. The annular Plenum Vessel with red arrows depicting air flow

Figure 3.26 further illustrates how air velocity within the plenum was found. At the point of introduction into the plenum, the air flow has already been divided in half. Inside the plenum, bulk air flow can only move in 2 directions (up or down). Approximating that the flow splits evenly between the two directions halves the flow again so that the characteristic mass flow rate for the plenum is actually one quarter of the total mass flow supplied. The cross-section encountered by the characteristic mass flow was assumed to be rectangular with length equal to the length of the Plenum Vessel and width equal to the annular gap. The density of the air inside the plenum was a function of the pressure and temperature. In turn, plenum pressure was largely a function of the air mass flow feeding into the test section. Because the plenum pressure was also quite sensitive to the number and size of holes in the orifice plate, the eventual dimensions of the plenum were found through iteration. The Plenum Vessel on the finished HSIC test rig is a 3 inch long

section of 12 inch diameter, schedule 40 pipe. At this pipe schedule, the wall thickness comes to roughly .365 inches, giving the Plenum Vessel an outer diameter of 12.73 inches. Consistent with both the Base component and the Center Cylinder, the Plenum Vessel material is also stainless steel 304. Two diametrically opposed, 1 inch diameter holes were added to the Plenum Vessel wall to serve as the flow entrances.

Figure 3.27. Plenum Vessel prior to welding with 1” diameter flow entrances visible

Contrary to initial expectations, the internal plenum velocity for the highest mass flow feed was not the highest at room temperature. Instead, the magnitude of the velocity as a function of mass flow was generally more consistent with a bell-shaped profile. The trend was attributed to the coupled but competing influences of pressure and mass flow. As the mass flow rate rises, fluid velocity tends to rise, and as pressure rises, the fluid density increases. At the lower mass flow rates where overall plenum pressure is relatively low, the former trend dominates. However, once the pressure rises above a certain point (this was typically near the point when the flow through the orifice plate became choked), the air is compressed to the point where fluid velocity in the plenum begins to drop for every incremental increase in mass flow. This is captured in table 3.5. From this same table, it

can also be seen that the peak pressure experienced by the plenum is 105 psia. This is comfortably within the structural limits of the plenum materials.

Table 3.5. Air Plenum Conditions at 70°F (21°C)

Air Mass Flow	Plenum Pressure	Plenum Air Density	Plenum Velocity	Test Velocity
1.99 lb/s	105.5 psia	0.534 lb/ft^3	14.9 ft/s	80 ft/s
1.386 lb/s	73.5 psia	0.33 lb/ft^3	16.8 ft/s	55 ft/s
1.232 lb/s	64.5 psia	0.279 lb/ft^3	17.7 ft/s	49 ft/s
1.078 lb/s	57.1 psia	0.279 lb/ft^3	15.5 ft/s	43 ft/s
0.924 lb/s	49.0 psia	0.228 lb/ft^3	16.2 ft/s	36 ft/s
0.77 lb/s	40.8 psia	0.177 lb/ft^3	17.4 ft/s	30 ft/s
0.616 lb/s	24.7 psia	0.126 lb/ft^3	19.6 ft/s	25 ft/s
0.462 lb/s	21.3 psia	0.101 lb/ft^3	18.3 ft/s	18 ft/s
0.308 lb/s	18.1 psia	0.075 lb/ft^3	16.4 ft/s	12 ft/s
0.154 lb/s	15.7 psia	0.075 lb/ft^3	8.2 ft/s	6 ft/s

When the temperature of the air is raised, for example, to 600°F, the calculated plenum velocity follows the expected trend of increasing velocity for increased plenum mass flow. This resulted from the overall reduced flowrates associated with air at elevated temperatures (consulting table 3.2 shows that all required flowrates for air at 600°F are within 1.015 lb/s, half of the range necessary for room temperature flow). From table 3.5, it is also evident that the plenum is most successful at slowing the air flow when the flow through the orifice plate is choked. The choked flow condition corresponds to the point where the plenum pressure is roughly 28 psia or greater. The observation of improved

plenum function under choked air conditions significantly impacted the approach to the orifice plate design.

The Orifice Plate was chiefly responsible for conveying distributed, uniform air to the test section of the of the HSIC rig. This part also fulfilled the secondary, but integral role of serving as a fastening surface for the Octagonal Duct. Broadly, the Orifice Plate is a .25 inch thick, 15 inch diameter, circular flat plate fashioned from stainless steel 304. At the center of the Orifice Plate is a 6 inch diameter hole created to accommodate the Center Cylinder. Sixteen threaded, equally spaced, .375 inch holes were located along the plate edge (see Appendix A.4).

Figure 3.28. The Orifice Plate prior to welding

The hole pattern visible in figure 3.28 is the final product of an analysis that underwent many iterations. In the previous paragraph, it was mentioned that the plenum most successfully slowed the oncoming air when the orifice plate reached a choked flow condition. Consistent with this finding, the Orifice Plate was designed to selectively choke to improve plenum performance at the highest mass flowrates. The principle

followed was that there was no need to choke the air feed at the lower test section velocities since the plenum velocity would be comparatively small even if it exceeded the velocity in the test section. Furthermore, if the Orifice Plate choked at lower mass flows, higher overall pressures would be encountered in the plenum. Coincident with reducing the pressure loads inside the plenum, reserving choked flow for the high mass feeds also made the provision for test velocities beyond the initial planned experimental range of 2-80 ft/s. Flow through the Orifice Plate was evaluated using 2 relations. The first is based on the incompressible mass flow equation derived from Bernoulli [23]:

$$\dot{m} = C_d\sqrt{2\rho\Delta p}A \qquad \text{[Eq. 3-38]}$$

$$\Delta p = p_{plenum} - p_{test\ section} \qquad \text{[Eq. 3-39]}$$

The air density is that of the plenum, C_d is the discharge coefficient through the Orifice Plate, and the area, *A*, is the aggregate orifice area of the plate. The aggregate area is the summation of the orifice areas of all the holes in the Orifice Plate and is treated as though it were a single opening for analytical purposes. The second relation used to evaluate air running through the Orifice Plate was equation 3-37 for compressible flow. The incompressible flow equation was initially assumed to apply for any given mass flow. Because the test section of the HSIC rig was left open to ambient, $p_{test\ section}$ was already known. The mass flow required and the temperature inside the plenum is also known based on the range of desired test conditions. The discharge coefficient and the area were determined with methods detailed later in this section. Thus, when the ideal gas law is used to express density in terms of temperature and pressure, equation 3-38 can be solved for the plenum pressure.

$$RT_{plenum}(.5)\left(\frac{\dot{m}}{C_d A}\right)^2 = P_{plenum}\left(p_{plenum} - p_{test\ section}\right) \qquad \text{[Eq. 3-40]}$$

Using the quadratic formula and taking the positive solution gives the plenum pressure, p_{plenum}. If this plenum pressure was in excess of 28 psia (rule of thumb for choked air [29]) then the compressible flow relation was used instead. Kolodize and Winkle [24] describe the discharge coefficient through dry perforated plates as a function of several factors. With the exception of very thin perforated plates, the key factors identified as increasing the discharge coefficient were: a decreasing ratio of hole pitch to hole diameter, an increasing upstream Reynolds number based on hole diameter, and an increasing ratio of plate thickness to hole diameter. Hole pitch, in this instance, is the average distance between the center point of two holes. These trends are shown in two charts taken from Kolodize and Winkle [24].

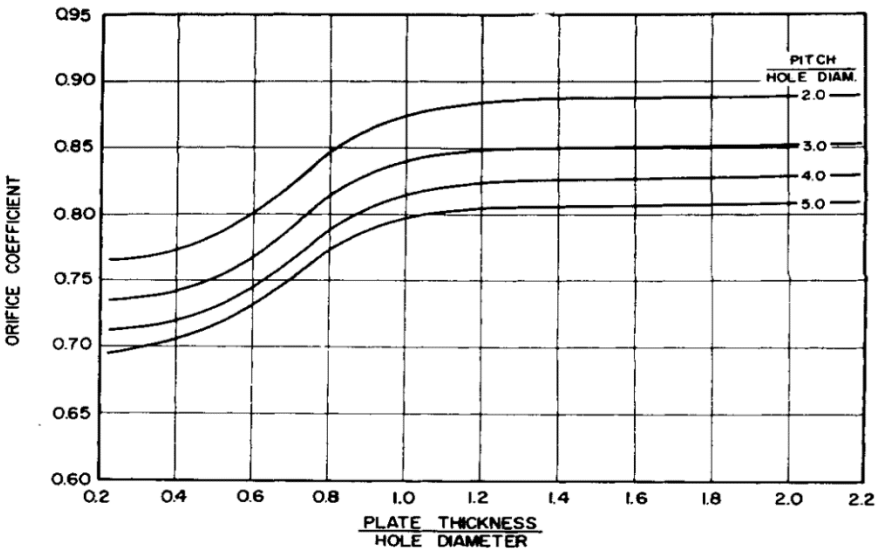

Figure 3.29. Effect of the ratio of plate thickness to hole diameter at Re=2000 on C_d [24]

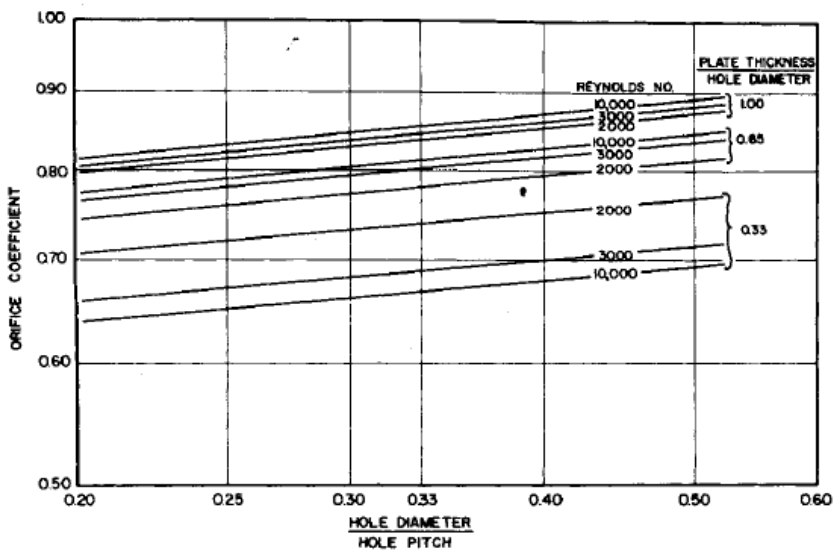

Figure 3.30. Effect of the ratio of hole diameter to hole pitch on C_d [24]

The process of checking a hole pattern design began by choosing an aggregate orifice area (typically as some percentage of the total available area of .334 sq. ft.), finding a compatible hole size, and choosing a plate thickness. A hole arrangement was then created and a discharge coefficient was taken from the appropriate chart. Equations 3-37 and 3-40 were then employed to indicate the flow regime and calculate the plenum pressure. The final Orifice Plate configuration has a total of 160 holes, each with a .0935 inch diameter. The holes are distributed across 4 rings with the first ring having 36 holes, the second having 39, the third having 41, and the fourth having 44. The Reynolds number was approximately 1300 based on a representative plenum velocity of 27 ft/s. The ratio of plate thickness to hole diameter is approximately 2.6, and the ratio of hole pitch to hole diameter varied between 4 and 5. Consulting the relevant graph from Kolodize [24] suggested a discharge coefficient of .79. As a final check on the Orifice

Plate's distribution of flow into the HSIC test section, the mass flows from the different rings were evaluated to confirm the flows per unit of arc length were within 5% agreement of each other.

Figure 3.31. The Orifice Plate, Plenum Vessel, Center Cylinder and Base post welding

The final major development for the HSIC rig's flow conditioning system was the plumbing assembly supplying air to the plenum. Just as the plenum was designed with the intention of slowing and distributing the mas flow upstream of the Orifice Plate, the plumbing feeding air to HSIC rig was designed to convey mass to the plenum without choking the airstream and while restricting its velocity. A permanent assembly was welded to the plenum, but the connection to the facility air supply was made changeable. The selected parts for the permanent assembly were all schedule 40, stainless 304, butt weld pipe fittings. Domestic fittings were used for all components in the permanent assembly because of their well-standardized construction. Flow is first brought in through a 2 inch, 300 pound, weld-neck flange that mates with the facility connection. The air is then introduced to a 2 inch tee fitting (pictured in the center of figure 3.33) which splits

the flow and directs it through a pair of 2 inch to 1.5 inch concentric reducers (pictured just to the left and right of the tee in figure 3.33). Flow travels through two equal sections of 1.5 inch, schedule 40 pipe before being turned upward by 1.5 inch, 90 degree elbow fittings (pictured on the far left and right of figure 3.33).

Figure 3.32. The 300 pound, 2 inch weld-neck flange prior to welding

Figure 3.33. Pipe fittings prior to welding (pipe lengths are not shown)

The flow is turned again by two additional 90 degree elbows and is guided through more lengths of 1.5 inch diameter pipe. Air finally enters the plenum through 1.5 to 1 inch concentric reducers.

Figure 3.34. The 90° elbow and 1.5 to 1 inch reducer

Under the assumptions that 2 lb/s of air at 70°F is the maximum mass flow supplied to the HSIC test section, and that the typical flow cross-section is a 1.5 inch diameter, the average velocity inside the plenum plumbing becomes 167 ft/s. This is both a suitably slow flow velocity and far below the sonic velocity associated with the choked condition (~1,126 ft/s).

Figure 3.35. Welded plumbing to plenum connection

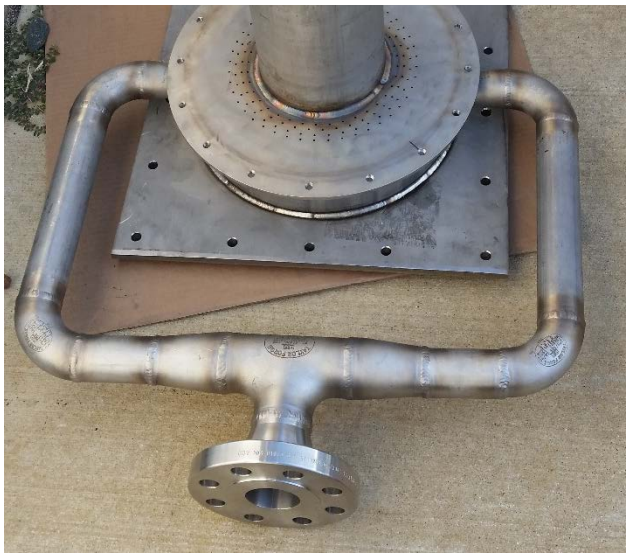

Figure 3.36. The permanent plumbing assembly after welding

The changeable facility connection is for two general arrangements. The first arrangement is for connection with the High Pressure facility's Secondary Air supply. The Secondary Air is intended for use with air flowrates that are below 1lb/s. The second arrangement for the Main Air supply is meant for any mass flow that exceeds this. The changeable facility connection begins with a 2 inch flange that attaches to the 2 inch flange at the base of the permanent plumbing weld assembly. This flange is welded to a section of 2 inch pipe with a 90 degree elbow, and terminates in a second 2 inch flange. The next pipe section is similarly a 90 degree elbow with 2 inch flanges welded to either end. After this second elbowed section, the pipe transitions to a braided stainless steel flexline. This flexline, and the flanges attached to it, can be reoriented and reconnected so that they transport air from either the Secondary or Main air lines. These connections are presented pictorially in figures 3.37 through 3.39. At the time of this writing, only the secondary air connection has been created. Provisions for the Main Air supply are left to future researchers as they expand the experimental envelop of the HSIC test article.

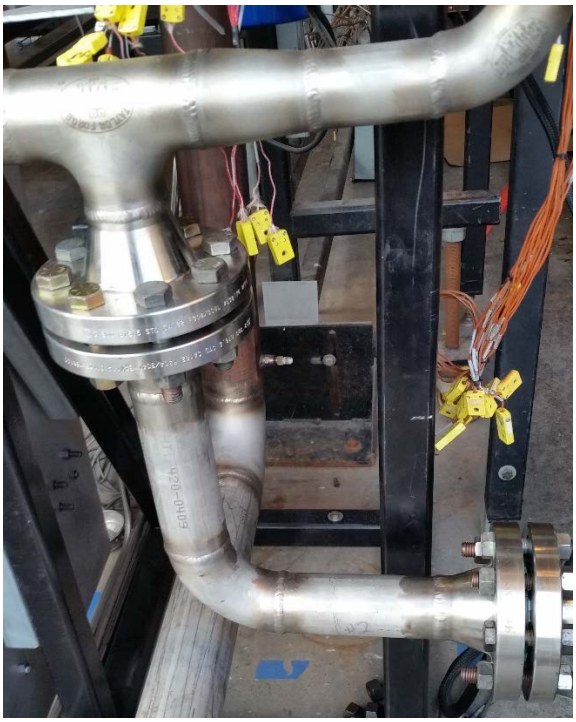

Figure 3.37. First elbowed pipe section connected to the permanent assembly

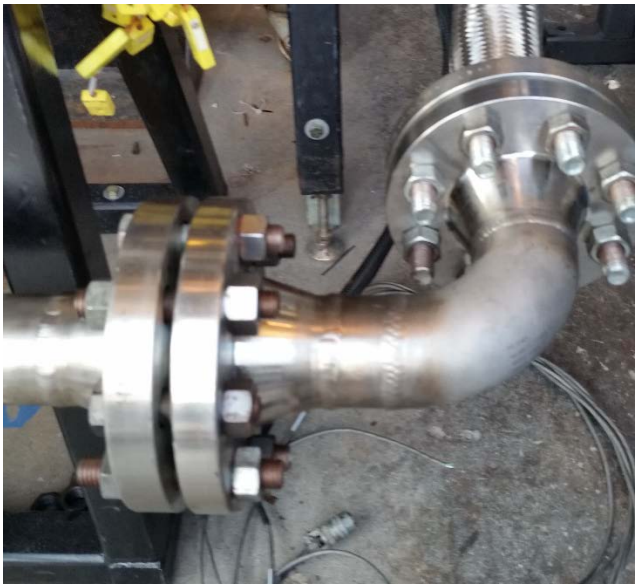

Figure 3.38. Second elbowed section with 2 inch flanges on either end

Figure 3.39. Braided stainless steel flexline

3.7 Window Assembly

An advancement of the HSIC rig over the Wright-Patterson test article is its ability to incorporate infrared imaging diagnostics. The window assembly on the finished rig was explicitly developed in support of this new capability. Window material, window fastening, and window protection were all examined when drafting the new window design.

The high speed IR camera intended for use with the HSIC rig detects signatures in the mid-infrared range and records them as voltage signals that can later be converted into a radiation intensity. More specifically, the camera is attuned to infrared signatures in the 2 to 4.3 micron range. Whatever material was chosen for the test section windows would need to demonstrate a radiative transmissivity compatible with this range while being

able to withstand exposure to a flame. Sapphire was initially identified as having an ideal transmissivity.

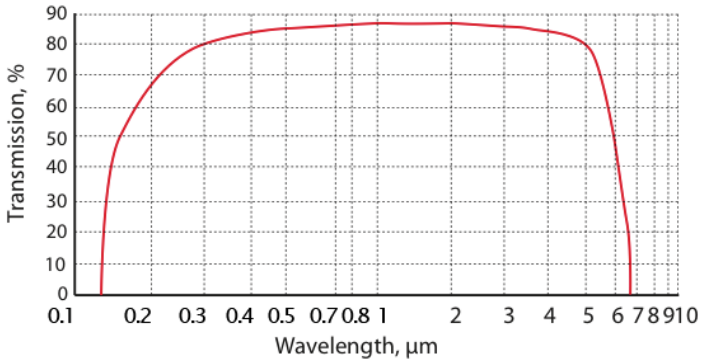

Figure 3.40. Transmission curve for sapphire [25]

The transmissivity of sapphire remains above 80% throughout the entire band of interest, then tapers off sharply above the 5 micron wavelength. However, the costs of procuring and machining sapphire proved to be prohibitive. As a compromise, fused silica, also referred to as fused quartz, was used as the window material instead. Fused silica's transmissivity is not as extensive as sapphire's, but it offers favorable high temperature characteristics consistent with exposure to a fire. Transmissivities from various grades of fused silica are presented below.

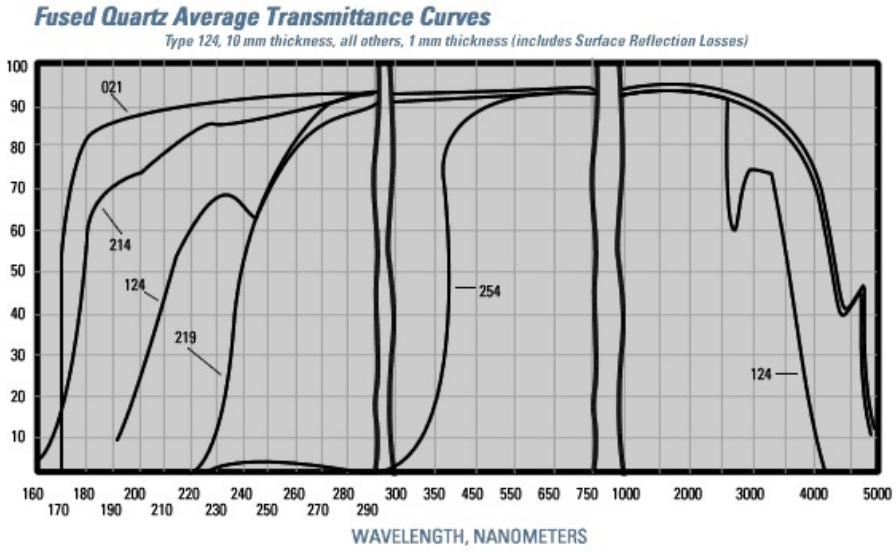

Figure 3.41. Transmission curves for various grades of fused silica [26]

The grade used to fashion the windows was GE 124. In figure 3.41, the transmission curve for GE 124 is shown as stable above 90% until the 2.7 micron wavelength where transmission falls to 60%; this drop coincides with water absorption due to the presence of trace amounts of OH^- in the finished glass. Transmission recovers beyond this wavelength, then subsequently falls to zero between 3.5 and 4 micron. GE 214 actually has less transmission degradation at the water absorption band, but is exclusively used with quartz tubing. At a lower total cost, fused silica is vetted as a tolerable alternative on the basis that only radiation in the CO_2 band (near 4.34 microns) is fully attenuated.

The Window Flange was created to secure the fused silica windows to the Octagonal Duct and leave space for protective gaskets. The 2 Window Flange parts are 6 by 4 inch stainless 304 rectangles with a .375 inch maximum thickness. The central rectangular frame for the window is a 3 by 5 inch opening. An interior lip sits along the edge of this frame at a depth of a quarter of an inch. Clearance holes for 26 size #5-40 screws cover

the outer edge of the window flange and allow it to be fastened in place via corresponding threaded holes in the Octagonal Duct.

Figure 3.42. Window Flanges with clearance hole detail

The fused silica windows are 3.375 by 5.375 inch rectangles that include an outer step which sits on the window lip. The maximum thickness of the window is .23 inches, and the thickness of the step is .125 inches. The overall window thickness was carefully measured so that no piece of the fused silica extended into the flow path of the air in the test section. The size #5-40 screws fastening the window flange to the Octagonal Duct were kept .5 inches long to prevent them from extruding into the air path. The rationale behind having so many fasteners was both the avoidance of air leaking from the test section and the desire to hold the fused silica inside the Window Flanges without excessive rattling or vibrating.

Figure 3.43. Fused silica window before being placed inside a window flange

Figure 3.44. The installed fused silica windows and window flanges

Space was left inside the lip of the window flange for 2 Grafoil® gaskets to be inserted. The Grafoil® is intended to protect the fused silica against any metal-glass contact points and to aid the seal of the windows when the flanges are fastened onto the Octagonal Duct. Grafoil® is a flexible, high-temperature graphite material commonly used in industry [27]. The dimensions of the gaskets match the step on the fused silica windows. The gaskets are .0625 inches thick, and are inserted on both sides of the window step. The compounded thinness and flexibility of the Grafoil® requires that these

components are handled delicately before insertion. The need to install gaskets on both sides of the window was unfortunately learned through an initial error. During an early test of the cartridge heater elements embedded in the Hot Centerbody, cracks were discovered in the corners of the windows. These cracks were believed to be the result of the stainless steel window flanges expanding and contracting against the windows due to the thermal cycling of the Hot Centerbody. Adding the second gasket to each window assembly corrects this oversight, and a reduction of the step width on the fused silica further shields the windows.

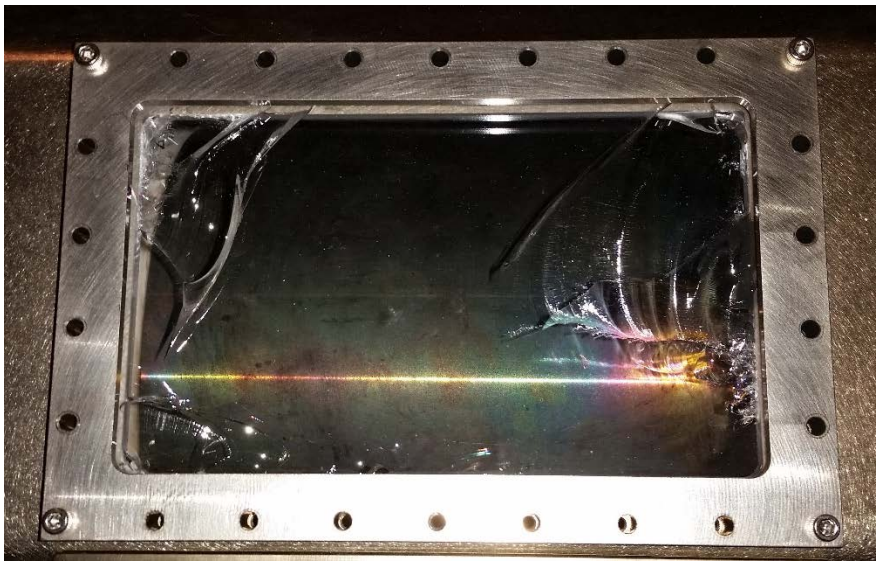

Figure 3.45. Cracked windows from initial thermal cycling

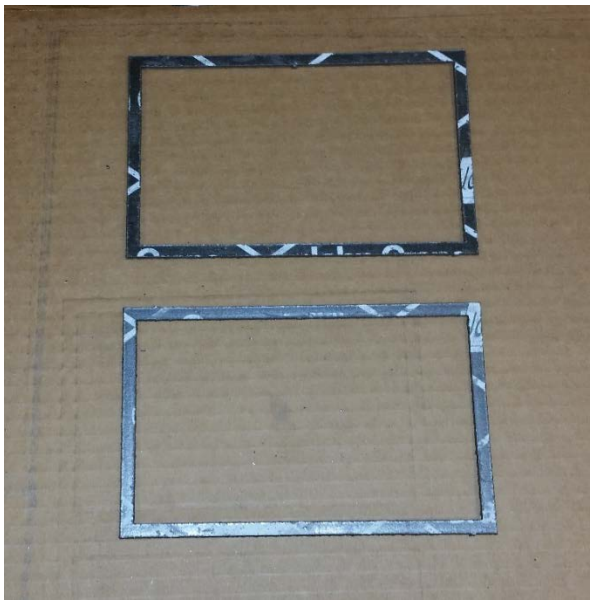

Figure 3.46. Grafoil® gaskets used to protect and seal window assemblies

3.8 Injection

Injection of flammable fluid into the test section of the HSIC rig was handled with an emphasis on simulating a leak. For this reason, minimal effort was directed toward establishing the stoichiometry of the injectant-air mixture. As long as the amount of test fluid present remains within its flammability limits, there is a potential for ignition. Precisely defining these flammability limits in terms of a leak flowrate, however, is left as a future experimental exercise. This section describes the determination of fuel types and flowrates for the experiment, the early momentum balance used to predict injection trajectories, and the hardware associated with fuel injection.

The leak flowrates for the HSIC test rig were found by simply scaling down from those used with the Wright-Patterson test article. In section 3.2, it was stated that the current air flow cross-section was reduced from Wright-Patterson's by a factor of 7.26. Leaving air temperature, air density, and air velocity unchanged from the Wright-Patterson experiment made area the scaling parameter for the relevant leak rates. The

flowrates presented in table 3.6 were obtained by dividing by the 7.26 scaling factor. The most common leak flowrate in the Wright-Patterson experiments was 8 ml/s [5]. In translation, 6.29 lb/hr becomes the general leak flowrate for the HSIC rig. It is noted that although Wright-Patterson found that none of their variations in flowrate had any effect on ignition probability, the same result is unlikely to be obtained on the HSIC rig. This would be the by-product of having test section velocities as much as 8 times greater than those used previously. In increasing the air flowrate so dramatically, it is practically guaranteed that a constant fuel flowrate will fall outside flammability limits. As a consequence, the flowrates given in table 3.6 are effectively starting flowrates for the first several experimental campaigns. Future researchers should be prepared to adjust leak flowrates as increasing amounts of data are gathered on the HSIC rig at higher air velocities.

Table 3.6. Initial Scaled Fuel Flowrates for HSIC Rig

Wright-Pat. Fuel Flowrate	Leak Type	Wright-Pat. Flowrate in lb/hr	Scaled HSIC rig flowrate
4 ml/sec	spray	22.84 lb/hr	3.15 lb/hr
8 ml/sec	spray	45.68 lb/hr	6.29 lb/hr
12 ml/sec	spray	68.52 lb/hr	9.44 lb/hr
1 ml/sec	stream	5.71 lb/hr	0.79 lb/hr
2 ml/sec	stream	11.42 lb/hr	1.57 lb/hr
3 ml/sec	stream	17.13 lb/hr	2.36 lb/hr

The flammable fluid substances injected as fuels into the HSIC rig test section were chosen, when possible, to be in agreement to those from the Wright-Patterson test article.

However, the Wright-Patterson data is over 2 ½ decades old. In multiple cases, the exact fluid blends used at the time of the experiment had become obsolete or, in the case of JP-4, had been phased out entirely. Updated blends of the aircraft fluids tested at Wright-Patterson have been recommended based on their enduring similarity to their older versions. The initial set of test fluids for the HSIC rig are: JP-8 (jet fuel), MIL-PRF-5606 (hydraulic fluid), MIL-PRF-83282 (hydraulic fluid), MIL-PRF-7808 (lubricant oil), and MIL-PRF-23699 (lubricant oil). The last of these fluids, MIL-PRF-23699 had no predecessor from the Wright-Patterson experiments, but was added at the behest of Younes Khamliche from Rolls-Royce.

A momentum balance was used to predict the droplet trajectories of the injected fluids. In turn, these trajectories influenced the location and orientation of the fuel nozzle inside the HSIC rig test section. Guildenbecher [28] describes the physics associated with a droplet being injected into a crossflow. The formulation given by Guildenbecher is for 2-dimensional flow with liquid droplets falling downward into a gaseous crossflow. The model assumes there is no evaporation since the size of the injected droplets does not change. This remains a reasonable approximation for those test cases where the air temperature is near 120°F but becomes unacceptable for conditions where the temperature reaches 600°F. Therefore, the droplet trajectories predicted within this section were used as guidelines rather than firm design expectations. A simple diagram of droplet injection into a crossflow is presented.

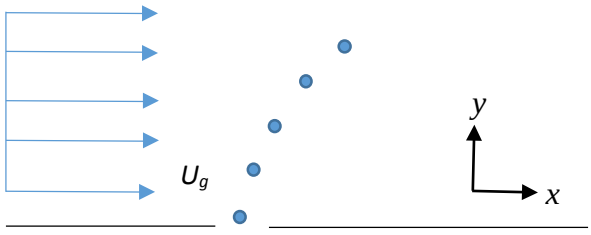

Figure 3.47. Top view of liquid drop injection into a gaseous cross-flow

Balancing the forces acting on the drop gives the x-component of the drop acceleration:

$$\frac{du_x}{dt} = \frac{3}{4}\frac{C_D\rho_g}{D\rho_l}\left(U_g - u_x\right)\sqrt{\left(U_g - u_x\right)^2 + u_y^2} \qquad \text{[Eq. 3-41]}$$

The right-hand side of equation 3-41 is the drag force that works to pull the liquid droplet in the direction of the bulk gas velocity. The subscripts *g* and *l* are for the gaseous and liquid mediums respectively. The bulk gas velocity is U_g and C_D is the droplet coefficient of drag. The upper case D is the droplet diameter. Guildenbecher originally incorporated a gravity term into the expression for the y-component of the droplet acceleration. This term was neglected from the final form of the adapted model since liquid is injected from the wall of the Octagonal Duct along a plane parallel to the ground. Gravity certainly effects droplet motion, but the length scales are small enough (less than 1.8 inches across the annular gap of the test section) that the ability of the drop to reach the target surface is not compromised. The y-acceleration becomes:

$$\frac{du_y}{dt} = -\frac{3}{4}\frac{C_D\rho_g}{D\rho_l}u_y\sqrt{\left(U_g - u_x\right)^2 + u_y^2} \qquad \text{[Eq. 3-42]}$$

The negative sign indicates that the drag of the bulk air velocity on the liquid slows the droplet motion in the y-direction. The x and y velocity components are taken from the

pressure drop driving injection (per Bernoulli's equation) and the angle, θ, at which the liquid enters the test section. Accordingly, the magnitude of the injection velocity is expressed as:

$$u_{inital} = \sqrt{\frac{2\Delta p}{\rho_l}} \quad \text{[Eq. 3-43]}$$

The initial x-velocity is:

$$u_x = u_{initial} \sin\theta \quad \text{[Eq. 3-44]}$$

The initial y-velocity is:

$$u_y = u_{initial} \cos\theta \quad \text{[Eq. 3-45]}$$

Applying simple numerical methods to equations 3-41 and 3-42 allows a droplet trajectory to be mapped. A time increment of 1 μs was chosen to discretize the time domain of the problem. The numerical approach was the following:

$$u(t) = u(t - \Delta t) + \frac{\mathrm{d}u}{\mathrm{d}t}\Delta t \quad \text{[Eq. 3-46]}$$

Returning to equations 3-41 and 3-42 one final time identifies those quantities that have yet to be defined. The parameter C_d is found to be .91 using the expression for the drag coefficient of a sphere [28]. The air density at room temperature has been mentioned elsewhere to be .075 lb/ft^3. The density of JP-8 is roughly 51.2 lb/ft^3 at the same temperature. The spray nozzle used for the earliest experiments on the HSIC rig had a .016 inch diameter orifice and an 80 degree cone angle. This nozzle produced the general 6.29 lb/hr leak rate when its feed pressure was 150 psia. A bulk velocity of 6 ft/s was assumed since it was a mid-range value for the Wright-Patterson tests. Although no attempt was made to directly measure the average droplet size during the Wright-Patterson experiments, a 50 micron average drop diameter was nevertheless expected.

The spray nozzles selected for the HSIC rig produce droplets of a similar size. With this expected droplet diameter, the remainder of the problem is constrained by the information already given. The results of the trajectory analysis for the 80 degree spray cone are summarized.

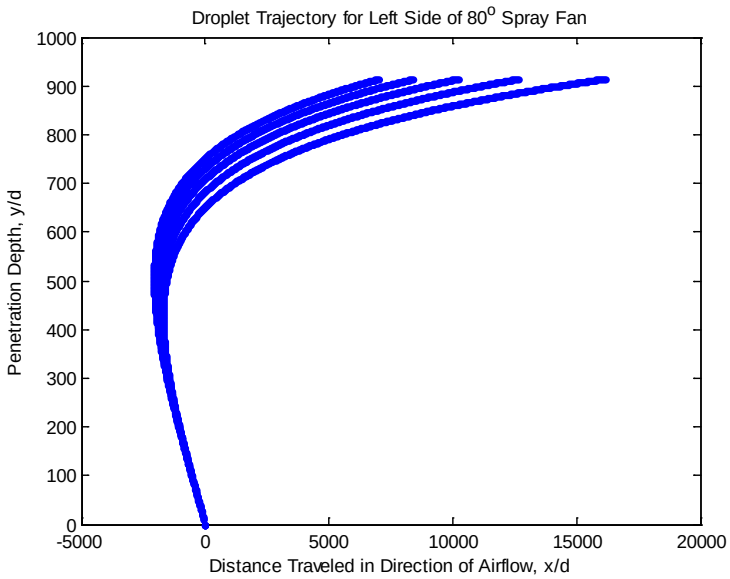

Figure 3.48. Droplet Trajectory for the Left Side of an 80° Spray Fan

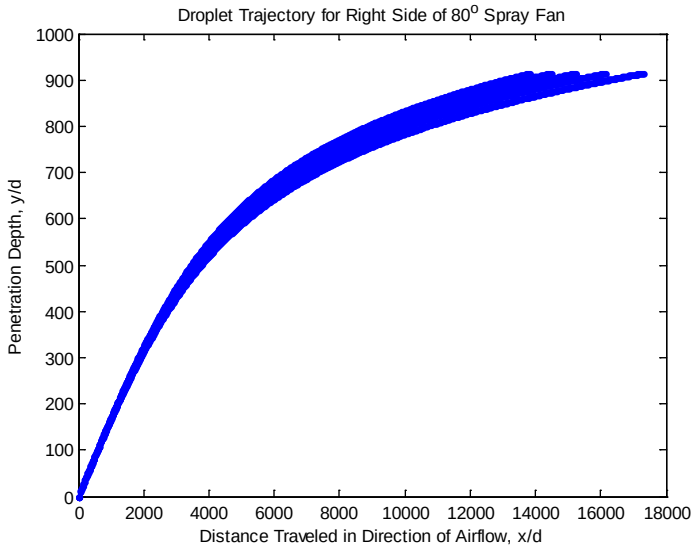

Figure 3.49. Droplet Trajectory for the Right Side of an 80° Spray Fan

The positive y vector points out from the wall and towards the centerline of the HSIC rig. The positive x vector points directly downstream and is normal to the test section exit plane. The MATLAB code running step-wise through the trajectory calculation was permitted to do so until the y/d displacement of the drop was 915. This was used as the bound since it indicated that the drop had traversed the full 1.8 inch annular gap of the test section. The length of the 6 inch Hot Centerbody component is equivalent to 3048 droplet diameters. For the left spray edge shown in figure 3.48, liquid is able to travel approximately 5 inches (2500 droplet diameters) upstream before being turned back by the bulk gas flow. The impact point for the left edge of the spray first occurs 10 inches from the point of injection when liquid is directly introduced from the wall of the Octagonal Duct. In figure 3.49, the right spray edge first impacts the inner diameter of the test section roughly 13000 droplet diameters from the point of injection. This translates to a contact point 25.4 inches from the injector location when liquid is directly injected from the wall of the duct. When locating the injector nozzle on the wall of the Octagonal Duct, the trajectory of the left edge of the spray was used as the delimiting factor. This was decided with due concern for liquid fuel propagating upstream and contacting the Orifice Plate feeding air to the test section. The left edge of the spray fan also reaches the center of the test section earlier than the right edge, and signifies earliest contact with test hardware. Therefore, it is recommended that if the spray nozzle described in this section is ported directly to the wall of the Octagonal Duct, the nozzle should be placed 12 inches downstream of the Orifice Plate.

The hardware chosen to deliver liquid fuel to the HSIC rig consisted of a series of pneumatic valves and multiple lengths of .25 inch stainless steel tubing. These

components were all mounted on a .25 inch thick, 24 by 30 inch aluminum panel. The panel was later secured to the left-hand side of the HSIC rig test stand via .375 inch, coarse threaded holes.

Figure 3.50. Aluminum Valve Panel prior to pluming and mounting

In figure 3.50, three pneumatic valves and a 1000 mL stainless steel fluid vessel can be seen. Given the wide variety of flammable fluids associated with the project, the High Pressure Lab facility supporting its operation did not have an integrated means of delivering them to the rig test section from remote reservoirs during experiments. Prior to testing, the flammable fluid of interest was poured into the vessel pictured above with the aid of a funnel. The valve in the top left corner is designated as HSIC-PV-N2-01. This valve is closed in its de-energized state and supplies the nitrogen used to pressurize the liquid in the vessel for injection. The valve in the lower left corner is HSIC-PV-N2-02. It is open in its de-energized state and runs a nitrogen purge through the .25 inch tubing to keep the lines clear of liquid between tests. The top right valve is the run valve and is

designated as HSIC-PV-FU-01. It is closed in its de-energized state. During injection, liquid runs up from the storage vessel, through the run valve and to the spray nozzle ported on the wall of the Octagonal Duct. This valve was only opened once the temperature of the Hot Centerbody, the air flow rate, and the air temperature inside the test section of the HSIC rig had been thoroughly stabilized. Injection is typically timed to last for 5 seconds. A number of supporting fittings were included in the plumbing assembly on the aluminum valve panel. One such feature was the fuel filter.

Figure 3.51. Fuel Filter procured from Norman Filter Company

The purpose of the filter is to remove any particulate matter that might accumulate inside the flow path of the rig plumbing prior to injection. The filter is located downstream of both the purge and run valves and carries a rating for 3 micron particles. The filter mates with the rest of the plumbing using .25 inch female NPT connections on either end. Proper filter operation is directional, so care must be taken to have the filter installed in the correct orientation.

Figure 3.52. Sample check valve

Two check valves were also added to the system plumbing; one went downstream of the purge valve, and the other went downstream of the pressurant valve delivering nitrogen to the storage vessel. The purpose of these valves is to prevent any backflow of flammable liquid from entering the nitrogen supply of the High Pressure Lab facility. Like the fuel filter, the functioning of the check valves is directional. Check valves are inserted with their inscribed arrows pointing in the direction of the fluid flow. A .25 inch manual ball valve was added to relieve the ullage pressure inside the liquid storage vessel after testing and to prevent fuel splashing on the test facility floor.

Figure 3.53. Manual ball valve used to relieve vessel pressure

The final fixture added was a relief valve intended to vent the nitrogen inside the storage vessel in the event of an over-pressurization. The current relief valve is rated to vent at 225 psia.

Figure 3.54. Relief valve

This pressure rating is not indicative of a critical system over-pressure since the supporting tubing and plenum material are generally rated to withstand pressures up to 1500 psia. The current relief valve is associated with the low relative liquid flowrates of the early experimental conditions. There is no prohibition on using a relief valve with a higher pressure rating for future experiments. These plumbing features and their integration into the infrastructure of the High Pressure Lab facility is documented visually in the Plumbing and Instrumentation Diagram found in appendix A.3.

3.9 Support Stand

A support stand was specifically designed to hold the rig apparatus in place. The stand is a welded assembly of 2 inch carbon steel box tubing; the box tubing has a .25 inch wall thickness. Carbon steel is a suitable material for the stand since its function is

purely structural, and it experiences no significant thermal loads. The finished carbon steel assembly stands 57 inches tall and has a total of 19 clearance holes for .375 bolt fasteners. The support stand was treated with a coat of high-temperature rust resistant paint to prolong its work life.

Figure 3.55. Test support stand prior to being bolted to the test facility floor

The square frame sitting atop the welded assembly in figure 3.55 mates to the Base component and contains 16 of the stand's clearance holes. Post welding, the Base component was machined in conjunction with the support stand to transfer these holes and ensure a close match.

Figure 3.56. Welded Base component with fastener thru-holes along the edges

The welds created throughout the experimental assembly as well as the strength of the materials used for fabrication guaranteed a high measure of structural rigidity for both the support stand and rig. The issue thus became determining the best method to locate the remaining 3 bolt holes on the floor bars of the support stand such that rig would be unable to topple over. Modeling the entire HSIC test rig as a simple cantilevered beam proved to be a reasonable approach to solving this problem []. In order to properly implement this method, it was first necessary to find the center of mass of the supported assembly.

$$x_{cm} = \frac{1}{M}\sum_{i=1}^{n} m_i x_i \qquad \text{[Eq. 3-47]}$$

The overall center of mass x_{cm} of the HSIC rig is taken by mass-weighting the center of mass x_i of each constituent feature. The mass m_i of the various constituents was estimated using geometry to first obtain a value for the volume, then multiplying by the material density. The masses of all of the major rig components is tabulated at the end of this paragraph. The axisymmetric nature of the assembly generally placed the different center of masses at the geometric center of each component. As a result, the various center of

masses were found to lie along the centerline of the HSIC test rig (the fused silica windows and window flanges were the only genuine exception to this trend, but their low collective mass made their influence minimal). The total approximate mass of the HSIC rig is 178.84 lbs. Equation 3-47 locates the center of mass on the rig centerline, 13.4 inches from the bottom edge of the Base. To counteract the downward moment the rig exerts on the support stand through this point, a moment balance was used to determine the ideal locations for the bolts securing the entire experimental apparatus to the facility floor. All of the .375 inch bolts used on the support stand are coarse thread, SAE grade 8 carbon steel bolts. Bolts of this standard are rated for a 9,300 lbf proof load. The force exerted by the 178.84 lbs of the HSIC assembly is 5,753 lbf. Ultimately, 2 bolts were placed 19.5 inches away from the rig Base on the Floor Crossbar (see appendix A.4 for drawings). This gave the stand the capacity to withstand a total moment of 30,225 lbf-ft against the actual 6,424 lb-ft moment generated by the supported experimental apparatus. The third and final bolt hole was placed on the Front Floor Crossbar of the stand to completely restrain its motion. All floor fasteners were secured by studs buried in the concrete floor of the High Pressure Lab facility.

Table 3.7. Masses for the Various HSIC rig parts

Part Name	Qty	Material	Density	Mass
Base	1	Stainless 304	0.289 lb/in^3	43.38 lb
Plenum Vessel	1	Stainless 304	0.289 lb/in^3	12.13 lb
Orifice Plate	1	Stainless 304	0.289 lb/in^3	10.52 lb
Center Cylinder	1	Stainless 304	0.289 lb/in^3	27.86 lb

Table 3.7 cont.

Cantilever Base Plate	1	Stainless 304	0.289 lb/in^3	1.80 lb
Cantilever Support	1	Stainless 304	0.289 lb/in^3	6.44 lb
Macor® Disk	2	Macor®	0.091 lb/in^3	2.31 lb
Ceramic Sleeve	1	Alumina silicate	.098 lb/in^3	2.31 lb
Hot Centerbody	1	Inconel 718	0.297 lb/in^3	22.63 lb
End Piece (End Lip)	1	Stainless 304	0.289 lb/in^3	0.65 lb
End Piece (Vessel)	1	Stainless 304	0.289 lb/in^3	6.37 lb
End Piece (End Face)	1	Stainless 304	0.289 lb/in^3	0.97 lb
IR Quartz Windows	2	Fused Silica	.079 lb/in^3	0.63 lb
Window Flange	2	Stainless 304	0.289 lb/in^3	2.42 lb
Octagonal Duct	1	Stainless 304	0.289 lb/in^3	38.42 lb
Total Mass	-	-	-	178.84 lb

A final function fulfilled by the support stand is the mounting of the electrical box used to route power between the facility and the cartridge heater elements embedded in the surface. The box itself is held on multiple pieces of uni-strut which in turn are clamped by the nuts of the .375 inch bolts fastening the base of the assembly to support stand. Images of the electrical box and the completely installed HSIC test rig and support stand are provided.

Figure 3.57. Electrical box secured by uni-strut pieces to the back of the HSIC test rig

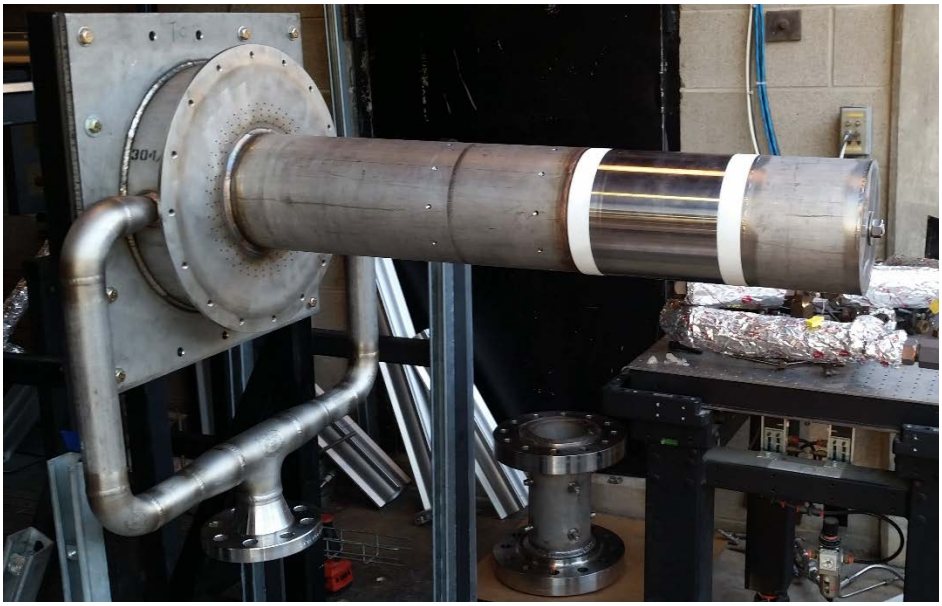

Figure 3.58. Assembled HSIC test rig without Octagonal Duct

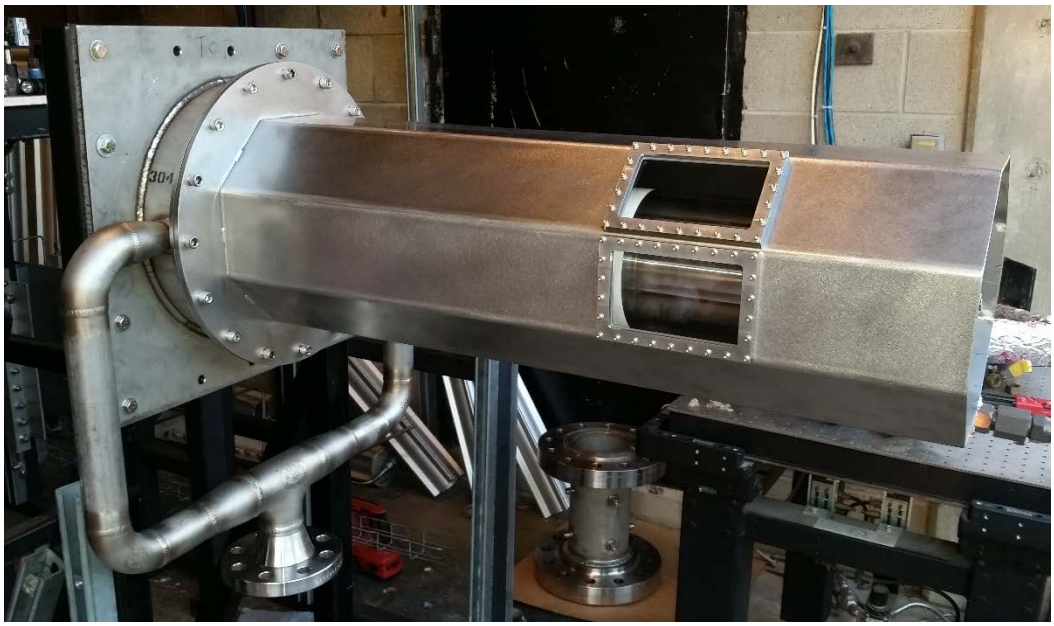

Figure 3.59. Assembled HSIC rig with Octagonal Duct and Window Assemblies

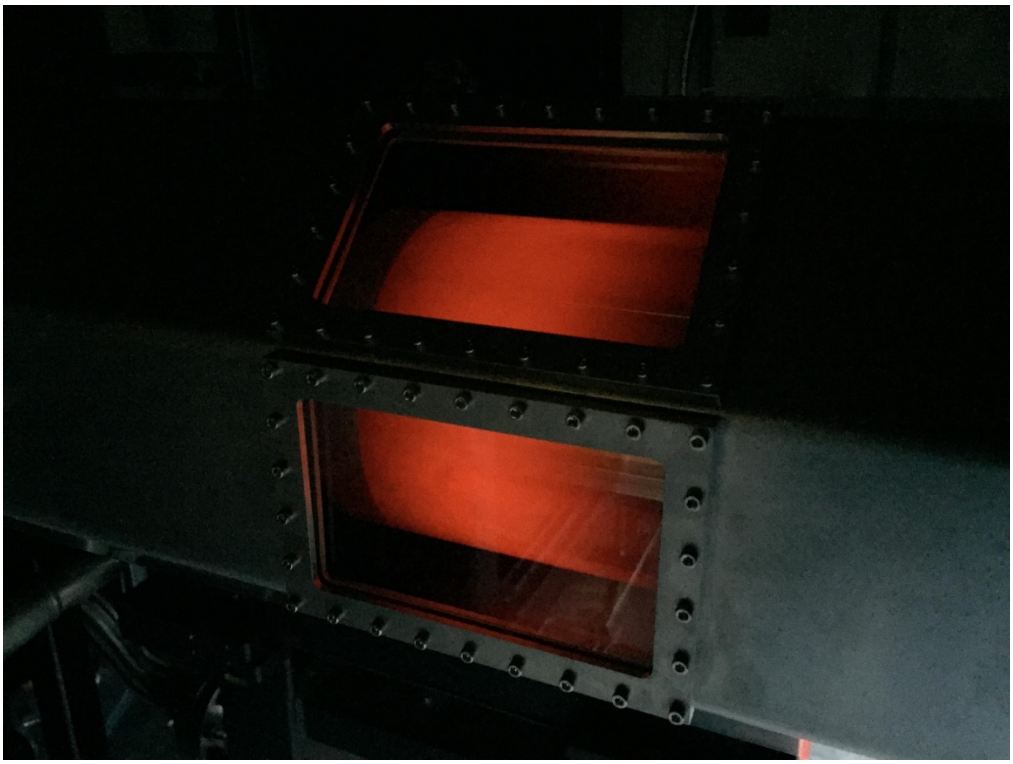

Figure 3.60. Assembled HSIC rig during cartridge heater test at 1400°F (760°C) set point

3.10 Instrumentation and Sensory Equipment

In addition to the profile probes monitoring and controlling the temperature of the Hot Centerbody, auxiliary thermocouples and pressure transducers were installed to report the conditions of the HSIC test rig's fluid systems. A high-speed, infrared camera is also intended to act as a flame visualization device and provide both average and time resolved information on the radiation intensity of the combustion product species. A pressure-temperature rake is being pursued to further supplement and expand the data that can be acquired for the test apparatus, but its specifications are detailed in a later section.

The thermocouple and pressure transducer instrumentation unique to the HSIC rig's fluid systems is primarily located on the Plenum Vessel. A .125 inch port was created at the top of the plenum to introduce a type K, ungrounded thermocouple. This thermocouple serves the purpose of verifying that the air entering the test section is at the desired experiment temperature prior to liquid injection. The port for the thermocouple is a .125 inch GG (pipe coupling) fitting welded to the top of the Plenum vessel with a corresponding hole drilled into the plenum to admit the tip of the thermocouple probe.

Figure 3.61. Thermocouple installed atop Plenum Vessel via welded port

Offset from the thermocouple by 45 degrees is a Druck 1200 series, PMP pressure transducer rated for 200 psia. It is similarly ported using a drilled hole and welded pipe coupling fitting. The fitting and connection is sized to .25 inches. The purpose of this particular transducer is to report the pressure inside the plenum vessel. This reading has the multifaceted distinction of indicating how well the plenum is working (as stated earlier, the higher the plenum pressure, the better for slowing and distributing flow), alerting the test operators of any dangerous over-pressure on the Plenum Vessel, and conveying the level of back-pressure occurring inside the air supply system feeding the rig. A second, identical transducer is used in the liquid plumbing to report the pressure head for injection.

Figure 3.62. Pressure transducer ported and mounted to the Plenum Vessel

The high-speed infrared camera planned for flame visualization takes planar, mid-spectrum infrared images. The camera contains a detector array whose sensitivity is aided by cooling from liquid nitrogen poured and stored into a dewar inside the camera body. Greater details of the camera set-up, operation, and maintenance are deliberately withheld due to the restricted nature of certain camera features, but the camera does possess multiple filters which allow species specific radiation intensity data to be obtained. Filters for water vapor, carbon dioxide, and soot are all available with the camera.

Figure 3.63. The high speed infrared camera

3.11 Provisions for Complicating Flow Features

Adaptability is essential for the functionality of the HSIC rig article. In that regard, the rig is meant to be capable of going from the bare central cylindrical volume pictured in figure 3.58 to a collection of features that more closely simulate the environment of an aircraft engine nacelle. An advantage the HSIC test rig has over the Wright-Patterson apparatus is the ability to gradually increment the complexity of the test section environment. The Wright-Patterson experiment existed as a sharp binary: either a single, 1.5 inch diameter Inconel tube was used as the hot target surface, or a full third of a full scale F-16 engine nacelle complete with a multi-stage bleed air duct, tubes, clamps, and fuel pump. Gradually adding disturbances allows the effects of an individual feature to be more accurately characterized. The sorts of features that have routinely been discussed in Purdue's interactions with Rolls-Royce have included: a flange-like feature to create a step obstruction, tubing that winds along the Center Cylinder, and cylindrical obstructions that extend into the annular gap of the test section. A recommended flange component scaled to the test section of the HSIC rig is included in the engineering drawings of appendix A.4. The dimensions for this part were concluded from interactions with Rolls-Royce and were based on flanges typical to those used in extant turbofan

engine nacelles. Similar collaborative interactions should take place between Purdue and Rolls-Royce to define dimensions for future flow components and configurations. In anticipation of the need to secure all manner of parts to the Center Cylinder, 20 size ¼-20 threaded holes have been added. This size and tread were chosen for their ubiquity. The feature attachment holes were also located sufficiently far downstream that the airflow would have an opportunity to settle after passing through the Orifice Plate. The reference by Pope [30] suggests a general settling distance of 100 hole diameters. This leaves the airflow of the HSIC rig completely settled 9.35 inches into the test section with a buffer of an extra inch before the flow features begin. When no feature is being attached to the Center Cylinder, these holes must be treated with anti-seize and plugged to keep liquid free of the passage for the electrical leads.

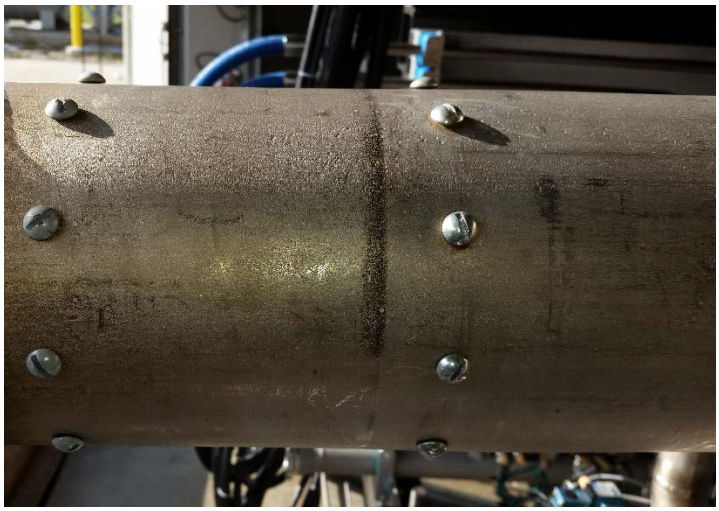

Figure 3.64. The plugged holes for flow features

3.12 Pressure and Temperature Rake

A planned feature currently under development for the HSIC rig is a pressure-temperature rake. The rake will serve a threefold purpose. It will be used to resolve the thermal and fluid boundary layers of the air above the Hot Centerbody, and it will be capable of giving in situ velocity measurements. The proposed rake design is presented below:

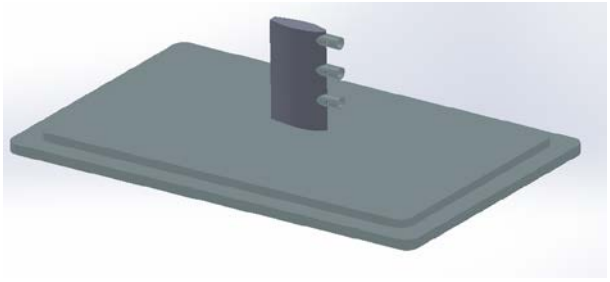

Figure 3.65. Proposed design for the pressure-temperature rake

The base of the rake will have dimensions identical to the fused silica windows, but be machined from stainless steel 304. This allows the rake to be secured to the HSIC rig with the Window Flange feature and supports interchangeability between the rake and the windows. The rake height extending into the test section gap is currently 1.2 inches. The rake is also to be outfitted with 3 sensing nodes. Each node contains a type K thermocouple to monitor temperature and a transducer to record stagnation pressure. A static pressure measurement is to be made at the base of the rake. The in situ velocity readings will be taken from comparing this static pressure measurement at the rake base with the stagnation measurement taken at any of the sensing nodes. The rake is also to be designed to withstand contact with both flames and liquid sprays. Discussions are ongoing to leverage the rake design expertise of Aerodyn Engineering Inc. to realize this component.

CHAPTER 4. PRELIMINARY TESTS

4.1 Flat Plate Test Article Experiments

As an exercise in characterizing the ignition behavior of the flammable aircraft fluids associated with the project, experiments were conducted using a simple flat plate test article. This afforded the opportunity to acquire baseline reference data absent the crossflow and curvature of the HSIC test rig and to practice infrared diagnostic methods. The general experimental approach of Colwell et al. [8] and Shaw et al. [13] for droplet ignition in a quiescent environment was followed. The fluids chosen for these preliminary tests were the jet fuel, JP-8, and the hydraulic fluid, MIL-PRF-5606. They were selected because they are the present-day iterations of JP-4 and MIL-H-5606, the earliest fuels used on the Wright-Patterson test article. This chapter contains descriptions of the flat plate apparatus, its test procedures, and the results from the preliminary experiments with JP-8 and MIL-PRF-5606.

The experimental apparatus for the flat plate tests consisted of a heated stainless steel plate surrounded by ceramic insulation. Drops of fuel were dispensed onto the plate from above. The experimental arrangement is presented in its entirety in the figure below.

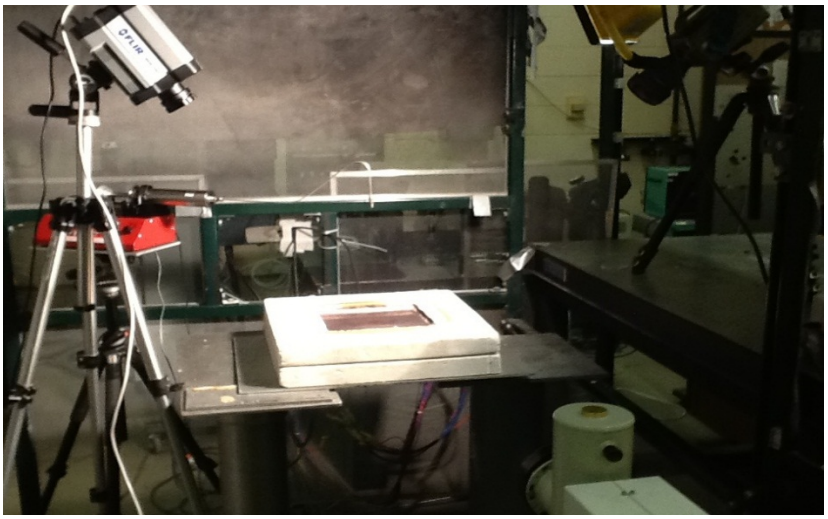

Figure 4.1. The complete experimental arrangement for the flat plate tests

The flat plate sits inside its white, high-temperature insulation at the center of figure 4.1. The plate is a 9 inch by 9 inch square of stainless steel which is bolted to a similarly dimensioned square of copper. Five evenly spaced, .375 inch diameter, 1KW cartridge heater elements are inserted into the copper in addition to the 5 type K thermocouples that are wired to the heater controller. The high thermal conductivity of the copper plate is leveraged to create a uniform temperature profile prior to conduction into the stainless steel. As a consequence, the temperature profile within the stainless steel plate is effectively isothermal. Five more thermocouples were embedded in the stainless steel and wired to a data acquisition system to provide real time measurements of the hot surface temperature.

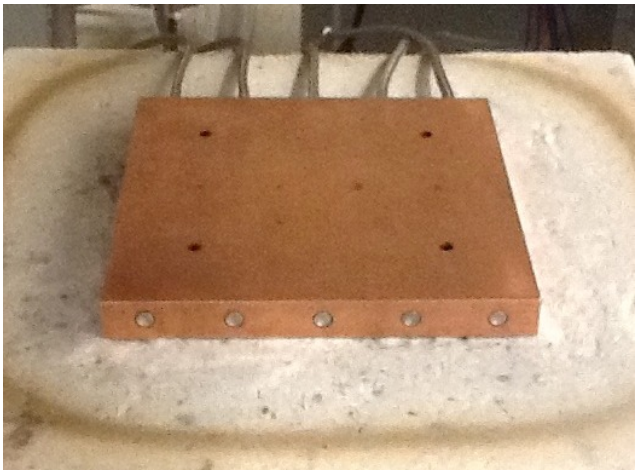

Figure 4.2. Copper plate with installed cartridge heaters and bolt holes for the steel plate

Figure 4.3. Copper and stainless steel plates together with electrical leads

A programmable, 160 mL syringe pump was used to deposit metered droplets on the stainless steel hot surface at regular intervals. Each drop had a volume of .25 mL. The tubing and orifice delivering fuel to the surface from the pump were positioned such that each drop fell a distance of 30 cm before impacting the stainless steel.

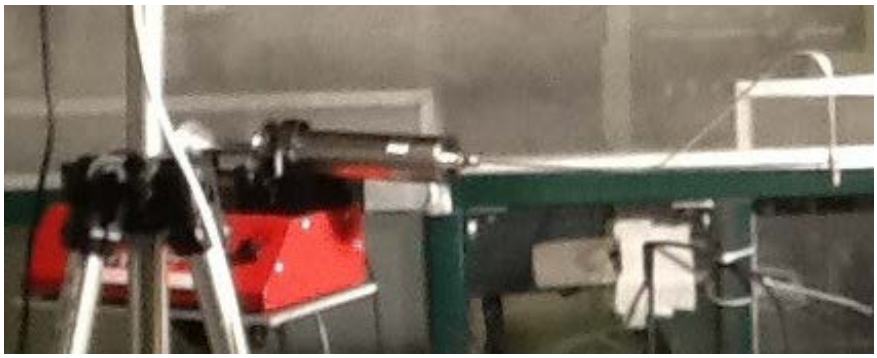

Figure 4.4. Syringe pump

A Phantom® series high speed camera was used to record droplet ignition at a rate of 3000 frames per second. This was used concurrently with the high-speed, nitrogen-cooled infrared camera described in section 3.10 of the previous chapter.

At the start of each test day, the surface was treated with isopropyl alcohol to remove any residues from the previous tests. It was discovered, however, that over the course of several experiments, a plate would develop an oxide layer that fundamentally altered ignition behavior. At this juncture, the plate was replaced. Isopropyl alcohol was also used to prime and clean the vacuum pump and its attendant tubing. While the surface and syringe pump were being cleaned, the high-speed infrared camera was centered, then focused at a distance 34.5 inches from the edge of the stainless steel. The high speed was positioned and angled so as to capture a top view of the flat plate surface. After the cleaning, the syringe pump was loaded with the test fluid, and the temperature controller was set near its auto-ignition temperature. For each temperature set point, 20 drops were dispensed onto the center of the plate surface at time intervals that allowed each drop to completely vaporize before the next one fell. The repeated drops at each set point conforms to the probabilistic understanding of hot surface ignition put forth by Colwell [8]. The plate temperature was initially raised in 100°C increments until the first ignition

was achieved. After first ignition, the set temperature was lowered by 50°C, and the drop series was begun anew. Temperature was raised in 10°C increments from this point onwards with the number of ignited drops at each set point being recorded by the test conductors. Tests were concluded when a 100% ignition probability had been demonstrated for two successive set temperatures. Throughout this process, the temperature being monitored was that of the stainless steel plate. This was in contrast to the temperature integrated into the controller feedback, which was read from the copper. Despite the emphasis placed on temperature uniformity in the experimental arrangement, the differing thermal conductivities of the steel and copper led to a natural discrepancy between the two plate temperatures. Time was therefore granted after each set point, to permit the individual plate temperatures to stabilize. During tests, the temperature of the steel was found to be roughly 50°C cooler than the copper. Due to the highly transient nature of the flames observed for droplet ignition, data was not taken on either of the high-speed cameras until the probability of ignition reached 100%. Data acquisition had to be triggered manually, so a principle of selective camera use was followed to maximize the potential for a captured flame. Because the generated files on both cameras were also quite large, this had the secondary effect of greatly reducing the storage space necessary for data management.

In broad agreement with the literature, the minimum hot surface ignition temperature demonstrated for both JP-8 and MIL-PRF-5606 were at least 400°C higher than their reported auto-ignition temperatures. The auto-ignition temperature of JP-8 is 223°C, but hot surface ignition was not achieved until the steel reached 676°C. Likewise, the auto-ignition temperature for MIL-PRF-5606 is 218°C, but no ignition was observed until the

plate was at 650°C. Visible images for the 100% ignition points of both JP-8 and MIL-PRF-5606 are shared in figure 4.5 and figure 4.6 respectively. Also in general agreement with the results from the literature, was the face that MIL-PRF-5606 proved to be slightly easier to ignite than JP-8 [5]. It reached both the initial and 100% ignition probability points approximately 15°C sooner.

Figure 4.5. JP-8 ignition at 737±2°C and 100% ignition probability

Figure 4.6. MIL-PRF-5606 ignition at 721±2°C and 100% ignition probability

A logistic regression curve fit [8] was performed to translate the raw data into a hot surface ignition temperature probability curve.

$$P(Y) = \frac{\exp(b_o + b_1.T)}{1+\exp(b_o + b_1.T)} \quad \text{[Eq. 4-1]}$$

The coefficients b_0 and b_1 were based on the two temperature points with the lowest observed ignition probability and the highest observed ignition probability less than 100%. A MATLAB script was used to aid in the computation. The results from the JP-8 and MIL-PRF-5606 tests are presented in the following tables and figures.

Table 4.1. Ignition Data for JP-8

Set temperature in copper plate (°C)	Mean temperature in Stainless steel plate (°C)	Standard deviation of Stainless steel temperature (°C)	Ignition probability
600	556	4	0
700	651	3	0
710	659	4	0
720	668	3	0
730	676	3	0.1
740	685	3	0.2
750	693	5	0.4
760	702	4	0.75
770	711	4	0.75
780	720	5	0.85
790	728	3	0.9
800	737	3	1
810	746	4	1

The coefficients for JP-8 were b_0 = -59.325 and b_1 = 0.084°C^{-1}.

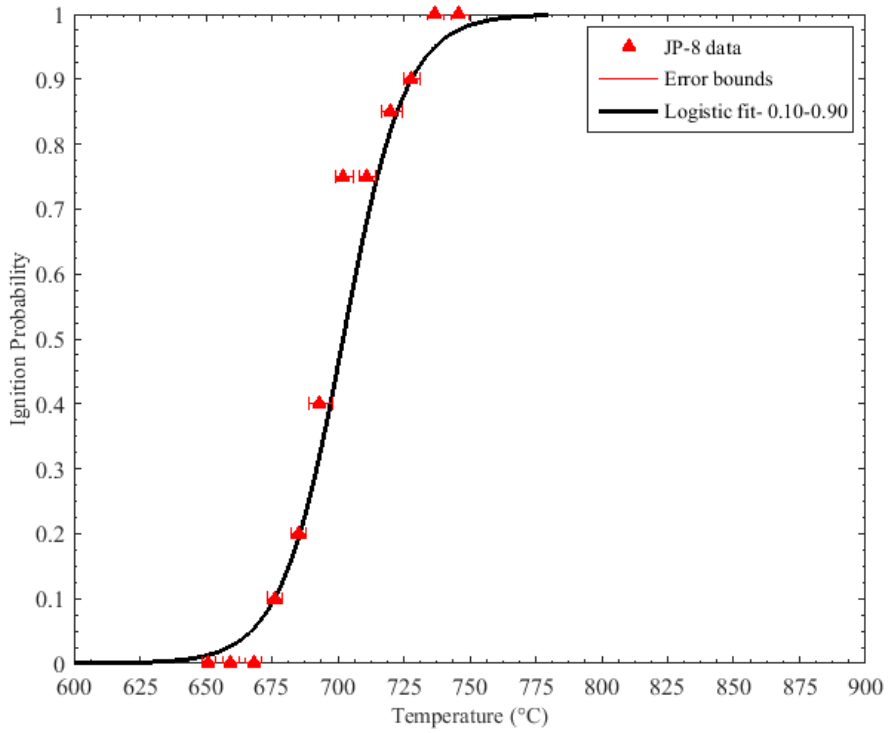

Figure 4.7. Ignition probability curve for JP-8

Table 4.2. Ignition Data for MIL-PRF-5606

Set temperature in copper plate (°C)	Mean temperature in Stainless steel plate (°C)	Standard deviation of Stainless steel temperature (°C)	Ignition probability
600	560	3	0
700	650	3	0.10
710	659	3	0.20
720	668	4	0.35
730	676	4	0.60
740	685	4	0.65
750	694	4	0.80
760	704	4	0.90

Table 4.2 cont.

770	713	5	0.95
780	721	3	1.00
790	730	4	1

The coefficients for MIL-PRF-5606 were b_0 = -55.246 and b_1 = 0.081°C^{-1}.

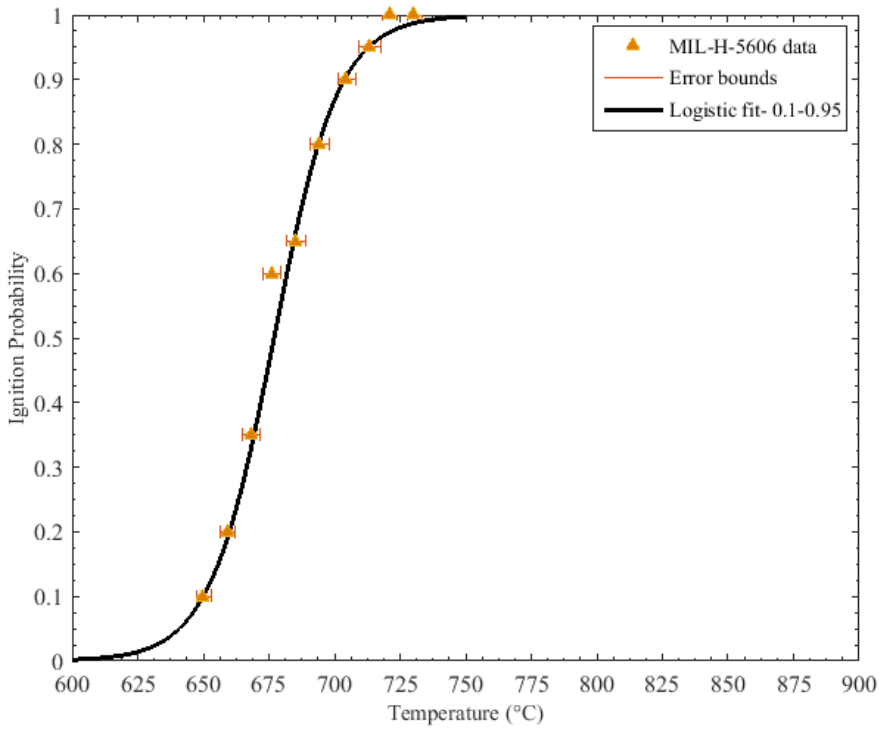

Figure 4.8. Ignition probability curve for MIL-PRF-5606

That the MIL-PRF-5606 ignited more readily than JP-8 is consistent with the finding by Johnson et al. [5] of the hydraulic fluid exhibiting a lower minimum ignition temperature for a variety of experimental conditions. This was at least partially attributed to the more viscous character of the hydraulic fluid and is also reflected in its higher overall flashpoint (89°C vs 48°C for JP-8) [5]. It was described in the literature review chapter

how ignition represents a competition between chemical rates and environmental conditions. With its higher viscosity, MIL-H-5606 would be more resistant to transport away from the heat source after being deposited. With its higher flashpoint, MIL-H-5606 would be less likely to evaporate early and more inclined to steadily collect in proportions conducive to flammability. It was noted with the simple duct test article at Wright-Patterson how the inclusion of even a single flow obstruction such as a cushion clamp lowered the minimum ignition temperature for MIL-H-5606 more dramatically than for than the less viscous, more volatile kerosene based JP-4 and JP-8 [5]. Supplementing the basic ignition probability data taken from these experiments were infrared images.

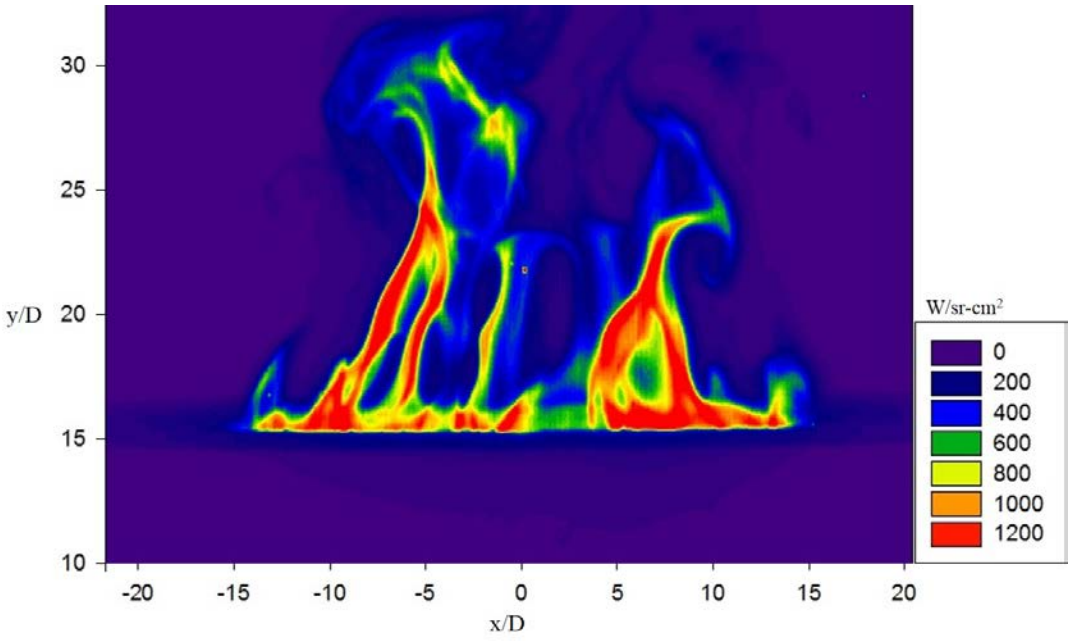

Figure 4.9. Instantaneous image of JP-8 ignition at 810°C set point for 2.58±.03µm

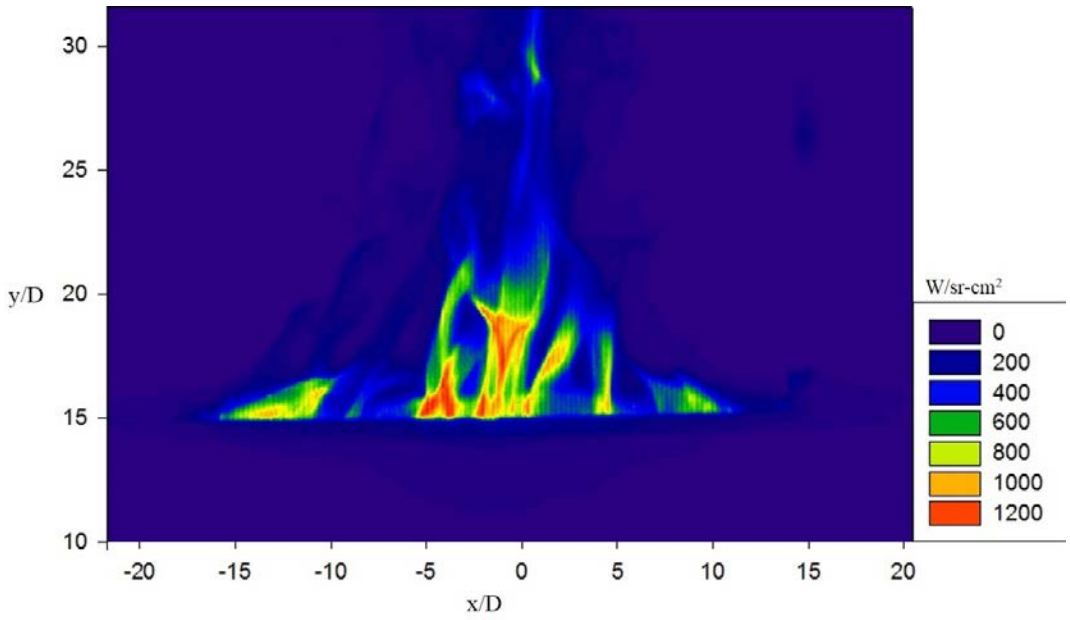

Figure 4.10. Instantaneous image of MIL-PRF-5606 ignition at 780°C set point for 2.58±.03µm

The wavelength range given in figures 4.9 and 4.10 corresponds to soot and water vapor species and the scale, *D*, is equal to 8mm. The images are reported in terms of the radiation intensity received from the targeted source with *sr* signifying the solid angle through which the signal is transmitted. The average spatial radiation intensity from the JP-8 flame is higher than that of MIL-PRF-5606. Higher energy density is to be expected considering its primary use as fuel. Herein lies the added diagnostic potential of infrared imagery. Although these images only give conclusive information on the radiation intensity of the sample, the radiation intensity correlates with the overall temperature and/or energy state of the filtered species. The temperature of product species is crucial to understanding the thermal formation of undesirable chemical species such as soot and NO_x [31]. Consequently, radiation intensity serves as an indirect measure of soot formation, oxidation, and emissions [31]. An issue that arose when acquiring the infrared

images of JP-8 and MIL-PRF-5606 was linked to the transient nature of droplet ignition. The flames evolved from the drop contacting the surface only lasted on the order of a few hundred milliseconds. There was ample time for the acquisition rate of the high speed infrared camera, but coordination was problematic for the camera operator having to trigger the recording (this was less of an issue with the Phantom® series camera since the output file includes the last few seconds prior to the trigger as a matter of function). Further complicating matters was the varied ignition delay time for the different test fluids. Johnson et al. noted the ignition delay time for MIL-H-5606 to be approximately 3 times that of JP-8 [5]. Direct comparison across separate trials, even for the same test fluid, carried the disadvantage of the acquired images falling at different edges of the flame lifetime. The general approach for capturing droplet ignition was to first take multiple recordings at the 100% probability point, then later sort through the data during post processing for the captured flame. These difficulties do not necessarily preclude hot surface ignition from more nuanced infrared work in the future. An alternative to manually triggering data acquisition could have the infrared camera in loop with a UV flame detector so that trigger response is tied directly to ignition. Another alternative would be to reconfigure data acquisition so that generated files include more of the time elapsed prior to triggering. On the larger scale HSIC test rig, a natural corrective seemed to present itself. Since fuel injection on the HSIC rig is designed to exist as a sustained leak for approximately 5 seconds, greater quantities of flammable fluid are present. Thus, the flames seen during the earliest experiments to benchmark the test rig were larger and tended to linger on the order of seconds prior to either self-extinguishment or blow-out from the nitrogen purge. Infrared imagery remains a promising avenue for future

experimental inquiry. Time lapsed images of JP-8 droplet ignition acquired by the Phantom® series camera at the 100% ignition point demonstrates the flame lifetime.

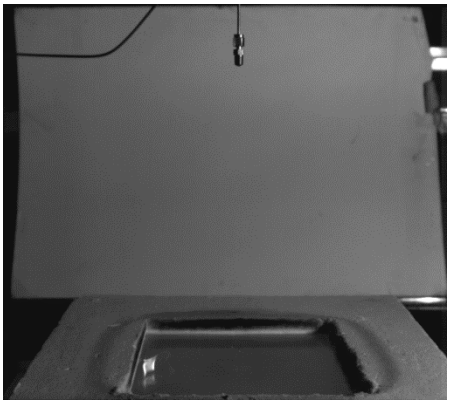

Figure 4.11. JP-8 at t = 0 secs, ignition starts

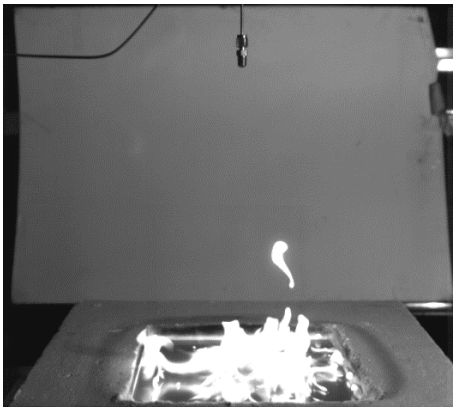

Figure 4.12. JP-8 at t = 100ms, initial flame rise

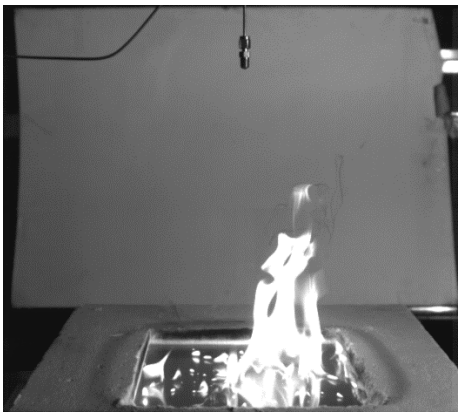

Figure 4.13. JP-8 at t = 200ms, flame peak

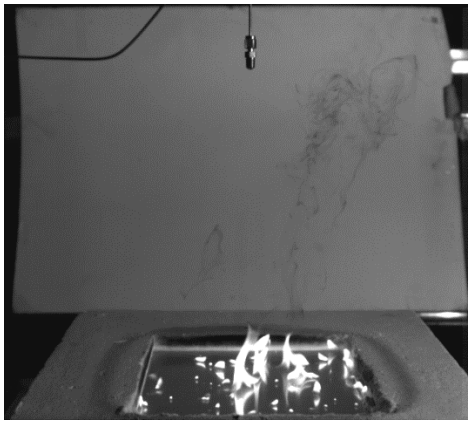

Figure 4.14. JP-8 at t = 300ms, flame diminishing prior to extinction

4.2 Simple Cylinder Tests

Work was also done to vet the capabilities of the cartridge heater elements settled on for the Hot Centerbody of the HSIC rig. To that effect, a 3 inch diameter, 6 inch long rod of stainless steel 304 was machined to accept a .5 inch diameter, 1 KW cartridge heater element nearly identical to those used in the Hot Centerbody (it lacked lead protection). A K type thermocouple was tack-welded to the surface and then directly connected to the temperature controller feedback. For this reason, only the temperature of the controller reading had to be monitored during the course of the experiment. In order to take advantage of the extant flat plate apparatus while avoiding facility damage, coarse blocks of porous ceramic insulation were stacked over the stainless steel plate for the cylindrical test article. A final bed of ceramic fiber wool was laid on top of the porous ceramic, and served as the resting place for the cylinder. The first tests done were those to exercise the cartridge heater.

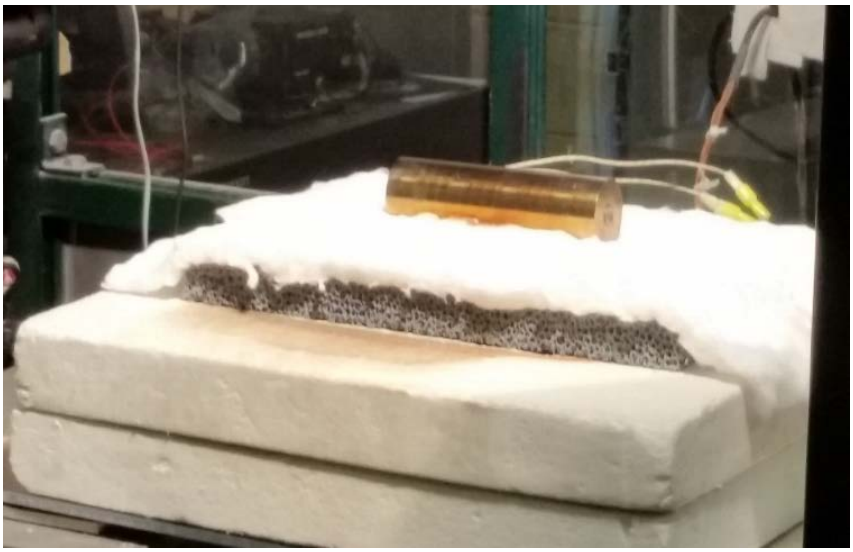

Figure 4.15. Cylindrical test article atop porous ceramic block and ceramic fiber bedding

Figure 4.16. Cylindrical test article at a 650°C set point

Figure 4.17. Cylindrical test article at a 1000°C set point

As shown in figure 4.17, the single heater element was able to bring the temperature of the stainless steel cylinder up to 1000°C (or 1832°F). This temperature is at the absolute upper end of the design envelope and was viewed as a final justification for the chosen heater elements. Greater confidence in the suitability of the cartridge heaters was derived from the realization that an individual element was able to take 12 lbs. of stainless steel (which exhibits a similar thermal conductivity to Inconel 718) to the maximum design temperature. This is compared against the Hot Centerbody component, which has a total mass of 22.63 lbs and a total of 15 available kilowatts for a mass loading of 1.5 lb./KW. The thermal load borne by an individual element inside the actual target surface is therefore considerably less than the heater limit at quiescent conditions.

In an effort to quantify the effects of surface curvature on the hot surface ignition temperature, the flat plate experiment for JP-8 was repeated with the heated cylindrical test article. In was observed during testing that the ceramic fiber wool used as bedding had a tendency to absorb the fuel droplets that were not completely vaporized by the

cylinder. In the event of a drop ignition, the soaked ceramic wool around the edges of the cylinder would also catch fire, and prolong the flame duration. The Phantom® high-speed camera was used to confirm that ignition began on the surface of the cylinder.

Figure 4.18. JP-8 on the cylinder at t = 0s, ignition starts

Figure 4.19. JP-8 on the cylinder at t = 110ms, flame propagates along cylinder length

Figure 4.20. JP-8 on the cylinder at t = 220ms, flame catches on the ceramic wool

Figure 4.21. JP-8 on the cylinder at t = 330ms, flame is prolonged by stabilization on the wool

The burning ceramic compromised the infrared images acquired for the cylinder, but the raw ignition probability data remained viable.

Table 4.3. Ignition Data for JP-8 on the cylindrical test article

Temperature (°C)	Ignited drops	Ignition probability
300	0	0
400	0	0
500	0	0
550	0	0

Table 4.3 cont.

600	0	0
650	0	0
675	0	0
695	3	0.3
700	5	0.5
705	5	0.5
710	6	0.6
715	8	0.8
720	10	1
750	10	1
800	10	1

The coefficients for JP-8 on the cylinder were b_0 = -96.96 and b_1 = 0.1379.

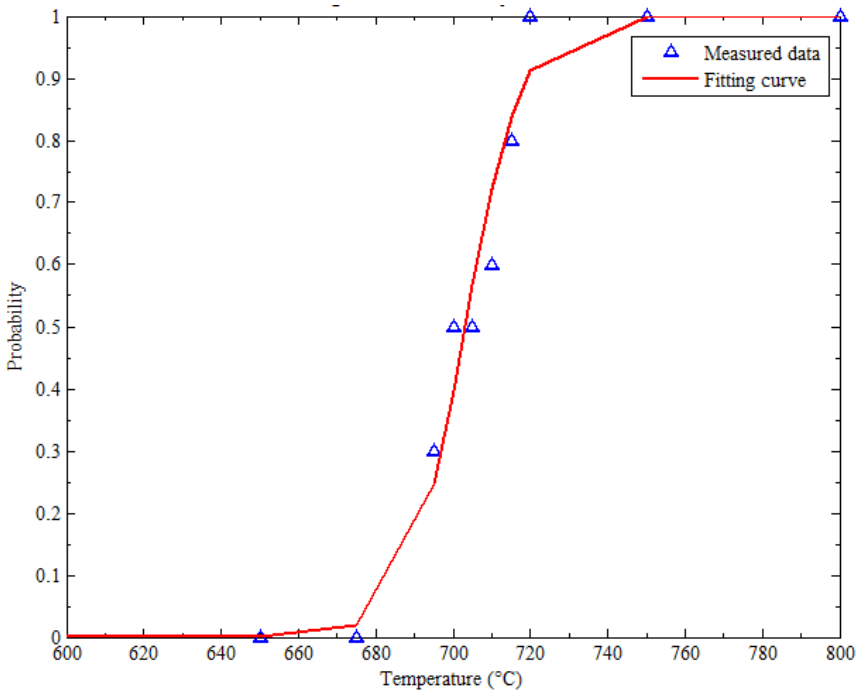

Figure 4.22. Ignition probability data for JP-8 on the cylindrical test article The start of the ignition probability curve in figure 4.22 is shifted over to the right from figure 4.7. The suggestion is that increasingly convex surface curvature has the effect of

raising the minimum hot surface ignition temperature. Considering that convex curvature would have the effect of forcing liquid drops to slide down the sides of any given surface, reducing their residence time near the ignition source, the result is to be expected. In fact, the curvature of the HSIC rig, and the irregular surface geometries of the engine nacelle environment in general, suggests that the barriers to hot surface ignition will only be higher in more realistic applications.

CHAPTER 5. VALIDATING THE RIG

5.1 Initial Test with Propane

Although the design and fabrication of the HSIC test rig preoccupies the majority of this thesis work, the validation of its operation was also undertaken. The work described throughout this brief chapter reflects the HSIC in its baseline configuration. No effort was made to include flow complicating features at this stage of experiments since the first opportunity for data continuity lies in reproducing the results from the *Simple Bare Duct* [5] test article of the Wright-Patterson rig. In addition to flowing air up to rates near .5 lb/s, tests were conducted with propane and JP-8 to confirm the rig's ability to ignite fuel and to begin the process of reproducing then extending the data gathered from the Wright-Patterson test articles.

The first attempted data collection on the HSIC rig was for tests with propane. Propane was selected to confirm the HSIC rig's ability to ignite hydrocarbon fuel based on the spray behavior observed by Graves [15] during hot surface experiments in a vertical duct. As discussed, in the literature review chapter, the genuine kerosene fuels used by Graves tended to atomize poorly, and pool in undesirable regions of the test apparatus. Graves noted that propane, which readily flashes at room temperature, acted as a more flammable surrogate for a well-atomized kerosene spray. When conducting the earliest experiments on the HSIC rig with propane, the intention was to identify then minimize any fundamental shortcomings of the apparatus without immediately exposing

the hardware to the risk of liquid collecting in hazardous quantities inside the test section. The propane tests led to successful ignition for an Inconel surface temperature of 782±3°C at an air velocity of .45±.05 m/s and an air temperature of 104±12°C. Propane was injected through the open end of a .125 inch stainless steel tube with .028 inch wall thickness. The pressure driving injection was roughly 60 psia in accordance with the approximate vapor pressure of propane on the day of testing, October 30, 2015 (12°C). A complete test matrix for the propane tests is provided in the table below.

Table 5.1 Propane Test Matrix, October 30, 2015

Air Mass Flow, kg/s	Surface Temp., °C	Air Temp., °C	Air Velocity, m/s	Ignition?
.016±.002 kg/s	427±3°C	94±12°C	.55±.05 m/s	No
.015±.002 kg/s	482±3°C	80±12°C	.51±.05 m/s	No
.020±.001 kg/s	482±3°C	82±12°C	.69±.04 m/s	No
.012±.002 kg/s	538±3°C	96±12°C	.40±.05 m/s	No
.023±.001 kg/s	538±3°C	84±12°C	.78±.04 m/s	No
.044±.001 kg/s	538±3°C	89±12°C	1.46±.01 m/s	No
.012±.002 kg/s	649±3°C	86±12°C	.41±.05 m/s	No
.022±.001 kg/s	649±3°C	83±12°C	.72±.04 m/s	No
.044±.001 kg/s	649±3°C	86±12°C	1.46±.01 m/s	No
.011±.002 kg/s	704±3°C	100±12°C	.37±.05 m/s	No
.022±.001 kg/s	704±3°C	93±12°C	.72±.04 m/s	No
.043±.001 kg/s	704±3°C	93±12°C	1.44±.01 m/s	No

Table 5.1 cont.

.064±.004 kg/s	704±3°C	118±12°C	2.13±.06 m/s	No
.014±.004 kg/s	760±3°C	122±12°C	.46±.05 m/s	No
.013±.004 kg/s	782±3°C	104±12°C	.45±.05 m/s	Yes
.013±.004 kg/s	782±3°C	84±12°C	.44±.05 m/s	Yes
.013±.004 kg/s	782±3°C	77±12°C	.44±.05 m/s	Yes

The propane flowrate in throughout these tests was approximately 17.3 ml/s, or slightly more than twice the standard flowrate of the Wright-Patterson test article for a duration of 5 seconds. This was permitted since the objective of the propane test was merely to verify ignition, not the reproduction of any particular data point.

5.2 Initial Tests with JP-8

Once ignition was demonstrated with propane, testing shifted toward recreating and augmenting data points taken on the Wright-Patterson test rig. The first fluid chosen for testing was JP-8. This was done to approximate the initial tests performed on the *Simple Bare Duct* test article of the Wright-Patterson experiment with JP-4. JP-8 was used in lieu of JP-4 due to the latter having been phased out of use because of its high volatility and tendency to build static charge at ambient, vaporous conditions. The .125 inch, stainless steel tubing was capped at its open end with a misting nozzle with an 80 degree spray fan and a .016 inch diameter orifice. The nozzle was installed to more precisely control the liquid flowrate to the test section and can be seen beside the glowing Inconel target in the subsequent photograph.

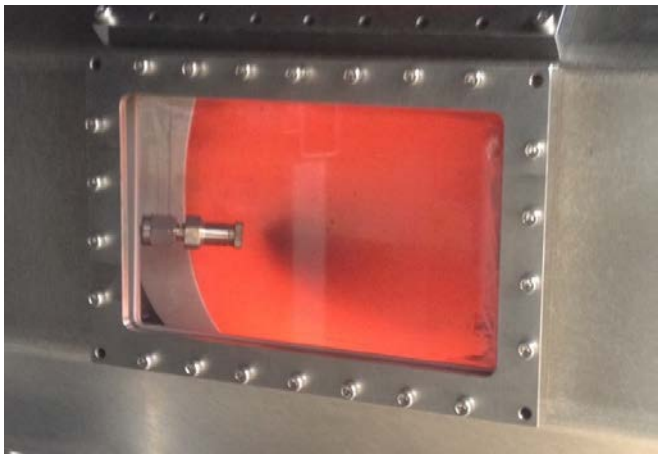

Figure 5.1 Test article heated to 843±3°C with spray nozzle visible

The nozzle produces droplets in the 50 micron range (consistent with the expected droplet size of the Wright-Patterson rig), and was injected at the scaled rate of 1.1 mL/s for a duration of 5 seconds with a driving pressure of 125 psia. Ignition was first achieved at a surface condition of 843±3°C. The air velocity was .35±.01 m/s and the air temperature was 106±15°C. The results are summarized in the table below.

Table 5.2 JP-8 Test Matrix, October 31, 2015

Air Mass Flow, kg/s	Surface Temp., °C	Air Temp., °C	Air Velocity, m/s	Ignition?
.012±.001 kg/s	704±3°C	62±15°C	.41±.03 m/s	No
.013±.001 kg/s	704±3°C	88±15°C	.44±.03 m/s	No
.011±.001 kg/s	732±3°C	81±15°C	.37±.03 m/s	No
.011±.001 kg/s	732±3°C	75±15°C	.37±.03 m/s	No
.023±.001 kg/s	760±3°C	66±15°C	.75±.02 m/s	No
.023±.001 kg/s	760±3°C	68±15°C	.75±.02 m/s	No

Table 5.2 cont.

.011±.001 kg/s	760±3°C	70±15°C	.35±.03 m/s	No
.010±.001 kg/s	760±3°C	68±15°C	.34±.03 m/s	No
.022±.001 kg/s	788±3°C	71±15°C	.75±.02 m/s	No
.041±.001 kg/s	788±3°C	86±15°C	1.38±.02 m/s	No
.041±.001 kg/s	816±3°C	101±15°C	1.38±.02 m/s	No
.064±.001 kg/s	816±3°C	107±15°C	2.13±.02 m/s	No
.011±.001 kg/s	816±3°C	106±15°C	.37±.03 m/s	Yes
.011±.001 kg/s	816±3°C	101±15°C	.37±.03 m/s	Yes
.021±.001 kg/s	816±3°C	96±15°C	.72±.02 m/s	Yes
.021±.001 kg/s	816±3°C	93±15°C	.72±.02 m/s	Yes

The first observed ignition for JP-8 on the baseline HSIC rig configuration is 38°C higher than the first observed ignition temperature for JP-4 [5]. This is consistent with JP-8's implementation as a less flammable version of JP-4.

Figure 5.2 JP-8 ignition for 816±3°C at 106±15°C air temperature and .37±.03 m/s air velocity

It is evident from figure 5.2 that the flame initiated at the Inconel surface very quickly propagates back to the nozzle head. This was a result of the flame speed easily exceeding the air velocity at these low flow rates and the nozzle face being placed too close to the Inconel target (~2mm away). Also gathered from these initial tests was the considerable drift in the measured air temperature. This was reduced notably in later experimental trials as the testing became more streamlined, and the researchers gained greater familiarity with the response of the rig's systems.

To more closely observe the degree to which air temperature and air velocity affect the hot surface ignition temperature, a new flight of data was targeted for the elevated air temperature of 149°C. This serves as the first new addition to the hot surface ignition database established at Wright-Patterson by more closely observing the fundamental effects elevated temperature and velocity have on JP-8 sprayed upstream of the hot surface. Under a modified test arrangement, JP-8 is now sprayed 6.5 inches upstream of the surface leading edge and is directly ported into the wall of the Octagonal Duct. This has the effect of forcing the flame to travel farther to propagate to the nozzle face and allowing the injectant spray more space to atomize and distribute inside the test section. The liquid flowrate and duration is unchanged from the previous experiment, remaining 1.1 mL/s and 5 seconds respectively.

Table 5.3 JP-8 Test Matrix, December 14, 2015

Air Flow, kg/s	Surface Temp., °C	Air Temp., °C	Air Vel., m/s	Ignition?
0.008±.001 kg/s	593±3°C	145±3°C	0.30±.02 m/s	No
0.008±.001 kg/s	621±2°C	148±3°C	0.31±.02 m/s	Yes
0.017±.001 kg/s	617±2°C	150±3°C	0.64±.03 m/s	No
0.008±.001 kg/s	649±3°C	151±3°C	0.30±.02 m/s	Yes
0.017±.001 kg/s	648±3°C	148±3°C	0.67±.03 m/s	No
0.031±.001 kg/s	644±3°C	149±3°C	1.19±.03 m/s	No
0.008±.001 kg/s	667±2°C	153±3°C	0.30±.02 m/s	Yes
0.017±.001 kg/s	667±2°C	148±3°C	0.67±.03 m/s	No
0.032±.001 kg/s	670±2°C	147±3°C	1.23±.03 m/s	No
0.048±.005 kg/s	672±2°C	154±3°C	1.85±.02 m/s	No
0.063±.005 kg/s	667±2°C	155±3°C	2.44±.01 m/s	No
0.008±.001 kg/s	694±3°C	147±3°C	0.30±.02 m/s	Yes
0.016±.001 kg/s	697±3°C	149±3°C	0.60±.03 m/s	Yes
0.033±.001 kg/s	694±3°C	149±3°C	1.28±.03 m/s	No
0.047±.005 kg/s	702±3°C	153±3°C	1.80±.02 m/s	No
0.063±.001 kg/s	698±3°C	150±3°C	2.44±.01 m/s	No
0.008±.001 kg/s	723±2°C	147±3°C	0.30±.02 m/s	Yes
0.017±.001 kg/s	728±3°C	150±3°C	0.67±.03 m/s	Yes
0.031±.001 kg/s	727±3°C	150±3°C	1.20±.03 m/s	No

Table 5.3 cont.

0.048±.005 kg/s	723±3°C	152±3°C	1.85±.02 m/s	No
0.063±.001 kg/s	728±3°C	151±3°C	2.45±.01 m/s	No
0.008±.001 kg/s	757±2°C	147±3°C	0.32±.02 m/s	Yes
0.016±.001 kg/s	762±2°C	148±3°C	0.60±.03 m/s	Yes
0.032±.001 kg/s	757±2°C	148±3°C	1.24±.03 m/s	No
0.048±.005 kg/s	757±2°C	152±3°C	1.84±.02 m/s	No
0.063±.001 kg/s	760±2°C	152±3°C	2.44±.01 m/s	No
0.008±.001 kg/s	788±3°C	147±3°C	0.30±.02 m/s	Yes
0.016±.001 kg/s	786±3°C	149±3°C	0.62±.03 m/s	Yes
0.031±.001 kg/s	792±3°C	150±3°C	1.21±.03 m/s	Yes
0.048±.005 kg/s	787±3°C	150±3°C	1.84±.02 m/s	No
0.063±.005 kg/s	783±3°C	150±3°C	2.44±.01 m/s	No
0.016±.001 kg/s	813±3°C	149±3°C	0.62±.03 m/s	Yes
0.032±.001 kg/s	813±3°C	149±3°C	1.24±.03 m/s	Yes
0.048±.005 kg/s	813±3°C	149±3°C	1.84±.02 m/s	Yes
0.063±.005 kg/s	813±3°C	151±3°C	2.45±.01 m/s	No
0.032±.001 kg/s	839±3°C	148±3°C	1.22±.03 m/s	Yes
0.048±.005 kg/s	843±3°C	151±3°C	1.84±.02 m/s	Yes
0.063±.005 kg/s	845±3°C	151±3°C	2.45±.01 m/s	Yes
0.048±.005 kg/s	874±5°C	148±3°C	1.84±.02 m/s	Yes
0.063±.005 kg/s	867±5°C	151±3°C	2.45±.01 m/s	Yes

The results shared in table 5.3 can be used to draft a plot for the minimum hot surface ignition temperature of JP-8 at 149°C as a function of air velocity.

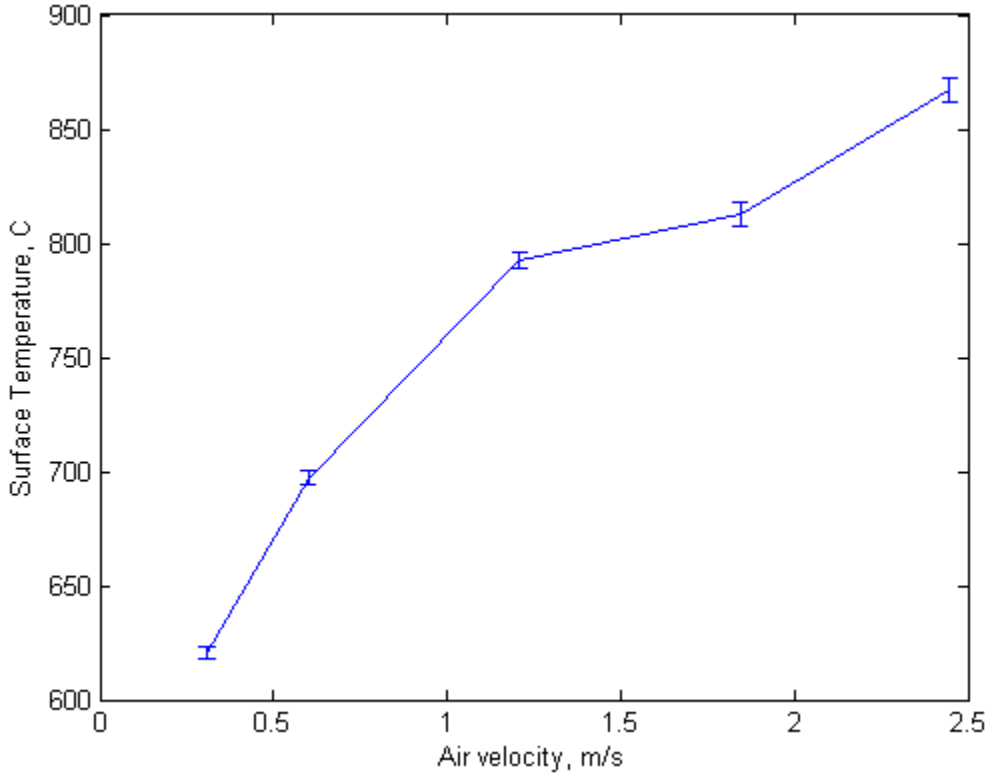

Figure 5.3 Effect of air velocity on MHSIT of JP-8 at 149°C air temperature

A clear positive correlation between increasing air velocity and increasing hot surface ignition temperature is displayed in the figure. This is justified in the bulk air velocity dominating the trajectory and motion of the fuel spray (as described in section 3.8). At higher bypass air velocities, the momentum ratio between the injected fluid and the crossflow skews more heavily in favor of the crossflow, making it more difficult for individual fuel droplets to reach the surface. Furthermore, those fuel drops that do reach the surface are still subject to the bulk motion of the air, and are consequently dragged or pulled from the target hot surface more quickly at the faster flow conditions. A non-

dimensional parameter for hot surface ignition suggested by this behavior is the Damköhler number, *Da*, which is the ratio of the residence time of a given reactant to its chemical reaction time [31]. The residence time can either be estimated numerically or with high speed imagery to track the time scale of droplet contact with the Inconel surface. The chemical rate is more elusive, although an ignition delay time observed during tests on the quiescent flat plat may provide an experimental basis for such a value. The effect of the elevated air temperature is reflected in the contrast between the minimum hot surface ignition temperature for 1 ft/s of air at 149°C and the earlier tests with air at the same velocity and 83°C. For those earlier tests, the JP-8 spray did not ignite until the surface reached 816°C vs 621°C for the later experiments. This is supported by Johnson et al.'s [5] findings that increased air temperature generally lowered the ignition temperature. It is also noted that the probabilistic range observed by Colwell et al. [8] for the quiescent flat plate experiments was not observed at all for the HSIC rig. It is theorized that the more aggressive flow environment inside of the HSIC, and similar rigs raises the overall barrier to ignition to the point that the ignition threshold is more definitively set. Considerable work lies ahead to more fully explore hot surface ignition phenomena, but these early results are encouraging that thorough experimentation with the HSIC test rig may yield some insight.

CHAPTER 6. CONCLUSIONS AND FUTURE WORK

The work reported in this thesis involved the design, construction, and preliminary experimentation for improved understanding of hot surface ignition in an environment representative of an aircraft engine. Future work will systematically change the air flow path through the rig test section to resemble engine nacelle environments and understand the effects of unique features. Previous researchers reported that fuel leak flow rates had little to no effect on the minimum hot surface ignition temperature [5]. The broader range of air flowrates designed for the HSIC rig will allow an investigation of the lean and rich flammability limits associated with a combination of the fuel leak rate and the airflow rate to describe an envelope of safe operating conditions.

Future work will involve cluttered engine compartments and complexities associated with the confluence of multiple boundary layers, wakes and pressure gradients. The bulk fluid velocity, fluid temperature, surface roughness, surface temperature, leak type (spray or stream), and state of fuel vaporization will all affect ignition. The number of potential test variables is in fact, so large that future work will have to involve systematic non-dimensional analysis and computational combustion studies to define the most relevant experimental conditions. The experimental apparatus described in this thesis has laid the foundation for the design of future studies aimed at continuous improvements in the fire safety of modern aircraft engines.

LIST OF REFERENCES

LIST OF REFERENCES

[1] L. Strawhorn, “Motor Vehicles,” in Fire Protection Handbook, Quincy, MA: National Fire Protection Association, 2003, Section 14, Chapter 1.

[2] National Transportation Safety Board, “Aircraft Accident Report: In-flight Breakup Over the Atlantic Ocean Trans World Airlines Flight 800,” August 23, 2000.

[3] ASTB Final Investigation Report, AO-2010-089, “In Flight Uncontained Engine Failure Overhead Batam Island, Indonesia 4 November 2010,” VH-OQA Airbus A380-842

[4] Drew, K. and Clark, N., “3 Airlines Halt A380 Flights Over Engine Explosion,” *The New York Times*, The New York Times, 4 Nov. 2010. Web 3 Jul. 2014

[5] Johnson, A.M., Roth, A.J., and Moussa, N. A., “Hot Surface Ignition Tests of Aircraft Fluids,” Air Force Wright Aeronautical Laboratories, AFWAL-TR-88-2101, Wright Patterson Air Force Base, OH, 1989

[6] Khamliche, Y., “Flammable Fluid Hot Surface Ignition,” PowerPoint Presentation given March 31, 3014 at Rolls Royce Corporation at 450 S Meridian St., Indianapolis, IN

[7] Davis, S., Kelly, S., and Somandepalli, V., “Hot Surface Ignition of Performance Fuels,” *Fire Technology*, Vol. 46, 2010, pp.363-374.

[8] Colwell, J. D., and Reza, A., “Hot Surface Ignition of Automotive and Aviation Fluids,” *Fire Technology*, Vol. 41, 2005, pp.105–123.

[9] Davis, S., and Somandepalli, V., “Hot Surface Ignition of Ethanol, Gasoline, E-85, Diesel, and E-Diesel,” *AIChE, 2007 Spring Meeting & 3rd Global Congress on Process Safety*, 27th April 2007, Houston, TX.

[10] Kuchta, J. M., “Summary of Ignition Properties of Jet Fuels and Other Aircraft Combustible Fluids,” Air Force Aero Propulsion Laboratories, AFAPL-TR-75-70, Wright Patterson Air Force Base, OH, 1975

[11] ASTM Standard E659, 2014, “Standard Test Method for Autoignition Temperature of Liquid Chemicals,” ASTM International, West Conshohocken, PA, DOI: 10.1520/E0659, www.astm.org

[12]Gottried B.S., Lee, C. J., and Bell, K.J., "The Leidnenfrost Phenomenon: Film Boiling of Liquid Droplets on a Flat Plate," *International Journal of Heat and Mass Transfer*, Vol.9, 1966, pp. 1167-1187

[13] Shaw, A., Epling, W., McKenna, C., and Weckman, B., "Evaluation of the Ignition of Diesel Fuels on Hot Surfaces," *Fire Technology*, Vol. 46, 2010, pp.407-423

[14] Myronuk, D.J., "Dynamic, Hot Surface Ignition of Aircraft Fuels and Hydraulic Fluids," Air Force Wright Aeronautical Laboratories, AFWAL-TR-79-2095, Wright Paterson Air Force Base, OH, 1980

[15] Graves, C.B., "Spray Ignition by a Hot Surface," MS Thesis, Purdue University, West Lafayette IN, 1984

[16] Ingerson, D., "Engine Nacelle Halon Replacement," FAA WJ Hughes Technical Center, Fire Safety Section AAR-422, Atlantic City International Airport, NJ, June 2002

[17] Smits, A. J., *A Physical Introduction to Fluid Mechanics*, John Wiley, New York, NY, 2000

[18] Bergman, T. L., Lavine, A. S., Incropera, F. P., and Dewitt, D. P., *Fundamentals of Heat and Mass Transfer 7th Edition*, John Wiley & Sons, Hoboken, NJ, 2011

[19] Greene, G. A., Finfrock, C. C., and Irvine Jr., T. F., "Total Hemispherical Emissivity of Oxidized Inconel 718 in the Temperature Range 300-1000°C," *Experimental Thermal and Fluid Science*, Vol. 22, Issues 3-4, 2000, pp.145-153

[20] Budynas, R. G., and Nisbett, J. K., *Shigley's Mechanical Engineering Design 9th Edition*, McGraw-Hill, New York, NY, 2010

[21] Special Metals, "Inconel 718 Alloy," Publication Number SMC-045, Sept. 2007

[22] Professional Plastics, "Ceramic-Comparative Material Data Sheets," Retrieved Mar. 2015

[23] Sutton, G. P., and Biblarz, O., *Rocket Propulsion Elements 8th Edition*, John Wiley & Sons, Hoboken, NJ, 2010

[24] Kolodize Jr., P. A., and Winkle, M. V., "Discharge Coefficients Through Perforated Plates," *American Institute of Chemical Engineers Journal*, Vol. 3, No. 3, Sept. 1957, pp. 303-312

[25] Miracrys, "Sapphire," *Miracrys*, 2007. [Online] Available: http://www.miracrys.com/CCinit.php?id=productsa [Accessed: Mar. 2015]

[26] Electron Microscopy Sciences, “Technical Data Sheets-GE 124 Quartz,” *Electron Microscopy Sciences*, 2015. [Online] Available: https://www.emsdiasum.com/microscopy/technical/datasheet/GE124.aspx [Accessed: Mar. 2015]

[27] GrafTech, “Grafoil® Engineering Design Manual 2nd Edition,” 2002

[28] Guildenbecher, D. R., “Droplet Physics,” School of Mechanical Engineering, Purdue University, West Lafayette, IN, Jan. 18, 2010

[29] O’Keefe Controls Co., “Choked Flow of Gases,” *O’Keefe Controls Co.*, Trumbull, CO, 2003

[30] Pope, S.B., Turbulent Flows. Cambridge: Cambridge University Press, 2000. Print

[31] Turns, S. R., *An Introduction to Combustion: Concepts and Applications 3rd Edition*, McGraw-Hill, New York, NY, 2012

[32] Bennett, J. M., and Ballal, D.R., “Ignition of Combustible Fluids by Heated Surfaces,” AIAA, 41st Aerospace Sciences Meeting and Exhibit, 6-9 January 2003, Reno, NV

[33] 4. Ramos, J.I., “Ignition of Confined Gaseous Mixtures by Hot Surfaces and Hot Wires,” AIAA, 21st Aerospace Sciences Meeting, 10-13 January 1983, Reno, NV

[34] Graves, C.B., Tang, Y.L., and Skifstad, J.G., “Ignition of a Fuel Spray by a Hot Surface,” AIAA 21st Joint Propulsion Conference, 8-10 July 1985, Monterey, CA.

[35] Parts, L., and Olt, R.G., “High Temperature (1649ºC, 3000ºF) Surface Ignition Test Apparatus for Fluids,” Air Force Wright Aeronautical Laboratories, AFWAL-TR-82-2110, Wright Paterson Air Force Base, OH, 1983

[36] Kumar, R.K., “Ignition of Hydrogen-Oxygen-Diluent Mixtures Adjacent to a Hot, Nonreactive Surface,” *Combustion and Flame*, Vol. 75, 1989, pp.197-215.

[37] Geyer, W.H., and Moussa, N.A., “Hot Surface Ignition and Fire Suppression Tests in an Aircraft Engine Bay,” 27th Joint Propulsion Conference, AIAA, Sacramento, CA, 1991

[38] Dehong, K., Eckhoff, R.K., and Alfert, F., “Auto-Ignition of CH4/air, C3H8/air, and CH4/CO2/air using a 1 L Ignition Bomb,” Journal of Hazardous Materials, Vol. 40, 1995, pp. 69-84

[39] Menon, S.K., Boettcher, P.A., Ventura, B., Sheperd, J.E., and Blanquart, G., “Modeling Hot-Surface Ignition of Hydrocarbon-Air Mixtures,” 7th US National Technical Meeting of the Combustion Institute Hosted by the Georgia Institute of Technology, Atlanta, GA March 20-23, 2011

[40] Reid, I.A.B., Robinson, C., and Smith, D.B., "Spontaneous Ignition of Methane: Measurement and Chemical Model," Twentieth Symposium (International) on Combustion/The Combustion Institute, 1984, pp. 1833-184

[41] Sano, T., and Yamashita, A., "Flame Ignition of Premixed Methane Air Mixtures on a High-Temperature Flat Plate," JSME International Journal, Series B, Vol. 37, No. 1, 1994

[42] Skifstad, J.G., Lefebvre, A.H., and Murthy, S.N.B., "Fuel Spray Ignition by Hot Surfaces and Aircraft Fire Stabilization," Air Force Office of Scientific Research, AFOSR-TR-86-0856, Purdue University-West Lafayette, IN, October 1986

[43] Hamins, A., and Borthwick, P. "Suppression of Ignition over a Heated Metal Surface," Combustion and Flame, Vol. 112, 1998, pp.161-170

[44] Law, C.K. and Law, H.K., "Thermal-ignition analysis in boundary-layer flows," *J. Fluid Mech.*, Vol. 92, No. 1, 1979, pp.97-108

[45] Kelly, M.S., "Probe System for Composition Measurements in Fuel Spray/Air Mixtures," MS Thesis, Purdue University, West Lafayette IN, 1983

[46] Tang, Y.L., "Surface Ignition of a Fuel Spray/Air Mixture in a Heated Cylindrical Duct," PhD Thesis, Purdue University, West Lafayette IN, 1987

[47] Kapaku, R. K., "Quantitative Imaging of Radiation Intensity from a Turbulent Sooting Flame," MS Thesis, Purdue University, West Lafayette IN, 2014

[48] Lefebvre, A.H., and Ballal, D.R., *Gas Turbine Combustion: Alternative Fuels and Emissions 3rd Edition*, CRC Press, Boca Rotan, NY, 2010

[49] Law, C.K., and Chung, S.H., "An Ignition Criterion for Droplets in Sprays," *Combustion Science and Technology*, Vol.22, 1980, pp.17-26

[50] Clodfelter, R.G., "Fire Safety in Military Aircraft Fuel Systems," *Aviation Fuels with Improved Fire Safety: A Proceedings*, 1997, pp.21-30

[51] Dexter, R., "Fire Modeling With the Fire Prediction Model (FPM): Application for Survivability Discipline," *Aircraft Survivability*, Spring 2008, pg. 14-17.

[52] Federal Aviation Administration AC No.33.17-1A, 3rd August, 2009

[53] Mizomoto, M., Ikai, S., and Morita, A., "Evaporation and Ignition of a Fuel Droplet on a Hot Surface (Part 4, Model of Evaporation and Ignition)," *Combustion and Flame*, Vol. 51, 1983, pp. 95-104

[54] Tamura, Z., and Tanasawa, Y., “Evaporation and Combustion of a Drop Contacting with a Hot Surface,” *Symposium (International) on Combustion*, Vol. 7, Issue 1, 1958, pp. 509-522

APPENDICES

APPENDICES

A.1 MATLAB Script for Droplet Trajectory Analysis

```
clc
clear all
close all

g = 9.81;       % [m/s]

%% Read in JP-8 Properties from Excel Sheet
data = xlsread('jp8props');
cond = data(1:150,:);
% Temperature, Pressure [psia], Density [lb/ft^3], Specific Heat
% [btu/lb-degF], Enthalpy [btu/lbm], Sound Speed [ft/s], Thermal
% Conductivity [btu/ft-hr-degF], Viscosity [lb/ft-hr]

Tj = 100;           % [deg F]
dj = 2.3*10^-4;     % [m]
rhoj = cond(cond(:,1)==Tj,3)*(1/2.20462)*(3.28084)^3;
% [lb/ft^3] --> [kg/m^3]
muj = cond(cond(:,1)==Tj,8)*(1/2.20462)*(3.28084)*(1/3600);
% [lb/ft-hr] --> [kg/m-s]
surften = 0.022;    % [N/m]

%% Set Crossflow Conditions
Tair = 70;                                          % [deg F]
Pair = 14.7;                                        % [psi]
Tg = (5/9)*(Tair-32)+273;                           % [deg F] --> [deg
K]
Pg = (Pair)*(101.325/14.7);                         % [psi] --> [kPa]
Vg = 24;                                             % [m/s]
rhog = refpropm('D','T',Tg,'P',Pg,'air.ppf');       % [kg/m^3]
mug = refpropm('V','T',Tg,'P',Pg,'air.ppf');        % [kg/m-s]

%% Calculate NonDimensional Parameters
We = rhog*(Vg^2)*(dj)/surften;          % Aerodynamic Weber Number
Oh = muj/sqrt(rhoj*dj*surften);         % Ohnesorge Number

%% Droplet Trajectory Model
a = 1;

for ang=0:10:80

j = 1;

for Vj = 30:.1:50

q(j) = rhoj*Vj^2/rhog/Vg^2;             % Momentum Ratio

%% Determine Breakup Point of Jet - Ragucci Correlation
x_jb_d(j) = 4.17*(q(j)^-0.096)*(We^0.383);
y_jb_d(j) = 3.85*(q(j)^0.387)*(We^0.126);
```

```
t_break(j) = 64*We^-0.58*q(j)^-0.34;

%% Initial Conditions
Vx(1) = Vj*sind(ang);       % Velocity - x-component - [m/s]
Vy(1) = Vj*cosd(ang);       % Velocity - y-component - [m/s]
x(1) = 0;                   % Position - x-axis - [m]
y(1) = 0;                   % Position - y-axis - [m]
time(1) = 0;                % Time - [s]

%% Iterate through Trajectory Until x/d = 100 or "Far Downstream"

i = 2;  % Count for spatial positions
do = 5e-5;      % estimated average drop size
dt =   0.000001;   % time step for calculation
Cd = 0.91;

while y(i-1)/do < 915

Vy(i) = Vy(i-1) - dt*((3/4)*(rhog/rhoj)*(Cd/do)*Vy(i-1)*...
        sqrt((Vg-Vx(i-1))^2+Vy(i-1)^2));
Vx(i) = Vx(i-1) + dt*(-3/4*(rhog/rhoj)*(Cd/do)*(Vx(i-1)-Vg)*...
        sqrt((Vg-Vx(i-1))^2+Vy(i-1)^2));

x(i) = Vx(i)*dt+x(i-1);
y(i) = Vy(i)*dt+y(i-1);

Re(i) = rhog*do*(sqrt((Vg-Vx(i-1))^2+Vy(i-1)^2))/mug;

time(i) = time(i-1) + dt;

x_d_traj(i,j) = x(i)/do;
y_d_traj(i,j) = y(i)/do;

i = i + 1;

end

% %% Penetration Timescale
% pendiff(:,j) = abs(y_d_traj(:,j) - 0.9*y_d_traj(i-1,j));
% penindex(j) = find(pendiff(:,j) == min(pendiff(:,j)));
% t_pen(j) = time(penindex(j))*1000;
%
%
% %% Breakup Timescale
% xdiff(:,j) = abs(x_jb_d(j)-x_d_traj(:,j));
% ydiff(:,j) = abs(y_jb_d(j)-y_d_traj(:,j));
% xindex(j) = find(xdiff(:,j) == min(xdiff(:,j)));
% yindex(j) = find(ydiff(:,j) == min(ydiff(:,j)));
%
% t_jb_x(j) = time(xindex(j))*1000; % <-- choose this time value
because
                        %droplet model tends to underpredict the
trajectory
```

```
% t_jb_y(j) = time(yindex(j))*1000;


Vjet(j) = Vj;
j = j + 1;
end



figure(a)
for k = 1:50:j-1
plot(x_d_traj(:,k),y_d_traj(:,k),'.')
hold on
end
xlabel('Distance Traveled in Direction of Airflow, x/d')
ylabel('Penetration Depth, y/d')

a = a + 1;
end


% Hz200 = ones(1,length(Vjet))*(1/2200)*1000;
% % Hz400 = ones(1,length(Vjet))*(1/400)*1000;
% % Hz600 = ones(1,length(Vjet))*(1/600)*1000;
%
% figure
% plot(Vjet,t_pen,'r')
% hold on
% plot(Vjet,t_jb_x,'g')
% % hold on
% % plot(Vjet,t_break,':')
% % hold on
% % plot(Vjet,Hz200,'--')
% % hold on
% % plot(Vjet,Hz400,'-.')
% % hold on
% % plot(Vjet,Hz600,'--')
% xlabel('Jet Velocity [m/s]')
% ylabel('Time [ms]')
% title('Timescale Comparison')
% legend('Penetration','Column Breakup','Ragucci Correlation'...
%     ,'Crossflow Frequency - 2200 Hz','Location','East')


% %% Wu Correlation
% y_d_Wu = 1.37*sqrt(q*(x_d_traj));
% % plot trajectory and Wu correlations...
% plot(x_d_traj,y_d_traj,'r')
% hold on
% plot(x_d_traj,y_d_Wu,'g')
%
% %% Penetration Timescale
% pendiff = abs(y_d_traj - 0.9*y_d_traj(end));
```

```
% penindex = find(pendiff == min(pendiff));
% t_pen = time(penindex)*1000;
%
%
% t_ff = time(end)*1000;
% t_break = 64*We^-0.58*q^-0.34;

% %% Momentum Ratio Comparison - Hot vs. Cold Fuel
%
% i = 1;
%
% mdotj = linspace(25,65,50)'*0.0001259978805556;  % [pph] --> [kg/s]
% rhoj_c = 860;                                    % [kg/m^3]
% for T = 100:10:600 % [deg F]
%
% rhoj_h(i,:) = cond(cond(:,1)==T,3)*(1/2.20462)*(3.28084)^3;
% % [lb/ft^3] --> [kg/m^3]
% Vj_h(i,:) = mdotj/rhoj_h(i,:)/(pi*dj^2);          % [m/s]
% Vj_c(i,:) = mdotj/rhoj_c/(pi*dj^2);              % [m/s]
% Tj(i,:) = T;
% i = i + 1;
%
% end
%
% rhoj_h = repmat(rhoj_h,1,50);
%
% q_c = (rhoj_c*Vj_c.^2)/(rhog*Vg^2);
% q_h = (rhoj_h.*Vj_h.^2)/(rhog*Vg^2);
% q_ratio = q_c./q_h;
%
% [row,col] = size(q_ratio);
% figure
%
% plot(Tj,q_ratio)
```

A.2 Suggested Flow Metering Tables

Table A.2-1 Low Flow Rate Regime for Sonic Venturi with d_t=.124”

Mass Flow	Air Temperature	Upstream Pressure	Air Density	Test Section Velocity
.02596 lb/s	600°F	133 psia	.038 lb/ft^3	2 ft/s
.05192 lb/s	600°F	266 psia	.038 lb/ft^3	4 ft/s
.07660 lb/s	600°F	393 psia	.038 lb/ft^3	6 ft/s
.10384 lb/s	600°F	533 psia	.038 lb/ft^3	8 ft/s
.11420 lb/s	600°F	587 psia	.038 lb/ft^3	9 ft/s
.03552 lb/s	300°F	155 psia	.052 lb/ft^3	2 ft/s
.07105 lb/s	300°F	309 psia	.052 lb/ft^3	4 ft/s
.10480 lb/s	300°F	456 psia	.052 lb/ft^3	6 ft/s
.04620 lb/s	120°F	176 psia	.069 lb/ft^3	2 ft/s

Table A.2-1 cont.

.09240 lb/s	120°F	351 psia	.069 lb/ft^3	4 ft/s
.13830 lb/s	120°F	525 psia	.069 lb/ft^3	6 ft/s
.05120 lb/s	70°F	186 psia	.075 lb/ ft^3	2 ft/s
.10240 lb/s	70°F	372 psia	.075 lb/ ft^3	4 ft/s
.15110 lb/s	70°F	549 psia	.075 lb/ ft^3	6 ft/s

Table A.2-2 Middle Flow Rate Regime for Sonic Venturi with d_t=.300”

Mass Flow	Air Temperature	Upstream Pressure	Air Density	Test Section Velocity
0.1148 lb/s	600°F	100 psia	.038 lb/ft^3	9 ft/s
0.2284 lb/s	600°F	199 psia	.038 lb/ft^3	18 ft/s

Table A.2-2 cont.

0.3426 lb/s	600°F	298 psia	.038 lb/ft^3	27 ft/s
0.4568 lb/s	600°F	398 psia	.038 lb/ft^3	36 ft/s
0.5710 lb/s	600°F	497 psia	.038 lb/ft^3	45 ft/s
0.6344 lb/s	600°F	553 psia	.038 lb/ft^3	50 ft/s
0.1389 lb/s	300°F	102 psia	.052 lb/ft^3	8 ft/s
0.2778 lb/s	300°F	205 psia	.052 lb/ft^3	16 ft/s
0.4167 lb/s	300°F	307 psia	.052 lb/ft^3	24 ft/s
0.5556 lb/s	300°F	410 psia	.052 lb/ft^3	32 ft/s
0.6945 lb/s	300°F	512 psia	.052 lb/ft^3	40 ft/s
0.1383 lb/s	120°F	89 psia	.069 lb/ ft^3	6 ft/s
0.2766 lb/s	120°F	178 psia	.069 lb/ ft^3	12 ft/s
0.4149 lb/s	120°F	267 psia	.069 lb/ ft^3	18 ft/s
0.5532 lb/s	120°F	356 psia	.069 lb/ ft^3	24 ft/s
0.6915 lb/s	120°F	446 psia	.069 lb/ ft^3	30 ft/s
0.8298 lb/s	120°F	535 psia	.069 lb/ ft^3	36 ft/s
0.4533 lb/s	70°F	279 psia	.075 lb/ft^3	18 ft/s
0.6044 lb/s	70°F	372 psia	.075 lb/ft^3	24 ft/s
0.7555 lb/s	70°F	465 psia	.075 lb/ft^3	30 ft/s
0.9066 lb/s	70°F	558 psia	.075 lb/ft^3	36 ft/s

Table A.2-3 High Flow Rate Regime for Sonic Venturi with d_t=.706”

Mass Flow	Air Temperature	Upstream Pressure	Air Density	Test Section Velocity
0.6344 lb/s	600°F	100 psia	.038 lb/ft^3	50 ft/s
0.7614 lb/s	600°F	120 psia	.038 lb/ft^3	60 ft/s
0.8884 lb/s	600°F	140 psia	.038 lb/ft^3	70 ft/s
1.0154 lb/s	600°F	160 psia	.038 lb/ft^3	80 ft/s
1.1424 lb/s	600°F	180 psia	.038 lb/ft^3	90 ft/s
1.2694 lb/s	600°F	200 psia	.038 lb/ft^3	100 ft/s
0.6945 lb/s	300°F	93 psia	.052 lb/ft^3	40ft/s
0.8681 lb/s	300°F	116 psia	.052 lb/ft^3	50 ft/s
1.0417 lb/s	300°F	139 psia	.052 lb/ft^3	60 ft/s
1.2153 lb/s	300°F	162 psia	.052 lb/ft^3	70 ft/s
1.3889 lb/s	300°F	185 psia	.052 lb/ft^3	80 ft/s
0.8759 lb/s	120°F	102 psia	.069 lb/ ft^3	38 ft/s
1.0949 lb/s	120°F	128 psia	.069 lb/ ft^3	48 ft/s
1.3139 lb/s	120°F	153 psia	.069 lb/ ft^3	57 ft/s
1.5329 lb/s	120°F	179 psia	.069 lb/ ft^3	67 ft/s
1.7519 lb/s	120°F	204 psia	.069 lb/ ft^3	76 ft/s
0.9066 lb/s	70°F	101 psia	.069 lb/ ft^3	36 ft/s
1.2088 lb/s	70°F	135 psia	.075 lb/ft^3	48 ft/s
1.3599 lb/s	70°F	152 psia	.075 lb/ft^3	54 ft/s

Table A.2-3 cont.

1.6621 lb/s	70°F	185 psia	.075 lb/ft^3	66 ft/s
1.9643 lb/s	70°F	219 psia	.075 lb/ft^3	78 ft/s

A.3 Plumbing and Instrumentation Diagram

LEGEND

- VALVE (NORMALLY OPEN)
- VALVE (NORMALLY CLOSED)
- BALL VALVE (NORMALLY OPEN)
- BALL VALVE (NORMALLY CLOSED)
- GLOBE VALVE (NORMALLY CLOSED)
- BUTTERFLY VALVE
- NEEDLE VALVE
- CV NEEDLE VALVE (COMPUTER LOADED)
- THREE WAY VALVE
- CHECK VALVE
- RELIEF VALVE
- MANUAL VALVE OPERATOR
- SOLENOID VALVE OPERATOR
- PNEUMATIC VALVE OPERATOR
- CAVITATING VENTURI
- FLOW MEASUREMENT DEVICE
- PRESSURE REGULATOR
- PRESSURE REGULATOR (HAND LOADED)
- PRESSURE REGULATOR (COMPUTER LOADED)
- QUICK DISCONNECT
- PUMP
- LPG PUMP
- Y STRAINER
- TURBINE FLOWMETER
- FILTER
- ORIFICE PLATE
- T THERMOCOUPLE
- PT PRESSURE TRANSDUCER
- PDT DIFFERENTIAL PRESSURE TRANSDUCER
- PHF HIGH FREQUENCY PRESSURE TRANSDUCER
- PG PRESSURE GAUGE
- IP ION PROBE

*Does not appear in Hsurf P&ID

Component Drawing
Plumbing
Instrumentation
Control

Jet Fuel System Ref (PID049)*

100 psi N2
PG-1
PG-2
Filter
PV-N2-02
MV-N2-05
MV-N2-04
MV-N2-06
NITROGEN TANKS
VOL = 253 FT^3
P = 6000 PSIA
To Liquid N2 Vapor
MV-N2-03
PG-5
MV-N2-09
MV-N2-11
MR-N2-04
PG-4
RV-N2-04
1500 psi Pilot N2
PG-3
RV-N2-03
100 psi Pilot N2 - Source A
MV-N2-10
MR-N2-03
PT-N2-000
PG-6
100 psi N2 - Source B
CR-N2-001
Ace Injector Purge
PV-N2-001
RR-N2-001
MR-GT-00
Fuel System Purge
PG-7
MV-GT-01
MR-GT-01
100 psi N2 - Source B
PG-8
MR-GT-02
HSIC Purge
ACE Purge
Siemens DCS Purge
PG-9
MV-GT-03
MR-GT-03
PG

CR-SA-001
TC-SA-001
PT-SA-001
RR-SA-001
100 psi N2 - Source B
PG
MV-AP-02
MV-ROOF
AIR-ISO-GT
1500 psi N2
PT-MA-000
AIR
VOL = 2000 FT^3
P = 2200 PSIA
RR-AS-02
100 psi N2 - Source A
CR-MA-001
PT-MA-001
TC-MA-001
PT-MA-002
Thin Orifice Plate
PT-MA-003
Air Heater
EV-NG-02
MV-NG-03
Natural Gas Supply
0.052
0.035
0.024
0.019
SV-SA-004
SV-SA-005
SV-SA-006
SV-SA-007
PT-SA-002
TC-SA-002
xxx
Secondary Air Supply
TC-EH-01
TC-EH-02
TC-EH-03
Electric Heat Exchanger
Primary Air Supply
.58 in
TC-AS-04
PT-AS-04
30 psi N2 from 100 psi N2 - Source B
PV-MA-001
PV-AIR-01-IND
From HSIC Purge
100 psi N2 - Source B
HSIC-PV-FU-01
PT-HSIC-02
Test Fluid
TC-HSIC-Surf-02
TC-HSIC-Surf-01
TC-HSIC-Surf-07
TC-HSIC-Surf-06
TC-HSIC-Surf-03
TC-HSIC-Surf-08
TC-HSIC-Surf-09
TC-HSIC-Surf-04
TC-HSIC-Surf-05
TC-HSIC-Surf-10
TC-HSIC-AIR-01
PT-HSIC-01
HSIC-PV-FU-02
To HSurf Injector
IR Camera
100 psi N2 - Source B
HSIC-PV-N2-01
From HSIC Purge
PT-HSIC-03
TC-HSIC-AIR-02
PT-HSIC-04
TC-HSIC-AIR-03
PT-HSIC-05
TC-HSIC-AIR-04
PT-HSIC-06
TC-HSIC-AIR-05

A.4 Engineering Drawings

151

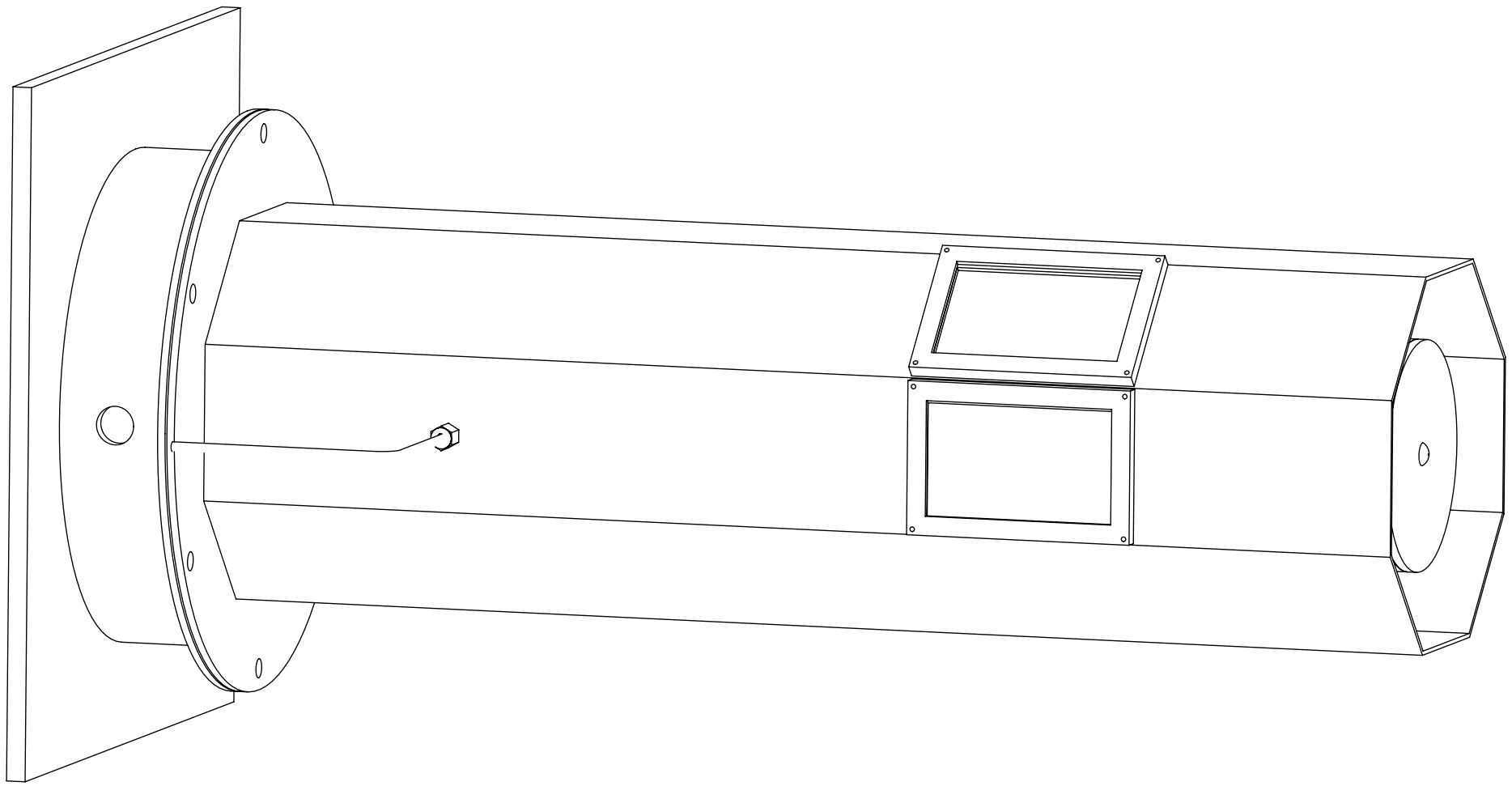

1. Part to be free of oil, grease, burrs, contaminants and surface imperfections

TOLERANCES UNLESS OTHERWISE NOTED X.X ± 0.015 Angles ± 0.5° X.XX ± .010 X/X ± 1/64 X.XXX ± 0.005 CORNER RADIUS OR CHAMFER 0.005 TO 0.015 UNITS ARE INCHES [MM]	125	PURDUE PROPULSION	QUANTITY: / REVISION A Part Name: Isometric Drawn By: MATERIAL: DATE: 8/22/2014 / 1 OF 1

152

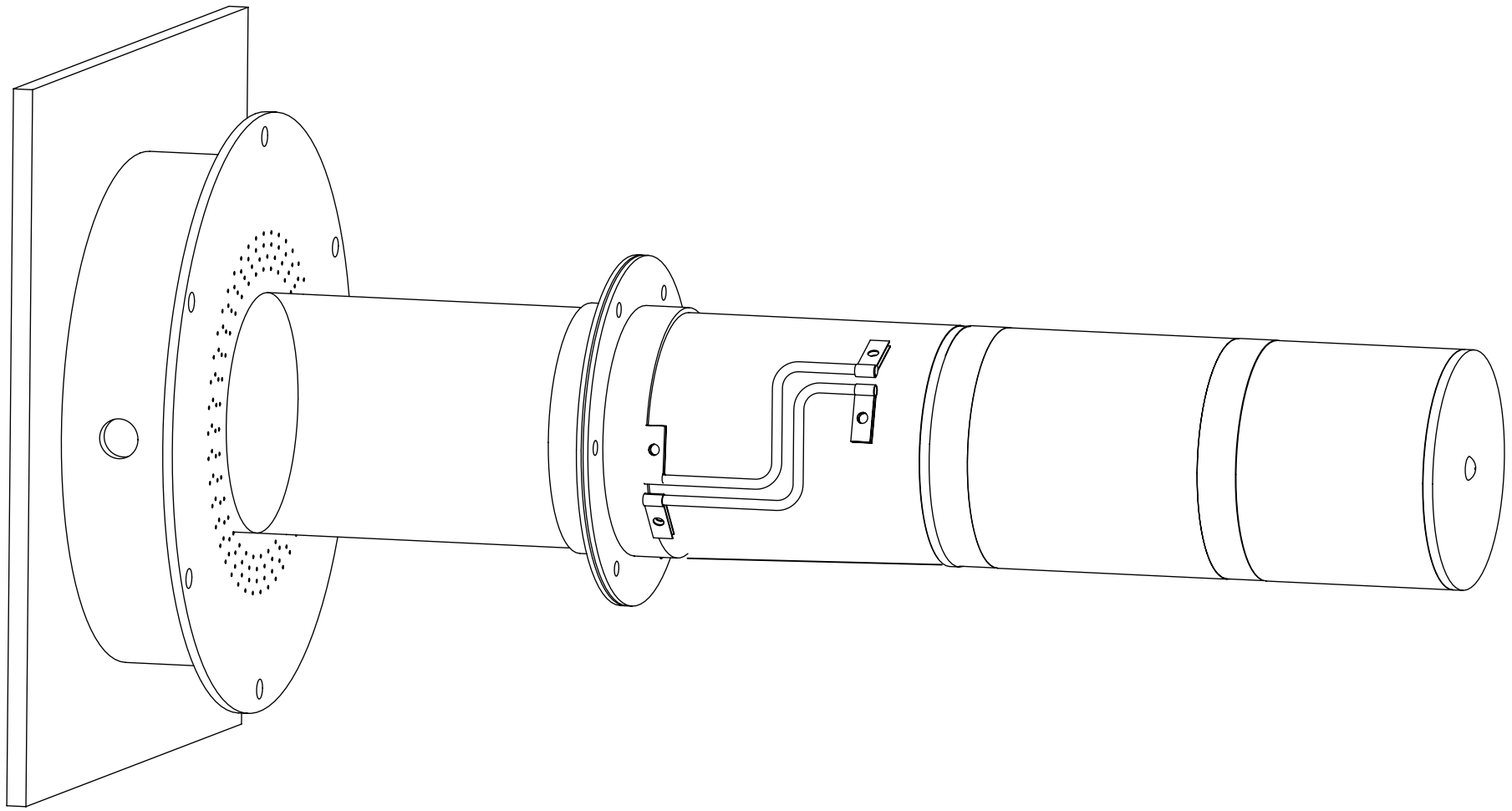

1. Part to be free of oil, grease, burrs, contaminants and surface imperfections

TOLERANCES UNLESS OTHERWISE NOTED X.X ± 0.015 Angles ± 0.5° X.XX ± .010 X/X ± 1/64 X.XXX ± 0.005 CORNER RADIUS OR CHAMFER 0.005 TO 0.015 UNITS ARE INCHES [MM]	125	PURDUE PROPULSION	QUANTITY: / REVISION A Part Name: Isometric without Duct Drawn By: MATERIAL: DATE: 8/22/2014 / 1 OF 1

153

PC NO	PART NAME	QTY
1	BASE	1
2	PLENUM VESSEL	1
3	ORIFICE PLATE	1
4	CENTER CYLINDER	1
5	CANTILEVER BASE PLATE	1
6	CERAMIC END	2
7	HOT CENTERBODY	1
8	END PIECE ASSEMBLY	1
10	CERAMIC SLEEVE	1
11	CANTILEVERED SUPPORT	1
12	BOLT	1
14	WINDOW FLANGE	2
15	WINDOW	2

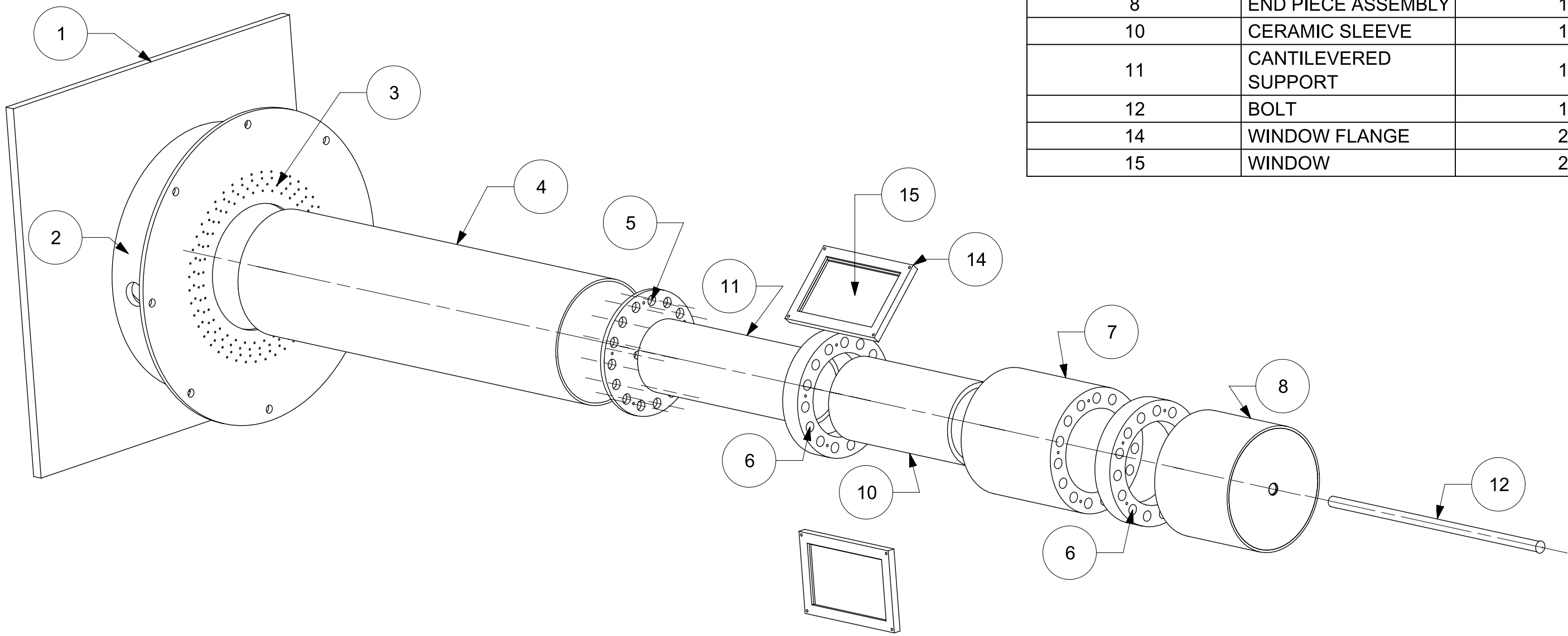

TOLERANCES UNLESS OTHERWISE NOTED
X.X ±0.015 Angles ±0.5°
X.XX ±.010 X/X ±1/64
X.XXX ±0.005
CORNER RADIUS OR CHAMFER 0.005 TO 0.015
UNITS ARE INCHES [MM]

125

PURDUE PROPULSION

QUANTITY:	REVISION A
Part Name: Exploded_View_Without Duct	
Drawn By:	
MATERIAL:	
DATE: 8/22/2014	1 OF 1

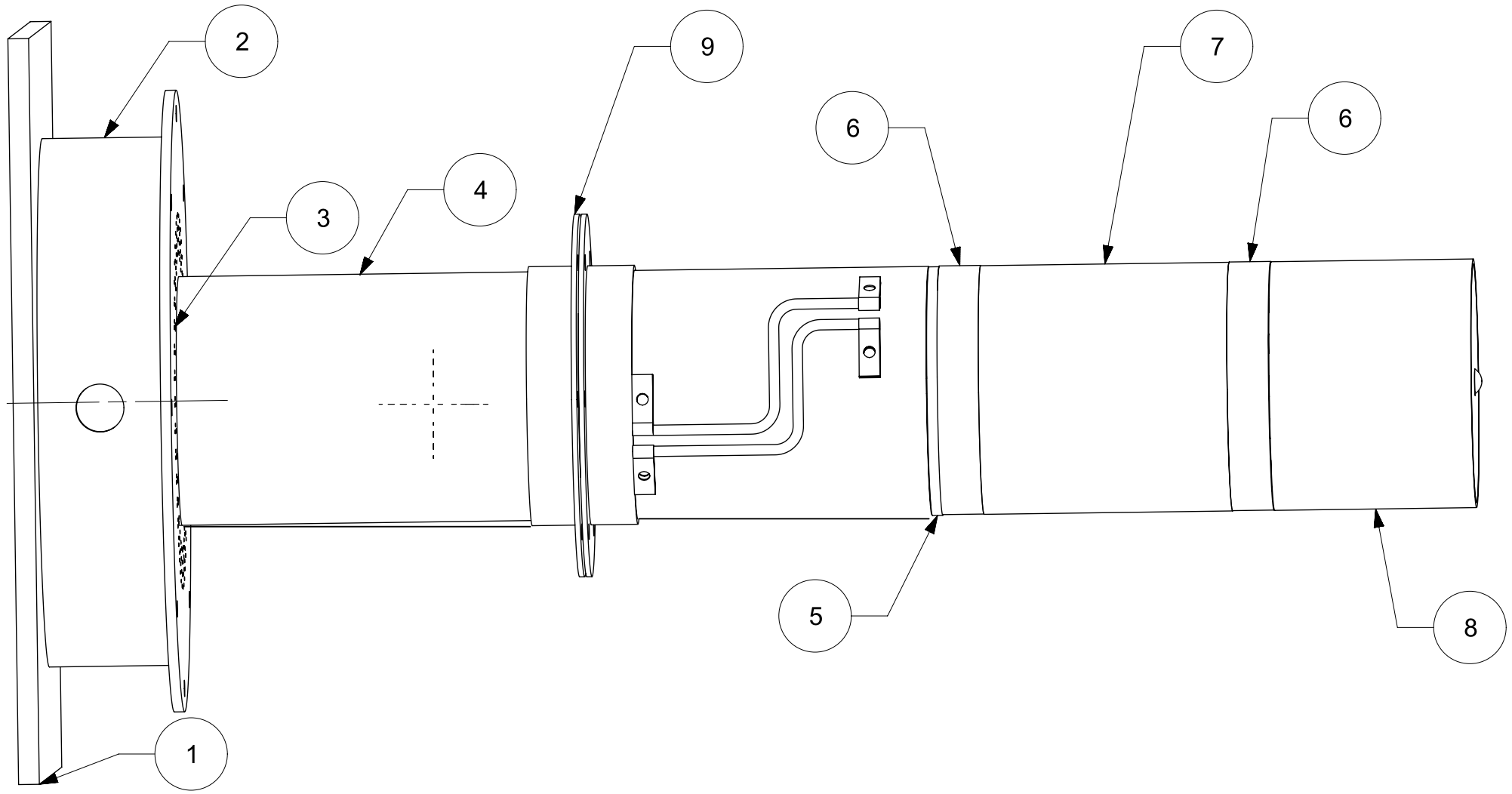

PC NO	PART NAME	QTY
1	BASE	1
2	PLENUM VESSEL	1
3	ORIFICE PLATE	1
4	CENTER CYLINDER	1
5	CANTELIEVER BASE PLATE	1
6	CERAMIC END	2
7	HOT CENTERBODY	1
8	END PIECE	1
9	FLANGE FEATURE	2

TOLERANCES UNLESS OTHERWISE NOTED
X.X ±0.015 Angles ±0.5°
X.XX ±.010 X/X ±1/64
X.XXX ±0.005
CORNER RADIUS OR CHAMFER 0.005 TO 0.015
UNITS ARE INCHES [MM]

125

PURDUE PROPULSION

QUANTITY:	REVISION A
Part Name: Assembly without Duct	
Drawn By:	
MATERIAL:	
DATE: 8/22/2014	1 OF 1

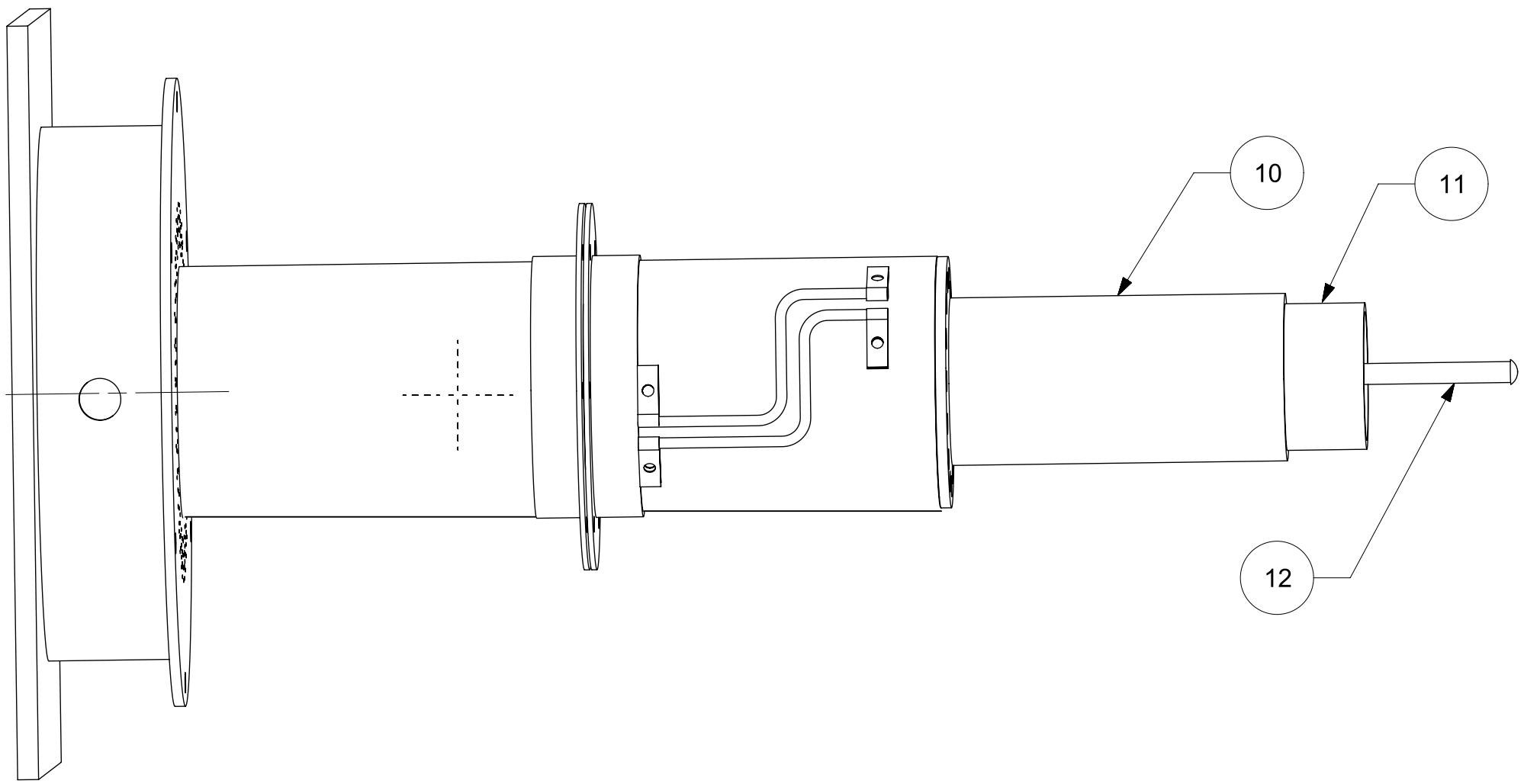

PC NO	PART NAME	QTY
10	CERAMIC SLEEVE	1
11	CANTILEVERED SUPPORT	1
12	BOLT	1

TOLERANCES UNLESS OTHERWISE NOTED
X.X ±0.015 Angles ±0.5°
X.XX ±.010 X/X ±1/64
X.XXX ±0.005
CORNER RADIUS OR CHAMFER 0.005 TO 0.015
UNITS ARE INCHES [MM]

125

PURDUE PROPULSION

QUANTITY:	REVISION A
Part Name: Assembly without Hot Surface	
Drawn By:	
MATERIAL:	
DATE: 8/22/2014	1 OF 1

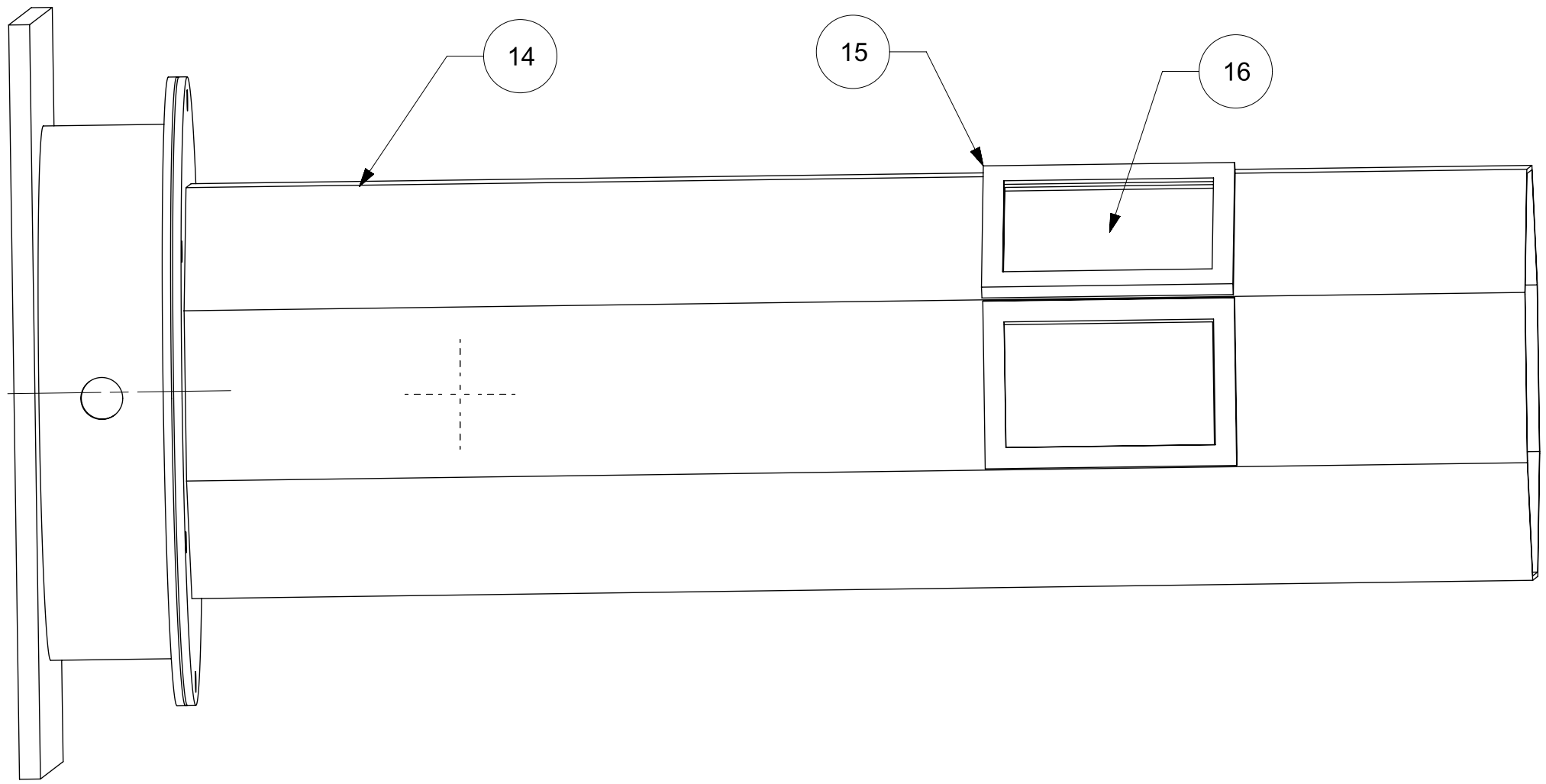

PC NO	PART NAME	QTY
13	OCTAGONAL DUCT	1
14	WINDOW FLANGE	2
15	WINDOW	2

TOLERANCES UNLESS OTHERWISE NOTED
X.X ±0.015 Angles ±0.5°
X.XX ±.010 X/X ±1/64
X.XXX ±0.005
CORNER RADIUS OR CHAMFER 0.005 TO 0.015
UNITS ARE INCHES [MM]

125

PURDUE PROPULSION

QUANTITY:	REVISION A
Part Name: Assembly with Duct	
Drawn By:	
MATERIAL:	
DATE: 8/22/2014	1 OF 1

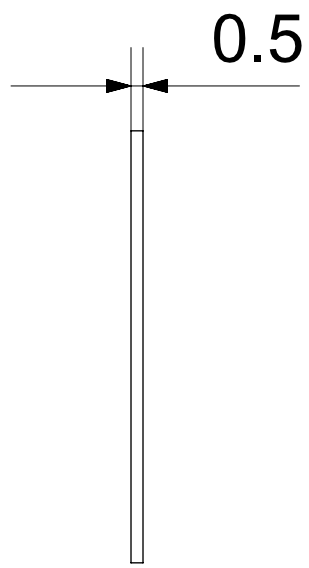

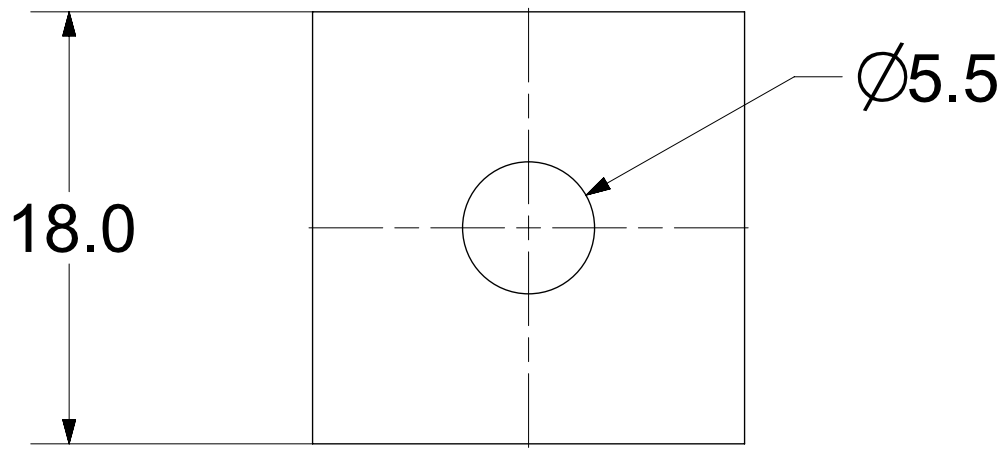

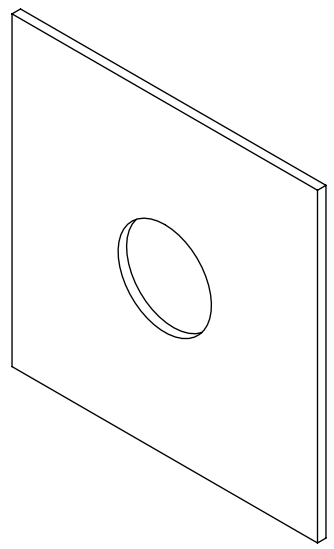

TOLERANCES UNLESS OTHERWISE NOTED X.X ±0.015 Angles ±0.5° X.XX ±.010 X/X ±1/64 X.XXX ±0.005 CORNER RADIUS OR CHAMFER 0.005 TO 0.015 UNITS ARE INCHES [MM]	125	QUANTITY:	REVISION A
		Part Name: Base	
		Drawn By:	
		MATERIAL: Stainless Steel 304	
		DATE: 8/22/2014	1 OF 1

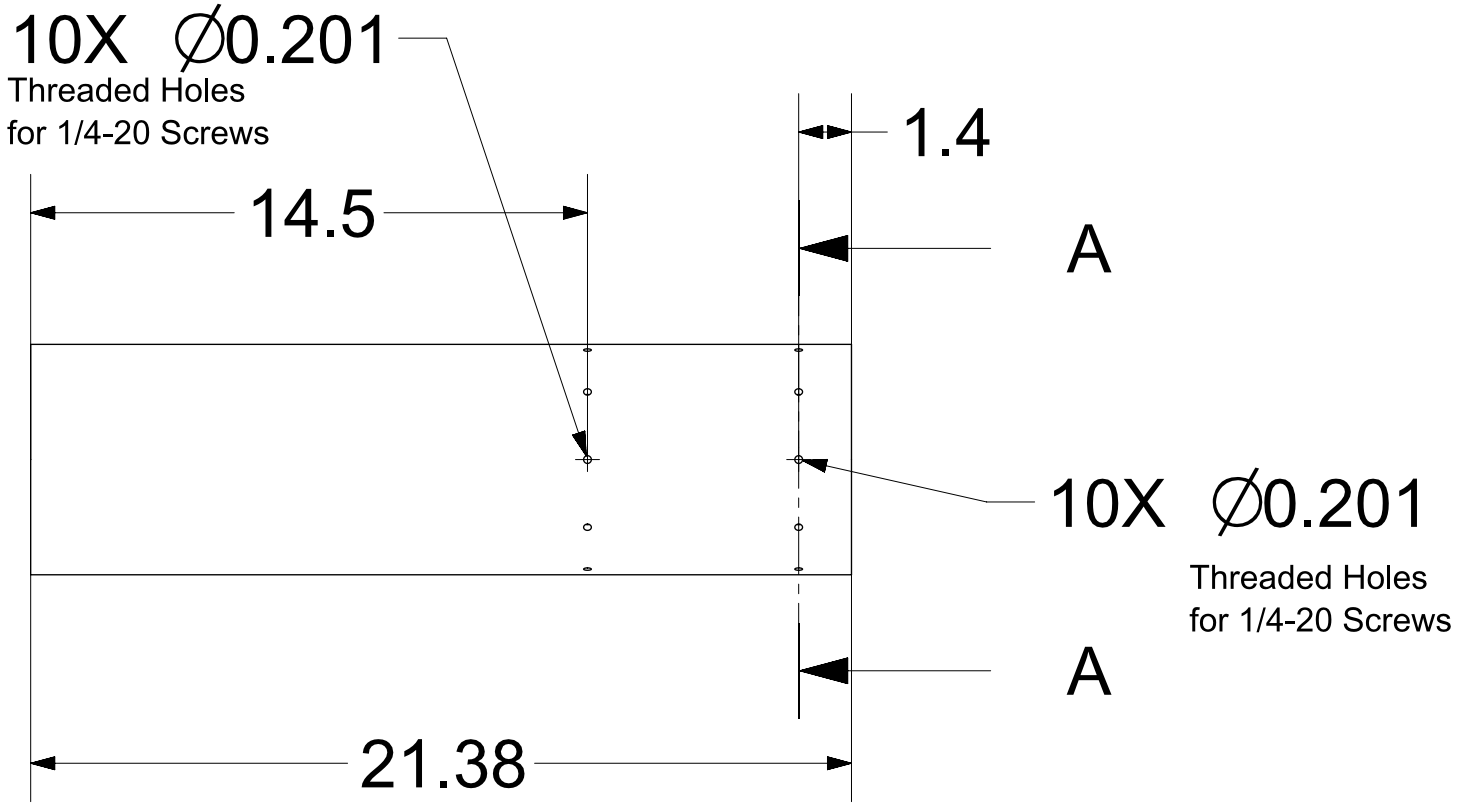

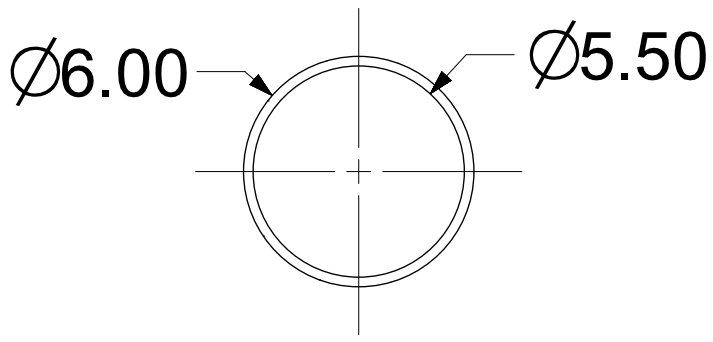

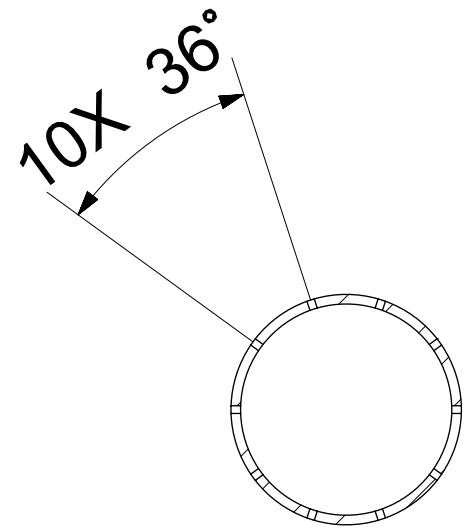

SECTION A-A

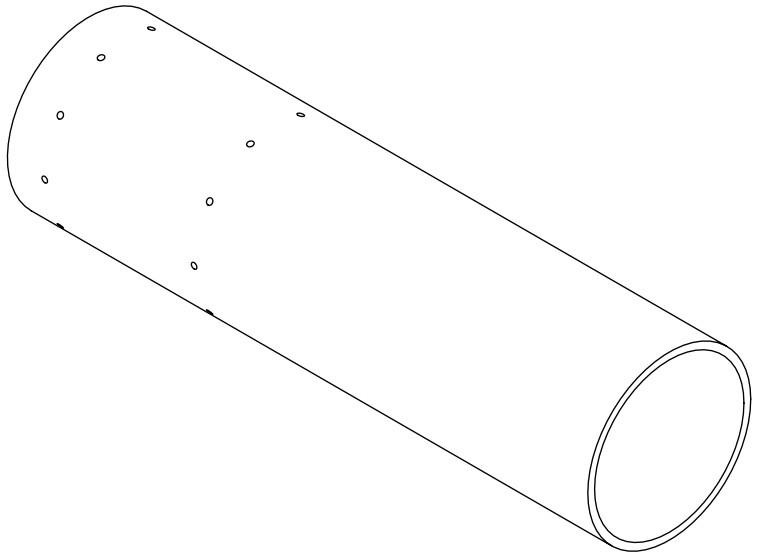

1. Part to be free of oil, grease, burrs, contaminants and surface imperfections

TOLERANCES UNLESS OTHERWISE NOTED X.X ±0.015 Angles ±0.5° X.XX ±.010 X/X ±1/64 X.XXX ±0.005 CORNER RADIUS OR CHAMFER 0.005 TO 0.015 UNITS ARE INCHES [MM]	125	QUANTITY:	REVISION A
		Part Name: Center_Cylinder	
		Drawn By:	
		MATERIAL: Stainless Steel 304	
		DATE: 8/22/2014	1 OF 1

159

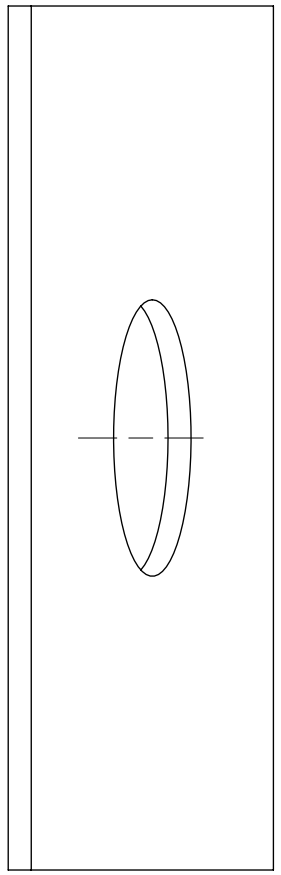

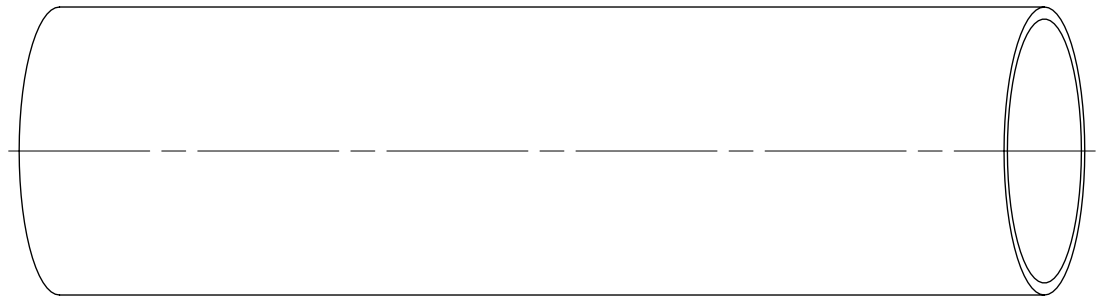

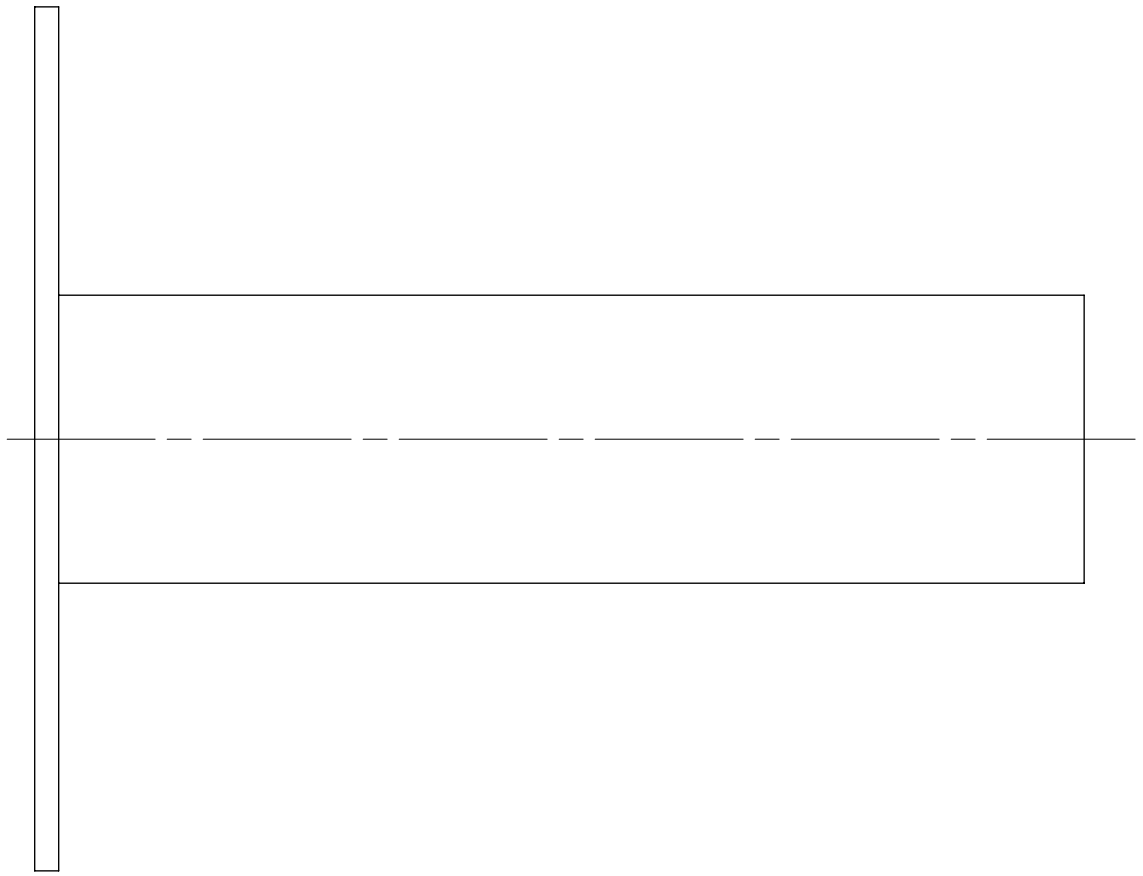

Note: Center Cylinder is welded to the base

TOLERANCES UNLESS OTHERWISE NOTED X.X ±0.015 Angles ±0.5° X.XX ±.010 X/X ±1/64 X.XXX ±0.005 CORNER RADIUS OR CHAMFER 0.005 TO 0.015 UNITS ARE INCHES [MM]	125	QUANTITY:	REVISION A
		Part Name: Phase 1	
		Drawn By:	
		MATERIAL:	
		DATE: 8/22/2014	1 OF 1

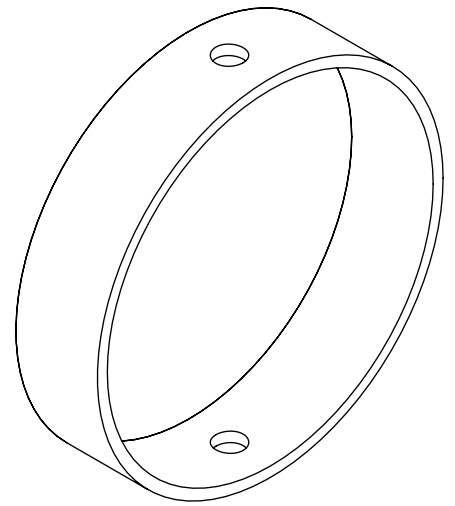

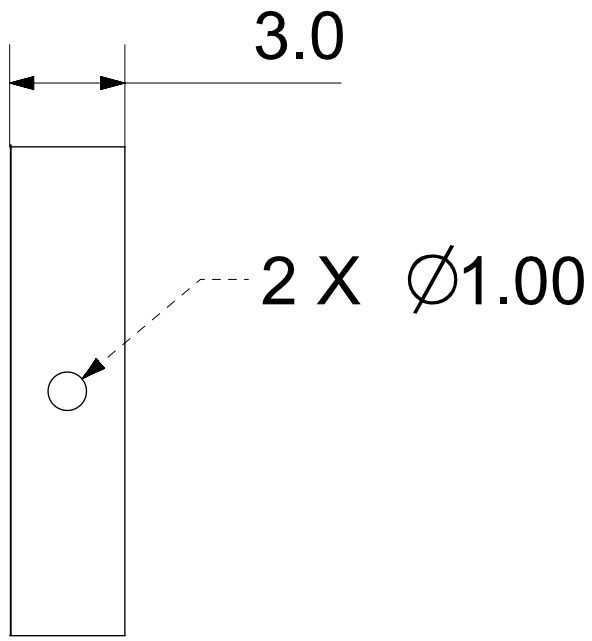

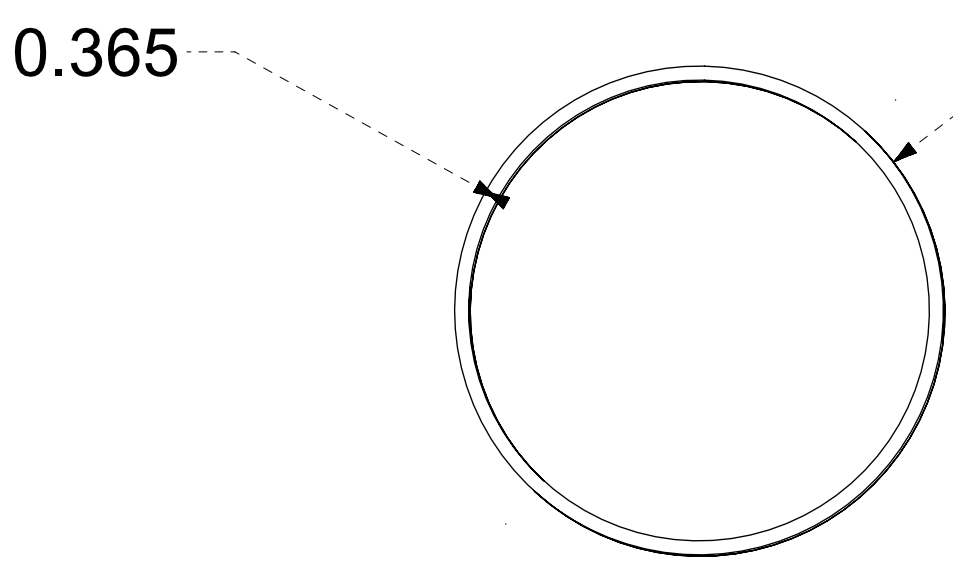

1. Part to be free of oil, grease, burrs, contaminants and surface imperfections

TOLERANCES UNLESS OTHERWISE NOTED		QUANTITY:	REVISION A
X.X ±0.015	Angles ±0.5°	Part Name: Plenum_Vessel	
X.XX ±.010	X/X ±1/64	Drawn By:	
X.XXX ±0.005	125	MATERIAL: Stainless Steel 304	
CORNER RADIUS OR CHAMFER 0.005 TO 0.015		DATE: 8/22/2014	1 OF 1
UNITS ARE INCHES [MM]			

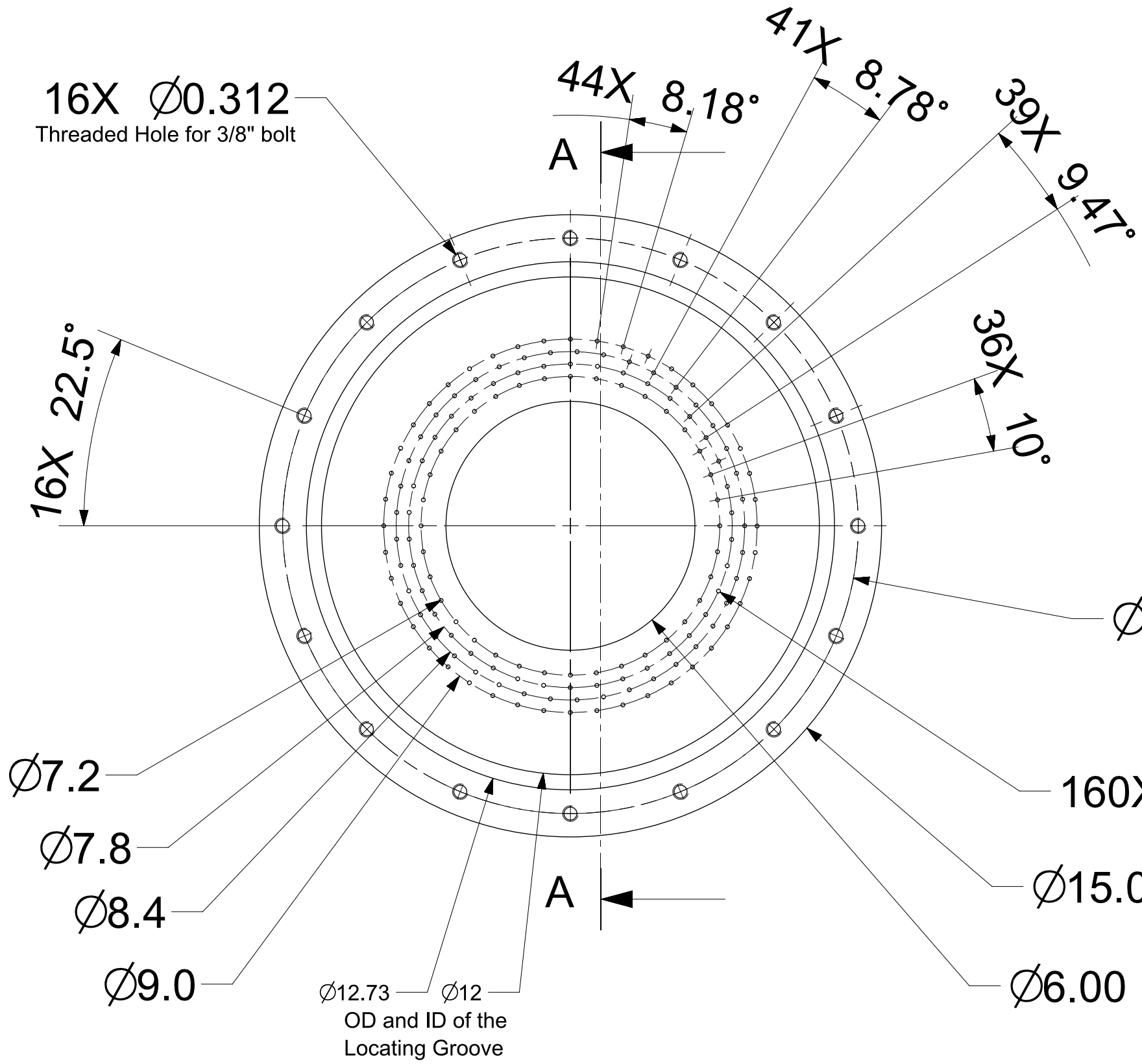

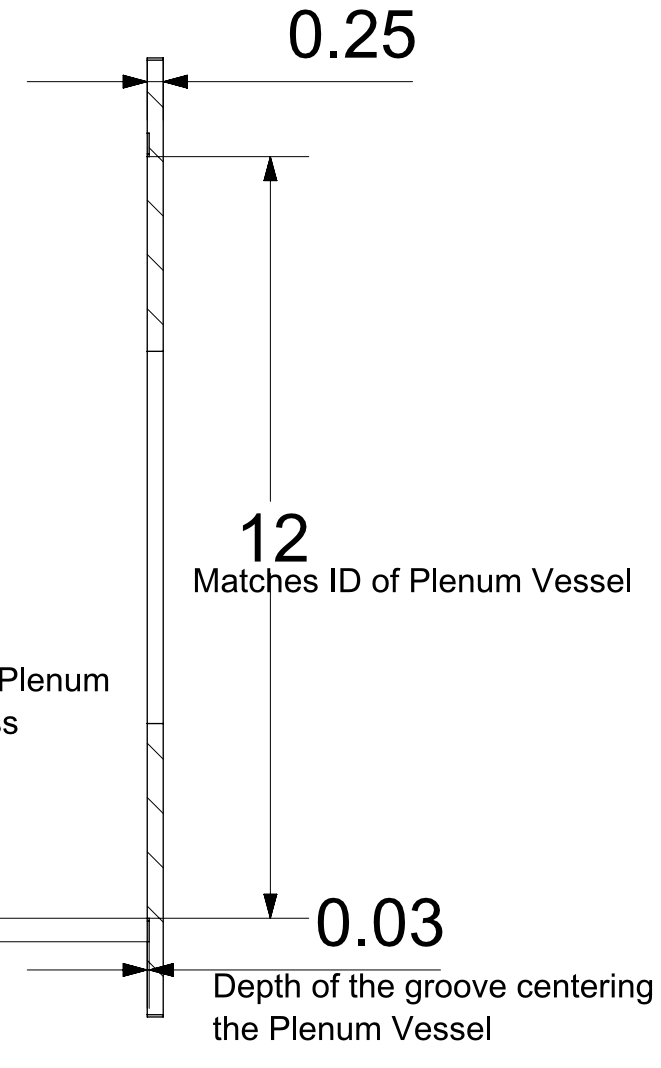

SECTION A-A

TOLERANCES UNLESS OTHERWISE NOTED X.X ±0.015 Angles ±0.5° X.XX ±.010 X/X ±1/64 X.XXX ±0.005 CORNER RADIUS OR CHAMFER 0.005 TO 0.015 UNITS ARE INCHES [MM] 125	PURDUE PROPULSION	QUANTITY:	REVISION A
		Part Name: Plenum_Orifice_Plate	
		Drawn By:	
		MATERIAL: Stainless Steel 304	
		DATE: 8/22/2014	1 OF 1

1. Part to be free of oil, grease, burrs, contaminants and surface imperfections

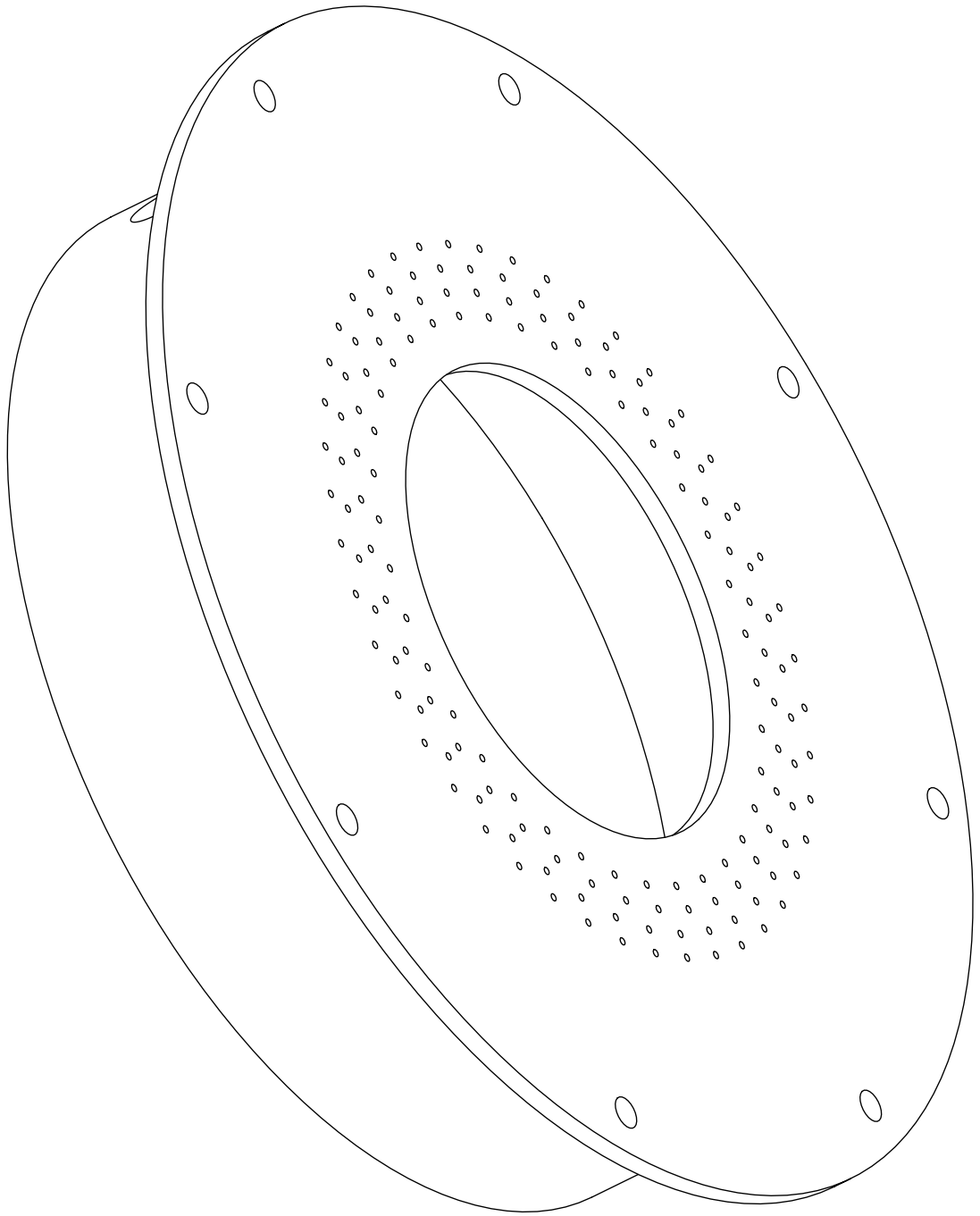

Note: The Plenum Vessel and Orifice Plate are centered and welded together.

TOLERANCES UNLESS OTHERWISE NOTED X.X ±0.015 Angles ±0.5° X.XX ±.010 X/X ±1/64 X.XXX ±0.005 CORNER RADIUS OR CHAMFER 0.005 TO 0.015 UNITS ARE INCHES [MM]	125	QUANTITY:	REVISION A
		Part Name: Plenum_Assembly	
		Drawn By:	
		MATERIAL:	
		DATE: 8/22/2014	1 OF 1

163

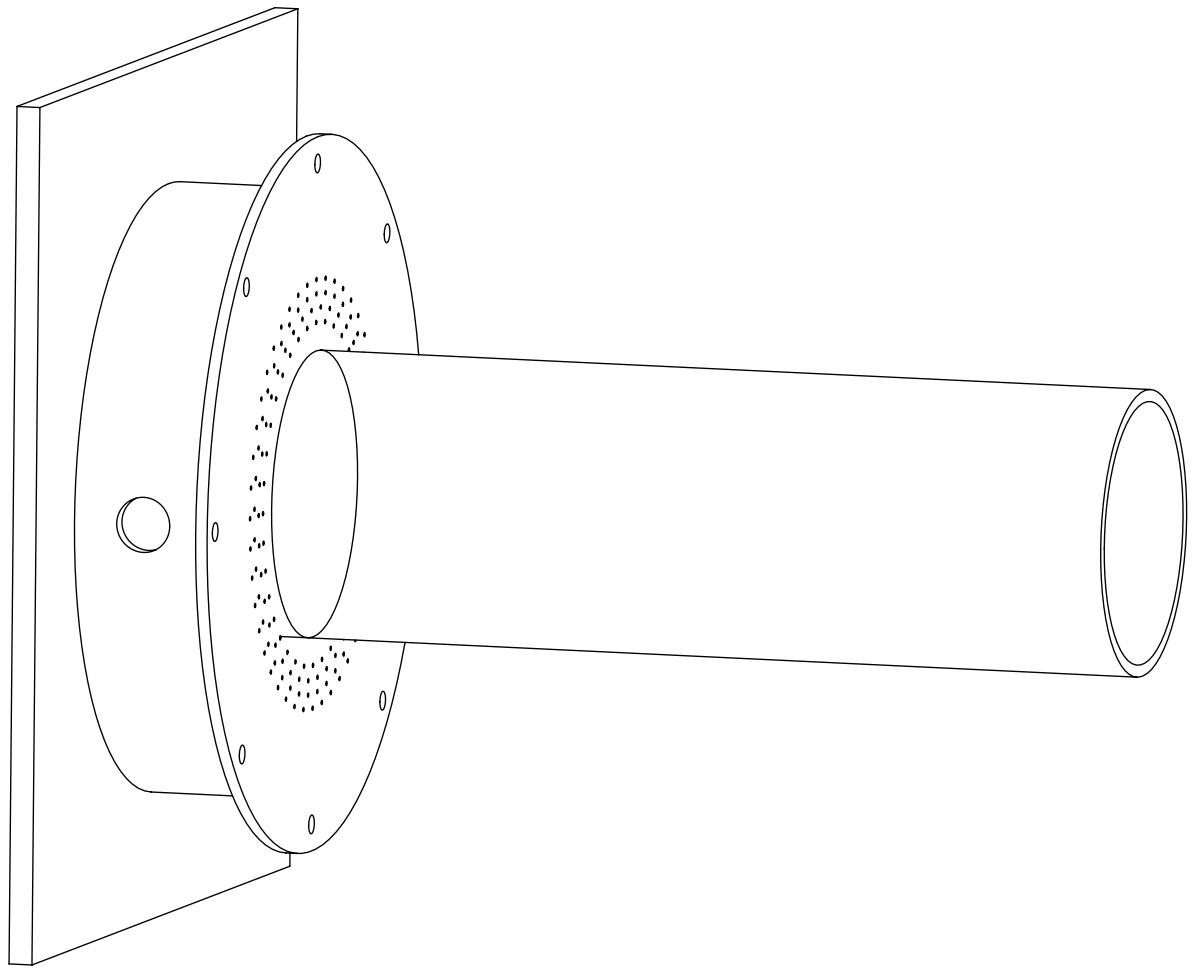

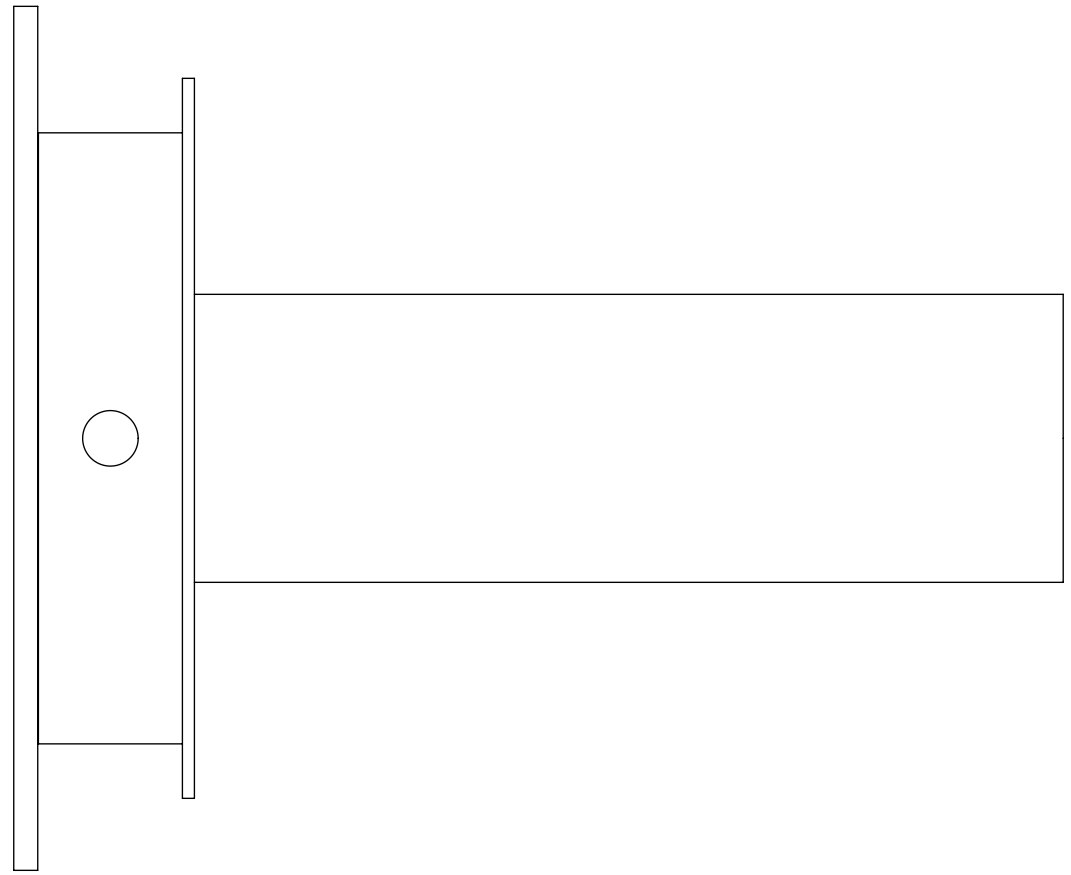

TOLERANCES UNLESS OTHERWISE NOTED		QUANTITY:	REVISION A
X.X ±0.015 Angles ±0.5°		Part Name: Phase 2	
X.XX ±.010 X/X ±1/64	125	Drawn By:	
X.XXX ±0.005		MATERIAL:	
CORNER RADIUS OR CHAMFER 0.005 TO 0.015		DATE: 8/22/2014	1 OF 1
UNITS ARE INCHES [MM]			

164

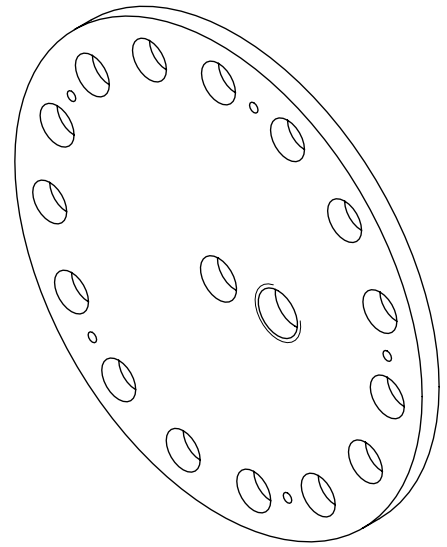

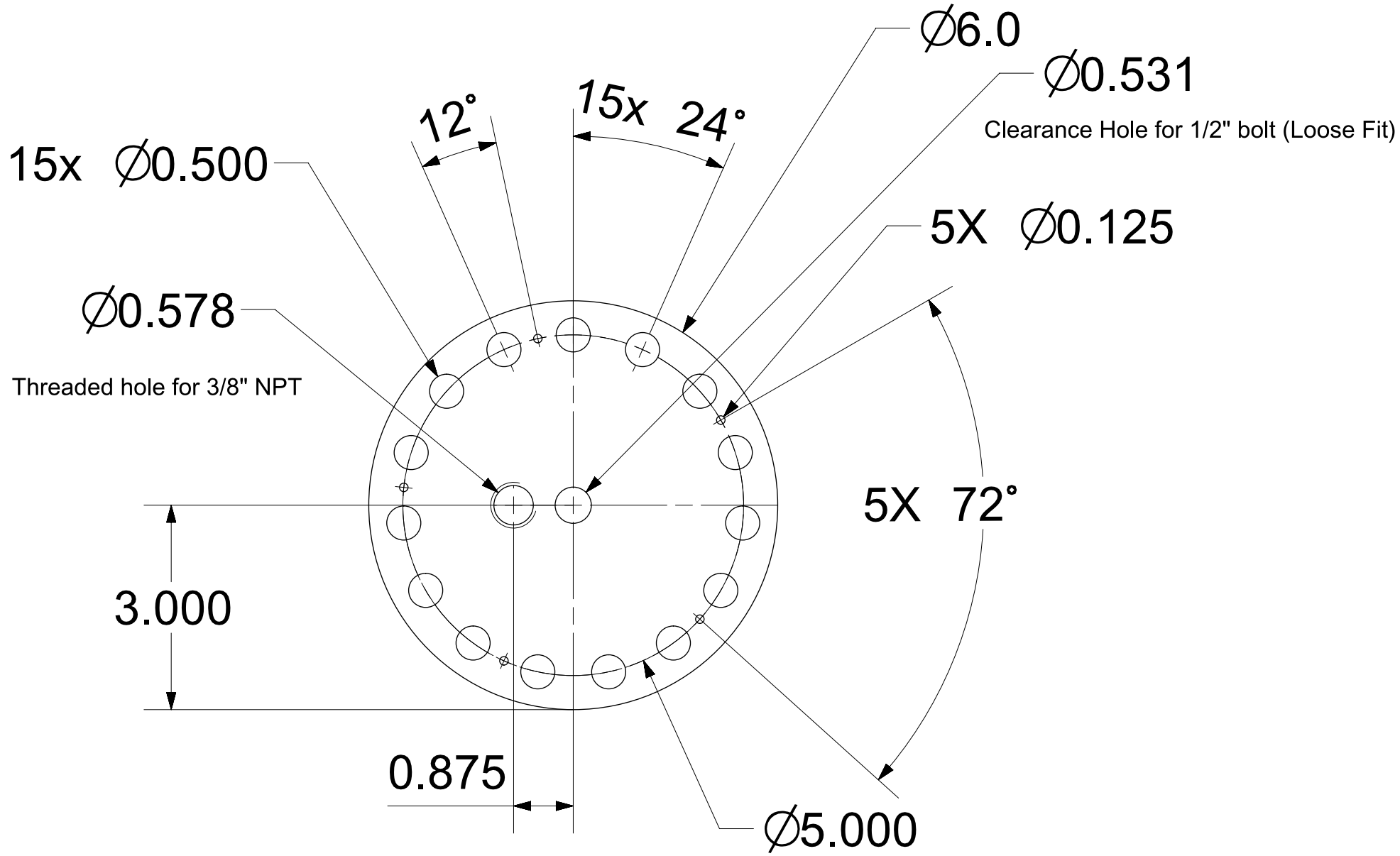

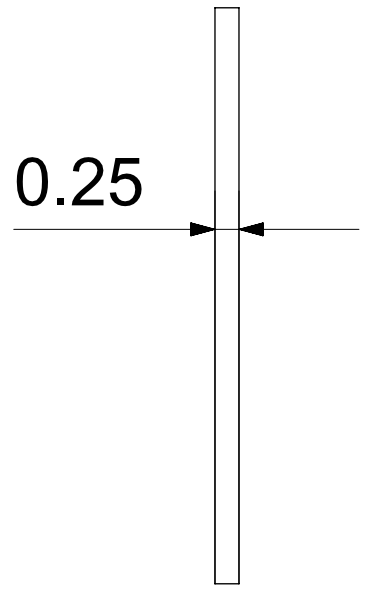

TOLERANCES UNLESS OTHERWISE NOTED X.X ±0.015 Angles ±0.5° X.XX ±.010 X/X ±1/64 X.XXX ±0.005 CORNER RADIUS OR CHAMFER 0.005 TO 0.015 UNITS ARE INCHES [MM]	125	PURDUE PROPULSION

QUANTITY:	REVISION A
Part Name: Cantilever_Base_Plate	
Drawn By:	
MATERIAL: Stainless Steel 304	
DATE: 8/22/2014	1 OF 1

1. Part to be free of oil, grease, burrs, contaminants and surface imperfections

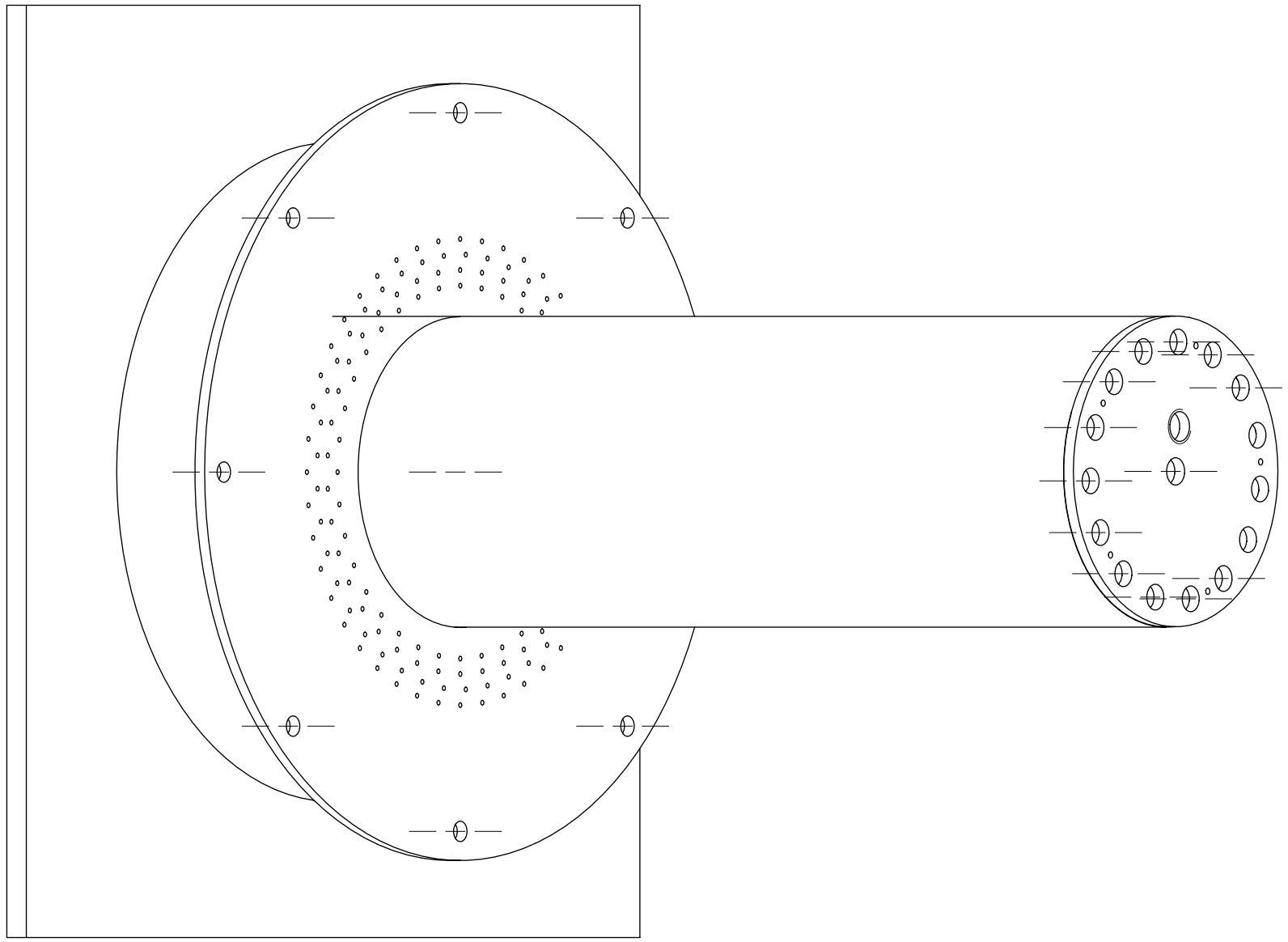

Note: Cantilever Base Plate is welded to the free end of the center cylinder.

TOLERANCES UNLESS OTHERWISE NOTED X.X ±0.015 Angles ±0.5° X.XX ±.010 X/X ±1/64 X.XXX ±0.005 CORNER RADIUS OR CHAMFER 0.005 TO 0.015 UNITS ARE INCHES [MM]	125	QUANTITY:	REVISION A
		Part Name: Phase 3	
		Drawn By:	
		MATERIAL:	
		DATE: 8/22/2014	1 OF 1

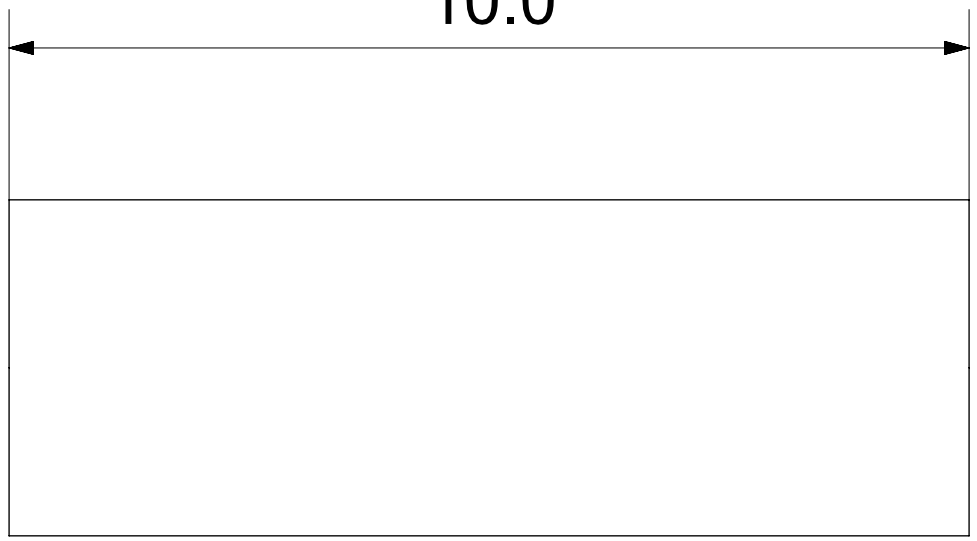

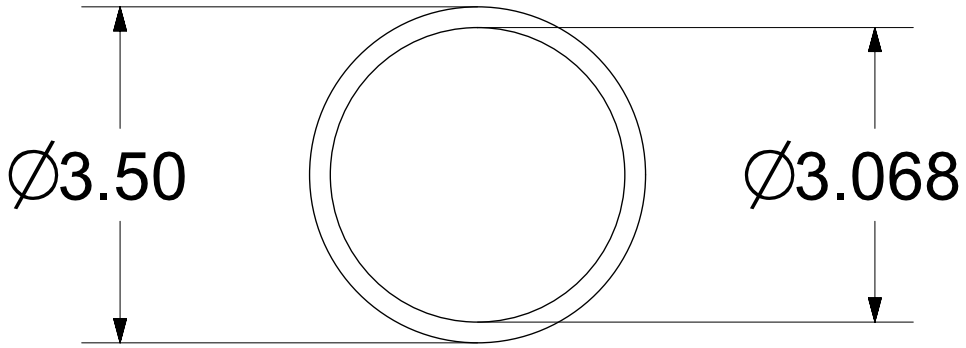

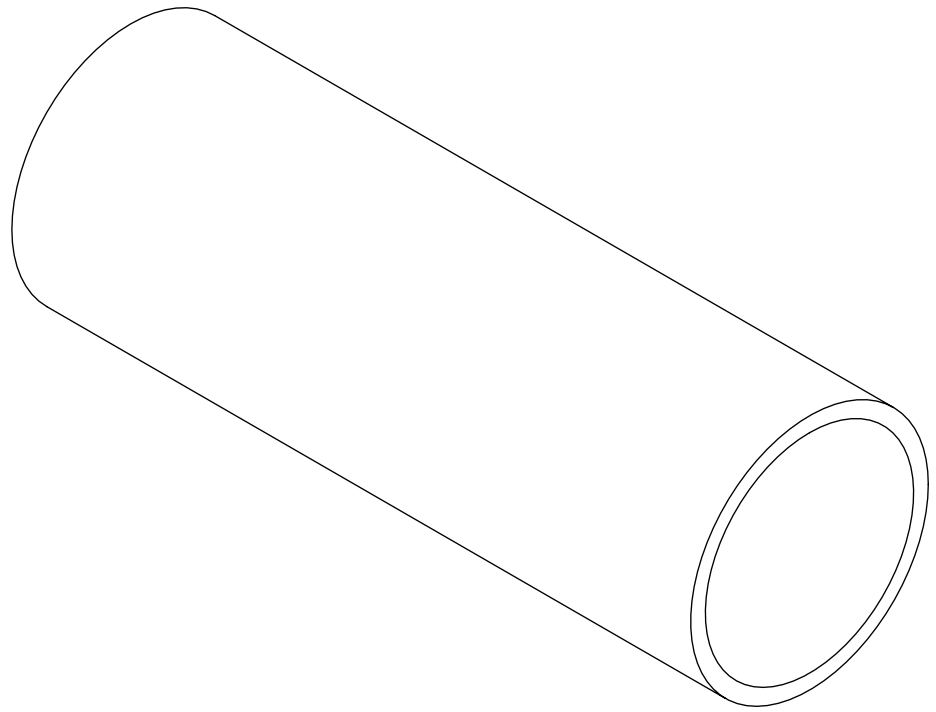

TOLERANCES UNLESS OTHERWISE NOTED X.X ± 0.015 Angles ± 0.5° X.XX ± .010 X/X ± 1/64 X.XXX ± 0.005 CORNER RADIUS OR CHAMFER 0.005 TO 0.015 UNITS ARE INCHES [MM]		QUANTITY:	REVISION A
		Part Name: Cantilever_Support	
		Drawn By:	
		MATERIAL: Stainless Steel 304	
		DATE: 8/22/2014	1 OF 1

125

1. Part to be free of oil, grease, burrs, contaminants and surface imperfections

167

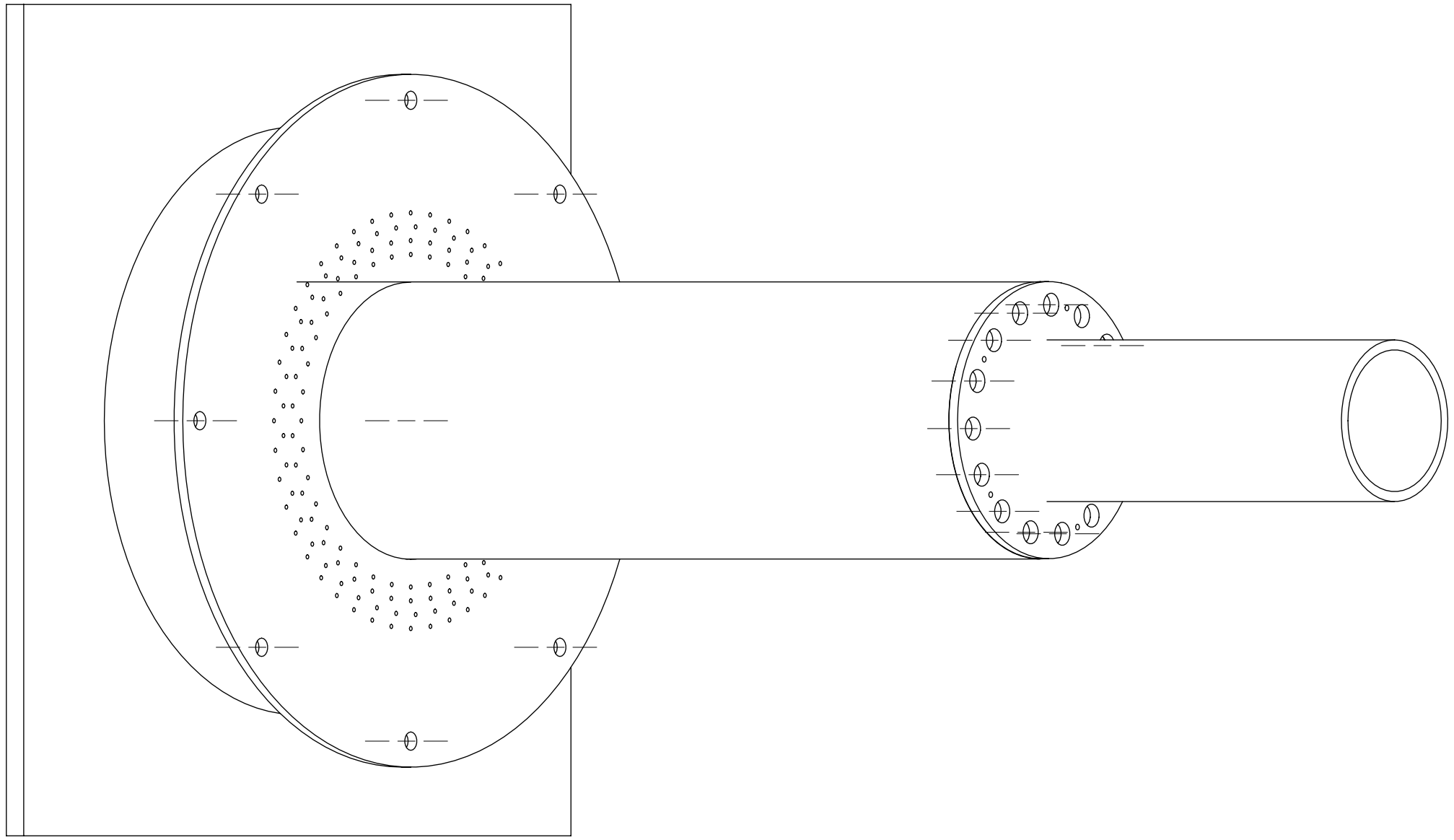

Note: Cantilevred Support is welded to the
Cantilevere Base Plate

TOLERANCES UNLESS OTHERWISE NOTED X.X ±0.015 Angles ±0.5° X.XX ±.010 X/X ±1/64 X.XXX ±0.005 CORNER RADIUS OR CHAMFER 0.005 TO 0.015 UNITS ARE INCHES [MM]	125	PURDUE PROPULSION	QUANTITY: / REVISION A Part Name: Phase 4 Drawn By: MATERIAL: DATE: 8/22/2014 / 1 OF 1

168

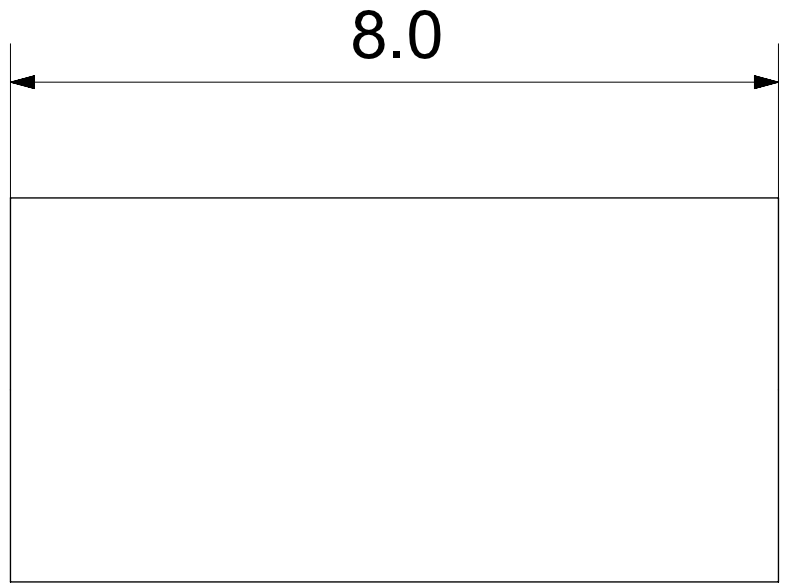

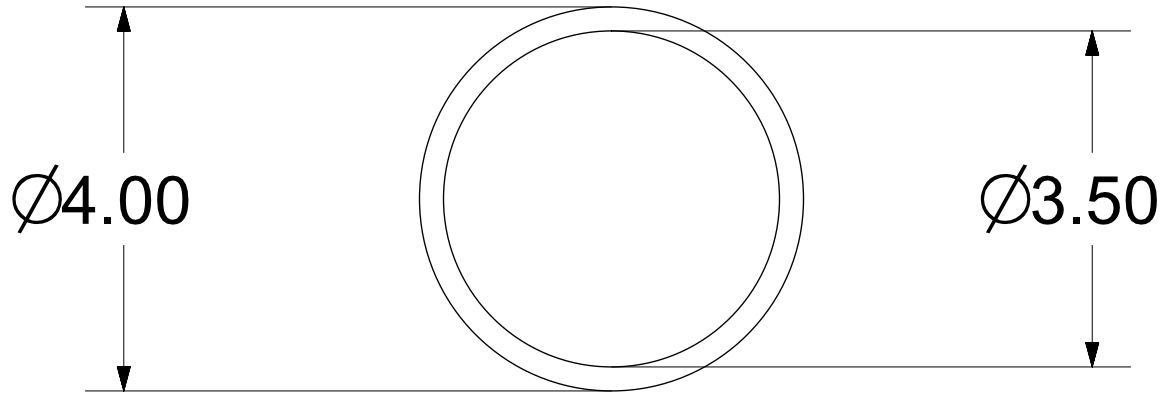

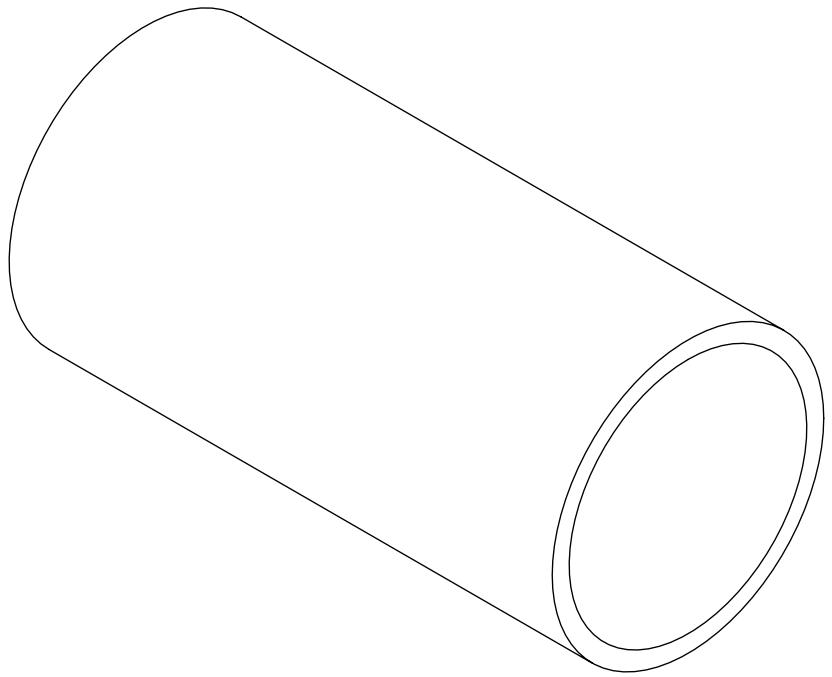

TOLERANCES UNLESS OTHERWISE NOTED X.X ± 0.015 Angles ± 0.5° X.XX ± .010 X/X ± 1/64 X.XXX ± 0.005 CORNER RADIUS OR CHAMFER 0.005 TO 0.015 UNITS ARE INCHES [MM]	125	QUANTITY:	REVISION A
		Part Name: Ceramic_Sleeve	
		Drawn By:	
		MATERIAL: Alumina Silicate, Grade "A" Lava	
		DATE: 8/22/2014	1 OF 1

1. Part to be free of oil, grease, burrs, contaminants and surface imperfections

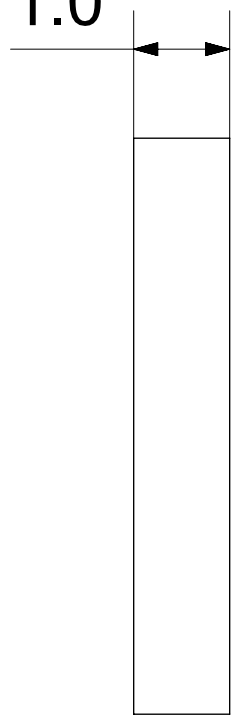

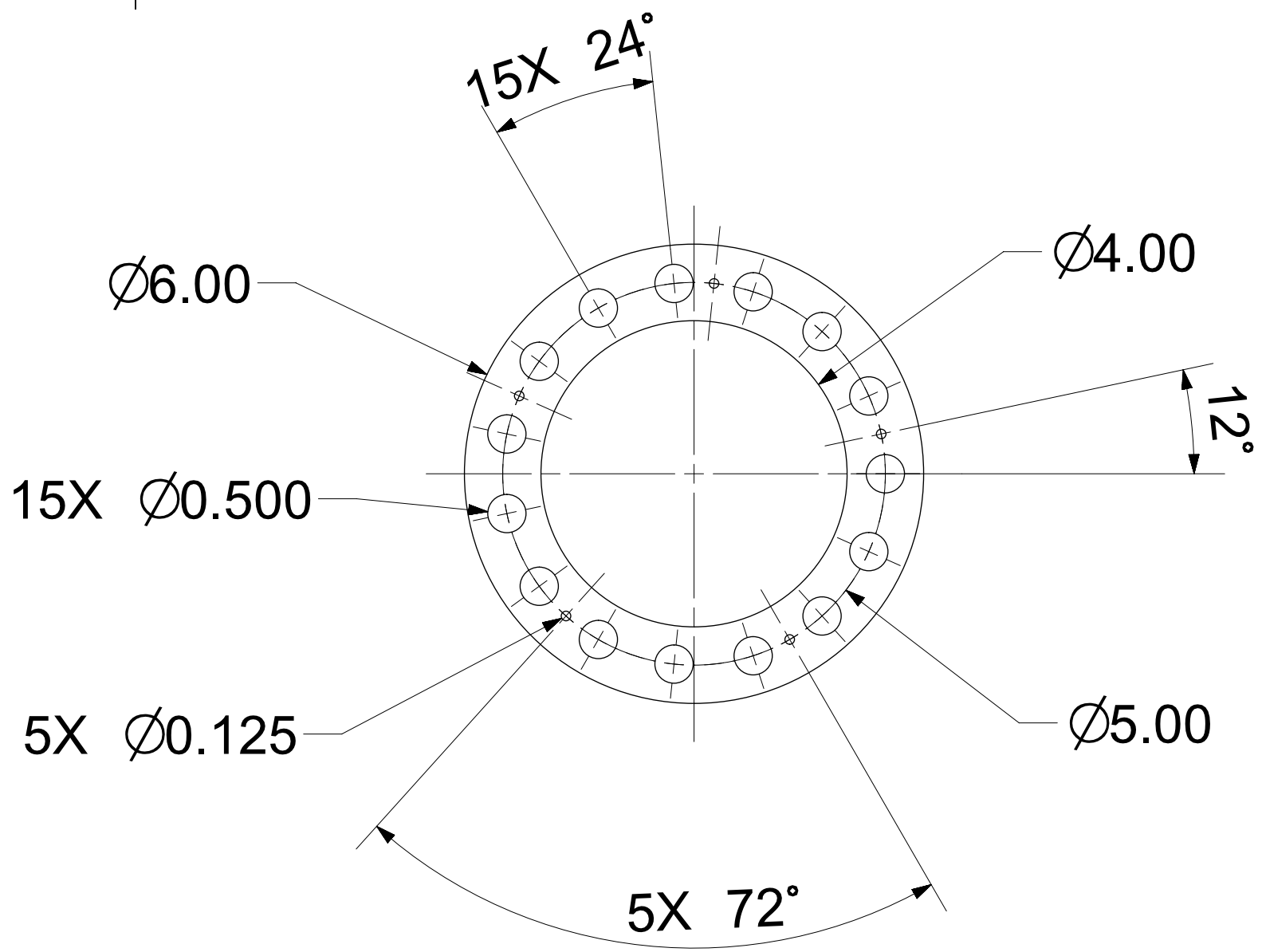

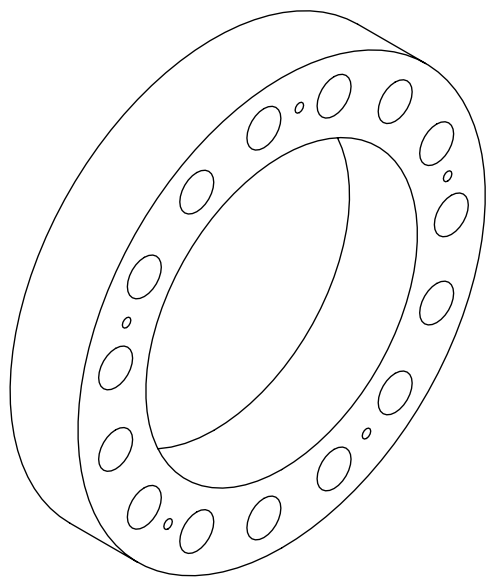

TOLERANCES UNLESS OTHERWISE NOTED X.X ±0.015 Angles ±0.5° X.XX ±.010 X/X ±1/64 X.XXX ±0.005 CORNER RADIUS OR CHAMFER 0.005 TO 0.015 UNITS ARE INCHES [MM]	125	QUANTITY:	REVISION A
		Part Name: Ceramic_End	
		Drawn By:	
		MATERIAL: Macor	
		DATE: 8/22/2014	1 OF 1

1. Part to be free of oil, grease, burrs, contaminants and surface imperfections

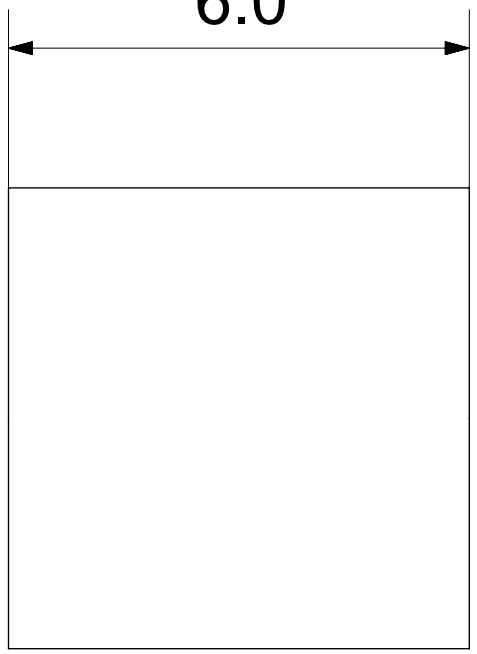

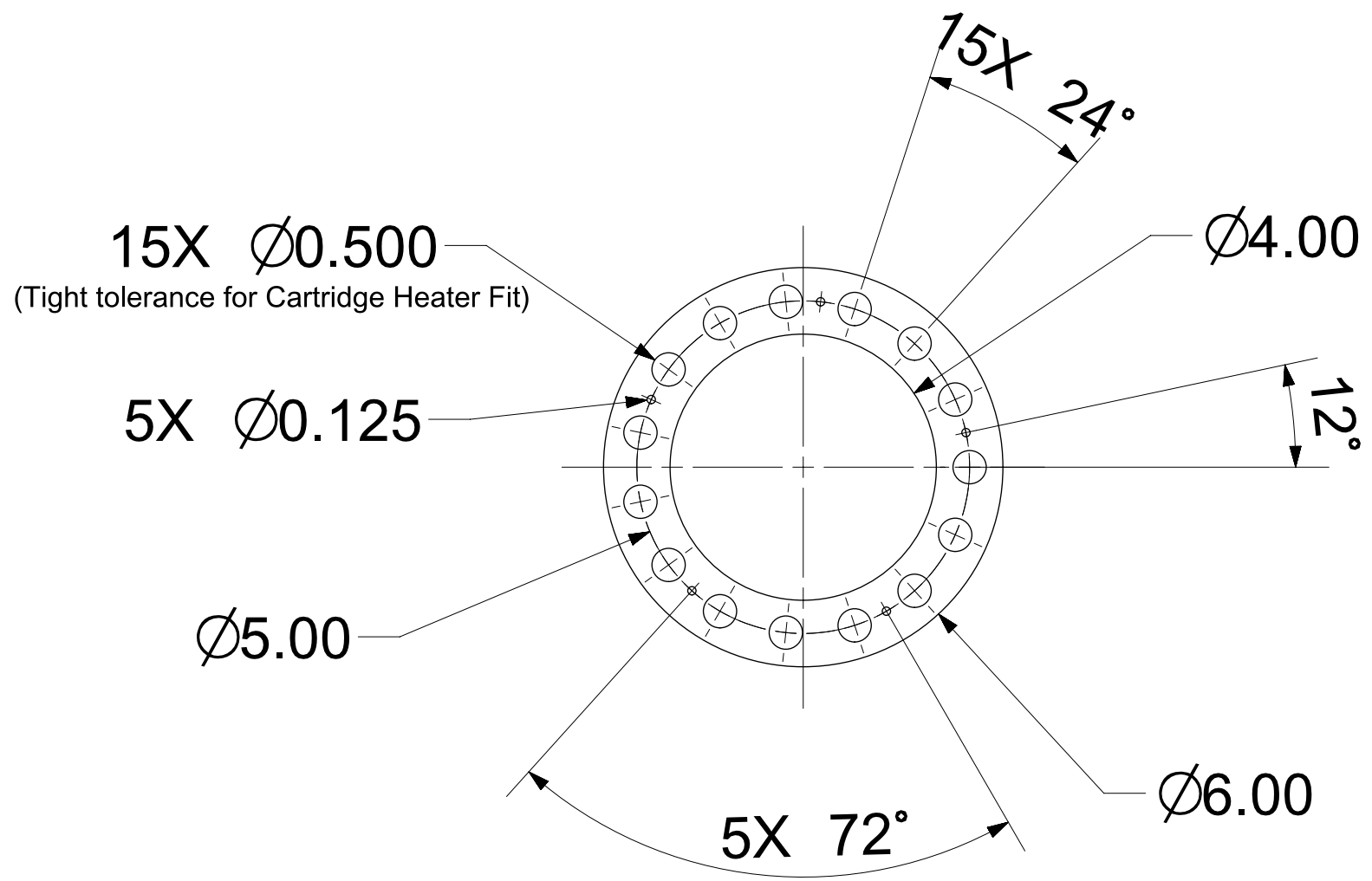

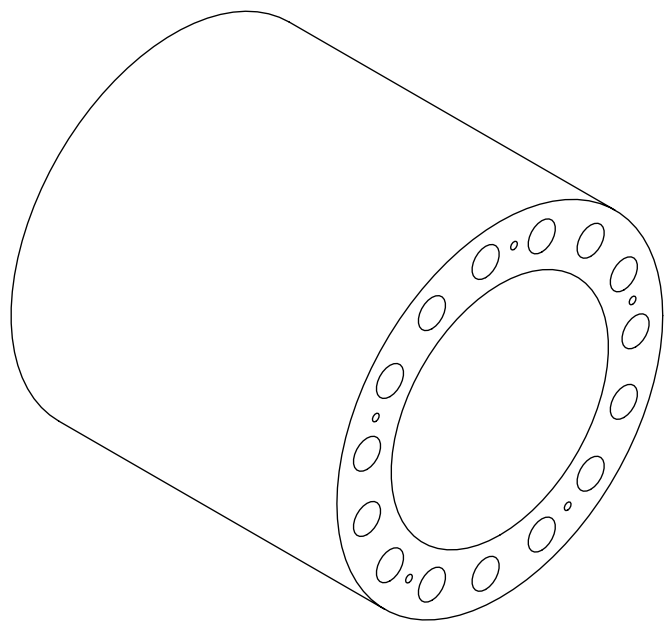

TOLERANCES UNLESS OTHERWISE NOTED		QUANTITY:	REVISION A
X.X ±0.015	Angles ±0.5°	Part Name: Hot_Centerbody	
X.XX ±.010	X/X ±1/64	Drawn By: Jesse Adams	
X.XXX ±0.005	125	MATERIAL: Inconel 718	
CORNER RADIUS OR CHAMFER 0.005 TO 0.015		DATE: 8/22/2014	1 OF 1
UNITS ARE INCHES [MM]			

1. Part to be free of oil, grease, burrs, contaminants and surface imperfections

PC NO	PART NAME	QTY
8a.	END LIP	1
8b.	END VESSEL	1
8c.	END FACE	1

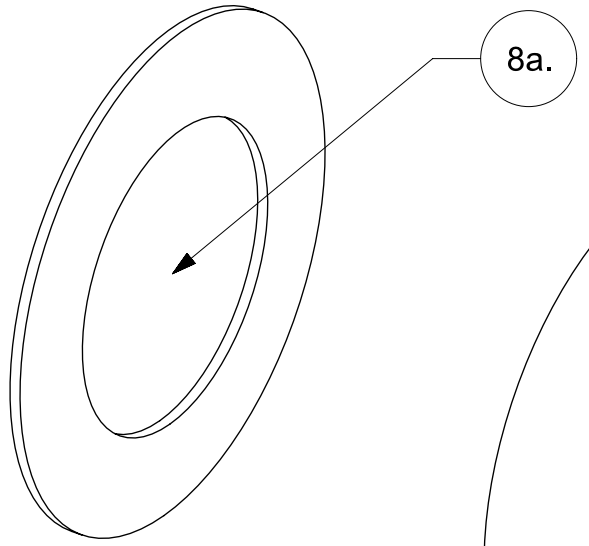

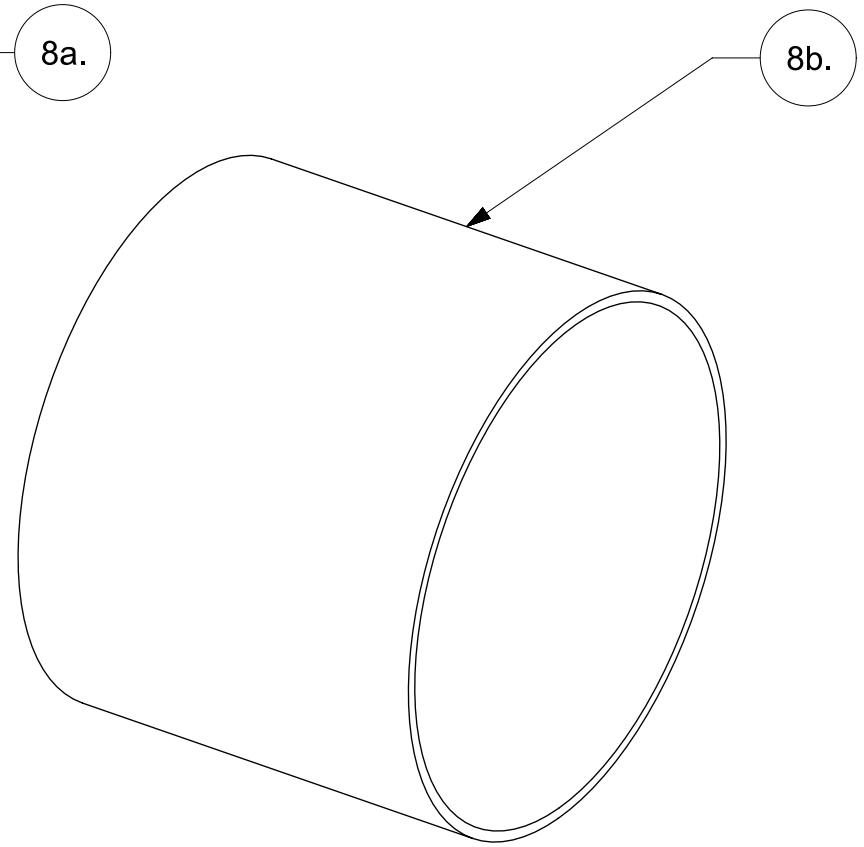

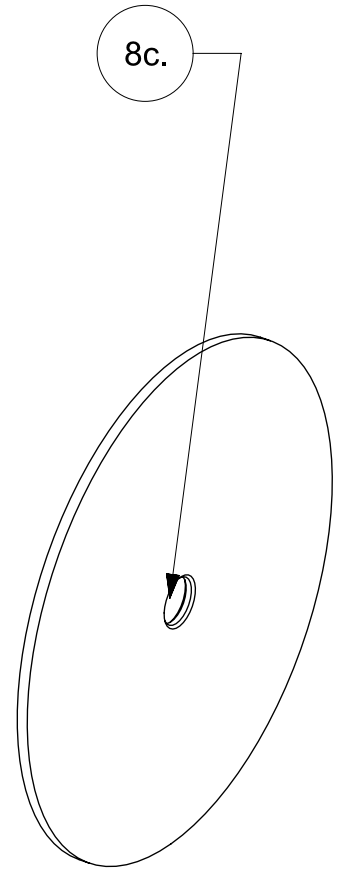

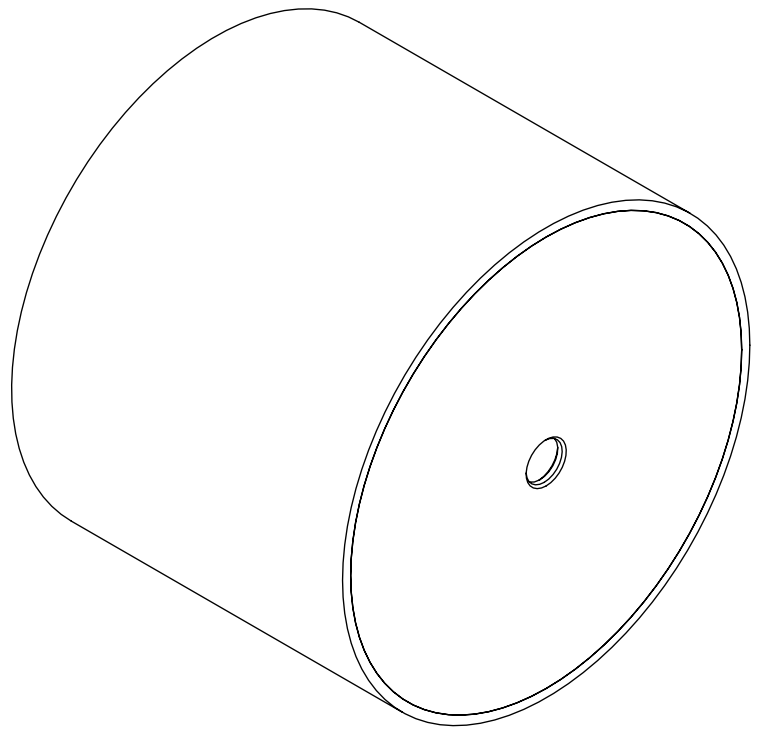

TOLERANCES UNLESS OTHERWISE NOTED X.X ± 0.015 Angles ± 0.5° X.XX ± .010 X/X ± 1/64 X.XXX ± 0.005 CORNER RADIUS OR CHAMFER 0.005 TO 0.015 UNITS ARE INCHES [MM]	125	PURDUE PROPULSION	QUANTITY: / REVISION A Part Name: End Piece_Assembly Drawn By: MATERIAL: DATE: 8/22/2014 / 1 OF 1

172

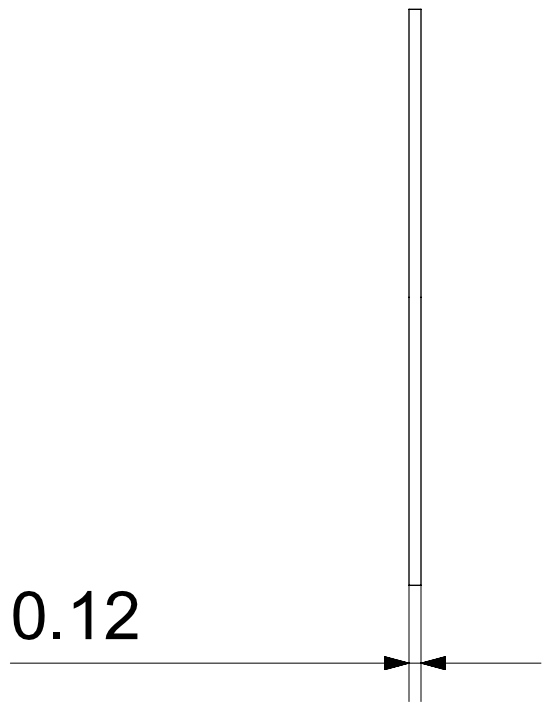

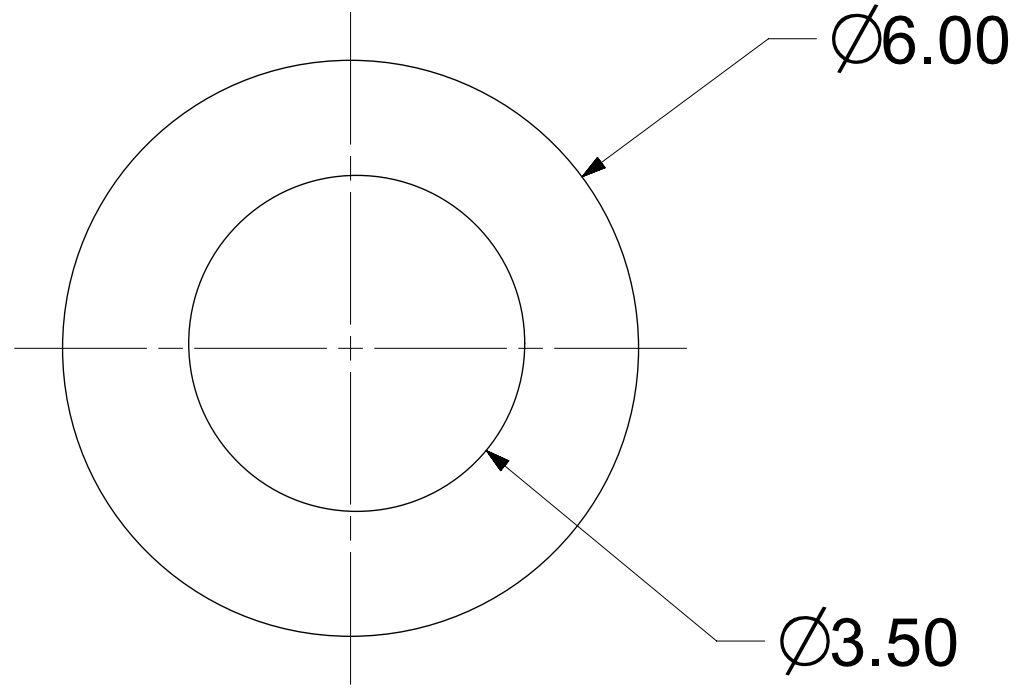

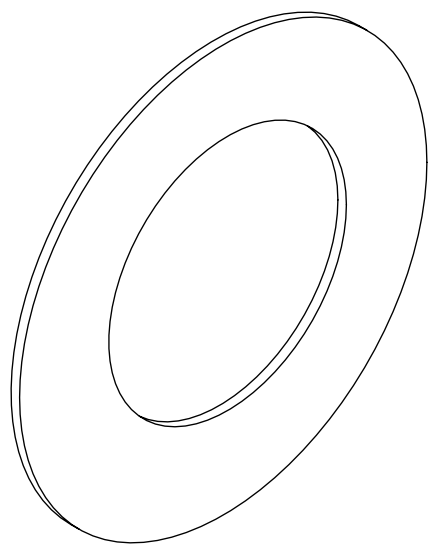

1. Part to be free of oil, grease, burrs, contaminants and surface imperfections

TOLERANCES UNLESS OTHERWISE NOTED X.X ± 0.015 Angles ± 0.5° X.XX ± .010 X/X ± 1/64 X.XXX ± 0.005 CORNER RADIUS OR CHAMFER 0.005 TO 0.015 UNITS ARE INCHES [MM]	125	PURDUE PROPULSION	QUANTITY: / REVISION A Part Name: 1st_End_Ring Drawn By: MATERIAL: Stainless Steel 304 DATE: 8/22/2014 / 1 OF 1

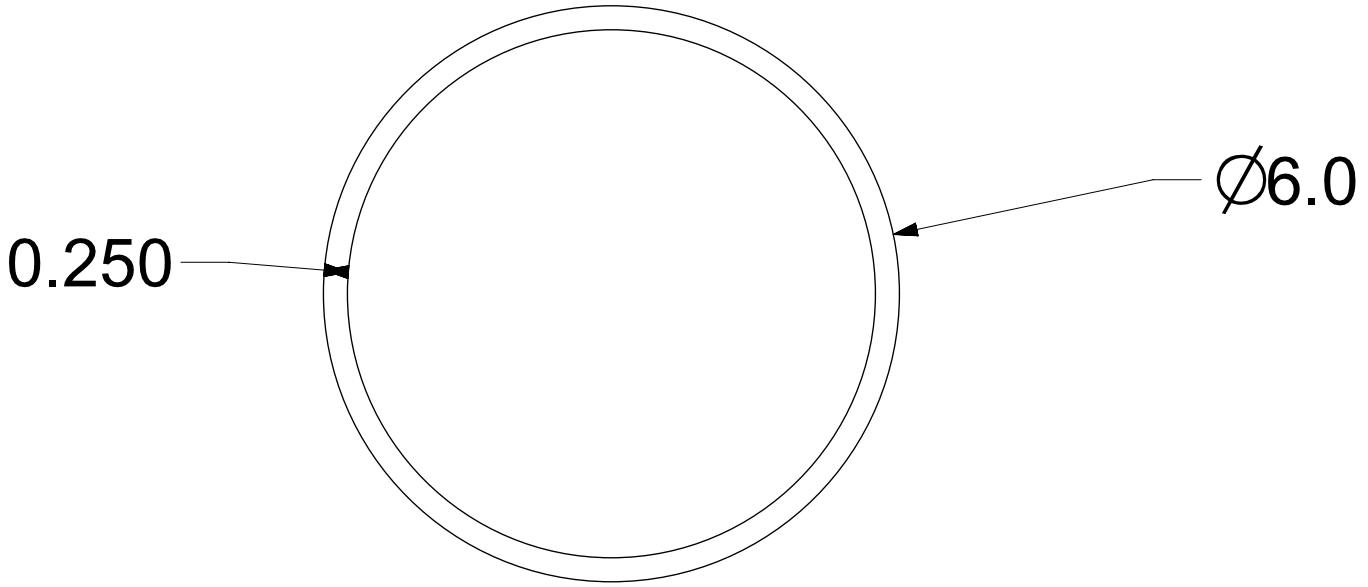

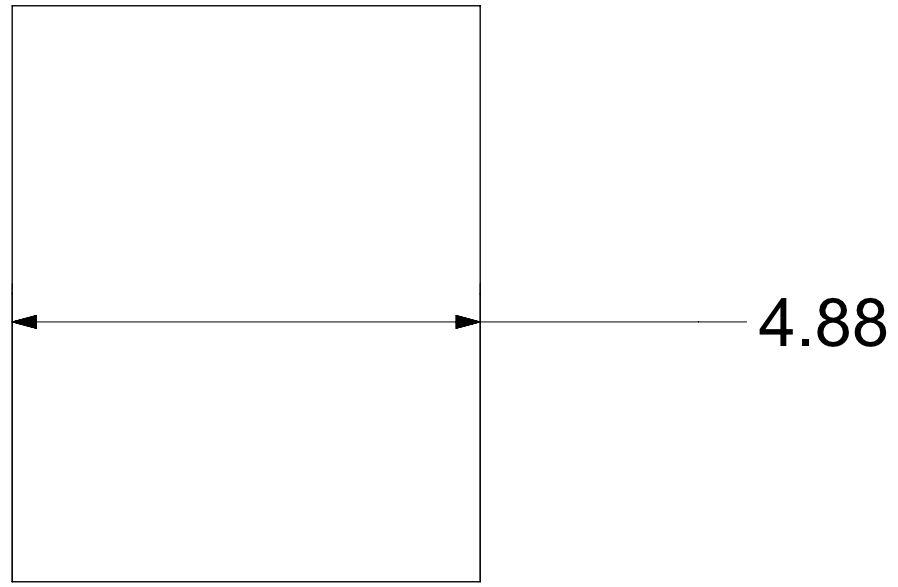

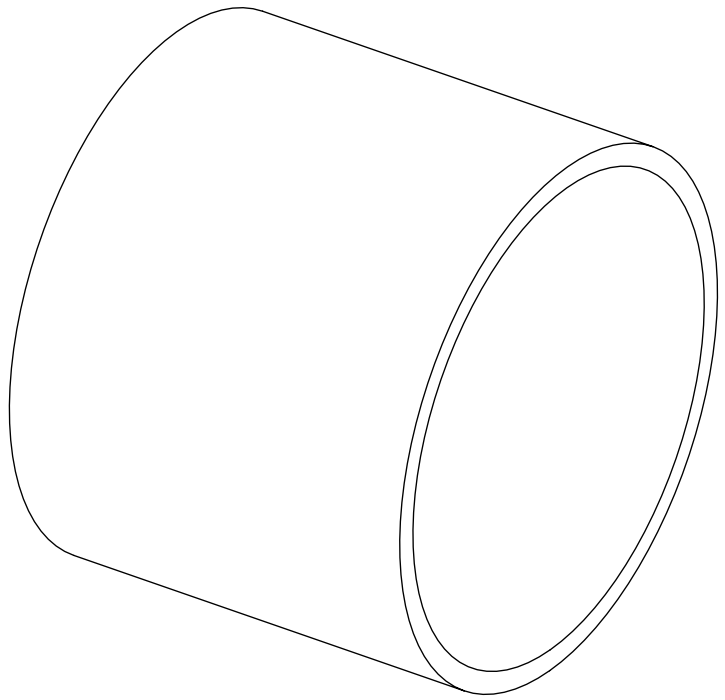

1. Part to be free of oil, grease, burrs, contaminants and surface imperfections

TOLERANCES UNLESS OTHERWISE NOTED X.X ± 0.015 Angles ± 0.5° X.XX ± .010 X/X ± 1/64 125 X.XXX ± 0.005 CORNER RADIUS OR CHAMFER 0.005 TO 0.015 UNITS ARE INCHES [MM]	PURDUE PROPULSION	QUANTITY:	REVISION A
		Part Name: End_Vessel	
		Drawn By:	
		MATERIAL: Stainless Steel 304	
		DATE: 8/22/2014	1 OF 1

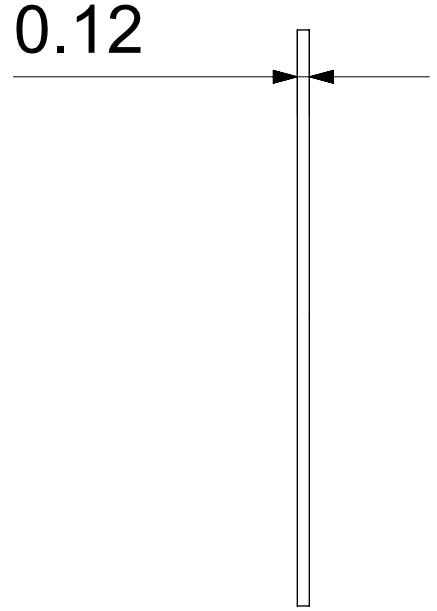

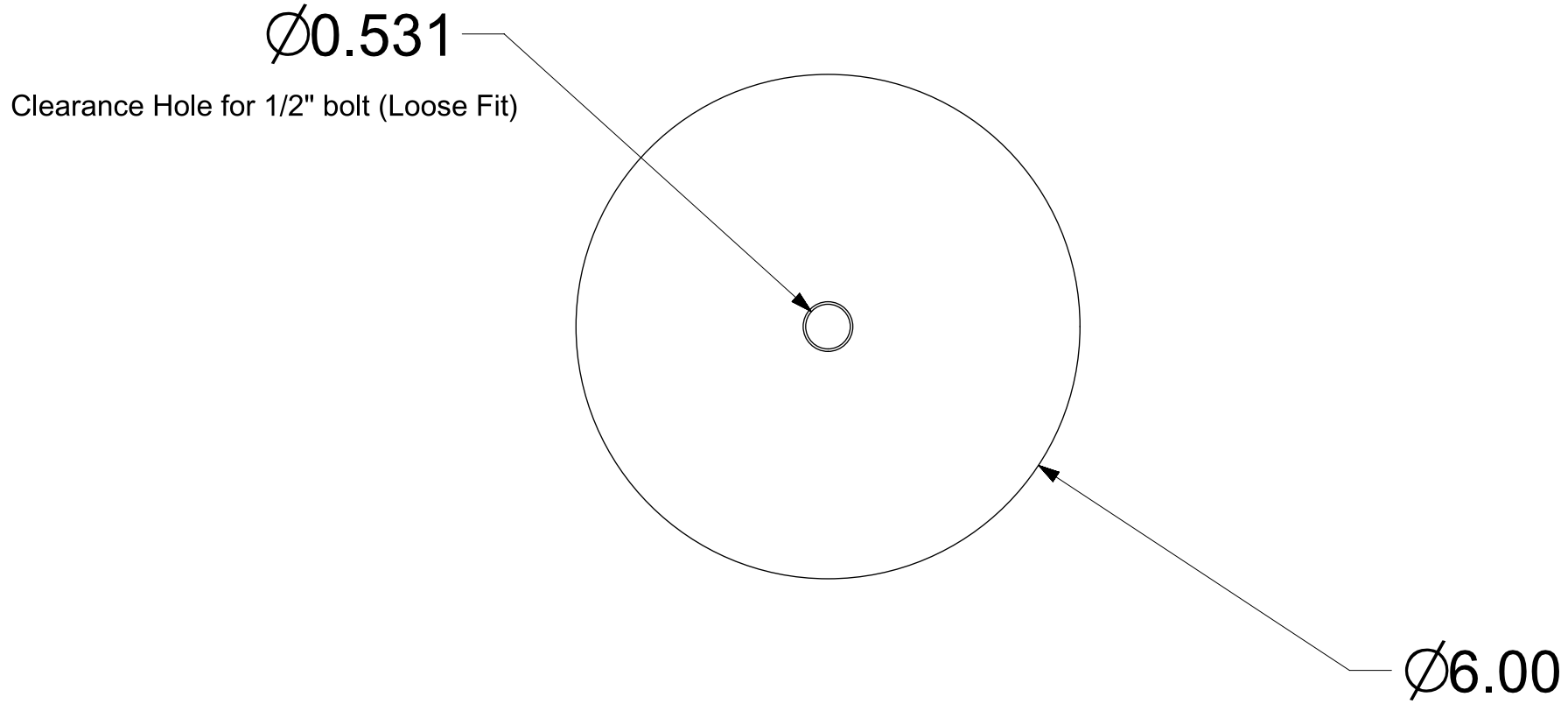

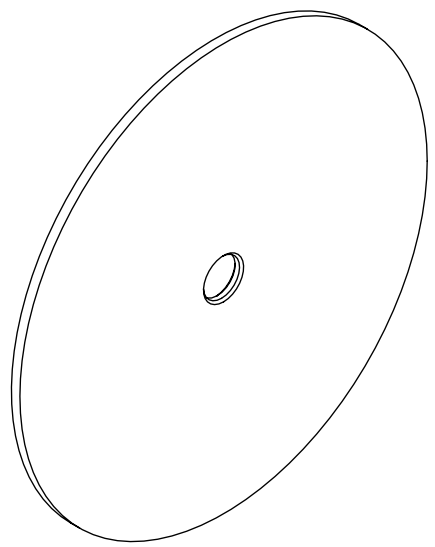

1. Part to be free of oil, grease, burrs, contaminants and surface imperfections

TOLERANCES UNLESS OTHERWISE NOTED X.X ± 0.015 Angles ± 0.5° X.XX ± .010 X/X ± 1/64 X.XXX ± 0.005 CORNER RADIUS OR CHAMFER 0.005 TO 0.015 UNITS ARE INCHES [MM]	125	PURDUE PROPULSION	QUANTITY: / REVISION A Part Name: 2nd_End_Ring Drawn By: MATERIAL: Stainless Steel 304 DATE: 8/22/2014 / 1 OF 1

175

SECTION A-A

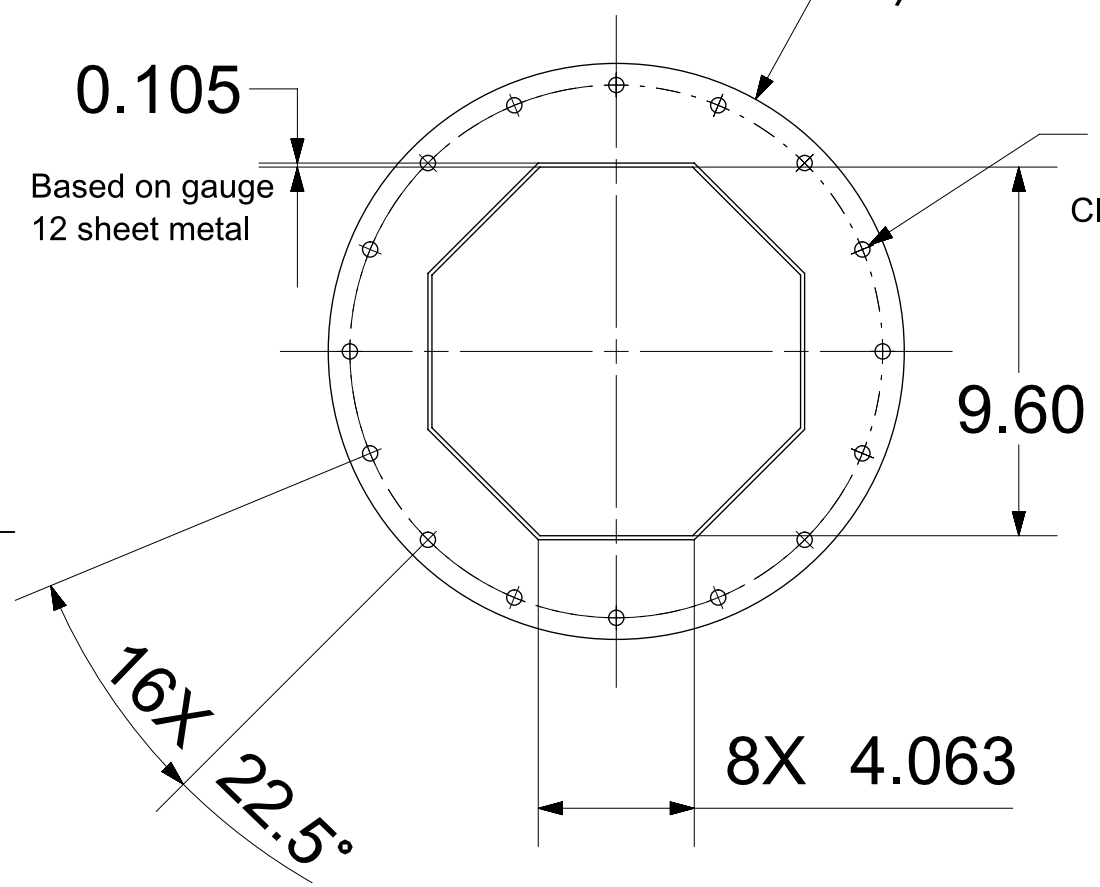

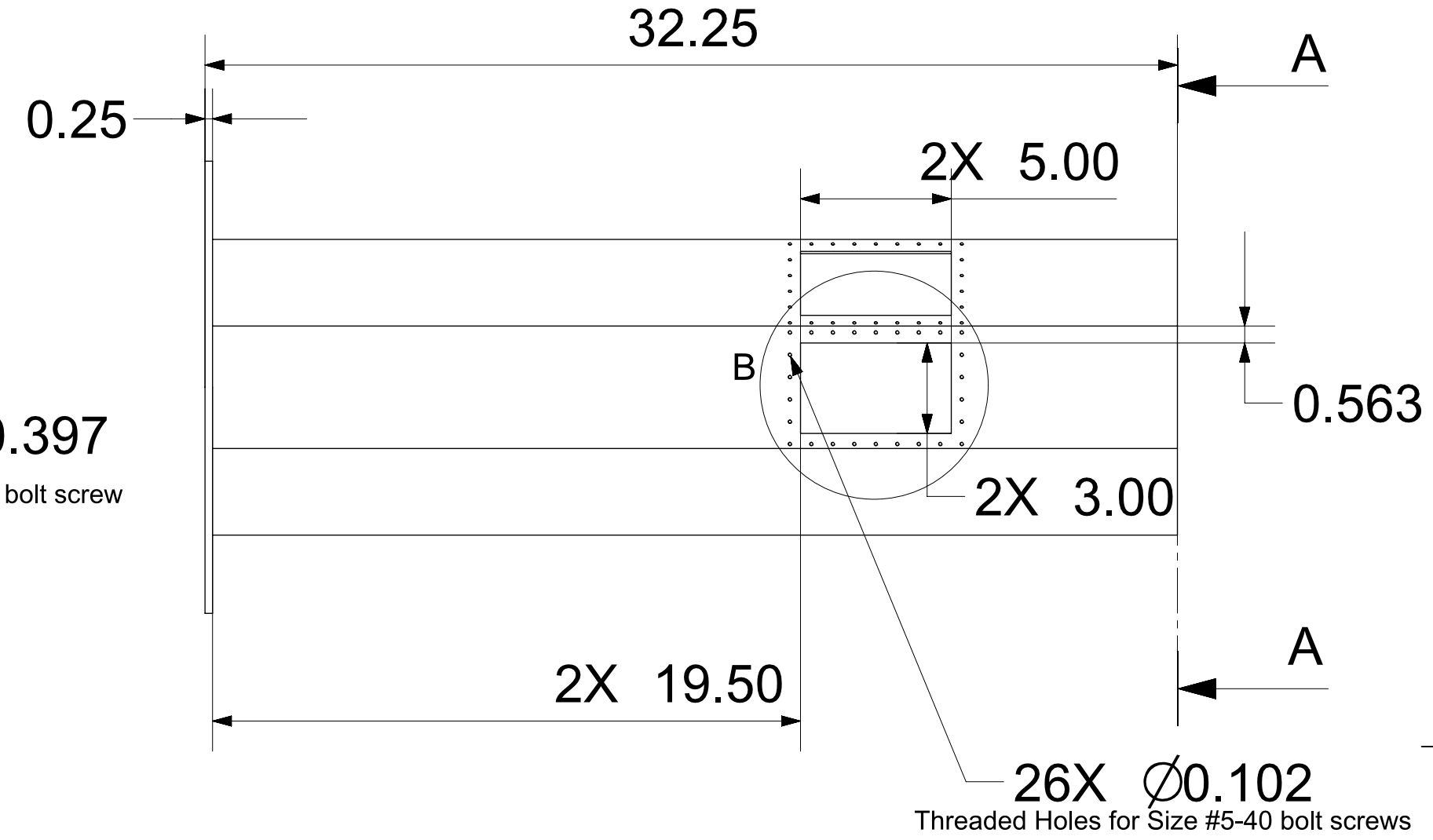

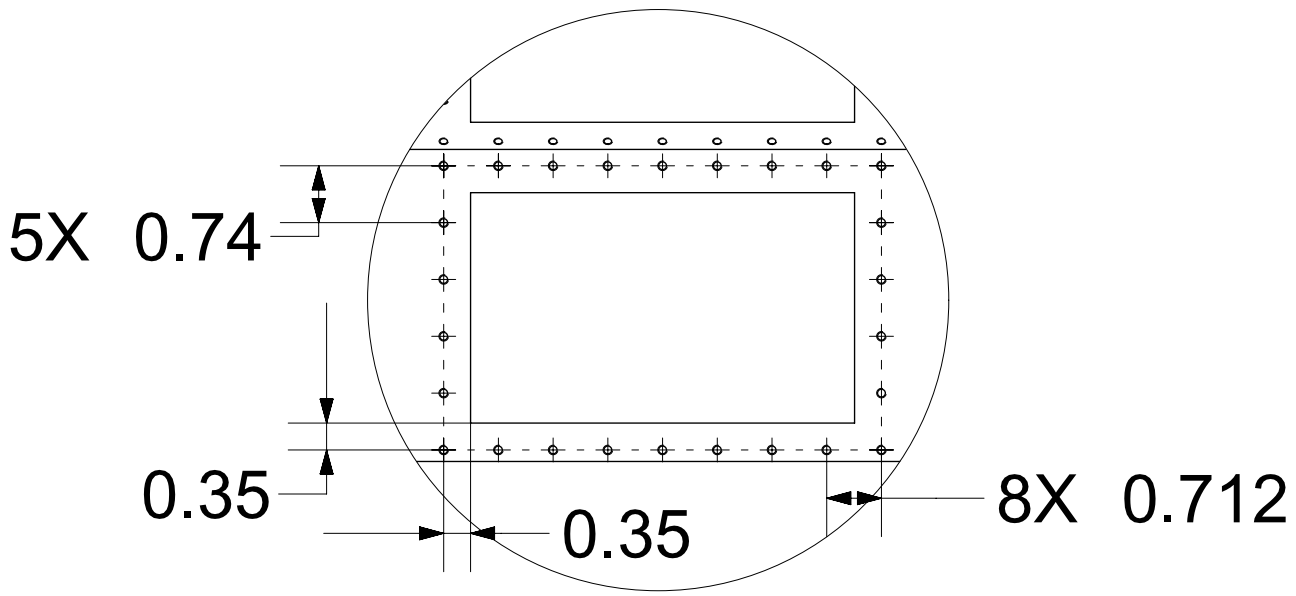

DETAIL B
SCALE 2:5

1. Part to be free of oil, grease, burrs, contaminants and surface imperfections

TOLERANCES UNLESS OTHERWISE NOTED X.X ±0.015 Angles ±0.5° X.XX ±.010 X/X ±1/64 X.XXX ±0.005 CORNER RADIUS OR CHAMFER 0.005 TO 0.015 UNITS ARE INCHES [MM]	125	QUANTITY:	REVISION A
		Part Name: Octagonal_Duct	
		Drawn By:	
		MATERIAL: Stainless Steel 304	
		DATE: 8/22/2014	1 OF 1

176

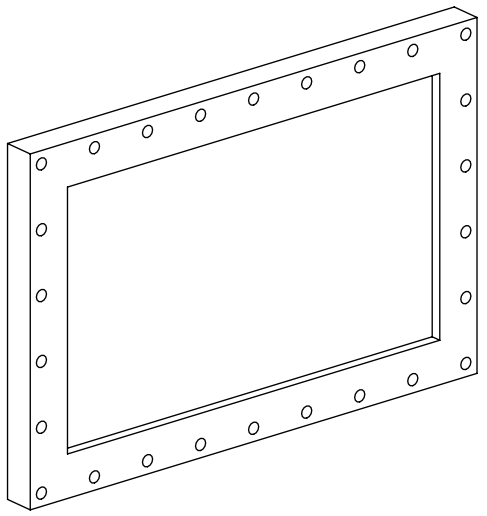

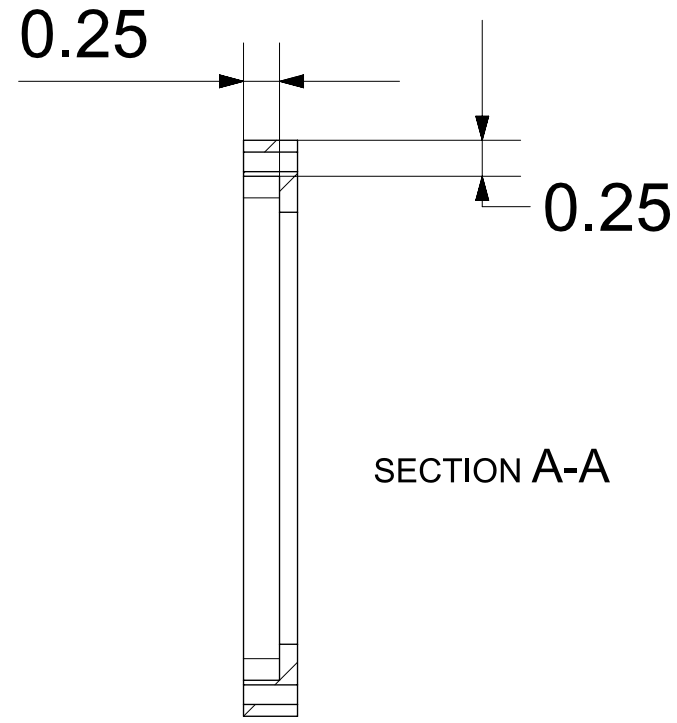

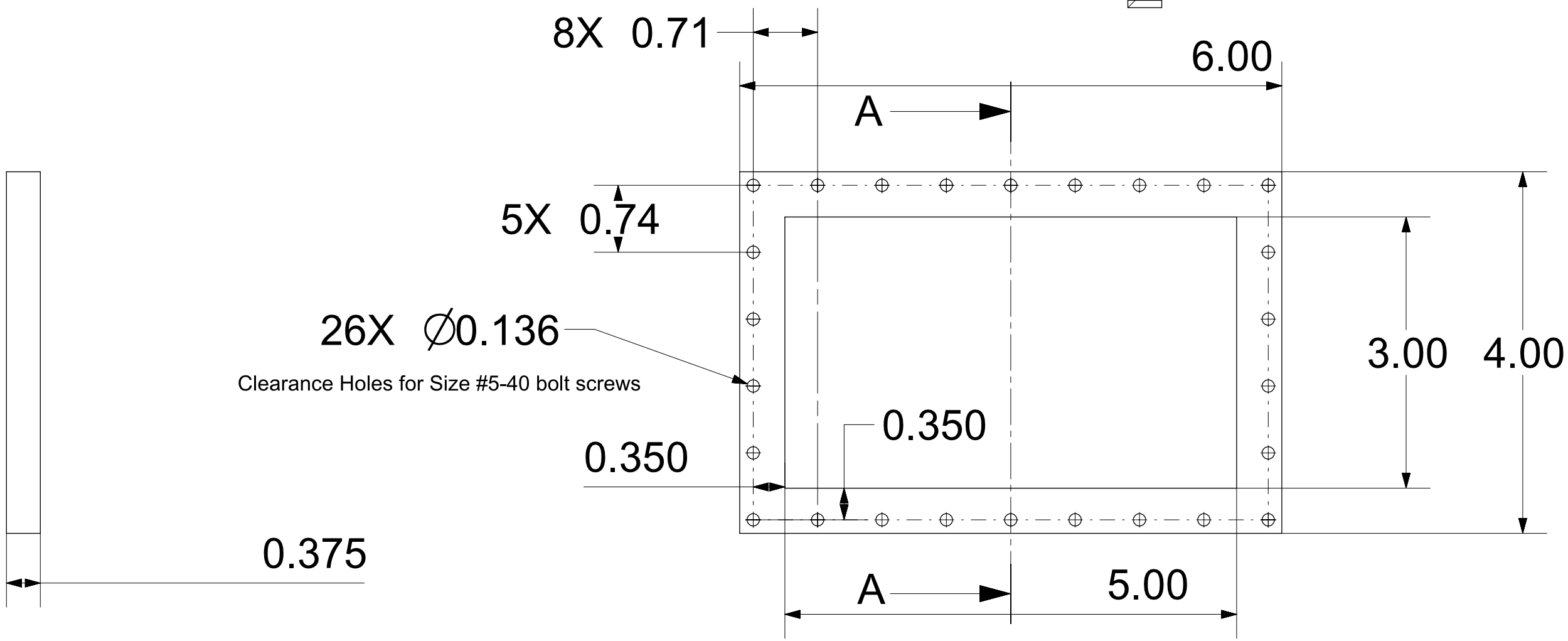

TOLERANCES UNLESS OTHERWISE NOTED X.X ±0.015 Angles ±0.5° X.XX ±.010 X/X ±1/64 X.XXX ±0.005 CORNER RADIUS OR CHAMFER 0.005 TO 0.015 UNITS ARE INCHES [MM]	125	QUANTITY:	REVISION A
		Part Name: Window_Flange	
		Drawn By:	
		MATERIAL: Stainless Steel 304	
		DATE: 8/22/2014	1 OF 1

1. Part to be free of oil, grease, burrs, contaminants and surface imperfections

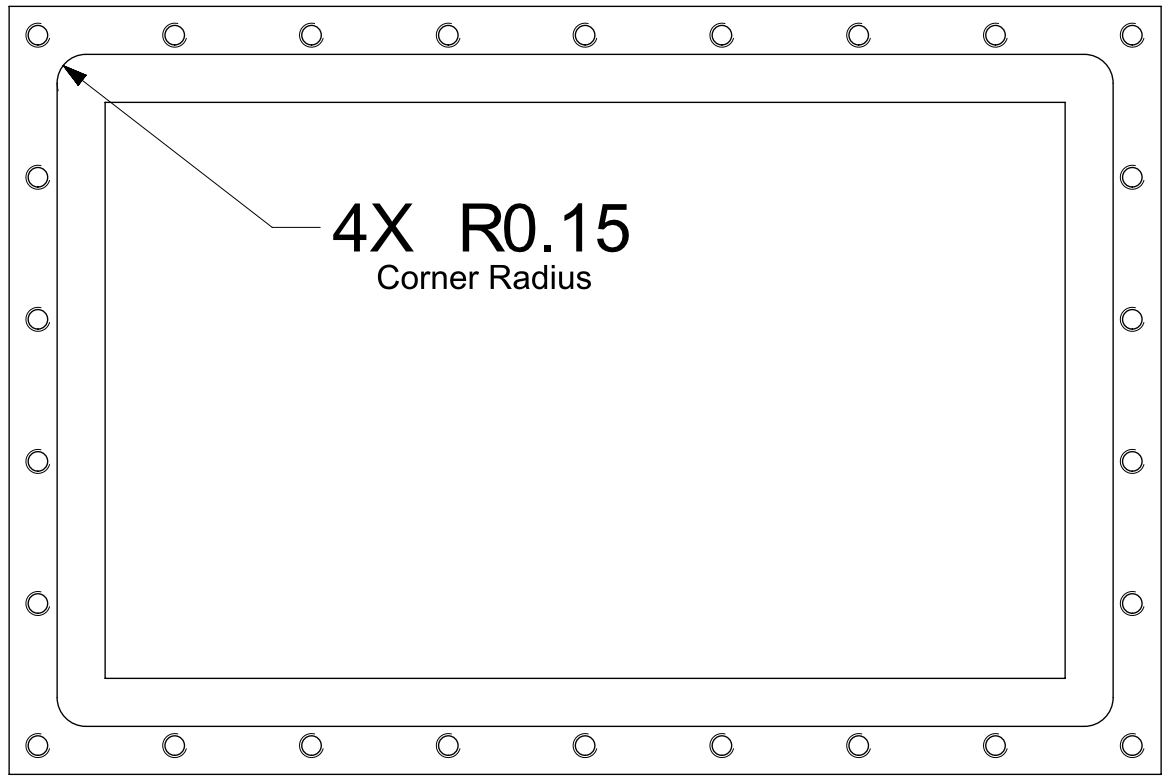

View from the interior of the widow flange

1. Part to be free of oil, grease, burrs, contaminants and surface imperfections

TOLERANCES UNLESS OTHERWISE NOTED		QUANTITY:	REVISION A
X.X ±0.015	Angles ±0.5°	Part Name: Window_Flange_pg2	
X.XX ±.010	X/X ±1/64	Drawn By:	
X.XXX ±0.005		MATERIAL: Stainless Steel 304	
CORNER RADIUS OR CHAMFER 0.005 TO 0.015		DATE: 8/22/2014	1 OF 1
UNITS ARE INCHES [MM]			

125

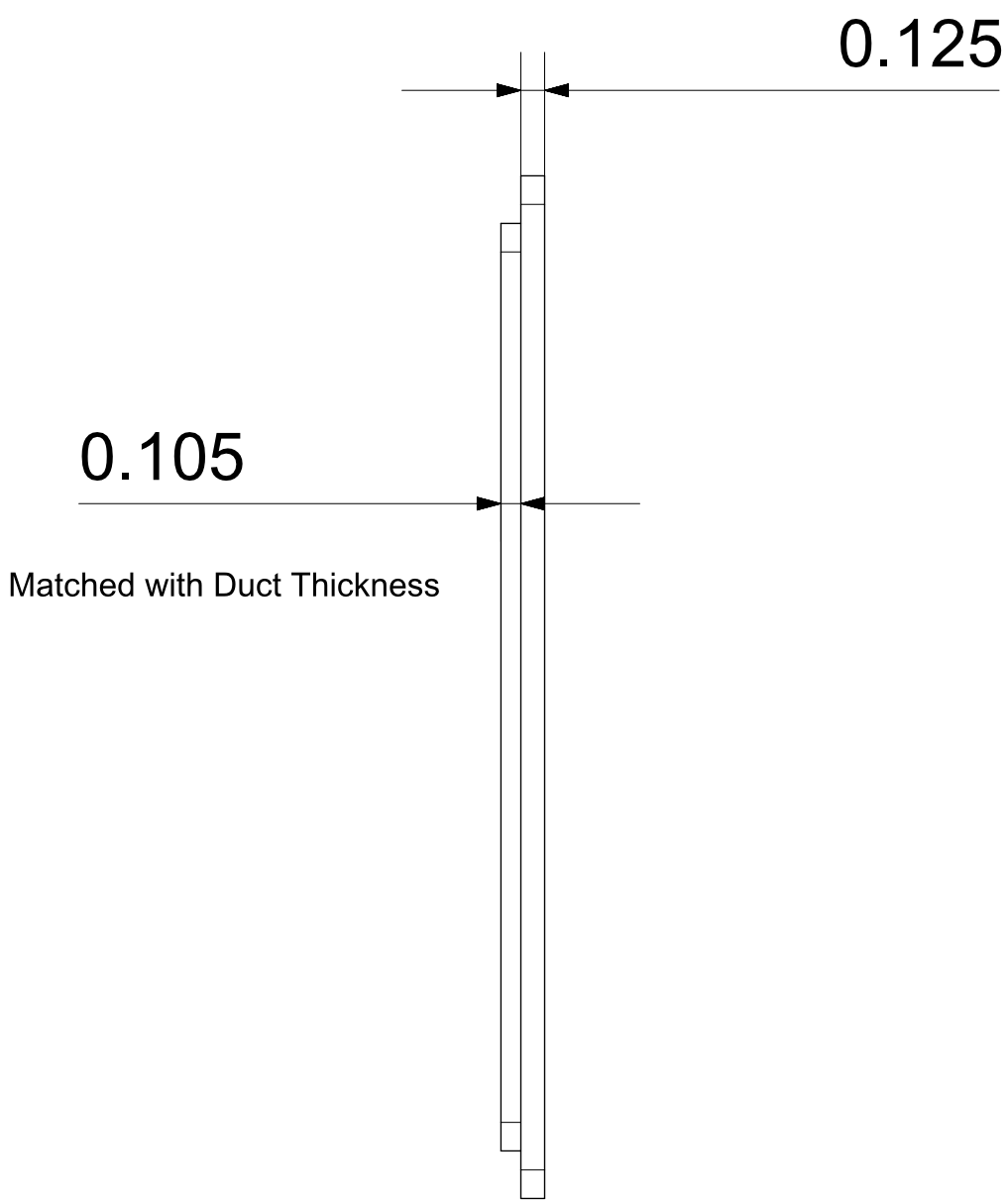

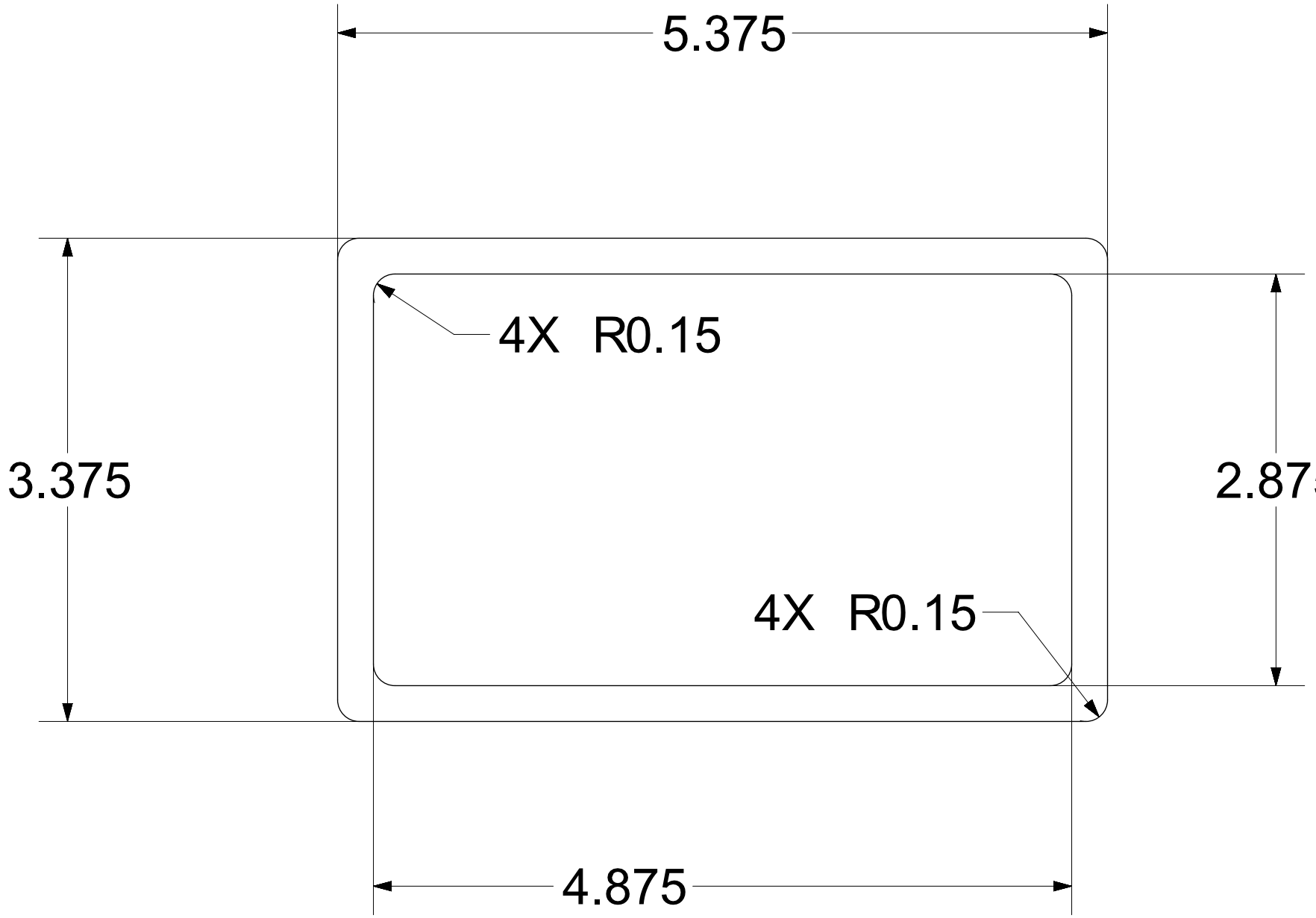

1. Part to be free of oil, grease, burrs, contaminants and surface imperfections

TOLERANCES UNLESS OTHERWISE NOTED		QUANTITY:	REVISION A
X.X ±0.015 Angles ±0.5°		Part Name: IR_Quartz_Window	
X.XX ±.010 X/X ±1/64		Drawn By: Jesse Adams	
X.XXX ±0.005		MATERIAL: GE 124	
CORNER RADIUS OR CHAMFER 0.005 TO 0.015		DATE: 8/22/2014	1 OF 1
UNITS ARE INCHES [MM]			

125

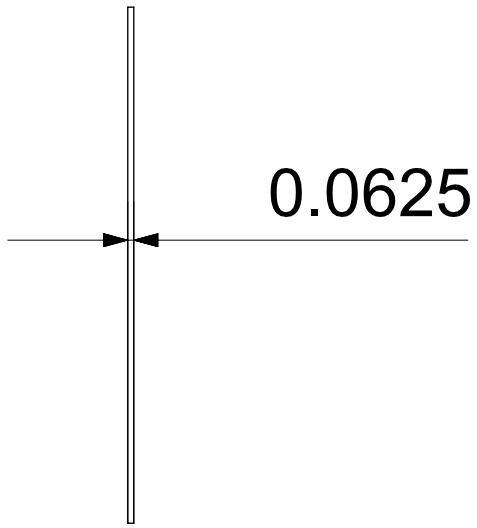

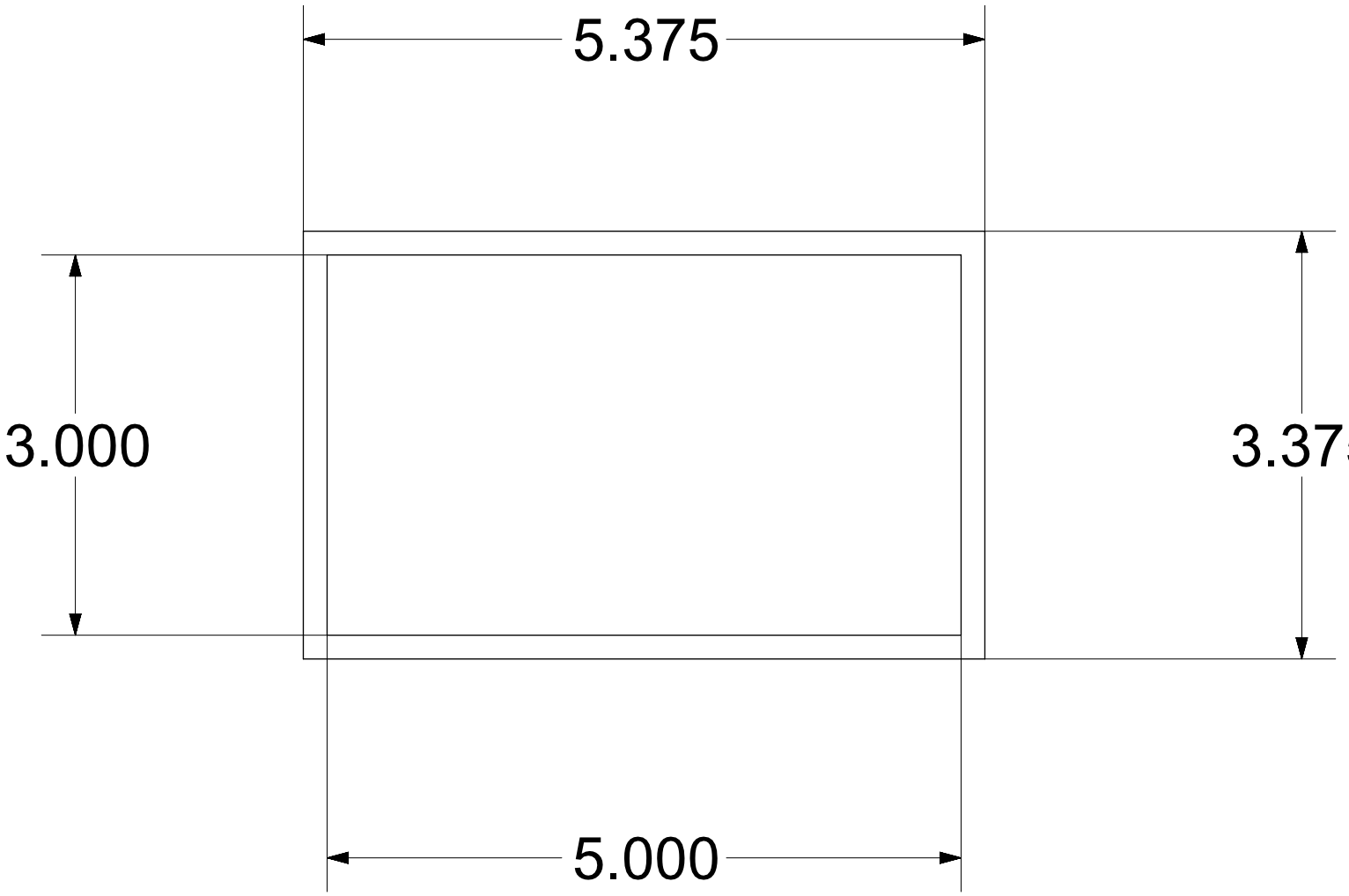

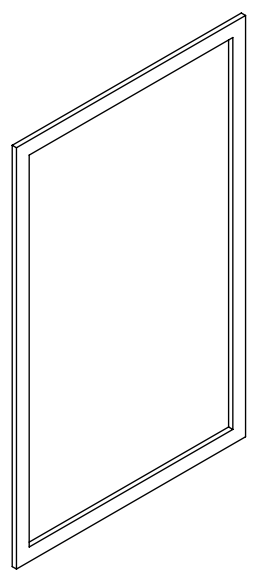

1. Part to be free of oil, grease, burrs, contaminants and surface imperfections

TOLERANCES UNLESS OTHERWISE NOTED X.X ±0.015 Angles ±0.5° X.XX ±.010 X/X ±1/64 X.XXX ±0.005 CORNER RADIUS OR CHAMFER 0.005 TO 0.015 UNITS ARE INCHES [MM]	125	QUANTITY:	REVISION A
		Part Name: Grafoil_Gasket	
		Drawn By: Jesse Adams	
		MATERIAL: Grafoil	
		DATE: 8/22/2014	1 OF 1

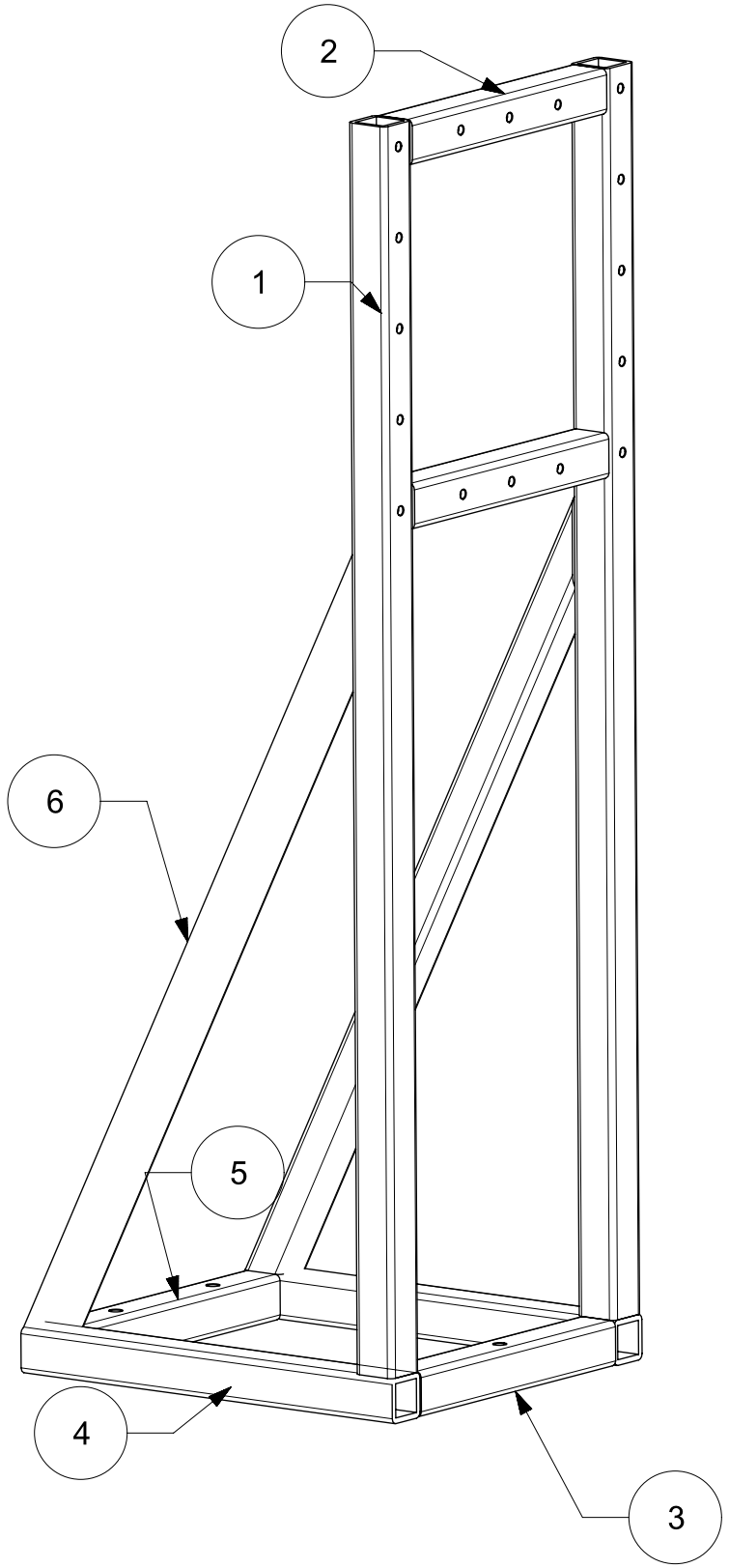

PC NO	Part Name	QTY
1	Vertical Support	2
2	Elevated Crossbar	2
3	Front Floor Crossbar	1
4	Longitudinal Floor Bar	2
5	Floor Crossbar	1
6	Slanted Support	2

1. Part to be free of oil, grease, burrs, contaminants and surface imperfections

TOLERANCES UNLESS OTHERWISE NOTED X.X ± 0.015 Angles ± 0.5° X.XX ± .010 X/X ± 1/64 125 X.XXX ± 0.005 CORNER RADIUS OR CHAMFER 0.005 TO 0.015 UNITS ARE INCHES [MM]	PURDUE PROPULSION	QUANTITY:	REVISION A
		Part Name: Test_Stand_3	
		Drawn By: Jesse Adams	
		MATERIAL: Stainless Steel 304	
		DATE: 8/22/2014	1 OF 1

181

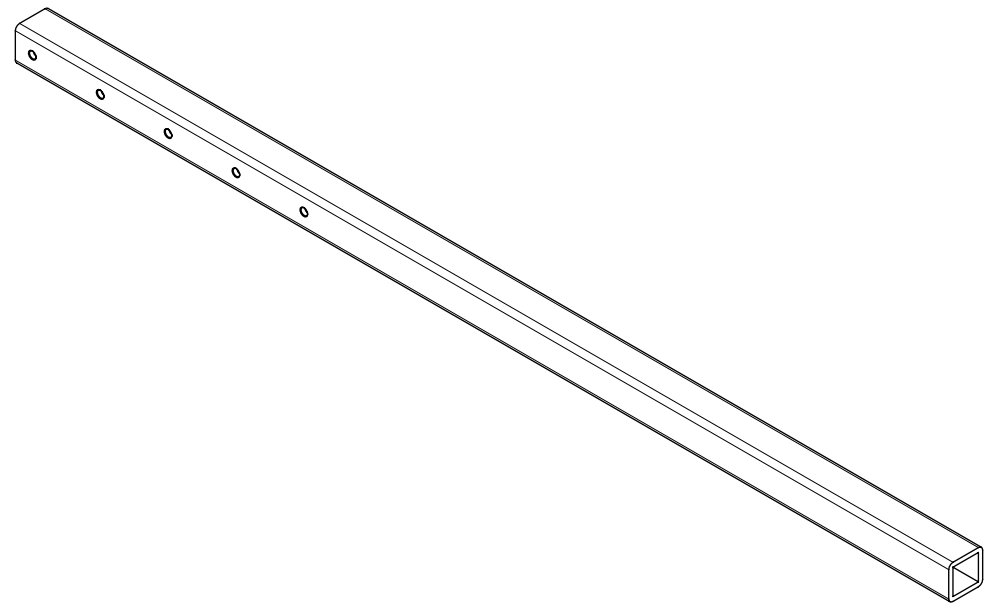

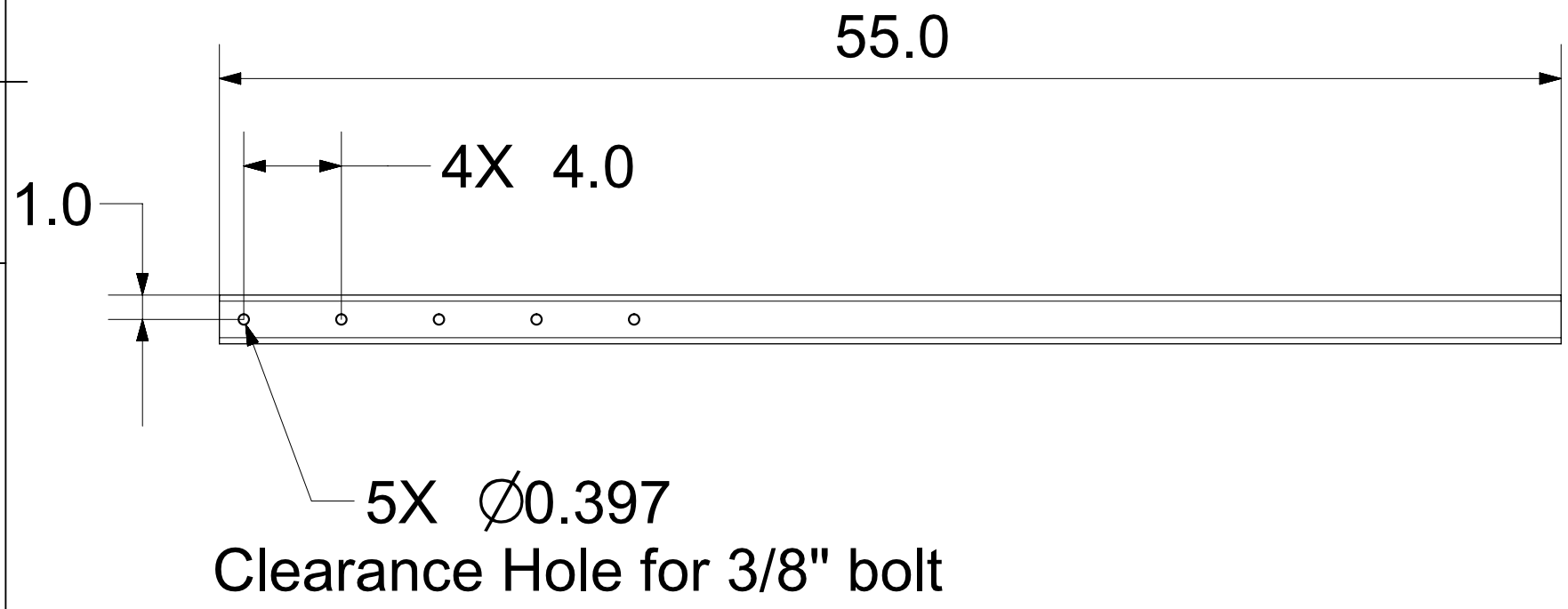

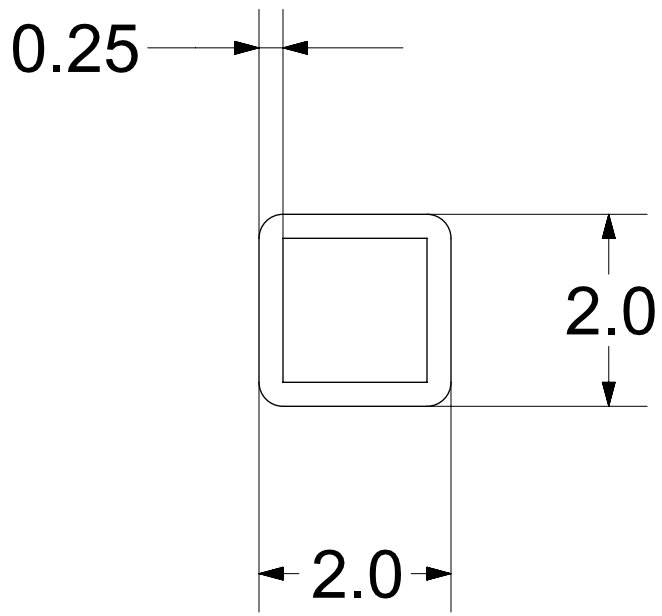

1. Part to be free of oil, grease, burrs, contaminants and surface imperfections

TOLERANCES UNLESS OTHERWISE NOTED X.X ±0.015 Angles ±0.5° X.XX ±.010 X/X ±1/64 X.XXX ±0.005 CORNER RADIUS OR CHAMFER 0.005 TO 0.015 UNITS ARE INCHES [MM]	125	QUANTITY:	REVISION A
		Part Name: Vertical_Support	
		Drawn By: Jesse Adams	
		MATERIAL: Stainless Steel 304	
		DATE: 8/22/2014	1 OF 1

182

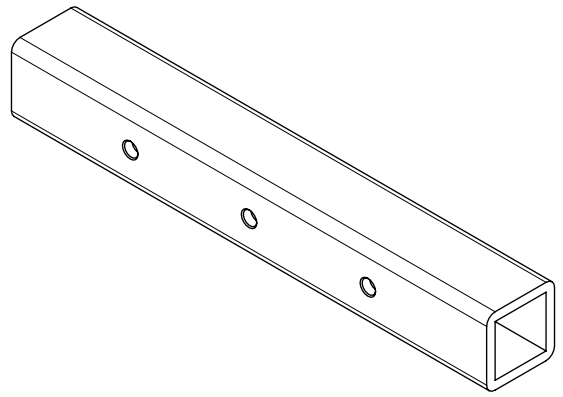

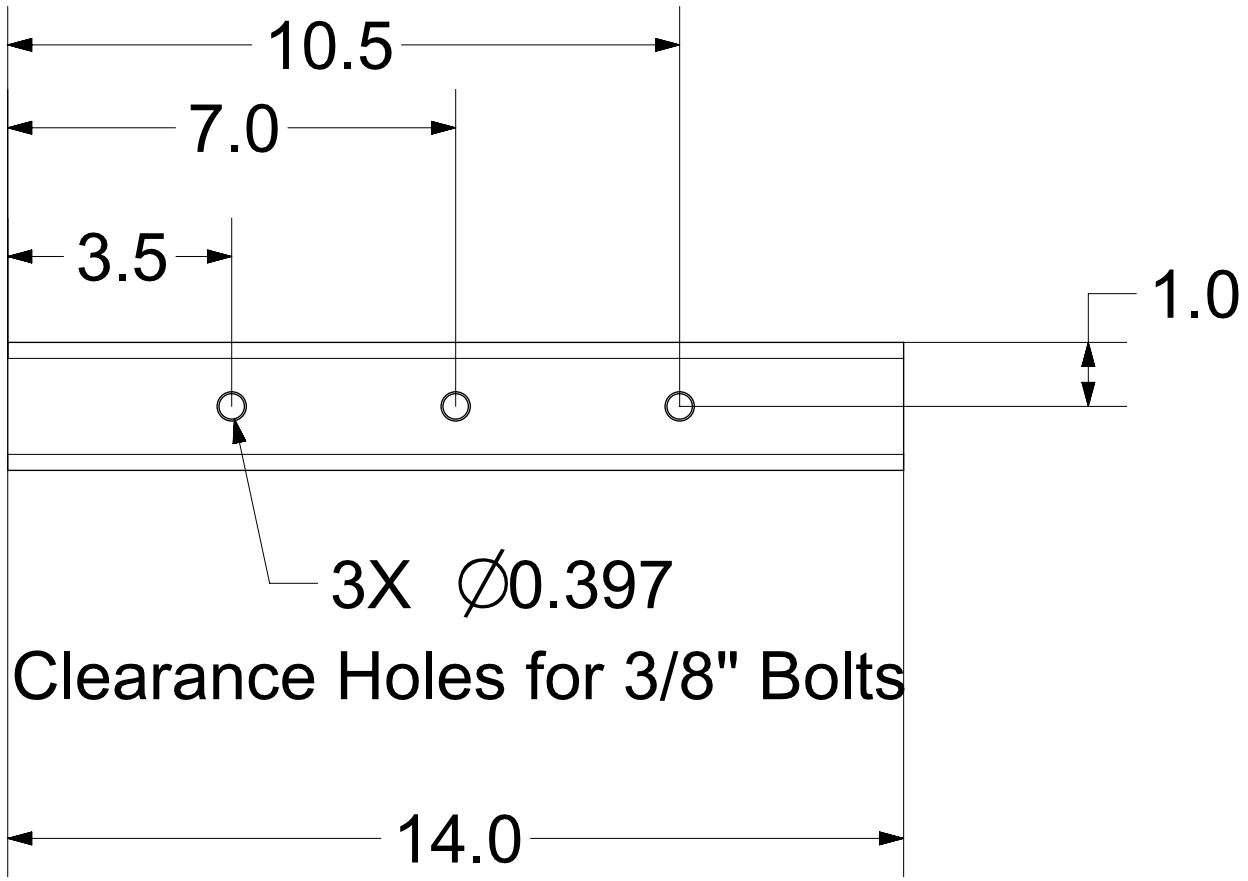

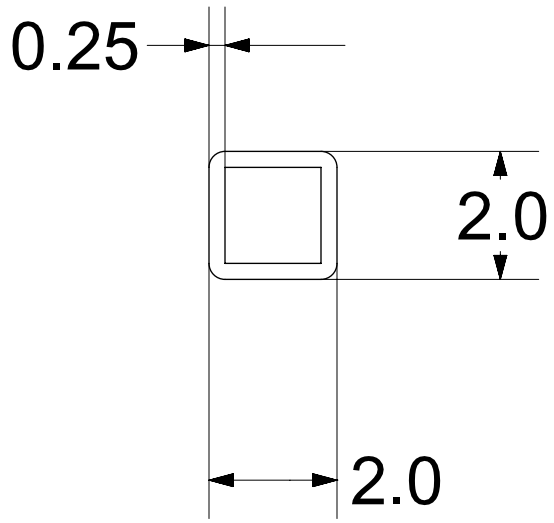

1. Part to be free of oil, grease, burrs, contaminants and surface imperfections

TOLERANCES UNLESS OTHERWISE NOTED X.X ±0.015 Angles ±0.5° X.XX ±.010 X/X ±1/64 X.XXX ±0.005 CORNER RADIUS OR CHAMFER 0.005 TO 0.015 UNITS ARE INCHES [MM]	125	QUANTITY:	REVISION A
		Part Name: Elevated_Crossbar	
		Drawn By: Jesse Adams	
		MATERIAL: Stainless Steel 304	
		DATE: 8/22/2014	1 OF 1

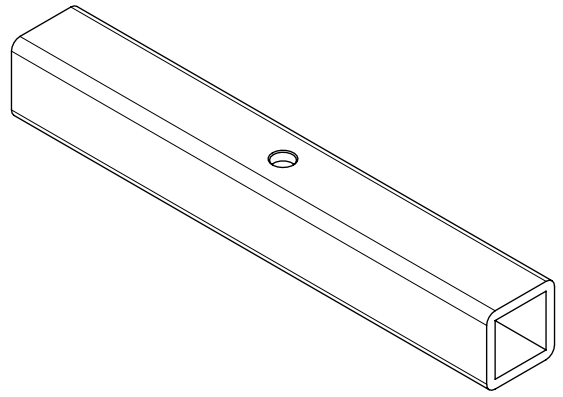

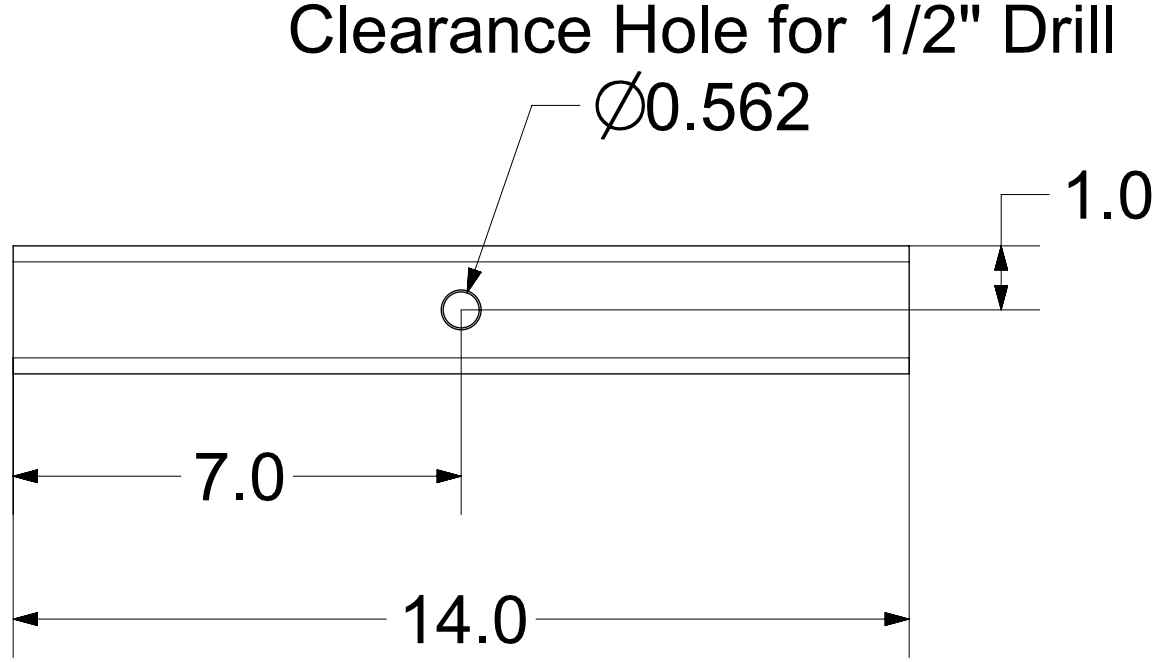

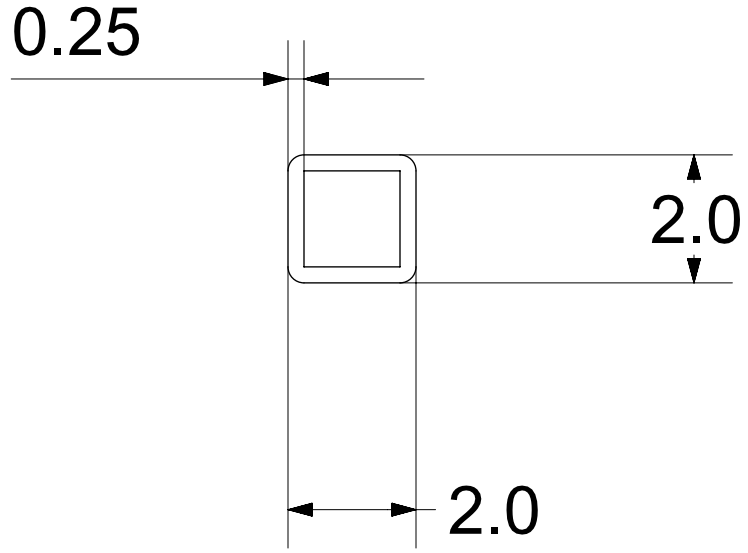

1. Part to be free of oil, grease, burrs, contaminants and surface imperfections

TOLERANCES UNLESS OTHERWISE NOTED X.X ±0.015 Angles ±0.5° X.XX ±.010 X/X ±1/64 X.XXX ±0.005 CORNER RADIUS OR CHAMFER 0.005 TO 0.015 UNITS ARE INCHES [MM]	125	QUANTITY:	REVISION A
		Part Name: Front_Floor_Crossbar	
		Drawn By: Jesse Adams	
		MATERIAL: Stainless Steel 304	
		DATE: 8/22/2014	1 OF 1

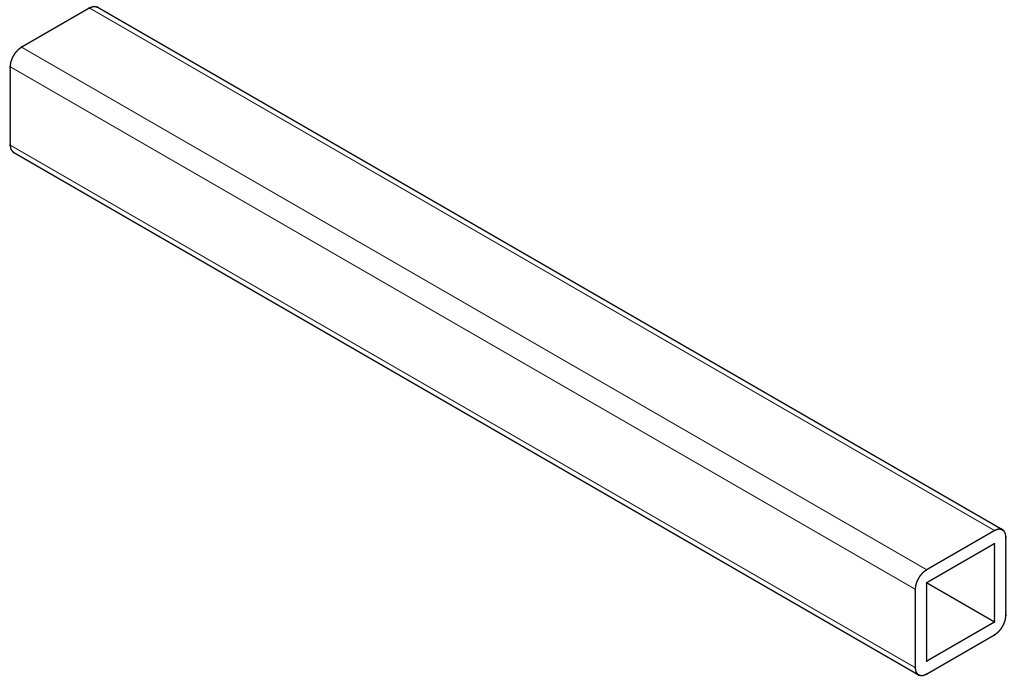

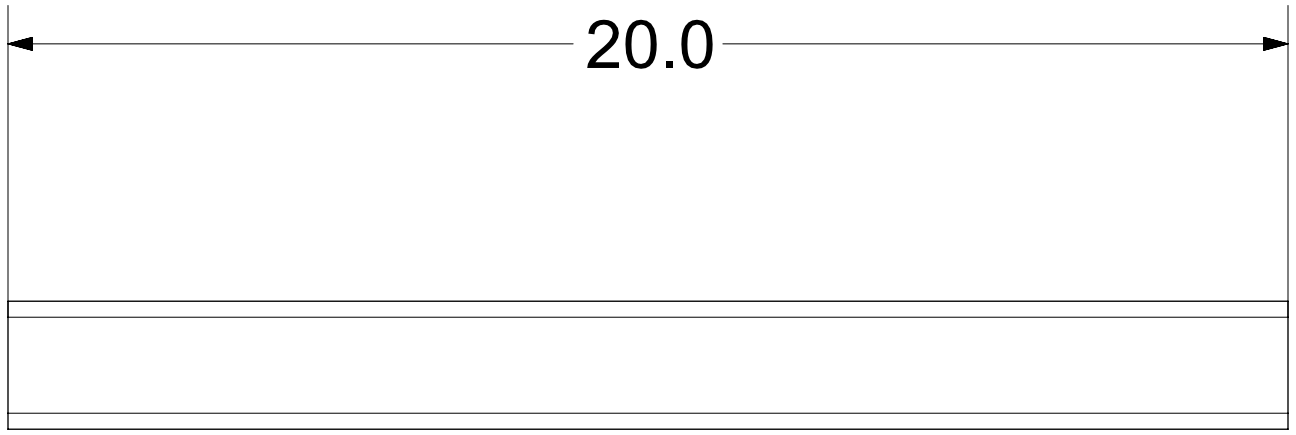

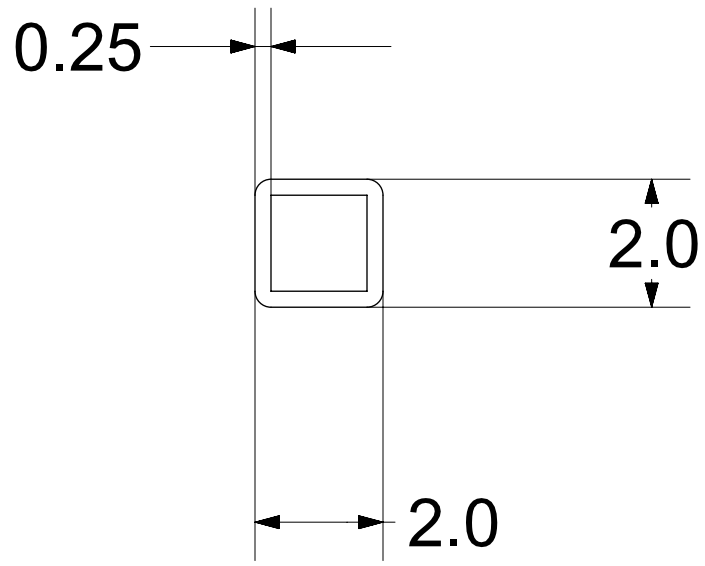

1. Part to be free of oil, grease, burrs, contaminants and surface imperfections

TOLERANCES UNLESS OTHERWISE NOTED X.X ±0.015 Angles ±0.5° X.XX ±.010 X/X ±1/64 X.XXX ±0.005 CORNER RADIUS OR CHAMFER 0.005 TO 0.015 UNITS ARE INCHES [MM]	125	PURDUE PROPULSION	QUANTITY: / REVISION A Part Name: Longitudinal_Floor_Bar Drawn By: Jesse Adams MATERIAL: Stainless Steel 304 DATE: 8/22/2014 / 1 OF 1

185

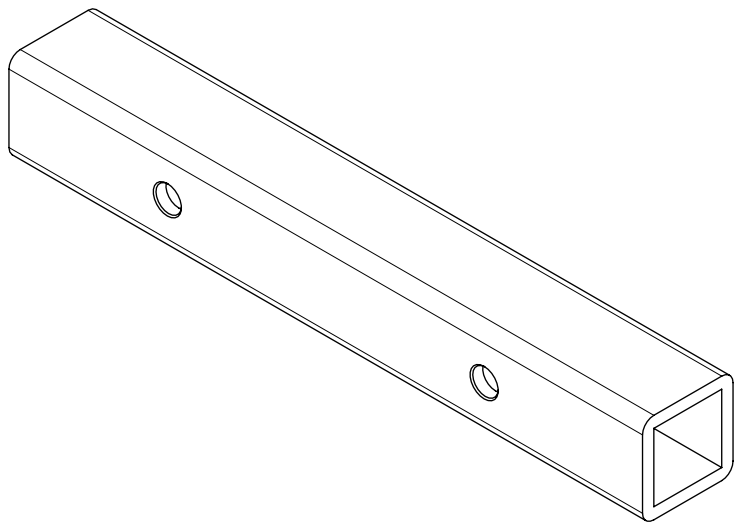

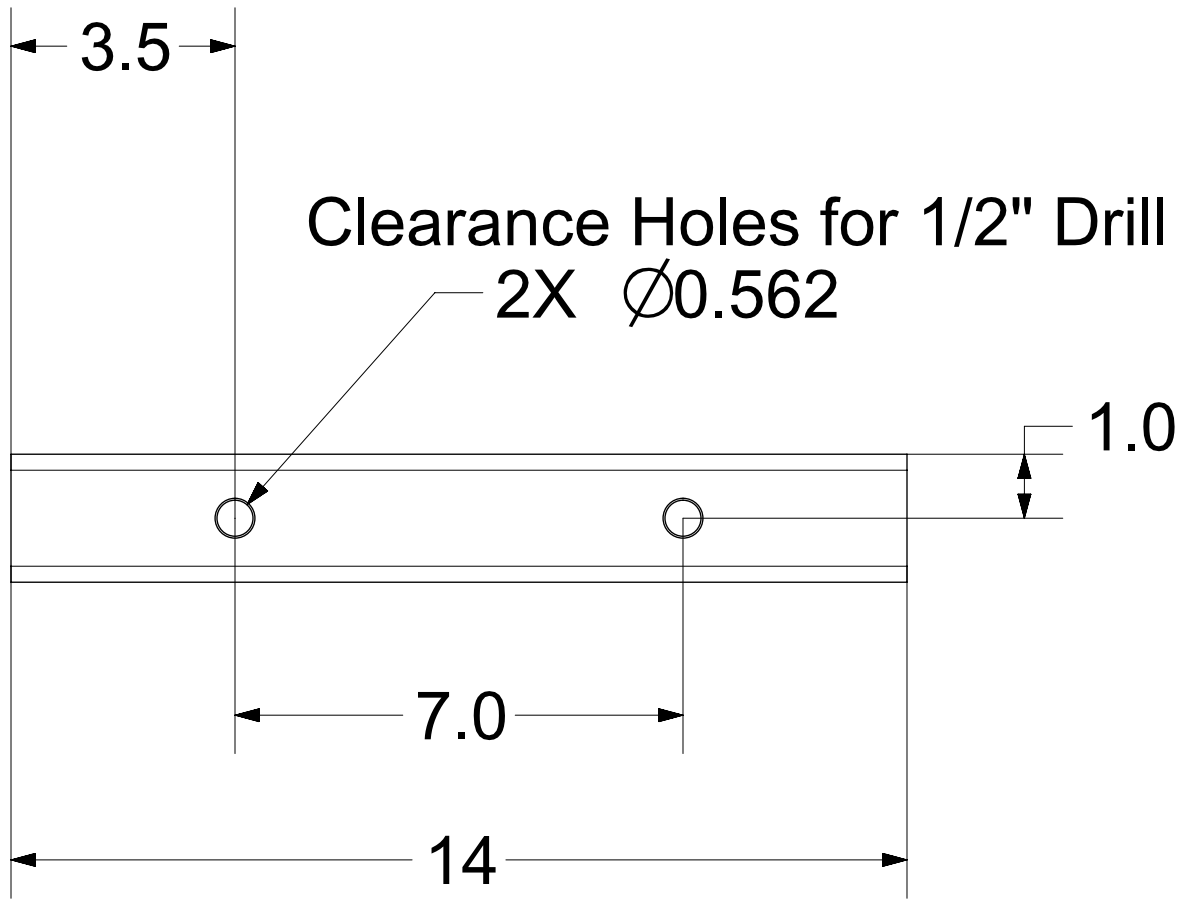

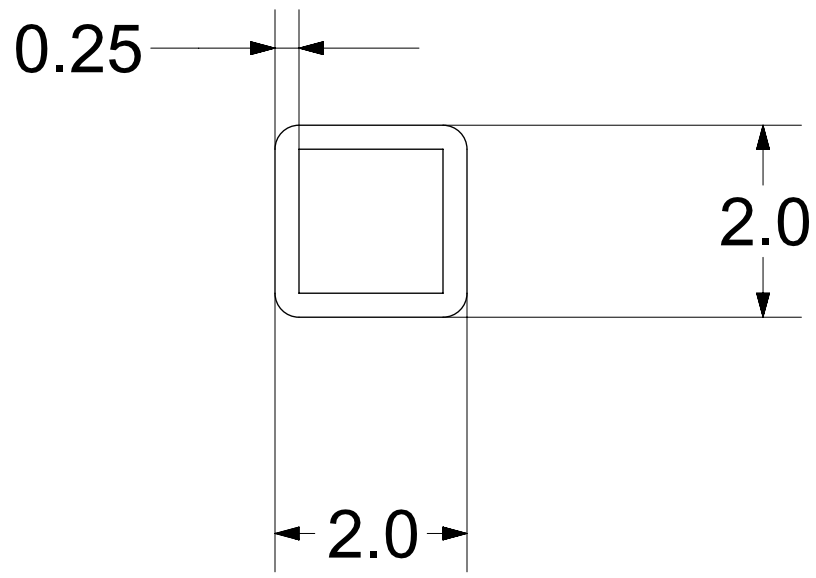

1. Part to be free of oil, grease, burrs, contaminants and surface imperfections

TOLERANCES UNLESS OTHERWISE NOTED X.X ±0.015 Angles ±0.5° X.XX ±.010 X/X ±1/64 X.XXX ±0.005 CORNER RADIUS OR CHAMFER 0.005 TO 0.015 UNITS ARE INCHES [MM]	125	QUANTITY:	REVISION A
		Part Name: Floor_Crossbar	
		Drawn By: Jesse Adams	
		MATERIAL: Stainless Steel 304	
		DATE: 8/22/2014	1 OF 1

186

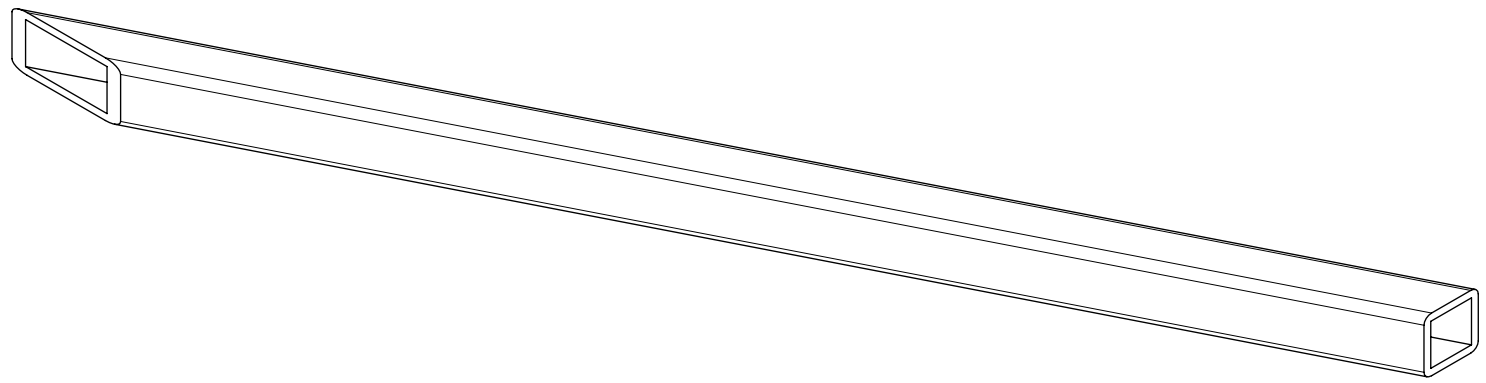

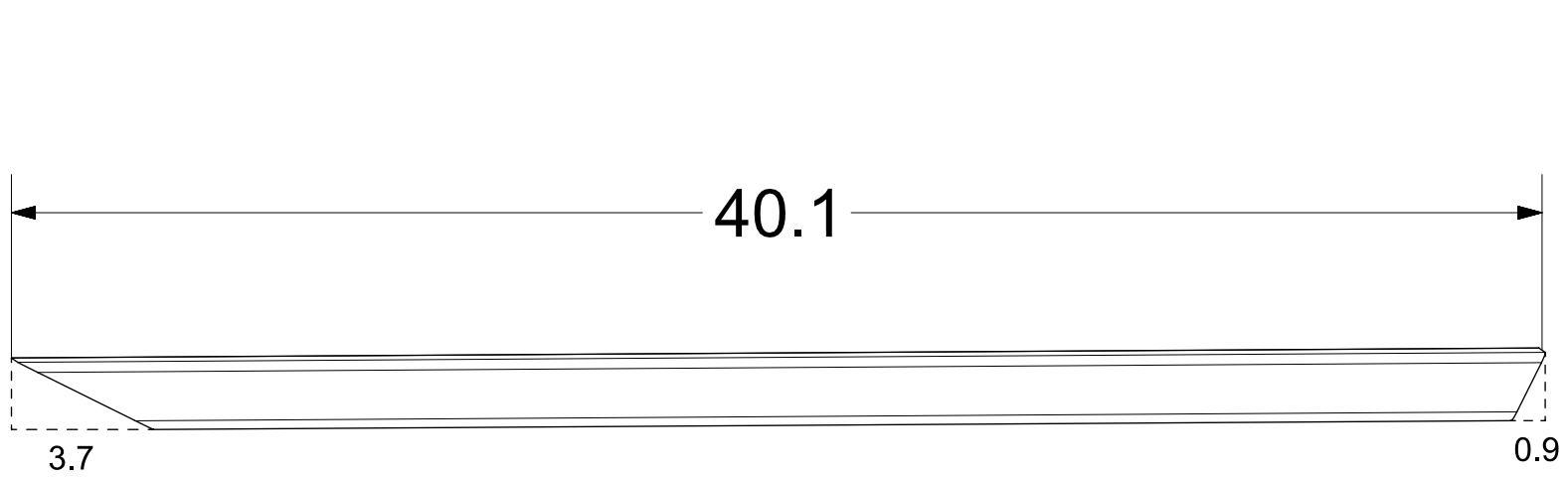

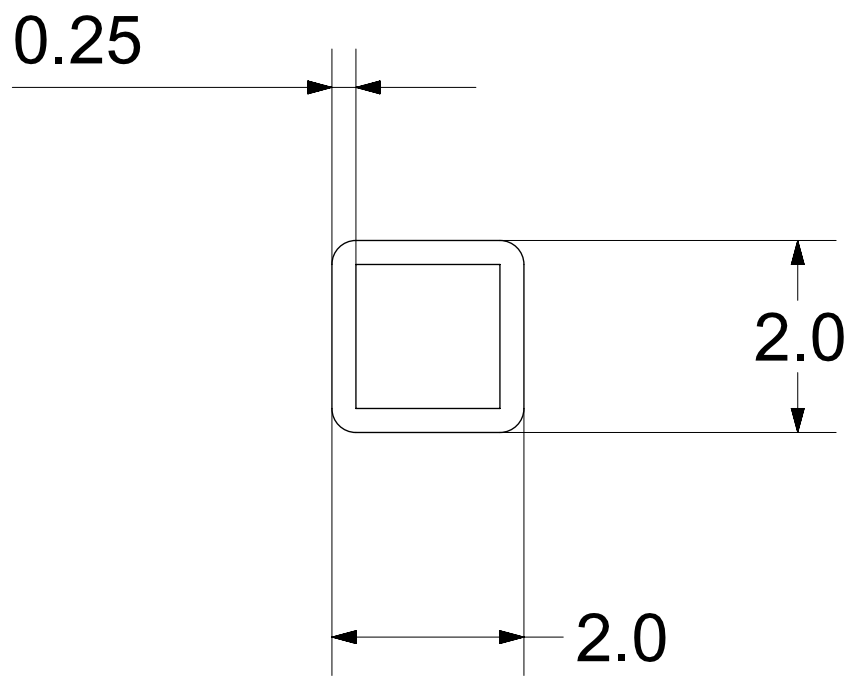

1. Part to be free of oil, grease, burrs, contaminants and surface imperfections

TOLERANCES UNLESS OTHERWISE NOTED X.X ±0.015 Angles ±0.5° X.XX ±.010 X/X ±1/64 X.XXX ±0.005 CORNER RADIUS OR CHAMFER 0.005 TO 0.015 UNITS ARE INCHES [MM]	125	QUANTITY:	REVISION A
		Part Name: Slanted_Support	
		Drawn By:Jesse Adams	
		MATERIAL: Stainless Steel 304	
		DATE: 8/22/2014	1 OF 1